TECHNISCHE UNIVERSITÄT MÜNCHEN
Lehrstuhl für Baumechanik

Frequency Dependent Modeling for the Prediction of the Sound Transmission in Timber Constructions

Christoph Karl Winter

Vollständiger Abdruck der von der Ingenieurfakultät Bau Geo Umwelt der Technischen Universität München zur Erlangung des akademischen Grades eines

Doktor-Ingenieurs

genehmigten Dissertation.

Vorsitzender: Prof. Dr.-Ing. Stefan Winter

Prüfer der Dissertation:

1. Prof. Dr.-Ing. habil. Gerhard H. Müller
2. Prof. Dr. Ulrich Schanda
3. Prof. Dr. Brian Mace

Die Dissertation wurde am 05.04.2018 bei der Technischen Universität München eingereicht und durch die Ingenieurfakultät Bau Geo Umwelt am 05.07.2018 angenommen.

Abstract

This thesis presents a numerical approach for the prediction of vibrational energy flow in structures. Thereby, the sound transmission across junctions of cross laminated timber (CLT) plates is determined. The thesis is part of the joint research project "Vibroacoustics in the planning process for timber constructions".

In order to predict the sound transmission, various modeling aspects, which additionally vary within the building acoustics frequency range, have to be taken into account: The spatial variation of the response, the uncertainty of material properties and loading positions, the adequate modeling of boundary and coupling conditions, as well as the numerous wave types which occur in an orthotropic, layered material including through-thickness effects. These lead to requirements which exceed the capability of a single, classical method.

In the low frequency range, the Finite Element Method (FEM) is a well-established tool. The applicability of the classical FEM is limited since the sensitivity of the results increases with frequency. For higher frequencies and thus shorter wave lengths, the plates adjacent to a junction can be considered as semi-infinite if reflections occur with a significantly smaller amplitude or incoherently to the excitation. This structural behavior enables the use of statistical methods like the Statistical Energy Analysis (SEA). It delivers averaged results and thus copes with their sensitivity. In structural dynamics, the SEA is typically limited to the wave transmission between plate-like structures. For wood, the elastic modulus perpendicular to the fiber direction is about one thirtieth of the one in fiber direction. Therefore, the thickness modes occur at comparatively low frequencies. Using the FEM, solid elements are able to represent these through-thickness effects. As the FEM and the SEA have a restricted validity regarding the frequency range, averaging techniques of the SEA are applied in the post-processing of the FEM to obtain an adapted hybrid approach, the Energy Flow Analysis (EFA).

This thesis begins with the fundamental theory related to CLT, wave types in orthotropic plates and the SEA. Then, the numerical implementation of the EFA as well as different evaluation techniques and output quantities are introduced. In practice, the structure-borne

sound transmission is described by means of the vibration reduction index according to DIN EN ISO 12354. This prediction model is not applicable for structures made of CLT since it is based on a simplified version of the SEA assuming thin, semi-infinite plates which only contain bending waves. Afterwards, several investigations at L-, T- and X-junctions are presented where physical properties of the components, the type of the connection and the way of loading are varied. The sensitivity of the energy flow prediction with respect to the varied parameters is discussed in dependency on the frequency range showing that the results are subject to a considerable variability. Moreover, the obtained results are compared to analytical solutions of the SEA. The investigations indicate that it is convenient to divide the frequency domain into three ranges which offer distinct methods, modeling techniques and evaluation quantities. A web-based, interactive application "Vibroacoustics of Plates" has been made available for the identification of the frequency range limits as a function of the physical properties of the structure of interest.

Contents

List of Symbols

Superscripts and diacritics

$(\tilde{\ })$	Averaged over frequency band
$(\bar{\ })$	Averaged over realizations
$(<\ >)$	Averaged over both transmission directions
$(\_)$	Complex quantity
$(\_^*)$	Conjugated complex quantity
$(\ ^*)$	Homogenized material parameter (only in subsection 2.1.3)
$(\ ^T)$	Transpose
$(\ ^{-1})$	Inverse
[ ]	Matrix

Subscripts

$\parallel$	Parallel to the fiber direction
$\perp$	Perpendicular to the fiber direction
0	Amplitude, Maximum value
diss	Dissipated
e	Element
eff	Effective
f	Frequency
g	Gauß point
g	Group wave (bending)
kin	Kinetic
hp	Half power bandwith
l	Lower
ij	Observed and loaded subsystem in the case of E_{ij} and A_{ij}

i,j		Index of eigenvectors, -modes
pot		Potential
ref		Reference
situ		Factual field situation
u		Upper
v_z		Based on the surface velocity perpendicular to the plane of the plate

A		Sum of all wave types
B		Bending
L		Longitudinal
P		Plate
R		Radial
T		Tangential
TM		Thickness Modes
S		Shear

Greek letters

α	N	Real part of F
β	N	Imaginary part of F
β_{ij}		Modal coupling factor
ε		Strain
ϕ	rad	Phase shift
γ		Engineering shear strain
δ		Dirac delta function
δ_{ij}		Kronecker delta
δf		Average modal frequency spacing
η		Loss factor
η^0		Total loss factor
η_{ii}		Damping (internal) loss factor
η_{ij}		Coupling loss Factor
η, ξ		Element coordinates
κ		Condition number
κ		Shear correction factor
λ	m	Wave length
μ	$\frac{\text{kg}}{\text{m}^2}$	Areal mass

μ		(True) mean
ν		Poisson's ratio
ρ	$\frac{\text{kg}}{\text{m}^3}$	Density
ρ_{FF}		Autocorrelation coefficient function of a random field $F(x,y)$
ρ_{XY}		Pearson correlation coefficient between two random variables X, Y
σ	$\frac{\text{N}}{\text{m}^2}$	Stress
τ	$\frac{\text{N}}{\text{m}^2}$	Shear stress
τ	s	Time interval between two observations
τ_{ij}		Transmission coefficient from subsystem i to subsystem j
ω	$\frac{\text{rad}}{\text{s}}$	Angular frequncy
ξ	m	Distance between two observation points

Δf_{hp}	$\frac{1}{\text{s}}$	Half power bandwith
Δf_k	$\frac{1}{\text{s}}$	Spacing between excitation frequencies
$\Delta\omega$	$\frac{\text{rad}}{\text{s}}$	Frequency band
$\boldsymbol{\Phi}$		Eigenvector
Π_{iv}	$\frac{\text{Nm}}{\text{m}^3}$	Elastic potential
Θ		Space
Ω	$\frac{\text{rad}}{\text{s}}$	Angular frequency of excitation

Latin letters

a	m	Equivalent absorption length
b	m	Width of a subsystem/ plate
c		Coefficient of variation
c	$\frac{\text{m}}{\text{s}}$	Wave velocity
c_0	$\frac{\text{m}}{\text{s}}$	Wave velocity of sound in air
d_l	m	Distance between center of the composite and of the individual layer
f	$\frac{1}{\text{s}}$	Frequency
f_c	$\frac{1}{\text{s}}$	Critical frequency
f_m	$\frac{1}{\text{s}}$	Center frequency of a frequency band
f_s	$\frac{1}{\text{s}}$	Cross-over frequency
h	m	Thickness of a subsystem/ plate
h_e	m	Element side length
h_{ij}	m	Thickness of the elastic interlayer between subsystem i and j
h_l	m	Thickness of a layer (CLT)

i		Imaginary number
k	$\frac{\text{rad}}{\text{m}}$	Wave number
l	m	Length of a subsystem/ plate
l_{ij}	m	Junction length
m		Number of subsystems
$n(\omega)$	$\frac{\text{s}}{\text{rad}}$	Modal density
n_e		Number of elements
n_f		Number of frequency steps per band
n_l		Number of loads
n_{mp}		Number of measurement positions
n_r		Number of realizations
n_{sn}		Number of surface nodes
p	$\frac{\text{N}}{\text{m}^2}$	Pressure
s		Sample standard deviation
t_α		α quantile of a Student's t-distribution
u	m	Displacement
$\ddot{u}$	m	Acceleration
v	$\frac{\text{m}}{\text{s}}$	Velocity
w		Weighting factor
$\mathbf{z}$	m	$= (x,y,z)$ Vector of location

A		Assembling
A	m^2	Area
A_{ij}	s	Energy influence coefficient,
		energy in subsystem i normalized to input power into subsystem j
B	Nm	Bending stiffness
B	$\frac{1}{\text{s}}$	Bandwith of frequency band
C_{ij}^{kl}	$\frac{\text{N}}{\text{m}^2}$	Component of fourth order stiffness tensor
D		Damping ratio
D	dB	Deviation from the true mean
D_v	dB	Velocity level difference
E	$\frac{\text{N}}{\text{m}^2}$	Elastic modulus
E_S	$\frac{\text{N}}{\text{m}^2}$	Stiffness modulus
E	Nm	Energy averaged over time and space
E_{ij}	Nm	E in subsystem i due to excitation of subsystem j
$\mathcal{E}$	Nm	Modal energy

E		Expected value
F	N	Force
F_T		Cumulative distribution function of Student's t-distribution
G	$\frac{\text{N}}{\text{m}^2}$	Shear modulus
H		Heaviside step function
$[I]$		Identity matrix
K_{ij}	dB	Vibration reduction index
K_{pp}		Autocovariance
$[K]$		Stiffness matrix
L_n	dB	Normalized impact sound pressure level
$L_{n,d}$	dB	Normalized impact level of the direct transmission path
$L_{n,ij}$	dB	Normalized impact level of a flanking transmission path
L_v	dB	Velocity level
$[M]$		Mass matrix
M		Modal overlap factor
N		Number of modes per frequency band
N		Shape function
P	$\frac{\text{Nm}}{\text{s}}$	Input power averaged over time and space
P_j	$\frac{\text{Nm}}{\text{s}}$	P due to excitation of subsystem j
$P_{i \to j}$	$\frac{\text{Nm}}{\text{s}}$	Power flow
P_{ij}	$\frac{\text{Nm}}{\text{s}}$	Net power flow
Pr		Probability
R	dB	Sound insulation index
R_{pp}		Autocorrelation
S_{pp}		Three-dimensional spectral density
T	s	Time period
Var		Variance
V	m^3	Volume

Acronyms

CLT	Cross Laminated Timber
DEA	Dynamic Energy Analysis
EFA	Energy Flow Analysis
EFEM	Energy Finite Element Method
FE	Finite Element
FEM	Finite Element Method
FE/WFE	Finite Element/Wave Finite Element
GUI	Graphical User Interface
PIM	Power Injection Method
RotR	Rain-on-the-Roof
SEA	Statistical Energy Analysis
WFE	Wave Finite Element
WIA	Wave Intensity Analysis

1 Introduction

1.1 Motivation

Within the context of efficient and sustainable design of buildings, a trend towards light-weight timber structures is recognizable. Jointly responsible for this trend is the commercial launch of cross laminated timber (CLT) which is a composite, plate-like timber product. Apart from the low weight, it allows a high degree of prefabrication. Compared to timber frame constructions, building structures made of CLT open up the possibility of a lower air permeability combined with a distinctive specific storage capacity for humidity and thermal energy [Brandner et al 2016].

Constructing multistory buildings made of CLT necessitates the ability to predict service-ability and comfort including the building acoustical behavior in order to fulfill vibroacoustic requirements. To develop reliable prediction methods, the transfer of energy between building components has to be investigated. Therefore, a detailed understanding of the modeling of building components, e.g. walls or ceilings, is compulsory. For CLT, the cross-wise layup of timber board layers and the low elastic modulus perpendicular to the fiber has to be taken into account.

Depending on the frequency range, the prediction of the structure-borne sound transmission is linked to different requirements, models and methods. Therefore, the hybrid method called Energy Flow Analysis (EFA) is proposed, which is applicable to the entire extended frequency range of building acoustics. In the low to mid frequency range, the EFA takes advantage of the versatility of the Finite Element Method (FEM), which enables an exact modeling of heterogeneous materials, complex geometries and connections between components. Moreover, the EFA uses averaging techniques based on the Statistical Energy Analysis (SEA) and thus, copes with sensitivity issues in the results which become relevant for higher frequencies [Mace and Shorter 2000]. As shown in the subsequent chapters, the EFA is also able to consider through-thickness effects using a solid element model [Winter et al 2017b] and can thus be applied above the limit of the Mindlin wave approximation [Mindlin 1951].

The EFA offers various evaluation quantities with different benefits. The energy influence coefficients describe the energy flow into adjacent components over the entire frequency range for any connection strength. Inverting the energy influence coefficients matrix, damping and coupling loss factors can be determined. If the SEA requirements are fulfilled, loss factors can serve as input data for an SEA model or for computing the vibration reduction index to predict the sound transmission according to DIN EN ISO 12354-1 [2017]. Beside the investigation of the parameters related to the structural model, the EFA enables the analysis of the influence of loading parameters, such as position, direction and phase shift.

1.2 State of the Art

For vibroacoustic predictions of sound transmission, various methods exist which all have their limitations concerning their applicability in the frequency range.

At low frequencies, numerical, element-based methods like the FEM are well-established for predictions of the vibroacoustic behavior. In the context of timber structures, Finite Element (FE) models have been used in various research projects, e.g. to predict the sound radiation of several types of ceilings [Kohrmann 2017].

The FEM results are accurate only if the fineness of the mesh complies with the minimum wavelength of the propagating waves, which depends on the upper limit of the frequency range. Therefore, the numerical effort increases with the investigated frequency. In addition, the sensitivity of the results due to uncertainties of model and input data like geometry and material rises with higher frequencies. Fulfilling the necessary requirements, such as a sufficient number of modes per frequency band [Culla and Sestieri 2006], energy-based methods like the SEA allow an appropriate prediction in terms of averaged quantities and thereby, they reduce effects linked with uncertainties.

Hence, the so-called mid frequency gap arises when neither the SEA assumptions like uncorrelated reflected waves at the boundaries are fulfilled nor pure deterministic, element-based approaches can reduce the uncertainty or the increased numerical effort. The current approaches to close the mid frequency gap can be classified into analytically-based methods, like the SEA, which aim at decreasing the lower limit, or numerical, deterministic approaches, like the FEM, which try to increase the upper frequency limit [Mace et al 2013]. Moreover, there are stochastic approaches or extensions of the foresaid methods, which include uncertainties in different manners.

By introducing more details, the lower limit of the SEA can be reduced leading to an hybrid application of the SEA. Langley [2008] gives a good overview over various related approaches. The hybrid approach of Shorter and Langley [2005] differs between big size, plate-like components which are modeled as SEA subsystems and comparatively small joining elements which are discretized by the FEM. This approach takes into account that within a certain frequency range the vibrational behavior of single components can be described differently, either with averaged quantities or with a deterministic resolution in space and frequency, depending on their geometry, density and stiffness. In frequency ranges where large, soft structures already exhibit a high modal density and therefore a big number of modes per frequency band, the eigenfrequencies of small and stiff components can still be well-separated or not even the first eigenfrequency is excited at resonance. This constellation is more common in automotive and aerospace structures [Peiffer et al 2011, 2013], whereas for typical geometries and junctions of buildings, this combination of large plates and small joining elements is less frequent.

Cicirello and Langley [2013] augmented this hybrid approach, which contains a non-parametric uncertainty in the SEA part, by a parametric model of uncertainty within the FE components. Ben Souf et al [2013] examine the effect of uncertainties of coupled structures. Therefore, a random variable is introduced at the junction. However, this does not correspond to an overall statistical approach since the single components are modeled deterministically by the Wave Finite Element (WFE) method.

Another method which implicates comparatively low numerical cost is the Dynamical Energy Analysis (DEA) since there, the mesh has only to resolve the components. Moreover, it is able to build on FE meshes and the diffuse field assumption known from the SEA has not to be fulfilled. Since the DEA states a cross-over of the SEA and Ray Tracing, the DEA is not suitable for low frequencies as resonances are not identified by the coarse meshing. This makes the approach rather insensitive to uncertainties which would lead to a shift of resonances in the response. Thus, the DEA is appropriate for big structures and high frequencies. [Tanner 2009; Chappell et al 2014]

For a similar field of application, such as big ships, the Energy FEM (EFEM) presented by Stritzelberger and von Estorff [2014] is appropriate. The high frequency range allows to work with the energy density of single wave types as state variables instead of using sound pressure and velocity. The EFEM enables a coarse, frequency-independent meshing and leads to spatial and time averaged results. The energy exchange between wave types of plate-like structures is introduced by analytically derived transmission coefficients [Langley and Heron 1990]. Nishino and Honda [2006] extended the calculation of transmission

coefficients to junctions between thick plates and applied it to the Wave Intensity Analysis (WIA). The WIA leads to direction-dependent wave intensities, which are also suitable for low frequencies, whereas the SEA has to comply with the requirement of the diffuse field assumption.

By contrast, Renno and Mace [2013] developed reflection and transmission coefficients for joints of structural components using FE within the scope of the hybrid Finite Element/Wave Finite Element (FE/WFE) approach. Since the adjacent components are described as waveguides by the WFE method, the components must have constant physical properties along the waveguide axis. To receive the wave properties, a small segment, which can be of arbitrary complexity, is modeled with FE and post-processed. Mitrou et al [2017] extended the FE/WFE approach to isotropic, two-dimensional structures. Further authors, like Finnveden [2004], Chazot et al [2013], Vergote et al [2013], Deckers et al [2014] as well as Kreutz and Müller [2014] use wave-based solutions for an efficient description of the system response which especially works for homogeneous beams, plates and cavities. These wave-based methods are also known as Trefftz methods because they develop approximate solutions on the basis of deterministic approaches using the exact solution as shape function. They have in common, that they benefit from their low numerical effort and thus they reach a higher frequency range compared to conventional element-based approaches, whereby the increasing sensitivity of the results is ignored.

Souza Lenzi et al [2013] chose Padé approximations to solve big matrices. Thereby, an initially coarse frequency resolution of direct solutions is augmented and refined by extrapolating intermediate frequencies.

Flodén et al [2014] compared various reduction methods at a wooden floor structure at low frequencies and concluded that realistic boundary conditions are decisive for the accuracy.

The EFA corresponds to a numerical implementation of the Power Injection Method (PIM), which aims to experimentally determine the coupling loss factors for an SEA model [de Langhe and Sas 1996]. Fredö [1997] shows that by means of the EFA also non-resonant transmissions can be considered. Mace and Shorter [2000] derived the EFA based on a component mode synthesis which is quite efficient for deterministic investigations of plate-like systems having a limited number of modes. By Thite and Mace [2007], the procedure is augmented to estimate ensemble average values of coupling loss factors as well as further statistical properties.

1.3 Research Project "Vibroacoustics"

This thesis forms part of the joint research project "Vibroacoustics in the planning process for timber constructions" which aims at improving and simplifying the planning process of buildings using Building Information Modeling. Starting with the architects' plan of a multistory timber building, information can be added step by step in the different planning phases and modifications by one partner are directly updated to the others.

To be able to predict the sound transmission in the planning phase, one goal was the generation of the corresponding input data especially for timber structures. Therefore, extensive measurements were performed by Mecking et al [2017a] and Châteauvieux-Hellwig et al [2017] as well as data was collected from other institutes [Timpte 2016] in order to catalog them in a web-based data base (`https://www.vabdat.de`) which can be linked to a Building Information Model. Thereby, mainly vibration reduction indices were measured on the basis of the vibration level difference for different types of junctions according to the recommendation of DIN EN ISO 12354-1 [2017] (cf. subsection 3.2.4).

Selected measurements were performed applying PIM and thus measuring additionally the input power. Therefore, the procedure of the EFA, which is introduced in chapter 3, was also applied to measurements estimating the total energy by means of measured surface velocities perpendicular to the plate [Winter et al 2014, 2015; Mecking et al 2017a]. Thereby, damping and coupling loss factors of a real structure can be determined, whereas by measuring exclusively the vibration level difference, only coupling properties can be estimated.

Since parametric, numerical models open up the possibility to easily modify physical properties of the subsystems and of the junctions as well as to apply specific loadings, further studies have been performed numerically [Winter and Müller 2017].

Therefore, the focus of this thesis lies on the numerical prediction of the structure-borne sound transmission behavior within CLT structures accompanied by an extensive parametric study.

1.4 Outline

The goal of this thesis is the numerical description and thus prediction of the structure-borne sound transmission by means of the EFA. Thereby, the focus lies on multistory buildings

made of CLT plates where different junction geometries are extracted, like an L-, a T- or an X-junction, to describe the energy flow across the junction.

In chapter 2, CLT is introduced and a procedure to homogenize its material properties across the thickness is presented. This leads to an orthotropic plate which is afterwards characterized by the inherent wave types including their phase and group velocities. Finally, a short introduction to the SEA, which can be derived by wave types of plate like structures, is given. Moreover, assumptions of the SEA as well as quantities to check these assumptions are presented.

Chapter 3 explains the application of the EFA on the basis of a harmonic analysis with the FEM including the evaluation of energy and input power. Then, the computation of various evaluation quantities like the energy influence coefficients is introduced. Thereby, it is possible to describe the energy flow within the structure. The averaging with respect to time, space, frequency and realization is assigned to the corresponding step in the post-processing of the EFA. Moreover, the averaging over realizations is augmented by its statistical properties and by a procedure to compute robust energy influence coefficients if a structure with unknown loading position is investigated.

In chapter 4, the EFA is applied to a variety of junctions consisting of either thin, isotropic or thick, orthotropic plates. By means of different evaluation techniques and corresponding quantities as well as by comparisons to the SEA, the energy flow behavior is analyzed in dependency of the frequency. Thereby, the sensitivity of the energy flow with respect to geometry and loading is investigated. Moreover, the influence of the connection strength as well as the effect of the number of connected subsystems is examined.

Chapter 5 summarizes the investigations of chapter 4 and assigns it to three different frequency ranges. Thereby, each of the frequency ranges is characterized by a specific vibroacoustic behavior linked to convenient methods, models as well as evaluation techniques and quantities. The assignment of a specific structure of interest to a convenient frequency range can be done in the pre-processing by means of the web-based application "Vibroacoustics of plates" which opens up the possibility to estimate the limits of the different frequency ranges analytically.

2 Fundamental Theory

This chapter provides fundamental theories on selected topics linked to the EFA of massive timber constructions. As the investigated structures in this contribution consist of CLT plates, section 2.1 presents the corresponding linear and orthotropic material law. Moreover, it offers a homogenization of the material constants through the thickness of the CLT plates. In section 2.2 the different wave types occurring in an orthotropic plate are introduced. They constitute the basis for one of the two approaches within the SEA. Since the EFA applies the averaging concept of the SEA, an overview of the SEA is given in section 2.3.

2.1 Cross Laminated Timber

CLT plates unify two functions building supporting structures as well as creating and separating rooms. Hence, entire buildings can be constructed using CLT for walls and ceilings [Gülzow 2008]. In chapter 4, the vibrational energy flow in between these components is investigated on the basis of an FE model.

CLT contains several layers which are arranged perpendicular to each other. Figure 2.1 shows that each layer consists of timber boards placed side-by-side [Brandner et al 2016]. The boards themselves are purified from branch zones which would reduce the stiffness. In order to manufacture plates of any length, the boards are glued together in longitudinal direction by v-shaped tines, which interlock perfectly [Schickhofer et al 2010].
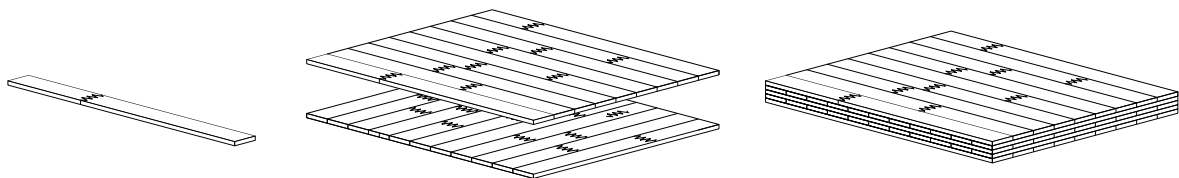
Figure 2.1: Manufacturing of CLT [Schickhofer et al 2010].
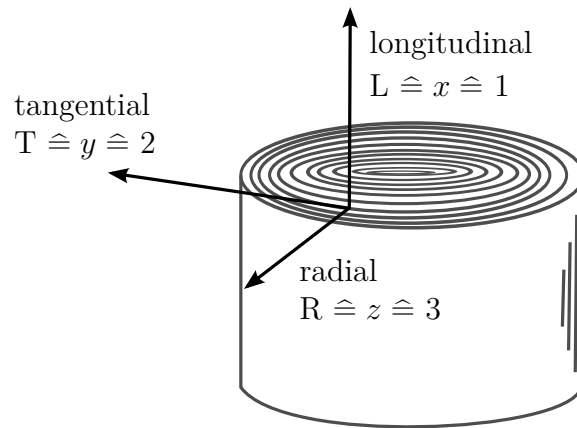
Figure 2.2: Orthogonal principal directions in wood [Gülzow 2008].

In this section, wood as an orthotropic material is introduced in subsection 2.1.1 followed by possible simplifications considering construction timber in subsection 2.1.2. To simplify the handling of CLT a homogenized material model is presented in subsection 2.1.3. Moreover, the hysteretic damping model chosen for CLT is explained in subsection 2.1.4.

2.1.1 Wood as Orthotropic Material

The fiber direction and the annular rings dominate the anatomy of wood and thus its elastic properties. Hence, three directions can be distinguished in Fig. 2.2: The first one is oriented parallel to the fiber and is named longitudinal (L), whereas the second and the third one lie tangential (T) and radial (R) to the annular rings in the cross-section plane of a trunk. These can be approximately associated with the three principal directions in the cartesian coordinates system x, y and z. [Gülzow 2008]

Looking at the micro structure, wood shows an inhomogeneous behavior, whereas on the macro level the cell bond can be described by smeared material properties. Thus, wood is assumed to be homogeneous per direction and to behave linear elastically up to a certain stress or strain limit showing only small deformations [Ranz 2007]. The relation between the second order tensors of the 2$^{\text{nd}}$ Piola-Kirchhoff stresses σ_{ij} and the Green-Langrangian strains ε_{kl} is defined for linear elastic, anisotropic material according to Hooke's law by the general constitutive equation:

$$\sigma_{ij} = C_{ij}^{kl}\, \varepsilon_{kl} \tag{2.1}$$

It can be solved using Einstein summation convention for $i,j,k,l = 1,2,3$ denoting cartesian coordinates. C_{ij}^{kl} states the fourth order stiffness tensor, which can be simplified by making use of the symmetry characteristics of stress and strain matrices as well as of stiffness and compliance matrices according to [Bodig and Jayne 1993; Müller 2015]. In the case of general, linear elastic and anisotropic material, the number of independent entries can be reduced from $3^4 = 81$ to 21 leading to the following stiffness matrix in Voigt notation:

$$\begin{bmatrix} \sigma_{11} \\ \sigma_{22} \\ \sigma_{33} \\ \sigma_{23} \\ \sigma_{13} \\ \sigma_{12} \end{bmatrix} = \begin{bmatrix} C_{11} & C_{12} & C_{13} & C_{14} & C_{15} & C_{16} \\ & C_{22} & C_{23} & C_{24} & C_{25} & C_{26} \\ & & C_{33} & C_{34} & C_{35} & C_{36} \\ & & & C_{44} & C_{45} & C_{46} \\ & \text{sym} & & & C_{55} & C_{56} \\ & & & & & C_{66} \end{bmatrix} \begin{bmatrix} \varepsilon_{11} \\ \varepsilon_{22} \\ \varepsilon_{33} \\ 2\varepsilon_{23} \\ 2\varepsilon_{13} \\ 2\varepsilon_{12} \end{bmatrix} \tag{2.2}$$

As the material behavior of wood depends on its direction, it is anisotropic. Due to the orthogonality of the principal directions, it can be described as orthogonal isotropic, also known as orthotropic, which is a special case of anisotropy with three symmetry planes. No coupling occurs between longitudinal and shear strains which is indicated by the zero values of C_{ij} for $i = 1$ to 3 and $j = 4$ to 6 [Grimsel 1999]. Moreover, the lower half of the stiffness matrix is diagonal implying that shear strains are not coupled, whereas normal strains are linked to each other by the passive strain transversal to the applied stress. This leads to nine independent entries for the orthotropic stiffness matrix $[C]$ in Eq. (2.3). Engineering strains result from a geometrical linearization assuming small strains. Unlike tensor strains, these can be measured. Hence, it is convenient to establish the physically linear relationship between the six independent stresses and the six independent engineering strains according to Hooke's law. The tensor shear strain ε_{ij} is replaced by the engineering shear strain $\gamma_{ij} = \varepsilon_{ij} + \varepsilon_{ji} = 2\varepsilon_{ij}$ as $\varepsilon_{ij} = \varepsilon_{ji}$ [Bodig and Jayne 1993; Müller 2015]. Furthermore, the two identical indices of normal strains and stresses are reduced to one and the shear stresses are represented by $\tau_{ij} = \sigma_{ij}$.

$$\begin{bmatrix} \sigma_{11} \\ \sigma_{22} \\ \sigma_{33} \\ \tau_{23} \\ \tau_{13} \\ \tau_{12} \end{bmatrix} = \begin{bmatrix} C_{11} & C_{12} & C_{13} & 0 & 0 & 0 \\ & C_{22} & C_{23} & 0 & 0 & 0 \\ & & C_{33} & 0 & 0 & 0 \\ & & & C_{44} & 0 & 0 \\ & \text{sym} & & & C_{55} & 0 \\ & & & & & C_{66} \end{bmatrix} \begin{bmatrix} \varepsilon_{11} \\ \varepsilon_{22} \\ \varepsilon_{33} \\ \gamma_{23} \\ \gamma_{13} \\ \gamma_{12} \end{bmatrix} \tag{2.3}$$

Inverting the stiffness matrix $[C]$ results in the compliance matrix $[S]$:

$$
\begin{bmatrix} \varepsilon_{11} \\ \varepsilon_{22} \\ \varepsilon_{33} \\ \gamma_{23} \\ \gamma_{13} \\ \gamma_{12} \end{bmatrix} = \begin{bmatrix} S_{11} & S_{12} & S_{13} & 0 & 0 & 0 \\ & S_{22} & S_{23} & 0 & 0 & 0 \\ & & S_{33} & 0 & 0 & 0 \\ & & & S_{44} & 0 & 0 \\ & \text{sym} & & & S_{55} & 0 \\ & & & & & S_{66} \end{bmatrix} \begin{bmatrix} \sigma_{11} \\ \sigma_{22} \\ \sigma_{33} \\ \tau_{23} \\ \tau_{13} \\ \tau_{12} \end{bmatrix}
\tag{2.4}
$$

The compliance matrix $[S]$ is useful for introducing the engineering elastic parameters. The six elastic moduli of orthotropic material are divided into two types: First, the three moduli of elasticity E_i state the ratios of normal stress σ_i to normal strain ε_i in the principal directions. Secondly, the three shear moduli G_{ij} denote the ratio of shear stress τ_{ij} to the shear strain γ_{ij} in the orthotropic planes. Thus, they represent the slope of the corresponding stress-strain curve and their reciprocals constitute the main diagonal of the compliance matrix [Bodig and Jayne 1993]:

$$
\begin{bmatrix} \varepsilon_x \\ \varepsilon_y \\ \varepsilon_z \\ \gamma_{yz} \\ \gamma_{xz} \\ \gamma_{xy} \end{bmatrix} = \begin{bmatrix} \frac{1}{E_x} & -\frac{\nu_{yx}}{E_y} & -\frac{\nu_{zx}}{E_z} & 0 & 0 & 0 \\ -\frac{\nu_{xy}}{E_x} & \frac{1}{E_y} & -\frac{\nu_{zy}}{E_z} & 0 & 0 & 0 \\ -\frac{\nu_{xz}}{E_x} & -\frac{\nu_{yz}}{E_y} & \frac{1}{E_z} & 0 & 0 & 0 \\ 0 & 0 & 0 & \frac{1}{G_{yz}} & 0 & 0 \\ 0 & 0 & 0 & 0 & \frac{1}{G_{xz}} & 0 \\ 0 & 0 & 0 & 0 & 0 & \frac{1}{G_{xy}} \end{bmatrix} \begin{bmatrix} \sigma_x \\ \sigma_y \\ \sigma_z \\ \tau_{yz} \\ \tau_{xz} \\ \tau_{xy} \end{bmatrix}
\tag{2.5}
$$

The Poisson's ratio ν_{ij} relates the transverse, passive strain ε_j to the axial, active strain ε_i as a result of an uniaxial stress σ_i:

$$
\nu_{ij} = -\frac{\varepsilon_j}{\varepsilon_i}
\tag{2.6}
$$

Thus, the coupling of the normal strains is described representing the off-diagonal entries in the compliance matrix. As the matrix is symmetric ($S_{ij} = S_{ji}$ for $i \neq j$), the minor Poisson's ratios ν_{ji} are related to the major ones ν_{ij}. Considering size indications, $E_i > E_j$ is assumed.

$$
-\frac{\nu_{ij}}{E_i} = -\frac{\nu_{ji}}{E_j} \quad \rightarrow \quad \nu_{ij} = \nu_{ji}\frac{E_i}{E_j}
\tag{2.7}
$$

Hence, the major Poisson's ratios can be expressed by the minor ones which leads to nine

independent engineering parameters for orthotropic materials. Looking at the stiffness matrix $[C]$ in Eq. (2.8), the first three entries on the main diagonal represent the stiffness moduli of an infinite solid and thus take into account the obstruction of transverse deformations:

$$[C] = \begin{bmatrix} \frac{1-\nu_{yz}\nu_{zy}}{D}E_x & \frac{\nu_{xz}\nu_{zy}+\nu_{xy}}{D}E_y & \frac{\nu_{xy}\nu_{yz}+\nu_{xz}}{D}E_z & 0 & 0 & 0 \\ \frac{\nu_{yz}\nu_{zx}+\nu_{yx}}{D}E_x & \frac{1-\nu_{xz}\nu_{zx}}{D}E_y & \frac{\nu_{yx}\nu_{xz}+\nu_{yz}}{D}E_z & 0 & 0 & 0 \\ \frac{\nu_{zy}\nu_{yx}+\nu_{zx}}{D}E_x & \frac{\nu_{zx}\nu_{xy}+\nu_{zy}}{D}E_y & \frac{1-\nu_{xy}\nu_{yx}}{D}E_z & 0 & 0 & 0 \\ 0 & 0 & 0 & G_{yz} & 0 & 0 \\ 0 & 0 & 0 & 0 & G_{xz} & 0 \\ 0 & 0 & 0 & 0 & 0 & G_{xy} \end{bmatrix} \tag{2.8}$$

$$\text{with } D = 1 - \nu_{xy}\nu_{yx} - \nu_{xz}\nu_{zx} - \nu_{yz}\nu_{zy} - 2\nu_{xy}\nu_{yz}\nu_{zx}$$

Since the elastic potential Π_{iv}, which is the internally stored energy per volume - also known as strain energy density - has to be positive [Müller 2015], stiffness and compliance matrices have to be positive definite.

$$\Pi_{iv} = \frac{1}{2}\sigma^{kl}\varepsilon_{kl} = \frac{1}{2}C^{klij}\varepsilon_{ij}\varepsilon_{kl} \tag{2.9}$$

This leads to the following conditions for stiffness and compliance matrices: The elements on the main diagonal have to be positive as the material has to elongate into direction of the applied tension. Moreover, the determinant of $[C]$ and $[S]$ must be positive which indicates compression under pressure. Hence, the engineering elastic parameters have to fulfill certain stability criteria [Altenbach et al 1996]:

$$E_i, \ G_{ij} > 0 \tag{2.10}$$

$$D > 0 \tag{2.11}$$

$$1 - \nu_{ij}\nu_{ji} > 0 \tag{2.12}$$

2.1.2 Construction Timber

The two directions in the cross section plane are unified and named perpendicular to the fiber ($\perp$), as manufactures do not distinguish whether planks have been cut out of the trunk in radial or tangential direction (cf. Fig. 2.3). This also holds for the selection of the plank for fabricating CLT [Gülzow 2008]. Hence, the description of construction timber can be
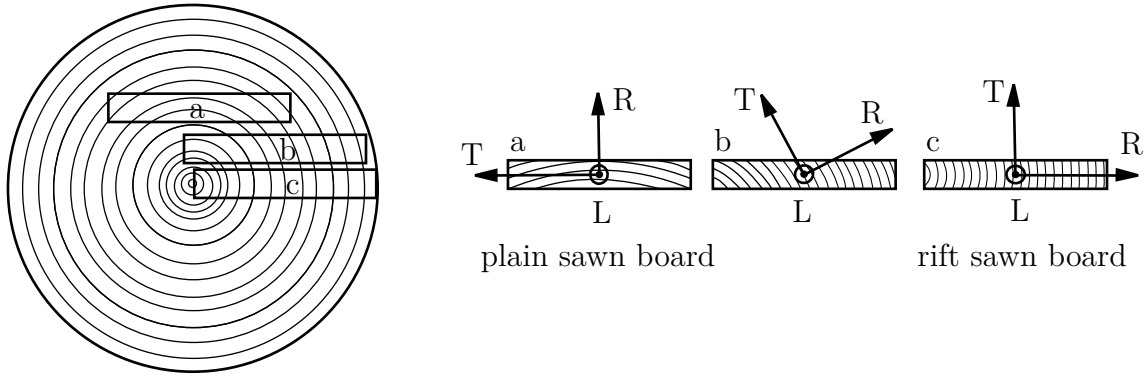
Figure 2.3: Sawing a trunk delivers different types of planks [Gülzow 2008].

simplified to six independent constants:

$$E_{\parallel} = E_x \qquad\qquad E_{\perp} = E_z = E_y \qquad\qquad (2.13)$$

$$G_{\parallel\perp} = G_{xy} = G_{xz} \qquad\qquad G_{\perp\perp} = G_{yz} \qquad\qquad (2.14)$$

$$\nu_{\parallel\perp} = \nu_{xy} = \nu_{xz} \qquad\qquad \nu_{\perp\perp} = \nu_{yz} \qquad\qquad (2.15)$$

The longitudinal direction is called parallel to the fiber ($\parallel$). The material model is not simplified to transverse isotropy since the following inequality applies to timber [Kohrmann 2017]:

$$G_{\perp\perp} \neq \frac{E_{\perp}}{2(1 + \nu_{\perp\perp})} \qquad\qquad (2.16)$$

Especially in the case of CLT plates, the rolling shear modulus $G_{\perp\perp}$ of the layers perpendicular to the main span direction plays an important role. This influences the effective bending stiffness of the plate [Aicher and Dill-Langer 2000].

2.1.3 Homogenized Model of Cross Laminated Timber

CLT plates show a biaxial, plate-like load-bearing behavior with minimized swelling and shrinkage rates on the one hand and varying material properties across the thickness on the other hand. The need to consider each layer individually can be avoided by treating CLT plates as homogeneous through thickness. This simplifies the modeling and meshing inside the FEM and it enables the use of shell elements as well as it facilitates the characterization by analytical estimations and measurements. To receive homogenized material parameters the engineering elastic parameters of the individual timber layers are weighted
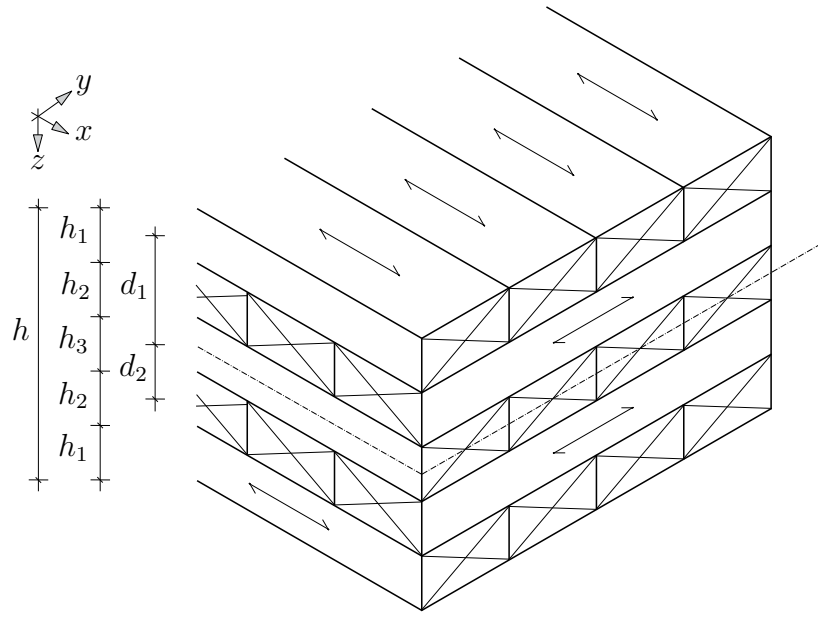
Figure 2.4: Sketch of a CLT plate with five layers and a symmetric layup with respect to the middle plane. h_l with $l = 1,2,3$ states the thickness of the individual layers and d_l the distance between their center and the one of the composite with the total thickness h.

by their proportionate height according to the rule of mixtures [Bodig and Jayne 1993]. The homogenization through thickness presupposes an odd number of layers and a symmetric layup with respect to the middle plane of the CLT plates like the ones depicted in Fig. 2.1 and 2.4. As the symmetry planes of the layers and the composite coincide or are parallel, no coupling between normal stress σ and shear strain γ or normal strain ϵ and shear stress τ has to be considered. Hence, the homogenized composite resulting from orthotropic layers can be described by the orthotropic material law. The composite stiffness can be idealized by connecting springs which represent individual layers. The effects of glue related to the wooden cell structure are assumed to be negligible. The elastic properties of the out-of-plane direction are calculated by a series connection, whereas the in-plane directions are modeled by a parallel connection.

Firstly, a uniform stress, which is equal for all layers, is applied perpendicular to the plate. By postulating that the total displacement corresponds to the sum of the layer displacements, the geometric compatibility is fulfilled. This applies for the calculation of the homogenized material parameters G_{xz}^* and G_{yz}^*:

$$G_{xz}^* = \frac{h}{\sum_\parallel \dfrac{h_l}{G_{xz}} + \sum_\perp \dfrac{h_l}{G_{yz}}} \qquad\qquad G_{yz}^* = \frac{h}{\sum_\parallel \dfrac{h_l}{G_{yz}} + \sum_\perp \dfrac{h_l}{G_{xz}}} \qquad (2.17)$$

In the case of G_{xz}^*, the layers oriented parallel to the main span axes ($\parallel$) contribute with G_{xz}, whereas the ones perpendicular to it ($\perp$) are characterized by G_{yz}. They are weighted by their individual layer thickness h_l with respect to the total thickness h.

Secondly, a uniform strain is applied in-plane, which is assumed to be equal for all layers due to the rigid bonding. Establishing the equilibrium, the sum of layer forces have to deliver the composite force. Thus, E_x^*, E_y^*, G_{xy}^* and the Poisson's ratios ν_{ij}^* can be calculated. G_{xy}^* is not concerned by the cross-wise layering, as the components along the edges of an infinitesimal cut element are equal due to equilibrium:

$$G_{xy}^* = G_{xy} = G_{yx} \tag{2.18}$$

The homogenized Poisson's ratios ν_{ij}^* result in:

$$\nu_{xy}^* = \frac{\sum_{\parallel} \nu_{xy} h_l + \sum_{\perp} \nu_{yx} h_l}{h} \qquad\qquad \nu_{yx}^* = \frac{\sum_{\parallel} \nu_{yx} h_l + \sum_{\perp} \nu_{xy} h_l}{h} \tag{2.19}$$

$$\nu_{xz}^* = \frac{\sum_{\parallel} \nu_{xz} h_l + \sum_{\perp} \nu_{yz} h_l}{h} \qquad\qquad \nu_{zx}^* = \frac{\sum_{\parallel} \nu_{zx} h_l + \sum_{\perp} \nu_{zy} h_l}{h} \tag{2.20}$$

$$\nu_{yz}^* = \frac{\sum_{\parallel} \nu_{yz} h_l + \sum_{\perp} \nu_{xz} h_l}{h} \qquad\qquad \nu_{zy}^* = \frac{\sum_{\parallel} \nu_{zy} h_l + \sum_{\perp} \nu_{zx} h_l}{h} \tag{2.21}$$

In the case of elastic moduli, this approach would be appropriate for pure in-plane tension but not for bending dominated problems. Therefore, the homogenized values are derived from the effective bending stiffness according to the elastic compound theory [Gülzow 2008; Blaß and Görlacher 2002; Bodig and Jayne 1993]. The bending stiffness of the individual layers are summed up complying with Steiner's theorem assuming rigid bonding and linear elastic strain through thickness. Hence, the distance between the center of the composite and of the individual layer d_l is introduced (cf. Fig. 2.4):

$$E_x^* = \frac{\sum_{\parallel} E_x (h_l^3 + h\, d_l^2) + \sum_{\perp} E_y (h_l^3 + h\, d_l^2)}{h^3} \tag{2.22}$$

$$E_y^* = \frac{\sum_{\parallel} E_y (h_l^3 + h\, d_l^2) + \sum_{\perp} E_x (h_l^3 + h\, d_l^2)}{h^3} \tag{2.23}$$

This leads to a stronger weighting of the outer layers and thus to a higher elastic modulus in the principal span axis compared to the thickness weighted average value according to the uniform strain approach. Due to the modified calculation of the elastic moduli, the relation between minor and major Poisson's ratios of expression (2.7) is violated. Thus, the Poisson's

ratios are averaged according to Gülzow [2008] to fulfill the orthotropic material law.

$$\overline{\nu_{ij}^*} = \frac{1}{2}\left(\nu_{ij}^* + \nu_{ji}^* \frac{E_i^*}{E_j^*}\right) = \overline{\nu_{ji}^*}\frac{E_i^*}{E_j^*} \tag{2.24}$$

This leads to nine independent material parameters. Below, homogenized material parameters are not explicitly marked by an asterisk.

The presented procedure has been validated performing modal analyses of a single-axis spanned ceiling as well as of an L-junction consisting of a wall and a ceiling. Moreover, the energy flow is compared at an L-junction. In both investigations, a model considering each timber layer separately is compared to a model with homogenized parameters using the same mesh and quadratic shape functions. The mentioned examples are summarized in subsection 4.1.2. They demonstrate that the differences on the eigenfrequencies and eigenmodes of these two variations turned out to be negligible at low frequencies and that the overall characteristic behavior corresponds also for higher frequencies.

2.1.4 Hysteretic Damping

The damping properties of CLT are approximated by hysteretic damping as it is convenient for materials like timber or metal [Petersen 2000]. The damping is described by a loss factor η which is assumed to be independent of frequency. On the basis of measurements at free-hanging plates in a reverberation room, Haut et al [2017] indicate that this assumption can be justified for orthotropic, layered timber plates up to their direction dependent critical frequencies. For higher frequencies, the losses due to radiation slightly start to matter. Their consideration would lead to a frequency dependent loss factor.

The loss factor is related to the damping ratio D by $\eta = 2D$. To perform a harmonic analysis, the hysteretic damping is considered in the equation of motion (3.6) by means of the complex elastic modulus leading to the complex stiffness matrix:

$$E\left(1 + i\eta\right) \rightarrow [K]\left(1 + i\eta\right) \tag{2.25}$$

As the hysteretic damping is set proportional to the stiffness matrix $[K]$, the damping can be verified comparing the time-averaged input power P and potential energy E_{pot} of the total system for any angular frequency of excitation Ω [Pavic 2005]:

$$\eta = \frac{P}{2E_{\text{pot}}\,\Omega} \tag{2.26}$$
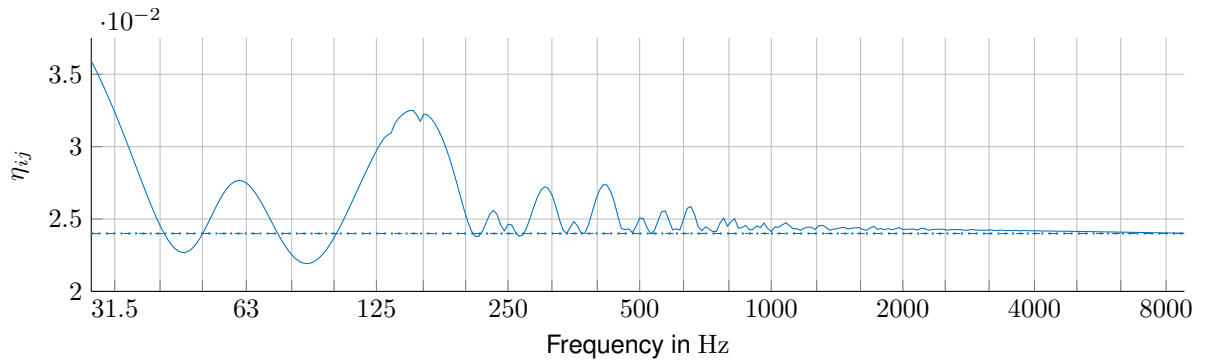
Figure 2.5: The damping loss factor of a single plate is calculated by the EFA using $E_{11} = E_{11,\text{kin}} + E_{11,\text{pot}}$ (−) according to subsection 3.2.2. If $2\,E_{11,\text{pot}}$ (−−) is used in the EFA procedure, it corresponds to the hysteretic damping of the FE model of $\eta = 0.024$ (· · ·) which demonstrates Eq. (2.26). The damping loss factors coincide at resonance where $E_{\text{pot}} = E_{\text{kin}}$.

Calculating the damping loss factor η_{ii} by means of the EFA, both the potential and the kinetic energy, are taken into account as explained in subsection 3.2.2. Fig. 2.5 demonstrates that the stiffness proportional loss factor η does not coincide with the damping loss factor η_{ii} determined by the EFA unless the system oscillates at resonance leading to $E_{\text{pot}} = E_{\text{kin}}$.

2.2 Wave Types in Isotropic and Orthotropic Plates

In the following passages, the wave propagation in orthotropic plates is presented which applies to the homogenized model of CLT of subsection 2.1.3. The explanations also include the simple, isotropic case with identical material properties in all directions. Therefore, a cartesian coordinate system is defined whereby the x- and y-direction span the plane of the plate and the z-axis points in the out-of-plane direction.

Whereas only longitudinal waves propagate in air (cf. subsection 2.2.1), shear waves additionally occur in a solid (cf. subsection 2.2.2). Moreover, bending waves arise in the case of beams or plates which are characterized by a finite thickness (cf. subsection 2.2.3). Subsection 2.2.4 explains that they exhibit different phase and group velocities. Figure 2.6 shows wave velocities in an exemplary orthotropic plate made of CLT. These velocities depend on the wave type and the direction. Furthermore, cross-over frequencies are indicated by vertical lines to distinguish between thin and thick plates. To margin the plate-like behavior, the first simple thickness resonance frequencies are shown which are introduced in subsection 2.2.5.
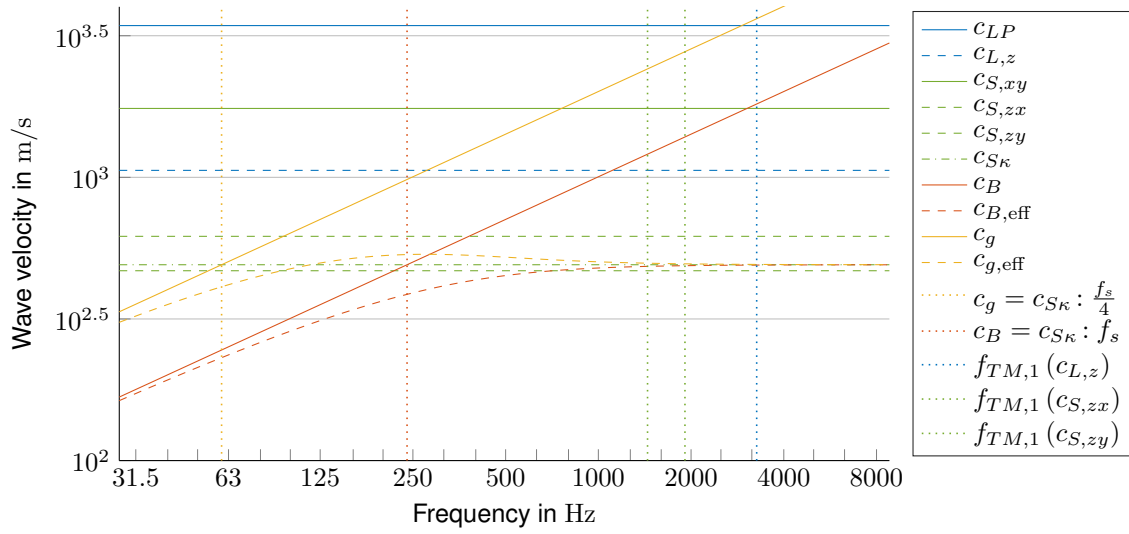
Figure 2.6: Velocities of the different wave types in an orthotropic plate including cross-over frequencies and the first simple thickness resonances.

2.2.1 Longitudinal Waves

Figure 2.7 shows that the direction of propagation and the resulting displacement in the medium are identical for longitudinal waves. They are also called primary waves since they propagate the fastest compared to other wave types as indicated by Fig. 2.6. Their velocity $c_{L,i}$ in the direction $i = x$, y or z depends on the corresponding stiffness modulus $E_{S,i}$ and the density ρ. The stiffness modulus corresponds to the main diagonal entry C_{ii} of the stiffness matrix in Eq. (2.3) or (2.8). In contrast to the elastic modulus, the stiffness modulus includes the influence of the transverse strain.

$$c_{L,i} = \sqrt{\frac{E_{S,i}}{\rho}} = \sqrt{\frac{C_{ii}}{\rho}} \tag{2.27}$$

Only if the wavelength is small compared to the dimensions perpendicular to the direction of propagation, a pure longitudinal wave propagates. Otherwise, in the case of plates or rods a transverse motion of the particles is additionally enabled. This reduces the velocity and leads to quasi-longitudinal waves along the axis of the rod

$$c_{LR} = \sqrt{\frac{E}{\rho}} \tag{2.28}$$

or in the plane of the plate

$$c_{LP,i} = \sqrt{\frac{E_i}{\rho \left(1 - \nu_{ij}\nu_{ji}\right)}} \tag{2.29}$$
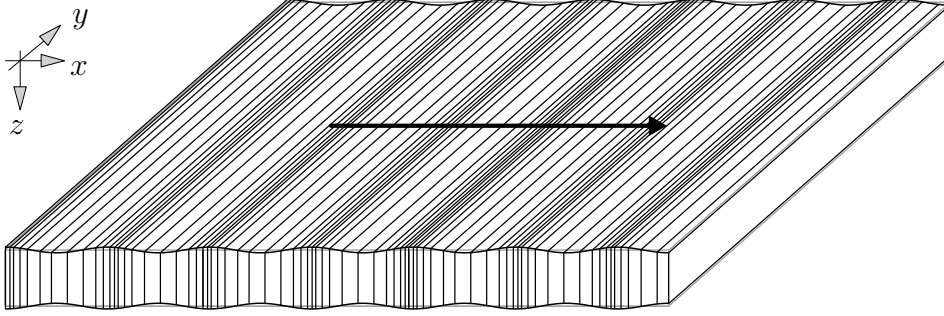
Figure 2.7: Propagation of a quasi-longitudinal wave in x-direction of a plate.

where the indices i and j correspond to the x or the y direction. Taking the geometric mean, the in-plane waves of an orthotropic plate can be summarized to an effective quasi-longitudinal velocity.

$$c_{LP} = \sqrt{c_{LP,x}\, c_{LP,y}} \tag{2.30}$$

This opens up the possibility to approximate an orthotropic plate by an isotropic one [Hopkins 2007]. In the case of isotropic material, the indices can be omitted as the properties are equal for all directions.

2.2.2 Shear Waves

Unlike fluids, solids are able to resist shear deformation. Shear waves belong to transversal waves as they oscillate perpendicular to their direction of propagation. They move slower than longitudinal ones and thus shear waves are additionally called secondary waves.

$$c_{S,ij} = \sqrt{\frac{G_{ij}}{\rho}} \tag{2.31}$$

Plane transversal waves only occur in solids which are large compared to the wave length in all three dimensions or in plates if the free surface is parallel to the directions of propagation and displacement. Thus, the free surface does not influence the so-called in-plane shear waves, which are depicted in Fig. 2.8 [Cremer 1967].

Contrary to infinite solids, the velocity of shear waves leading to displacements perpendicular to the beam axis or the plane of a plate (cf. Fig. 2.9) depends on the shape of the cross section. Moreover, they typically occur combined with bending waves which are introduced
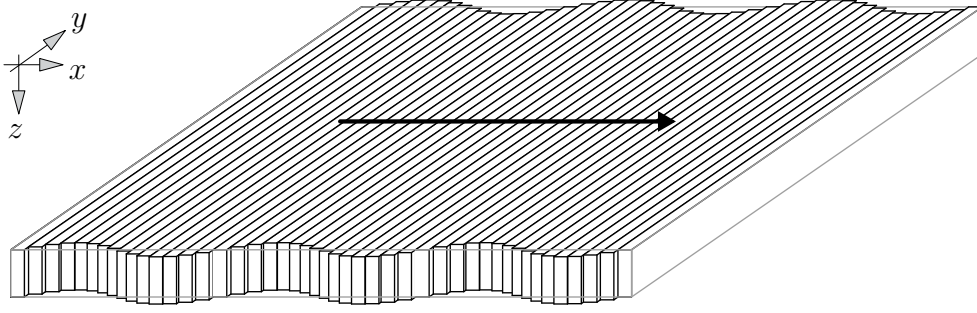
Figure 2.8: The depicted in-plane shear wave propagates in x-direction and oscillates in y-direction of the plate.
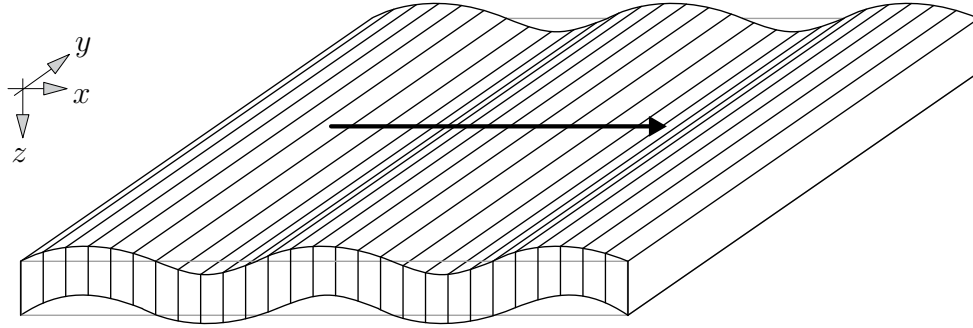
Figure 2.9: The depicted out-of-plane pure shear wave propagates in x-direction and oscillates in z-direction of the plate [Hopkins 2007].

in subsection 2.2.3. The first-order shear deformation theory of Mindlin [1951] contains a linear approach for longitudinal displacements which results in a constant shear strain. In order to achieve more accurate results, a parabolic shear stress distribution through thickness can be considered by the shear correction factor κ, as shown in Eq. (2.32). For rectangular cross sections, κ is equal to $\frac{5}{6}$ [Hambric et al 2016].

$$c_{S\kappa,iz} = \sqrt{\frac{\kappa\, G_{iz}}{\rho}} \tag{2.32}$$

The directional dependent out-of-plane shear wave velocities of an orthotropic plate can be combined calculating the geometric mean analogously to the effective quasi-longitudinal velocity:

$$c_{S\kappa} = \sqrt{c_{S\kappa,xz}\, c_{S\kappa,yz}} \tag{2.33}$$

The validity of this simplification depends on the distinctness of the two directions.

2.2.3 Bending Waves

Thin and thick beams or plates have to be distinguished for the description of bending waves. The partial differential equation for a thin beam is based on the Euler-Bernoulli beam theory being extended to the Kirchhoff-Love plate theory assuming pure bending waves. Considering higher frequencies and smaller wavelenghts, the differential equations have been extended for the one-dimensional case by Timoshenko [1922] and for two dimensions by Mindlin [1951] representing effective bending waves. In the case of deformations, all mentioned theories assume that the cross sections remain plane.

Pure Bending Waves - Thin Plates

Pure bending waves occur if the bending wave length λ_B is large compared to the thickness h of the beam or the plate which are then referred to as thin. Bending waves oscillate perpendicular to their direction of propagation. Contrary to pure shear, Fig. 2.10 shows a rotation of the cross section related to the neutral axis. In case of pure bending, the cross sections remain perpendicular to the axis of the beam or plate. As the phase velocity of bending waves depends on the frequency, they are dispersive [Cremer and Heckl 1996]:

$$c_B = \sqrt[4]{\frac{B\,\omega^2}{\mu}} \tag{2.34}$$

For plates, the areal mass reads $\mu = \rho h$ and the bending stiffness is given by $B = \frac{Eh^3}{12\,(1-\nu^2)}$. According to Heckl [1960] in the case of orthotropic material the bending stiffness can be approximated by:

$$B = \frac{\sqrt{E_x E_y}h^3}{12\,(1 - \nu_{xy}\nu_{yx})} \tag{2.35}$$

Effective Bending Waves - Thick Plates

The bending wave lenghts become shorter with increasing frequency approaching the order of magnitude of the thickness of the plate. Hence, from a dynamic point of view the plate is considered to be thick. In this case, the shear deformation and the rotatory inertia have to be taken into account because they influence the bending waves. Cremer [1967] defines a
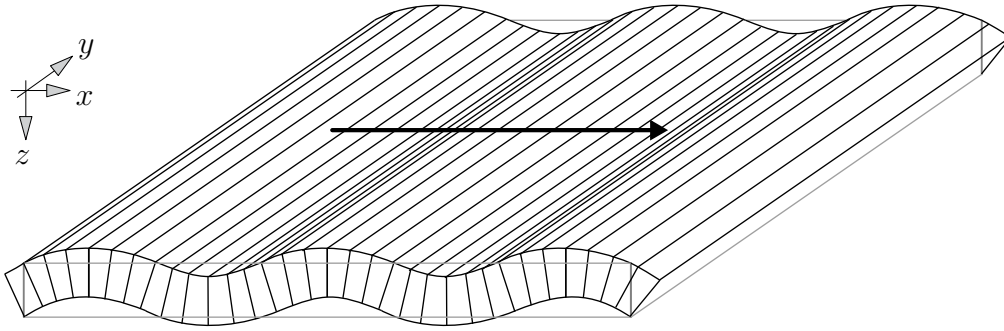
Figure 2.10: The depicted pure bending wave propagates in x-direction of a thin plate [Wilhelm 2017].

limit for thin plates by the following relation of thickness h and pure bending wave length $\lambda_B = \frac{c_B}{f}$:

$$\lambda_{B,\text{limit}} = 6\,h \tag{2.36}$$

For smaller λ_B, the deviation between the velocity of pure bending waves and of so-called effective bending waves exceeds $10\,\%$. Thereby, Cremer [1967] assumed an isotropic plate with $\nu = 0.3$. Effective bending waves represent a combination of bending and out-of-plane shear waves and approach the out-of-plane shear waves with increasing frequency. These are additionally characterized by the shear correction factor in Eq. (2.32) [Hambric et al 2016].

The transition between thin and thick plates depends on the investigated quantity. As shown in the subsections 2.2.4 and 2.3.2, the phase velocity, the group velocity and the modal density are affected differently [Meier 2000]. Therefore, a cross-over frequency f_s is proposed on the basis of [Rindel 1994] for $c_B = c_{S\kappa}$:

$$f_s = c_{S\kappa}^2 \, \frac{1}{2\,\pi} \, \sqrt{\frac{\mu}{B}} \tag{2.37}$$

The group velocity (cf. subsection 2.2.4) and thus the energy transport is influenced already at the frequency $\frac{f_s}{4}$ by the shear deformation as the condition $c_g = 2\,c_B = c_{S\kappa}$ is fulfilled. Thus, $\frac{f_s}{4}$ is named energetic thin plate limit within this thesis. Exceeding the frequency $\frac{f_s}{2}$, the modal density shows a frequency dependent behavior according to Eq. (2.65) [Meier 2000]. The effective bending wave velocity is derived from the wave equation of a Mindlin plate considering shear deformation and rotatory inertia [Mindlin 1951; Cremer and Heckl

1996]:

$$c_{B,\text{eff}} = \left[\frac{1}{2}\left(\frac{\rho\,h^3}{12\,B} + \frac{\rho}{\kappa\,G} \right) + \frac{1}{2}\sqrt{\left(\frac{\rho\,h^3}{12\,B} + \frac{\rho}{\kappa\,G} \right)^2 + 4\,\frac{\rho\,h}{B\,\omega^2} - 4\,\frac{\rho^2\,h^3}{12\,B\kappa\,G}} \right]^{-\frac{1}{2}} \tag{2.38}$$

According to the Mindlin wave approximation, sections normal to the surface remain plane due to the deflection of the plate, but not perpendicular as for pure bending waves. Approaching pure shear waves, the rotation of the cross section becomes smaller [Pedersen 1995]. Equation (2.38) can be approximated e.g. on the basis of [Rindel 1994; Meier 2000]:

$$c_{B,\text{eff}} = c_{S\kappa}\,\frac{f}{f_s}\sqrt{-\frac{1}{2} + \frac{1}{2}\sqrt{1 + \left(\frac{2\cdot f_s}{f} \right)^2}} \tag{2.39}$$

Depending on the literature source, the aspired velocity of the effective bending waves varies. In the expressions (2.37) and (2.39), either the shear correction factor within $c_{S\kappa}$ is omitted [Rindel 1994; Pedersen 1995] or instead of $c_{S\kappa}$ the velocity of the Rayleigh waves c_R is used which is almost identical to $c_{S\kappa}$. For isotropic materials, the relation can be simplified to $c_{S\kappa} = \sqrt{\kappa}\,c_S = \sqrt{\frac{5}{6}}\,c_S \approx 0.9\,c_S \approx c_R$ [Cremer 1967; Meier 2000]. As Rayleigh waves are pure surface waves, they arise if the structure is much thicker than $\frac{\lambda_B}{6}$ or if the frequency is much higher than f_s.

2.2.4 Group Velocity

The group velocity constitutes the velocity of propagation of the envelope of a superposition of waves with different amplitudes and wave lengths. It describes the velocity by which energy is transported [Cremer 1967].

For the simple case of two waves with identical amplitudes but different angular frequencies ω_1 and ω_2 as well as wave numbers k_1 and k_2, the group wave velocity yields:

$$c_g = \frac{\omega_1 - \omega_2}{k_1 - k_2} \tag{2.40}$$

In the limit case, the frequencies and wave numbers are arbitrarily close to each other. This leads to the mathematical description by means of the differential quotient:

$$c_g = \frac{d\omega}{dk} \tag{2.41}$$

Hence, the group velocity of longitudinal and shear waves equals their respective phase velocity. Inserting the expression $c = \frac{\omega}{k}$ into Eq. (2.34), the group velocity of bending waves can be derived. It corresponds to two times the phase velocity [Cremer 1967]:

$$c_g = 2\,c_B \tag{2.42}$$

Exceeding the energetic thin plate limit $\frac{f_s}{4}$ for $c_g = c_{S\kappa}$, the group velocity of effective bending waves can be described by [Rindel 1994; Meier 2000]:

$$c_{g,\text{eff}} = \frac{c_{B,\text{eff}}^3}{c_{S\kappa}^2} \sqrt{1 + \left(\frac{2\,f_s}{f}\right)^2} \tag{2.43}$$

2.2.5 Simple Thickness Modes

A structure containing plate-like components can be modeled by shell or solid elements. While shell elements lead to lower computation times, they cannot factor in through-thickness effects. As soon as thickness modes might be excited inside a plate, solid elements must be used to build up its dynamic behavior correctly. By means of the following expressions the resonance frequencies of the thickness modes can be identified:

$$f_{TM,n} = \frac{n\,c_{L/S}}{2h} \tag{2.44}$$

In Eq. (2.44) $c_{L/S}$ represents the longitudinal wave velocity $c_{L,z} = \sqrt{\frac{E_{S,z}}{\rho}}$ (Eq. (2.27)) of the thickness-stretch modes or the shear wave velocity $c_{S,zi} = \sqrt{\frac{G_{zi}}{\rho}}$ (Eq. (2.31)) of the thickness-shear modes. The nth simple thickness resonance frequency $f_{TM,n}$ depends on the stiffness modulus perpendicular to the plate $E_{S,z}$, which considers the constraint of the lateral in-plane strain, or the shear modulus G_{zi} (with $i = x$ or y), respectively. As the two types of thickness modes are uncoupled for isotropic and orthotropic materials, thickness-stretch modes cause displacements normal to the faces of the plate, whereas the thickness-shear modes lead to displacements parallel to it as depicted in Fig. 2.11. Their mode shapes can be described by $\sin\left(\frac{n\pi z}{h}\right)$ and $\cos\left(\frac{n\pi z}{h}\right)$ with n as even or odd integer, respectively.

As the modes of a finite plate cannot be described in closed form, approximations for limited frequency ranges of applications have been made by means of the solution for an infinite plate. In contrast to the full space, reflections occur in an infinite plate with traction-free faces. Therefore, longitudinal and shear waves couple to an infinite number of uncoupled symmetric and antisymmetric modes with respect to the middle plane of a plate.
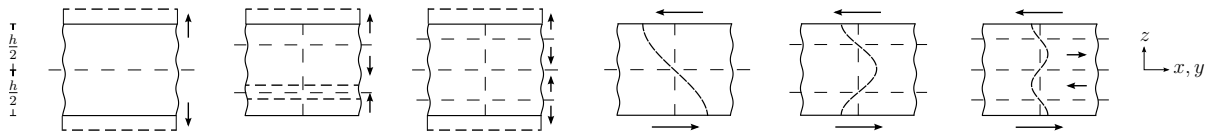
Figure 2.11: The first three thickness-strech modes (left) and thickness-shear modes (right) [Mindlin and Yang 2006].

The simple thickness resonances are defined to behave independently of the location in the plane of the plate. Hence, as this corresponds to a wave-number equal to zero, they represent the lower limiting frequencies of the symmetric and antisymmetric vibration modes occurring at high frequencies. For $n = 1$ and the minimum shear modulus, Eq. (2.44) delivers the upper limit of the applicability of shell elements based on the Mindlin wave approximation. Here, the first antisymmetric thickness-shear mode vibrates at resonance. Especially for wood, this upper limit already occurs at comparatively low frequencies as the elastic modulus perpendicular to the fiber direction is about one thirtieth of the one in fiber direction. Thus, a conflict between applicability and efficiency of FE models occurs. [Mindlin 1951; Mindlin and Yang 2006; Yu 1996; DIN EN 338 2016]

Airborne sound is able to excite the longitudinal wave motion through the thickness of a plate which leads to an efficient radiation from the backside of the plate at the thickness-stretch resonance frequencies. Therefore, they have practical relevance for the sound reduction index of a plate. Whereas the sound reduction increases with frequency, this behaviour changes significantly at the thickness resonances above the critical frequency. They lead to dips which can be estimated by a plateau. In the case of thick plates with a comparatively low stiffness perpendicular to the plate (like e.g. CLT), the thickness resonances occur below 5 kHz and thus inside the relevant frequency range for building acoustics. [Ljunggren 1991; Hopkins 2007]

2.3 Statistical Energy Analysis

The SEA enables the prediction of the energy flow within complex systems under certain restrictions. These are mainly linked to large uncertainties of the response values which can be handled by suitable averaging techniques. By contrast and as shown in chapter 3, the EFA uses a deterministic FE model without the requirement of an a priori focus on averaged quantities like e.g. mean energies. As the sensitivity of the results increases with frequency, averaging techniques of the SEA are applied in the post-processing of the EFA. Therefore,

the basic procedure of the SEA and its assumptions are introduced in this section in order to be able to refer to them in the subsequent chapters.

In the case of the SEA, the structure is divided into subsystems which can be characterized by two physical explanations: Firstly, in the case of the modal approach, the subsystems are grouped by similar resonant modes per frequency band. Secondly, the wave approach classifies a subsystem as a diffuse field consisting in a single wave type. The two methods are linked as a mode can be described as a superposition of waves and a wave can be interpreted as a sum of modes [Lyon and DeJong 1995].

A decisive parameter regarding the applicability of the SEA is the number of resonant modes within the investigated frequency band. Together with the modal overlap factor, which additionally considers the damping of the subsystem, the applicability of the SEA is attempted to be estimated as explained in subsection 2.3.2. In subsection 2.3.1, the basic SEA procedure is presented. Further assumptions of the SEA are complemented in subsection 2.3.3.

2.3.1 Power Balance Equation

The excitation of a system is modeled by injecting power into a part of the system. Depending on its physical properties, this excited part belongs to one or more subsystems of the SEA model. The input power flows between the individual subsystems due to the coupling and is dissipated according to the damping of the subsystems. As each of the subsystems can be described as groups of resonant modes, the power flow between them is proportional to the difference of their average modal energies $\mathcal{E}_i$ within the frequency band $\Delta\omega$. It is hereby assumed that the energy is distributed equivalently on the modes. The number of modes N_i in a frequency band with the bandwidth $\Delta\omega$ leads to the modal energy:

$$\mathcal{E}_i = \frac{E_i}{N_i} \tag{2.45}$$

Firstly, the SEA model in Fig. 2.12 consisting of two coupled subsystems is observed. Each subsystem i is characterized by a number of modes N_i and a total energy E_i within the frequency band $\Delta\omega$. Subsystem 1 is excited and, thus, the input power P_1 is injected. Due to damping, the power $P_{i,\mathrm{diss}}$ is dissipated by the subsystem i depending on the corresponding energy E_i, the angular frequency ω and the damping loss factor η_{ii}:

$$P_{i,\mathrm{diss}} = \omega\,\eta_{ii}\,E_i \tag{2.46}$$
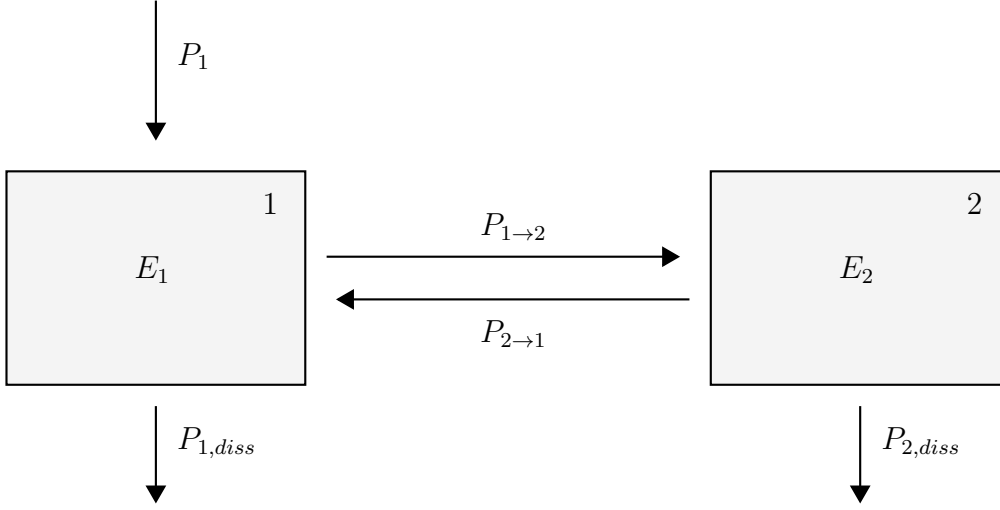
Figure 2.12: SEA model of two coupled subsystems.

The SEA investigates the steady state and, thus, an equilibrium can be set up. Inside a frequency band, all modes of a subsystem are assumed to couple equivalently strong with the ones of another subsystem, whereas no coupling is admitted within the modes of one subsystem. If the modal energies differ ($\mathcal{E}_1 \neq \mathcal{E}_2$), there is a proportional power flow between the two subsystems. This is known as coupling power proportionality and can be described by $P_{1\rightarrow2}$ and $P_{2\rightarrow1}$ for each direction separately. They can be balanced to the net flow P_{12} or P_{21} dependent on the direction:

$$P_1 = P_{1,\text{diss}} + P_{1\rightarrow2} - P_{2\rightarrow1} = P_{1,\text{diss}} + P_{12} \tag{2.47}$$

$$0 = P_{2,\text{diss}} + P_{2\rightarrow1} - P_{1\rightarrow2} = P_{2,\text{diss}} + P_{21} \tag{2.48}$$

The net flow P_{12} can be calculated by Eq. (2.49) on the basis of the modal coupling factor β_{12}. The factor β_{12} exclusively depends on the physical properties of the subsystems and scales the flow from the subsystem with the higher average modal energy to the subsystem with the lower one. Thereby, the number of modes N_i in a frequency band $\Delta\omega$ is expressed by the average modal frequency spacing $\delta f_i = \frac{\Delta\omega}{2\pi N_i}$.

$$P_{12} = \Delta\omega\beta_{12}(\mathcal{E}_1 - \mathcal{E}_2) = \Delta\omega\beta_{12}\left(\frac{E_1}{N_1} - \frac{E_2}{N_2}\right) = 2\pi\,\beta_{12}\left(E_1\,\overline{\delta f_1} - E_2\,\overline{\delta f_2}\right) \tag{2.49}$$

Analogously to the damping loss factor in Eq. (2.46), a coupling loss factor η_{ij} is introduced describing the losses due to the coupling of the subsystems:

$$P_{12} = \omega(E_1\eta_{12} - E_2\eta_{21}) = -P_{21} \tag{2.50}$$

The coupling loss factor denotes the amount of energy which is transmitted into the adjacent subsystem. The wave approach is suitable to derive the coupling loss factor η_{ij} by means of the transmission coefficient τ_{ij} characterizing only the junction for a transmission from one specific wave field to another one. The assumptions of the wave approach are briefly discussed in subsection 3.2.4. Moreover, it is shown that the coupling loss factor η_{ij} results from inserting the physical properties of the source subsystem i into Eq. (3.59). Derivations of τ_{ij} for different types of junctions, where plates contain bending and optionally in-plane waves, can be found in [Kihlmann 1967; Craik 2003; Hopkins 2007].

Determining coupling loss factors, PIM constitutes an experimental alternative which can be applied numerically as shown in subsection 3.2.2. This leads to so-called effective coupling loss factors because they describe the energy exchange between two structural components each containing different wave types.

η_{ji} can be derived from η_{ij} by means of the consistency relation:

$$N_1\eta_{12} = N_2\eta_{21} \tag{2.51}$$

The validity of this expression can be shown by means of the coupling power proportionality setting the power flow P_{12} in Eq. (2.50) equal to zero:

$$P_{12} = \omega(E_1\eta_{12} - E_2\eta_{21}) \overset{!}{=} 0 \tag{2.52}$$

If there is no power flow, the modal energies have to be equal ($\mathcal{E}_1 = \mathcal{E}_2 = \mathcal{E}$), which leads to:

$$P_{12} = \omega(\mathcal{E}N_1\eta_{12} - \mathcal{E}N_2\eta_{21}) = 0 \tag{2.53}$$

which results in Eq. (2.51). Now the power balance equations (2.47) and (2.48) can be rewritten as:

$$P_1 = P_{1,\text{diss}} + P_{12} = \omega((\eta_1 + \eta_{12})E_1 - \eta_{21}E_2) \tag{2.54}$$

$$0 = P_{2,\text{diss}} + P_{21} = \omega((\eta_2 + \eta_{21})E_2 - \eta_{12}E_1). \tag{2.55}$$

For a SEA model with m subsystems the power balance of one subsystem yields:

$$P_i = P_{i,\text{diss}} + \sum_j P_{i,j} \tag{2.56}$$

$$P_i = \omega \left(\eta_{ii} E_i + \sum_j \eta_{ij} E_i - \eta_{ji} E_j \right) \tag{2.57}$$

Rewriting this expression for all subsystems the total loss factor matrix results, which characterizes the SEA model and enables the prediction of subsystem energies due to a certain input power:

$$\omega \begin{bmatrix} \eta_{11} + \sum\limits_{j \neq 1} \eta_{1j} & -\eta_{21} & \cdots & -\eta_{m1} \\ -\eta_{12} & \eta_{22} + \sum\limits_{j \neq 2} \eta_{2j} & \cdots & -\eta_{m2} \\ \vdots & \vdots & \ddots & \vdots \\ -\eta_{1m} & -\eta_{2m} & \cdots & \eta_{mm} + \sum\limits_{j \neq m} \eta_{mj} \end{bmatrix} \begin{bmatrix} E_1 \\ E_2 \\ \vdots \\ E_m \end{bmatrix} = \begin{bmatrix} P_1 \\ P_2 \\ \vdots \\ P_m \end{bmatrix} \tag{2.58}$$

Usually this matrix is not fully occupied as not all subsystems couple with each other. Moreover, the sum of the ith column has to be equal $\omega \, \eta_{ii}$ to fulfill the conservation of energy. According to [Mace 2003], this is the second necessary criterion of the SEA beside the coupling power proportionality leading to the consistency relation. These criteria have to be satisfied in an ensemble average sense by several slightly different systems.

2.3.2 Important Quantities

Unlike the FEM, the SEA does not consider modes individually but as a randomly distributed set per subsystem and frequency band. Hence, statistical prerequisites have to be fulfilled: A sufficient number of modes per band belongs to these. According to literature, a minimum of three [Möser and Kropp 2010] to six [Fasold et al 1984] modes are assumed to be acceptable. The modal density as well as the average modal frequency spacing can be derived from the number of modes. These aspects represent the average distance between the individual eigenfrequencies. The modal overlap factor also takes the damping into consideration. Thereby, the width of the amplification functions is taken into account additionally to characterize the interaction of the modes.

Number of Modes

The number of modes N_i in a frequency band $\Delta\omega = 2\pi(f_u - f_l)$ can be expressed either by the modal density

$$n_i(\omega) = \frac{dN}{d\omega} \qquad \text{in } \frac{\text{s}}{\text{rad}} \qquad (2.59)$$

or by the average modal frequency spacing between the resonance frequencies [Lyon and DeJong 1995]:

$$\overline{\delta f_i} = \frac{1}{2\pi\, n_i(\omega)} \qquad \text{in Hz} \qquad (2.60)$$

The frequency band with the center frequency f_m is characterized by the lower and the upper band limiting frequencies f_l and f_u. In the case of one-third octave bands, they are linked by the expression:

$$f_u = 2^{\frac{1}{3}} f_l = 2^{\frac{1}{6}} f_m \qquad (2.61)$$

The number of resonant modes are calculated analytically for a four-sided, simply supported plate with the area A in Eq. (2.62) to (2.65). At higher frequencies, this serves as an estimate for a plate with any boundary condition. The following expressions are given by Lyon and DeJong [1995] and they base upon the wave velocities derived in section 2.2. The in-plane modes of the plate consist of the longitudinal modes

$$\overline{\delta f_{LP}} = \frac{c_{LP}^2}{2\pi\, f\, A} \qquad (2.62)$$

and the shear modes:

$$\overline{\delta f_S} = \frac{c_{S,xy}^2}{2\pi\, f\, A} \qquad (2.63)$$

The bending modes in the case of thin plates are given by

$$\overline{\delta f_B} = \frac{2\, c_B^2}{2\pi\, f\, A} = \frac{c_B\, c_g}{2\pi\, f\, A} \qquad (2.64)$$

(a) Modal density $n(\omega)$

(b) Number of modes per one-third octave band
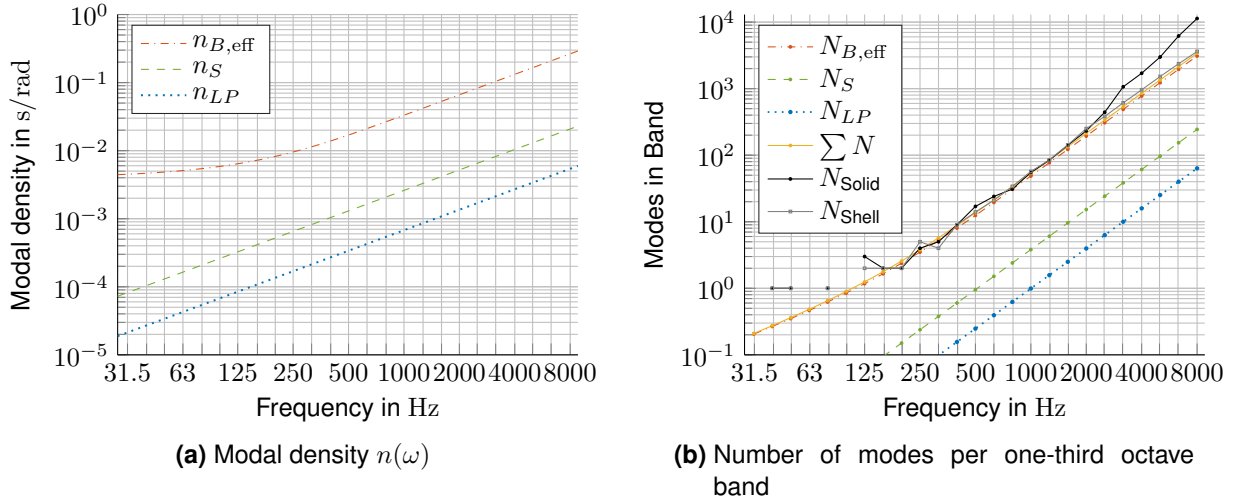
Figure 2.13: Modal characteristics of an exemplary orthotropic plate described by quasi-longitudinal, in-plane shear and effective bending waves compared to FE models.

whereas in the case of thick plates different approximations are offered by literature. In accordance with subsection 2.2.3, the phase and the group velocity are replaced by the effective velocities [Meier 2000]:

$$\overline{\delta f_{B,\text{eff}}} = \frac{c_{B,\text{eff}}\, c_{g,\text{eff}}}{2\,\pi\,f\,A} \tag{2.65}$$

Figure 2.13 shows the modal density and the number of modes per one-third octave band based on the quasi-longitudinal, the in-plane shear and the effective bending wave velocity for an exemplary orthotropic plate. The sum of the analytically estimated number of modes $\sum N$ is opposed to the number of modes resulting from a modal analysis performed with the FEM. Figure 2.13b shows a good agreement above the first eigenfrequencies, which strongly depend on the boundary conditions. From the first thickness resonances on, the number of modes detected by the solid element model clearly increase whereas the analytical solution and the shell element model are based on the Mindlin plate theory, which ignores through thickness effects (cf. subsection 2.2.5).

Modal Overlap Factor

The modal overlap factor relates the width of a resonance to the average modal frequency spacing $\overline{\delta f_i}$. The width of the resonance at a frequency f is described by the modal band-width $\Delta f_{hp} = f\eta_{ii}$ characterized by the half power points of the transfer function. On the logarithmic scale, these points occur $3\,\text{dB}$ down from the resonance peak which corresponds
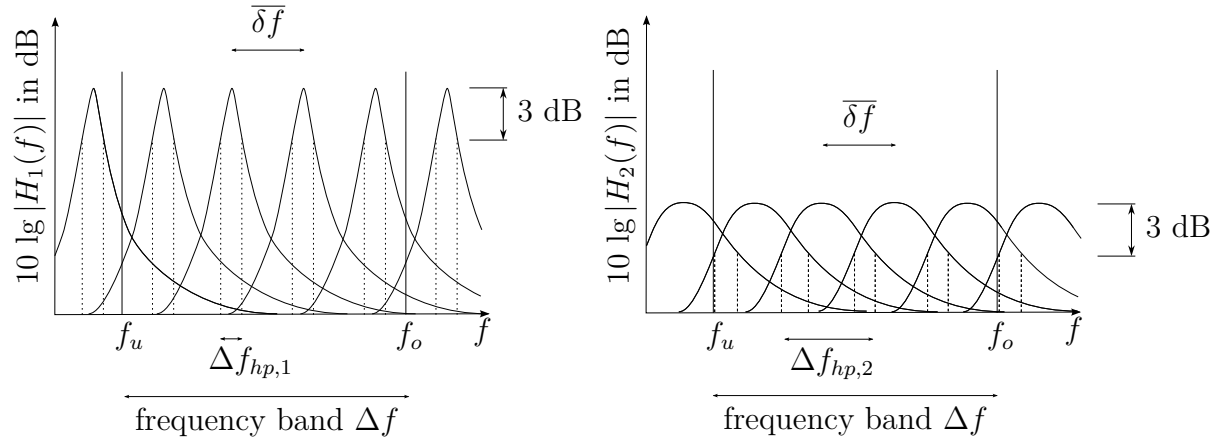
Figure 2.14: The half power bandwidth $\Delta f_{hp,i}$ of the two transfer functions with equal modal frequency spacing $\overline{\delta f_i}$ varies due to a low damping on the left and a high damping on the right [Weineisen 2014].

to a halving of the power [Zaveri 1984]. This leads to the so-called half power bandwidth modal overlap factor:

$$M_{hp,i} = \frac{f\,\eta_{ii}}{\overline{\delta f_i}} = \omega\eta_{ii}n_i \tag{2.66}$$

The so-called noise or energy bandwidth modal overlap factor is common in literature, too. The energy or noise bandwidth is defined as the theoretical bandwidth of a band-limited white noise. It contains the same amount of energy as the modal response and its power spectral density corresponds to the maximum of the modal transfer function: [Woyczynski 2011; Lyon and DeJong 1995].

$$M_{en,i} = \omega\eta_{ii}n_i\frac{\pi}{2} \tag{2.67}$$

Within this thesis, the half power bandwidth modal overlap factor will be used exclusively and thus just named modal overlap factor. Generally, the modal overlap factor depends on the modal density n_i and on the damping loss factor η_{ii} of subsystem i. At resonance, the shape of the modal response is dominated by the damping. Figure 2.14 shows two transfer functions with equal modal frequency spacing $\overline{\delta f_i}$ but different damping values. Higher damping leads to a smoother spectrum and to a higher modal overlap. For the application of the SEA, literature recommends a modal overlap factor greater than unity to guarantee uncorrelated wave transmission between subsystems. Hence, the SEA assumption that subsystems are diffuse wave fields is fulfilled as the waves which transport energy from one subsystem to another are assumed to be uncorrelated from those waves which transport energy in the opposite direction. [Lyon and DeJong 1995; Culla and Sestieri 2006]

2.3.3 Further Assumptions and Postulations

Several basic postulations of the SEA are mentioned in subsection 2.3.1, where the power balance equation is derived, and in subsection 2.3.2. In the following, further assumptions on which the SEA is based are emphasized. Moreover, these assumptions and their validity are discussed in the context of the EFA in subsection 3.2.3.

Conservative Coupling The coupling between subsystems is characterized through coupling loss factors leading to energy exchange in between them but not to dissipation. This occurs only inside the subsystems and is described by the damping loss factors.

Weak Coupling Based on the hypothesis of weak coupling, the energy of the subsystem or the modal group coincides with the uncoupled energy. This means the groups of modes or, respectively, subsystems are treated separately. The participation of various subsystems at a so-called global mode cannot be modeled. Modes should be localized in such a way that most or all of its energy excites one subsystem [Finnveden 2011]. Indirect couplings with the subsystem after the next subsystem are not possible in the classical SEA [Culla and Sestieri 2006]. This leads to the so-called Smith criterion: $\eta_{ij} \ll \eta_{ii}$. Finnveden [2011] compares this to further measures in order to estimate the strength of coupling and thereby to verify the weak coupling assumption.

Hence, only in the case of weakly coupled subsystems, Eq. (2.49) and (2.50) hold for a system containing more than two subsystems [Mace 1994]. Otherwise, the transmissions have to be solved for the whole system which is contrary to the basic concept of the classical SEA.

Resonant Energy Transfer The classical SEA exclusively treats energy flows between groups of resonant modes of direct coupled subsystems.

Non-resonant, Stiffness or Mass Dominated Paths A mode can be excited below or above its resonance frequency in the stiffness or mass dominated region of its amplification function, respectively. Considering the non-resonant transmission in the SEA, stiffness or mass dominated paths have to be added to the model. One example is the non-resonant sound transmission through a wall which separates two rooms. Below the critical frequency, the air excites the wall above its resonance frequencies since the wave length of air is greater than the bending wave length of the wall. In this frequency range, the stiffness and the damping of the wall can be neglected, which means the energy transmission between two cavities is caused by the inertia of the wall. The

forced excitation of the wall leads two an indirect coupling of the two cavities. [Fahy 1987; Weineisen 2014]

Uniform Damping All modes of a subsystem in a certain frequency band are characterized by the same damping.

Subsystem Size Sufficient but not necessary criteria for the lower limit of a subsystem are given by means of the number of modes and the modal overlap factor presented in subsection 2.3.2. Due to large damping, the direct field dominates at high frequencies, which leads to a strong decrease in vibration with increasing distance. Thus, Lyon and DeJong [1995] recommend the following limit for the maximum dimension l of a subsystem, since the energy decays with $e^{-\omega \eta_{ii} \frac{x}{c_g}}$, if waves travel across a distance x.

$$l < \frac{c_g}{\omega \, \eta_{ii}} \tag{2.68}$$

On the other hand, the evaluation of the energy should not be carried out in the direct field.

3 Energy Flow Analysis

The objective of the EFA is to predcit the vibrational energy that flows through a structure. The energy flow is described by the energy influence coefficients A which relate the total, time-averaged subsystem energy E to a corresponding input power P.

For the application of the EFA, the structure is divided into subsystems according to its subdivision into components. In contrast to the SEA, the prerequisite of the so-called weak coupling, which is introduced in subsection 2.3.3, is not imperative for the EFA and the subsystem definition is independent of wave types. This leads to a greater flexibility for the subsystem division. Moreover, it facilitates the precise detection and optimization of critical components with respect to the energy transmission. [Mace and Shorter 2000]

Figure 3.1 shows e.g. the partition of an L-junction into subsystems, i.e. into a wall and a ceiling. In chapter 4, the L-junction is investigated beside T- and X-junctions. The subsystems are modeled with FE as the FEM is a convenient tool to predict the vibroacoustic behavior. Either a continuum model composed of solid elements is chosen or shell elements allowing shear deformations are applied. The shell elements are based on the Mindlin plate theory [Mindlin 1951] whereby through-thickness effects which occur particularly at high
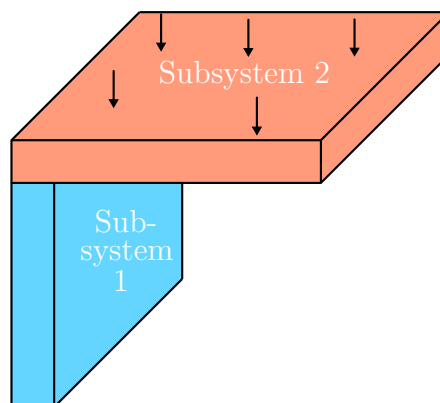
Figure 3.1: Partition of L-junction into subsystems, loading of subsystem 2.

frequencies are not considered. For modeling the properties of CLT, section 2.1 introduces a linear and orthotropic material including the simple case of isotropy.

At a given location and frequency, the sensitivity of the response to small changes in material or load data increases with frequency. This leads to non robust results if a high resolution with respect to the spatial distribution and the frequency content is aimed at. Without appropriate post-processing, the FEM is limited due to the sensitivity of the results at higher frequencies. Moreover, the physical properties influence the robustness of the results. For instance, high damping values lead to a large modal overlap which reduces the sensitivity of the frequency response function varying e.g. the point of observation.

In the mid-frequency range, an adequate number of modes per band and a sufficiently high modal overlap enable the use of statistical methods like the SEA. It provides averaged results and thus copes with their sensitivity. But also the wave transmission inside the SEA is limited to the governing partial differential equation, e.g. the Mindlin plate theory. Adding the restrictions mentioned in section 2.3, the SEA based on the Mindlin plate theory is only applicable to the mid-frequency range. Due to a restricted validity of the displacement solution of the FEM and of the results of the SEA assuming semi-infinite Mindlin plates, averaging techniques of the SEA are applied in the post-processing of the FEM to obtain valid and robust results in a wider frequency range. Thus, the EFA can be considered as an adapted hybrid approach.

The basic approach in section 3.1 comprises the step from the classical FEM to averaged output quantities. It follows an introduction of various evaluation options for the energy flow in section 3.2 starting with the primary quantity of the method, the energy influence coefficients. Section 3.3 presents a procedure to compute robust energy influence coefficients and to evaluate their statistical properties, if a structure with unknown load position is investigated.

3.1 Basic Approach

The primary aim of the EFA is to calculate the system response using an FE model as explained in subsection 3.1.1. Afterwards, input power and energy are derived, which are treated in subsections 3.1.2 and 3.1.3, respectively. By averaging energy and power, energy influence coefficients, which are robust with respect to time, space and frequency dependent

fluctuations, shall be provided:

$$\tilde{A}_{ij} = \frac{\int_{f_l}^{f_u} \int_0^T \int_{\Theta_i} E_e\left(\mathbf{z},t,f\right) \, d\Theta dt df}{\int_{f_l}^{f_u} \int_0^T \int_{\Theta_j} P_e\left(\mathbf{z},t,f\right) \, d\Theta dt df} \tag{3.1}$$

To solve the integrals in Eq. (3.1) over the space Θ, the time t and the frequency f different techniques are applied. The space average is obtained by using an FE post-processing approach and by summing up the element quantities marked by the index e. Their cartesian coordinates are summarized in the vector $\mathbf{z} = (x,y,z)$. Assuming a time-harmonic oscillation, the integral over time can be solved analytically. Initially, energy, power and energy influence coefficients are calculated for discrete frequency points. Subsection 3.1.4 shows the integration by means of the composite trapezoidal rule to deliver frequency band averages which are marked by a tilde.

3.1.1 Displacement Solution of the Equation of Motion

Finite Element Method

The FEM offers to either do a modal analysis which provides eigenfrequencies and -modes or to undertake a harmonic analysis which results in the response behavior due to a time-harmonic force. Both applications work in the frequency domain.

By means of numerical methods like the FEM, it is possible to model structures consisting of various components out of different materials with complex boundary and coupling conditions. By contrast, analytical approaches are restricted to components and boundary conditions for which a function exists that fulfills the differential equation at the boundaries and anywhere inside the domain. This is also known as strong formulation of the problem. Replacing the exact solution by an approximate one leads to a residuum which states the difference between the two solutions. The differential equation is thus not anymore exactly fulfilled at any location inside the domain. Introducing a weighting function the error must vanish on average by integrating over the domain. After rearranging this integral postulation, the so-called weak formulation of the problem results. The basic idea of the FEM is to approximate the unknown displacement by dividing the whole domain into subdomains, the Finite Elements. Thereby, the weighting functions use the same shape functions as the displacements do according to Galerkin. [Merkel and Öchsner 2014]

By means of the FEM, the equation of motion can be solved numerically. Its weak formulation is discretized to obtain a finite number of degrees of freedom. Firstly, the whole domain

is divided into Finite Elements by a mesh. Secondly, within each element the displacement is approximated by a linear combination of shape functions and local degrees of freedom. The assembling of the system matrix out of the element matrices as well as the coordinate transformation from local to global degrees of freedom leads to the linear system of equations (cf. Eq. (3.2) and (3.6)). The size of the problem and the accuracy of the solution depend on both, the mesh and the shape functions. [Cook 1989; Paolini et al 2017]

Modal Analysis

For the interpretation of the energy flow inside a structure and to characterize its dynamical behavior, it is important to know its eigenfrequencies and eigenmodes. Both quantities are calculated by a modal analysis. Therein, the structure is not subjected to a load leading to a homogeneous, differential system of equations:

$$[K]\,\mathbf{u} + [M]\,\ddot{\mathbf{u}} = 0 \tag{3.2}$$

The unknowns of Eq. 3.2 are the global degrees of freedom $\mathbf{u}$ and their second time derivative $\ddot{\mathbf{u}}$. They state the nodal displacement and acceleration vector, respectively. $[M]$ and $[K]$ denote the mass and the stiffness matrix of the system. The order of damping magnitude which is typical in most applications of civil engineering only leads to slight changes in the eigenfrequencies. As the eigenfrequencies and the eigenmodes are used to discuss the results of the EFA, damping is neglected. However, damping has to be taken into account in the case of locally damped structures, e.g. due to elastic interlayers. Assuming time-harmonic oscillations, the product approach for an unknown displacement vector separates the spatial $\boldsymbol{\Phi}$ and the time domain $\sin(\omega t)$:

$$\mathbf{u} = \boldsymbol{\Phi}\,\sin(\omega t) \tag{3.3}$$

Inserting this expression into the differential equation of motion yields:

$$\left([K] - \omega^2\,[M]\right)\boldsymbol{\Phi} = 0 \tag{3.4}$$

A non-trivial solution, i.e. $\boldsymbol{\Phi} \neq 0$, for this matrix eigenvalue problem only exists, if it holds:

$$det\left([K] - \omega^2\,[M]\right) = 0 \tag{3.5}$$

Equation (3.5) denotes the characteristic polynomial whose order corresponds to the number of degrees of freedom of the FE model. This leads to an identical number of roots, which are the eigenvalues representing the squared angular eigenfrequencies $\omega_i^2 = (2\pi f_i)^2$. The eigenvectors $\boldsymbol{\Phi_i}$ are the eigenmodes of the structure. They can be obtained by inserting the corresponding eigenvalues ω_i^2 into Eq. (3.4). [Müller 2016]

Harmonic Analysis

To calculate the response behavior of a structure due to a time-harmonic excitation, a harmonic analysis is performed. For this purpose, the consideration of damping is decisive. The damping is described by the loss factor η. A hysteretic damping is chosen and thus, the system is damped proportional to the stiffness matrix $[K]$ as introduced in subsection 2.1.4. Hence, the damping forces are proportional to the displacement $\mathbf{u}$. It results the inhomogeneous equation of motion:

$$[K]\,(1+i\eta)\,\mathbf{u} + [M]\,\ddot{\mathbf{u}} = \mathbf{F} \tag{3.6}$$

The force vector $\mathbf{F}$, which excites the structure sinusoidally with the frequency $f = \frac{\Omega}{2\pi}$, contains the loads F having an amplitude F_0 and a certain phase shift ϕ:

$$F\left(\mathbf{z},t,f\right) = F_0 \cos\left(2\pi f\,t + \phi(\mathbf{z})\right) \tag{3.7}$$

$$= F_0\,\cos(\phi)\cos(\Omega t) - F_0\,\sin(\phi)\sin(\Omega t) \tag{3.8}$$

After expressing the phase shift by a combination of sine and cosine, for simplicity the constant parts are summarized to $\alpha = F_0\cos(\phi)$ and $\beta = F_0\sin(\phi)$:

$$F\left(\mathbf{z},t,f\right) = \alpha\cos(\Omega t) - \beta\sin(\Omega t) \tag{3.9}$$

Applying Euler's formula, the time-harmonic excitation can also be described in complex notation, where α denotes the real part and β the imaginary one.

$$F\left(\mathbf{z},t,f\right) = \frac{1}{2}\left(\alpha + i\,\beta\right)e^{i\Omega t} + \frac{1}{2}\left(\alpha - i\,\beta\right)e^{-i\Omega t} \qquad = \Re\left[(\alpha + i\,\beta)e^{i\Omega t}\right] \tag{3.10}$$

The complex force $\underline{F} = F_0\,e^{i\phi} = \alpha + i\,\beta$ is marked by an underscore and includes the amplitude $F_0 = \sqrt{\alpha^2 + \beta^2}$ and the phase shift $\phi = \arctan\left(\frac{\beta}{\alpha}\right)$:

$$F(\mathbf{z},t,f) = \frac{1}{2}F_0\,e^{i\phi}\,e^{i\Omega t} + \frac{1}{2}F_0\,e^{-i\phi}\,e^{-i\Omega t} \qquad\qquad = \Re\left(F_0\,e^{i\phi}\,e^{i\Omega t}\right) \tag{3.11}$$

$$= \frac{1}{2}\underline{F}\,e^{i\Omega t} + \frac{1}{2}\underline{F}^*\,e^{-i\Omega t} \qquad\qquad = \Re\left(\underline{F}\,e^{i\Omega t}\right) \tag{3.12}$$

The equations (3.10) to (3.12) show that the excitation can also be split into a complex and a conjugated complex pointer marked by an asterisk which oscillates with the negative frequency. To solve Eq. (3.6), the excitation may be described using just one component. Thereby, the same time dependency is assumed for the complex displacement vector $\underline{\mathbf{u}}$ leading to its second derivative $-\Omega^2\,\underline{\mathbf{u}}$:

$$\left[[K]\,(1 + i\eta) - \Omega^2\,[M]\right]\underline{\mathbf{u}}\,e^{i\Omega t} = \underline{\mathbf{F}}\,e^{i\Omega t} \tag{3.13}$$

$e^{i\Omega t}$ can be canceled out on both sides of the equation and the particular solution for $\underline{\mathbf{u}}$ can be obtained.

The total displacement solution is composed of the homogeneous and the particular solution. The homogeneous solution takes the initial conditions into account and decays for damped structures during the transient starting phase. Since the homogeneous solution can be regarded as faded away for typical time and frequency scales in the acoustic domain, the particular solution, which describes the steady state for a time-harmonic loading, is exclusively considered:

$$\underline{\mathbf{u}} = \left[[K]\,(1 + i\eta) - \Omega^2\,[M]\right]^{-1}\underline{\mathbf{F}} \tag{3.14}$$

The individual material properties of the different subsystems and elastic interlayers are taken into account on element basis. This is expressed by the following equation representing the element matrices and their assembling to the complex dynamic stiffness matrix $[\underline{K}(\Omega)]$:

$$\underline{\mathbf{u}} = \overset{n_e}{\underset{e=1}{\mathbb{A}}}\left[[K_e]\,(1 + i\eta_e) - \Omega^2\,[M_e]\right]^{-1}\underline{\mathbf{F}} \tag{3.15}$$

$$\underline{\mathbf{u}} = [\underline{K}(\Omega)]^{-1}\,\underline{\mathbf{F}} \tag{3.16}$$

In the case of a varying, element dependent damping η_e, the system is no longer proportionally damped. The complex dynamic stiffness matrix $[\underline{K}(\Omega)]$ characterizes the whole system for a certain frequency of excitation. To perform a harmonic analysis, Eq. (3.16) is solved for each frequency of interest. For the presented approach, this procedure is computationally

more efficient compared to a modal approach because above the first antisymmetric mode of thickness-shear (cf. subsection 2.2.5) the number of modes is increasing significantly. For timber or fiber composite plates, this limit already occurs at comparatively low frequencies as its elastic modulus perpendicular to the fiber is a fraction of the one in fiber direction.

3.1.2 Input Power

First of all, the subsystems are excited one by one by a time-harmonic excitation. Instead of using nodal loads, pressure is applied on selected elements to be able to build up more realistically planar excitations like airborne sound pressure and especially to avoid that singularities affect the resulting input power [Winter and Müller 2017]. The pressure is considered as a surface load which is transformed to equivalent nodal loads by weighting it with the shape functions and integrating over the elements. Due to the weighting, the equivalent nodal loads are referred as consistent. It is assumed that both surface load and equivalent nodal loads perform the same external virtual work with their corresponding virtual displacements. Unlike a single nodal load, the equivalent ones do not lead to a mesh dependent displacement ending up in a singularity. Within the scope of the approximate solution, the FEM is hereby able to provide correct displacements at the nodes belonging to loaded elements which are then used to calculate the input power [Müller and Groth 2007; Werkle 2008]. If realistic loads would be modeled, the deviations linked to the discretization should be taken into account.

The pressure vector $\mathbf{p}$ consists of three entries

$$p_{x/y/z} = \frac{F(\mathbf{z},t,f)}{A_e(\mathbf{z})} \tag{3.17}$$

in the space directions x, y and z. The pressure components contain the load amplitude F_0, which is evenly distributed on the surface A_e of the selected element and excites the structure harmonically with a phase shift ϕ as shown in Eq. (3.7) to (3.12). The time-averaged element input power is calculated by a double integral over the dot product of the applied pressure $\mathbf{p}$ and the resulting velocity $\mathbf{v}$ [Müller 2016; Cremer 1967]:

$$P_e(f) = \frac{1}{T} \int_0^T \int\limits_{(A_e)} \mathbf{p}(\mathbf{z},t,f) \cdot \mathbf{v}(\mathbf{z},t,f) \, dA \, dt \tag{3.18}$$
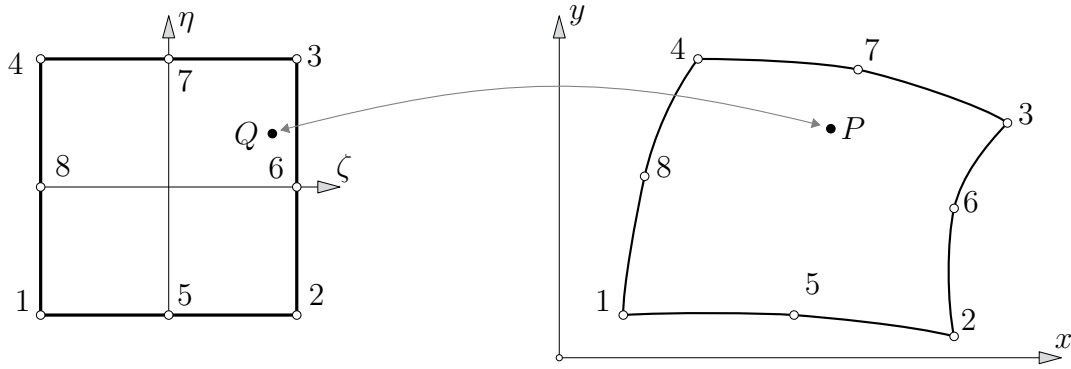
Figure 3.2: The element coordinates ξ and η are related to the global coordinates x and y by the Jacobian matrix $[J]$ - here depicted for a shell element with quadratic shape functions [Cook 1989].

For simplicity, a unidirectional loading is assumed and complex expressions of pressure and velocity are used according to Eq. (3.12).

$$P_e(f) = \frac{1}{T} \int_0^T \int_{(A_e)} \frac{1}{2} \left(\underline{p}\, e^{i\Omega t} + \underline{p}^*\, e^{-i\Omega t} \right) \frac{1}{2} \left(\underline{v}\, e^{i\Omega t} + \underline{v}^*\, e^{-i\Omega t} \right) \, dA \, dt \tag{3.19}$$

$$= \frac{1}{T} \int_0^T \int_{(A_e)} \frac{1}{4} \left(\underline{p}\underline{v}\, e^{2i\Omega t} + \underline{p}^*\underline{v}\, e^0 + \underline{p}\underline{v}^*\, e^0 + \underline{p}^*\underline{v}^*\, e^{-2i\Omega t} \right) \, dA \, dt \tag{3.20}$$

Due to the integration over one period $T = \frac{2\pi}{\Omega}$, the contribution of the reactive power oscillating with double frequency vanishes.

$$P_e(f) = \frac{1}{2} \int_{(A_e)} \Re \left(\underline{p}\,\underline{v}^* \right) \, dA \tag{3.21}$$

To solve the integral in Eq. (3.21), both physical quantities $\underline{p}$ and $\underline{v}$ as well as the coordinates x and y are approximated across the loaded surface of the elements e by the values at the nodes k and the respective, quadratic shape functions $N_{e,k}$. This corresponds to a weighted sum over $n_k = 8$ nodal values. In the case of the velocity, which results as first time derivative of the displacement solution applying $\underline{v} = i\Omega\,\underline{u}$, this leads to:

$$\underline{v}_e(\xi, \eta) = \sum_{k=1}^{n_k} \underline{v}_{e,k} N_{e,k}(\xi, \eta) \tag{3.22}$$

As the shape functions are expressed in dependency on the element coordinates ξ and η, the coordinates of the integral have to be transformed from x, y to ξ, η by means of the Jacobian matrix $[J]$ [Felippa 2004]. Figure 3.2 visualizes the coordinate transformation for a shell element having quadratic shape functions.

$$\int\limits_{(x)} \int\limits_{(y)} f(x,y)\, dy\, dx = \int\limits_{(s)} \int\limits_{(t)} g(\xi, \eta)\, \det[J]\, d\xi\, d\eta \tag{3.23}$$

$$[J] = \begin{bmatrix} \dfrac{\partial x}{\partial \xi} & \dfrac{\partial x}{\partial \eta} \\[2ex] \dfrac{\partial y}{\partial \xi} & \dfrac{\partial y}{\partial \eta} \end{bmatrix} \tag{3.24}$$

The integral can be solved analytically in advance and the resulting expression can then be evaluated element-wise with the corresponding nodal values in the post-processing. This leads to the time-averaged element input power P_e which is subsequently summed up over all loaded elements n_l in subsystem j. Hence, Eq. (3.25) delivers the injected power into subsystem j averaged with respect to time and space.

$$P_j(f) = \sum_e^{n_l} P_e(f) = \sum_e^{n_l} \frac{1}{2} \int\limits_{-1}^{1} \int\limits_{-1}^{1} \Re\left(\underline{p}_e\, \underline{v}_e^*\right) \det[J]\, d\xi\, d\eta \tag{3.25}$$

3.1.3 Subsystem Energy

According to Eq. (2.9), the stored energy in the investigated system due to deformations, i.e. the potential energy, can be calculated by integrating over the volume of the tensor product of stress and strain, also known as the elastic potential [Müller 2015].

$$\Pi_v = \int_{(V)} \Pi_{iv}(\varepsilon) dV = \int_{(V)} \frac{1}{2} \sigma^{kl} \varepsilon_{kl} dV \tag{3.26}$$

Within the scope of the FEM, Eq. (3.26) is evaluated element-wise by a Gauß integration. This leads to the inner sum in Eq. (3.27) whereby w_g represents the weighting factor corresponding to the integration point g.

$$E_{ij,\mathrm{pot}}(f) = \frac{1}{2} \sum_{e \in \Theta_i} \sum_g \frac{1}{2} \boldsymbol{\sigma}^{*T} \boldsymbol{\varepsilon}\, w_g \tag{3.27}$$

To calculate the potential element energy by the displacement solution in Eq. (3.16), the governing equations have to be applied. Firstly, the material law is inserted by the constitutive equation (2.1) and secondly, the resulting strains are expressed through displacements

by the kinematic equation:

$$
\begin{bmatrix} \varepsilon_x \\ \varepsilon_y \\ \varepsilon_z \\ \gamma_{yz} \\ \gamma_{xz} \\ \gamma_{xy} \end{bmatrix} = \begin{bmatrix} \dfrac{\partial}{\partial x} & 0 & 0 \\ 0 & \dfrac{\partial}{\partial y} & 0 \\ \dfrac{\partial}{\partial y} & \dfrac{\partial}{\partial x} & 0 \\ \dfrac{\partial}{\partial z} & 0 & \dfrac{\partial}{\partial x} \\ 0 & \dfrac{\partial}{\partial z} & \dfrac{\partial}{\partial y} \end{bmatrix} \begin{bmatrix} u_x \\ u_y \\ u_z \end{bmatrix} \tag{3.28}
$$

Discretizing the displacement field by means of the shape functions (cf. Eq. (3.22) and Fig. 3.2) the potential element energy is computed on the basis of the squared, complex element degree of freedom vector $\underline{\mathbf{u}}_e$ and the element stiffness matrix $[K_e]$ in Eq. (3.29) [Felippa 2004]. The expressions (3.27) respectively (3.29) and (3.30) state the time and space average of the potential energy $E_{ij,\text{pot}}$ and of the kinetic energy $E_{ij,\text{kin}}$ inside the subsystem i due to loading of subsystem j:

$$
E_{ij,\text{pot}}(f) = \frac{1}{2} \sum_{e \in \Theta_i} \frac{1}{2} \underline{\mathbf{u}}_e^{*T} [K_e] \, \underline{\mathbf{u}}_e \tag{3.29}
$$

As depicted in Eq. (3.30), the time derivative of $\underline{\mathbf{u}}_e$ and the element mass matrix $[M_e]$ lead to the kinetic energy in the post-processing of an FE simulation:

$$
E_{ij,\text{kin}}(f) = \frac{1}{2} \sum_{e \in \Theta_i} \frac{1}{2} \Omega^2 \, \underline{\mathbf{u}}_e^{*T} [M_e] \, \underline{\mathbf{u}}_e \tag{3.30}
$$

The element energies are added for each subsystem according to the sum in Eq. (3.29) and (3.30), respectively, yielding space averaged energies. Here, Θ_i describes the set of elements belonging to subsystem i.

As shown above, both energy types are proportional to the quadratic displacement:

$$
E(t) \sim u^2(t) = u_0^2 \left[\cos\left(\Omega t + \varphi \right) \right]^2 = \left[\frac{1}{2} \left(\underline{u} \, e^{i\Omega t} + \underline{u}^* e^{-i\Omega t} \right) \right]^2 \tag{3.31}
$$

$$
\max(E(t)) = E_0 \sim u_0^2 \tag{3.32}
$$

Averaging of $E(t)$ with respect to time corresponds to the integration over one period of a quadratic, sinusoidal function in the case of a time-harmonic excitation.

$$E \sim \frac{1}{2}\, u_0^2 \;=\; \frac{1}{T} \int_0^T u^2(t)\, dt \qquad = \frac{1}{T} \int_0^T u_0^2 \left[\cos\left(\Omega t + \phi_u\right)\right]^2 dt \qquad (3.33)$$

$$= \frac{1}{T} \int_0^T \left[\frac{1}{2}\left(\underline{u}\, e^{i\Omega t} + \underline{u}^*\, e^{-i\Omega t}\right)\right]^2 dt$$

Thus, the time-averaged energy E is one-half of the maximum value E_0 of the energy over time $E(t)$:

$$E = \frac{1}{2}\, E_0 \qquad\qquad (3.34)$$

For each excited frequency f, the sum over the element energies in Eq. (3.29) and (3.30) is therefore multiplied by one-half to receive the time and space average of the potential and the kinetic energy, respectively. Summing them up leads to the total energy per subsystem and frequency:

$$E_{ij}(f) = E_{ij,\mathrm{kin}}(f) + E_{ij,\mathrm{pot}}(f) \qquad\qquad (3.35)$$

3.1.4 Resolution and Average in the Frequency Range

To cover the whole frequency range of interest - e.g. the extended one for building acoustics from 50 to 5000 Hz - a logarithmically equidistant spacing Δf_k between the excited frequencies is applied. This leads to an identical number of evaluated frequencies n_f for each one-third octave band. Averaging the time and space averaged input power and subsystem energies over the frequencies of excitation, the governing equations can be referred to an averaged ensemble of slightly different, but similar coupled systems in the steady state presuming a sufficient modal density [Lyon and DeJong 1995].

The frequency average for a frequency band with limits f_l and f_u is approximated by a summation over discrete frequencies. For each frequency step, Eq. (3.16) is solved. The approximation of the continuous frequency curve by the composite rectangle rule would result in case of the energy E:

$$\frac{1}{f_u - f_l} \int_{f_l}^{f_u} E\left(f\right) df \approx \frac{1}{f_u - f_l} \sum_k^{n_f} E\left(f_k\right) \Delta f_k = \frac{f_u - f_l}{f_u - f_l} \sum_k^{n_f} E\left(f_k\right) w_k = \sum_k^{n_f} E\left(f_k\right) w_k \quad (3.36)$$

Here, the logarithmically equidistant spacing over frequency $\Delta f_k = f_{k+1} - f_k = w_k(f_u - f_l)$ is described in dependency on a weighting factor w_k with $k \in \{1, 2, \ldots, n_f\}$. Inside a band, w_k increases with frequency as the range represented by one discrete frequency becomes wider, whereas in case of a constant spacing the weighting factor would be $w_k = \frac{1}{n_f} = w$. Applying the composite trapezoidal rule instead of the rectangle rule leads to a closer approximation of the frequency average for the same number of frequency steps per band. Again the numerical integration, which can be performed identically for the subsystem energy and the input power, is exemplary shown for the energy E:

$$\frac{1}{f_u - f_l} \int_{f_l}^{f_u} E\left(f\right) \approx \frac{1}{f_u - f_l} \sum_{k}^{n_f} T_K(E) = \frac{1}{f_u - f_l} \sum_{k}^{n_f} \frac{1}{2} \left(E\left(f_{k+1}\right) + E\left(f_k\right)\right) \Delta f_k \qquad (3.37)$$

$$= \sum_{k}^{n_f} \frac{1}{2} \left(E\left(f_{k+1}\right) + E\left(f_k\right)\right) w_k \qquad (3.38)$$

$$= \tilde{E} \qquad (3.39)$$

With the presented interpolation techniques as well as with higher order polynomials and cubic splines, investigations have been performed to identify a suitable number of frequency steps per one-third octave band. They are summarized in dependency on the frequency range in subsection 4.1.6 and Tab. 4.5.

3.2 Evaluation Quantities

Having excited each of the m subsystems one by one, the average with respect to time, space and - optionally - frequency of the input power and of the corresponding total energies per subsystem can be calculated. Thereby, energy influence coefficients can be derived as shown in subsection 3.2.1 to describe the energy flow, which is normalized to the input power, inside the whole system. Fulfilling criteria like e.g. weak coupling which is assumed to be sufficient but not necessary, the energy influence coefficients matrix can be inverted. As explained in subsection 3.2.2, coupling loss factors are obtained which are ideally characterized exclusively by the junction and the source subsystem. In subsection 3.2.3, the condition number of the energy influence coefficients matrix is introduced. It enables to verify the invertibility and hereby mathematically the weak coupling condition. Moreover, the validity of coupling loss factors is discussed.

The European standard [DIN EN ISO 12354-1 2017] uses engineering quantities in order to perform simplified, approximate predictions which implicates a reduced quality of the results.

In this regard, the vibration reduction index aims to exclusively characterize the transmission behavior of the junction itself. This concept bases upon the transmission coefficient, which can be derived by the wave approach leading to the coupling loss factors known from the SEA. The limitations and drawbacks of the vibration reduction index as well as a calculation by means of the coupling loss factors from the EFA are discussed in subsection 3.2.4.

3.2.1 Energy Influence Coefficients

The quadratic energy matrix $[E]$ can be normalized by the diagonal input power matrix $[P]$ yielding the matrix $[A]$ of the energy influence coefficients A_{ij}. The column j in the mentioned matrices corresponds to the excitation of the subsystem j:

$$
\begin{aligned}
[A] = [E]\,[P]^{-1} &=
\begin{bmatrix}
E_{11} & E_{12} & \dots & E_{1m} \\
E_{21} & E_{22} & \dots & E_{2m} \\
\vdots & \vdots & \ddots & \vdots \\
E_{m1} & E_{m2} & \dots & E_{mm}
\end{bmatrix}
\begin{bmatrix}
P_1 & 0 & \dots & 0 \\
0 & P_2 & \dots & 0 \\
\vdots & \vdots & \ddots & \vdots \\
0 & 0 & \dots & P_m
\end{bmatrix}^{-1} \\[2mm]
&=
\begin{bmatrix}
\dfrac{E_{11}}{P_1} & \dfrac{E_{12}}{P_2} & \dots & \dfrac{E_{1m}}{P_m} \\[2mm]
\dfrac{E_{21}}{P_1} & \dfrac{E_{22}}{P_2} & \dots & \dfrac{E_{2m}}{P_m} \\[2mm]
\vdots & \vdots & \ddots & \vdots \\[2mm]
\dfrac{E_{m1}}{P_1} & \dfrac{E_{m2}}{P_2} & \dots & \dfrac{E_{mm}}{P_m}
\end{bmatrix}
=
\begin{bmatrix}
A_{11} & A_{12} & \dots & A_{1m} \\
A_{21} & A_{22} & \dots & A_{2m} \\
\vdots & \vdots & \ddots & \vdots \\
A_{m1} & A_{m2} & \dots & A_{mm}
\end{bmatrix}
\end{aligned}
\tag{3.40}
$$

The matrix entry $A_{ij} = \frac{E_{ij}}{P_j}$ represents the energy in the subsystem i related to a unit power which is injected into subsystem j. It describes the energy flow inside the system which can be calculated for different types of loads by Eq. (3.40). It is convenient to compare the energy flow by these A_{ij} which refer to the same receiving subsystem i but for different loaded subsystems j or different types of loads. For a comparison of the normalized energies in different receiving subsystems due to the same load case, it should be kept in mind that the energy in a subsystem depends on its physical properties. Therefore, e.g. in case of subsystems with different size or stiffness, a rank order among the energy influence coefficients is not linked directly to the amplitudes of vibration.

Frequency Averaged Energy Influence Coefficients

To obtain the band averaged energy influence coefficients, the time and space averaged subsystem energies and the corresponding input power are numerically integrated within each band according to Eq. (3.38) and inserted into Eq. (3.40). Equation (3.41) shows the resulting matrix entries, where the average per frequency band is marked by a tilde. Inverting the resulting matrix leads to the band averaged coupling loss factors according to subsection 3.2.2. If a structure is characterized by energy influence coefficients, the energy flow into the different subsystems can be predicted for a certain input power. Hence, this relation is only valid for band averaged values if the subsystem energies and the input power are summed separately before computing the energy influence coefficients. This corresponds to the weighted arithmetic mean of the energy influence coefficient with respect to the input power:

$$\tilde{A} = \frac{\tilde{E}}{\tilde{P}} = \frac{\sum_k^{n_f} \frac{1}{2} \left(E\left(f_{k+1} \right) + E\left(f_k \right) \right) w_k}{\sum_k^{n_f} \frac{1}{2} \left(P\left(f_{k+1} \right) + P\left(f_k \right) \right) w_k} = \frac{\sum_k^{n_f} T_k(E)}{\sum_k^{n_f} T_k(P)} = \frac{\sum_k^{n_f} T_k(A) T_k(P)}{\sum_k^{n_f} T_k(P)} \tag{3.41}$$

The subsystem indices are omitted here for readability.

3.2.2 Loss Factors

As derived in section 2.3, another way to express the relation of the diagonal input power matrix $[P]$ with the energy content of the subsystems $[E]$ in the steady state is:

$$[P] = \Omega \left[\eta^0 \right] [E] \tag{3.42}$$

Equation (3.42) describes the global power balance of the structure in matrix form. Compared to the related Eq. (2.58) of the SEA, the vector of the subsystem energies is replaced by the matrix $[E]$ containing the response of the system due to the separate excitation of each subsystem. Exercising the EFA, one subsystem represents an entire component instead of a single wave type of a component. Moreover, the vector of the input power is replaced by the diagonal matrix $[P]$. $[\eta^0]$ states the total loss factor matrix of the system known from the SEA. The main diagonal entries η_{ii}^0 describe the total losses of subsystem i by adding

the losses due to coupling η_{ij} to the internal one due to damping η_{ii}. It holds:

$$\eta_{ii}^0 = \sum_{j=1}^{m} \eta_{ij} \tag{3.43}$$

$$\eta_{ij}^0 = -\eta_{ji}, \quad i \neq j \tag{3.44}$$

If in Eq. (3.42) the input power is substituted by a unit input power and therefore, the energy is replaced by the normalized one, the following expression results:

$$[I] = \Omega \left[\eta^0\right] [A] = \Omega \begin{bmatrix} \eta_{11}^0 & \eta_{12}^0 & \dots & \eta_{1m}^0 \\ \eta_{21}^0 & \eta_{22} & \dots & \eta_{2m}^0 \\ \vdots & \vdots & \ddots & \vdots \\ \eta_{m1}^0 & \eta_{m2}^0 & \dots & \eta_{mm}^0 \end{bmatrix} \begin{bmatrix} A_{11} & A_{12} & \dots & A_{1m} \\ A_{21} & A_{22} & \dots & A_{2m} \\ \vdots & \vdots & \ddots & \vdots \\ A_{m1} & A_{m2} & \dots & A_{mm} \end{bmatrix} \tag{3.45}$$

Hence, the total loss factor matrix $[\eta_0]$ can be assessed by inverting $[A]$ and normalizing it by the angular frequency. The presented approach corresponds to the numerical execution of the PIM [de Langhe and Sas 1996]. In subsection 3.2.3, criteria of the validity of the coupling and damping properties, which are predicted by means of the EFA, are discussed.

$$\left[\eta^0\right] = \frac{1}{\Omega} [A]^{-1} = \begin{bmatrix} \eta_{11} + \sum\limits_{j\neq 1} \eta_{1j} & -\eta_{21} & \dots & -\eta_{m1} \\ -\eta_{12} & \eta_{22} + \sum\limits_{j\neq 2} \eta_{2j} & \dots & -\eta_{m2} \\ \vdots & \vdots & \ddots & \vdots \\ -\eta_{1m} & -\eta_{2m} & \dots & \eta_{mm} + \sum\limits_{j\neq m} \eta_{mj} \end{bmatrix} \tag{3.46}$$

After rearranging the entries of $[\eta^0]$ the loss factor matrix $[\eta]$ results, which contains the damping loss factors η_{ii} on the diagonal and the coupling loss factors η_{ij} on the off-diagonals:

$$[\eta] = \begin{bmatrix} \eta_{11} & \eta_{21} & \dots & \eta_{m1} \\ \eta_{12} & \eta_{22} & \dots & \eta_{m2} \\ \vdots & \vdots & \ddots & \vdots \\ \eta_{1m} & \eta_{2m} & \dots & \eta_{mm} \end{bmatrix} \tag{3.47}$$

The EFA considers all the transmission paths, also the non-resonant ones, and all types of couplings between subsystems, also the indirect ones. The loss factor matrix is therefore generally fully occupied and not necessarily symmetrical.

3.2.3 Validity of Coupling Loss Factors

Condition Number of the Energy Influence Coefficient Matrix

The condition number κ of a matrix measures the sensitivity of the solution of a system of linear equations to variations of the input data. It gives an indication about the accuracy of the results from matrix inversion.

$$\kappa\left([A]\right) = \parallel [A] \parallel_2 \parallel [A]^{-1} \parallel_2 \tag{3.48}$$

The condition number of a matrix is calculated by a multiplication of the norm of a matrix with the norm of its inverse. Here, the spectral norm of the matrix is used, which corresponds to its largest singular value. This can be described as largest possible scaling factor in the case of a multiplication with a vector of the length one. The reciprocal of the smallest singular value of a matrix states the spectral norm of its inverse. Hence, the condition number is the ratio of the largest to the smallest singular value and can be interpreted as the factor by which the input error might be increased in the worst case. [Råde and Westergren 2000; Zeidler 2013]

As long as the condition number is close to unity, the matrix is called well-conditioned and can be inverted. This holds for diagonally dominant matrices, which means that in every row of the matrix, the diagonal entry is larger than the sum of all non-diagonal entries. Looking at the energy influence coefficients matrix $[A]$, this is the case for weakly coupled subsystems. For instance, higher damping leads to higher entries on the main diagonal and therefore to a lower condition number promising a higher accuracy of the results.

Global mode shapes occurring in the low frequency region might deteriorate the results depending on the structure and the division into subsystems. They lead to strongly coupled subsystems and high values on the off-diagonals of the energy influence coefficients matrix. Here, the condition number can be used as a mathematical criterion to identify this physical behavior and the corresponding frequency region, which then shows comparatively high values of the condition number especially for non-band-averaged energy influence coefficients. Hence, strongly coupled subsystems lead to an ill-conditioned energy influence coefficients matrix whose inverse, the total loss factor matrix $[\eta^0]$, is reduced in accuracy. The loss factors might no longer indicate a correct physical behavior.

Strong coupling can also lead to negative coupling loss factors η_{ij} which are not necessarily physically incorrect. As Fredö [1997] explains, exciting a subsystem below its first eigenfre-

quency may lead to a high energy transmission into the adjacent, non-excited but resonant subsystem. It results an extremely high coupling loss factor for the energy flow from the excited subsystem with very little energy to the non-excited subsystem oscillating at resonance. This possibly leads to a negative coupling loss factor between the resonant and the excited subsystem, because otherwise the power flow across the excited into the resonant subsystem cannot be justified (cf. Eq. (2.50)).

Independently of the condition number, the energy influence coefficients contain physically correct information unless there are errors in the input power or in the subsystem energies. Especially, the assessment of the input power by means of measurements is challenging [Mecking et al 2017a]. For instance, the determination of the phase shift between force and velocity at the shaker position is error-prone. Then, the condition number can be used to detect these errors which might be helpful for both numerical simulations and measurements. Hence, an ill-conditioned energy influence coefficients matrix is not necessarily an indicator of strong coupling, which would impede a modeling by the classical SEA.

The condition number is not able to detect other violations of the SEA requirements like e.g. an indirect coupling or a high variation in coupling strength due to coupling loss factors of different orders of magnitude. As long as the direct or indirect coupling of two subsystems is not exceptionally strong, the condition number does not indicate that as exemplified in subsection 4.4.2.

"SEA-like" vs. Classical SEA

For a single realization, the coupling loss factors based on the EFA are valid over the whole frequency range including negative values and indirect coupling. To emphasize that they do not necessarily fulfill the SEA assumptions they are also called apparent coupling loss factors by Thite and Mace [2007]. The specific loading potentially leads to non-resonant contributions, especially in the case of large damping since the phase shift between velocity and force reaches more slowly the asymptotic value of $+/-\frac{\pi}{2}$ where the power input equals to zero (cf. Fig. 3.3). Moreover, the loading might only excite a few modes within a frequency band which may not represent the modes of the ensemble properly.

A Rain-on-the-Roof excitation, which is presented in subsection 3.3.1, is used to excite sufficient modes within a frequency band. Furthermore, these mode shapes should be typical of all the modes characterizing the energy distribution within the system. Here, also the SEA assumption of uniform damping mentioned in subsection 2.3.2 applies. In this case, the two necessary SEA conditions - the conservation of energy and the consistency relation,
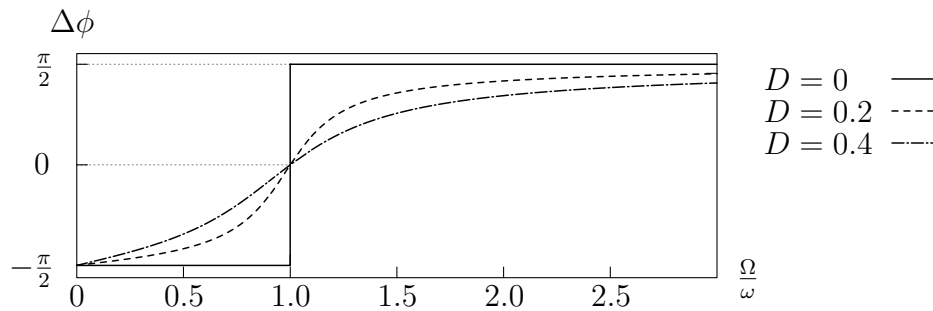
Figure 3.3: Excitation of a single eigenmode: The phase shift $\Delta\phi = \phi_v - \phi_F$ between velocity and force varies for different values of the damping ratio D.

which are introduced in subsection 2.3.1 - should be fulfilled according to Mace [2003]. This indicates that only resonant transmission is considered or is at least dominating [Wang and Lai 2005]. It results a quasi-SEA matrix which can be evaluated by an "SEA-like" analysis. The quasi-SEA matrix may contain negative or indirect coupling [Mace 2003]. Especially in case of light damping, the coupling loss factors depend on the damping and on the global properties of the structure rather than on the local ones.

Finnveden [2011] presents and relates various criteria to estimate the strength of coupling (cf. subsection 2.3.3). However, there is no generally agreed property to determine weak coupling. Independently of the strength of coupling, the coupling power proportionality, which is linked to the consistency relation, strictly is only exact for the ensemble average. The reciprocity relationship is still valid for all power flow paths indicating that only resonant transmissions, either direct or indirect, are considered. Averaging then over suitable wide frequency bands with enough typical modes can also be interpreted as an approximation of an ensemble average over similar, but slightly different systems. [Mace 2003]

Excluding indirect and negative coupling leads to a proper-SEA matrix fulfilling all SEA assumptions [Mace 2003]. If this is done manually, the loss factor matrix describes a modified system which can be evaluated using the classical SEA. Then, the coupling loss factors are assumed to be independent of the damping loss factors and to depend only on the junction plus the physical properties of the subsystems connected to that junction. Thus, isolating the subsystems connected to one junction leads to equal coupling loss factors as if the subsystems form part of a larger structure. Based on this assumption of weakly coupled subsystems, e.g. an L-, T- or X-junction can be extracted out of a multistory building. In contrast, the energy influence coefficients implicitly depend on the whole system. [Mace 2003]

3.2.4 Vibration Reduction Index - Engineering Quantity

The European standard [DIN EN ISO 12354-1 2017] applies engineering quantities which enable simplified, approximate predictions implicating a considerably reduced validity. Within the scope of the subsequent paragraphs, the concept based on approximations is shortly presented for the impact sound insulation between two rooms. Subsequently, the so-called vibration reduction index, which aims to characterize the sound transmission behavior of a junction, is firstly introduced on the basis of the velocity level difference between two adjacent components, secondly derived from the wave approach and thirdly linked to the coupling loss factors from the EFA. In this regard, the computation based on surface velocities resulting from a measurement or a simulation is addressed. Moreover, the different simplifications and drawbacks are contrasted.

The sound transmission between two adjacent rooms consists of various transmission paths. Beside the direct transmission through the separating component, the flanking transmission plays an important role for the prediction of structure-borne sound transmission. Thus, the proof of the suitability of individual components has been augmented towards a proof of the suitability of buildings in the past decades [Schneider et al 2006]. By means of an energetic addition, the individual paths, for which the sound transmission is assumed to be independent, are taken into account.

For the impact sound insulation between two rooms on top of each other, the normalized impact sound pressure level due to direct transmission $L_{n,d}$ and the normalized impact sound pressure levels of each flanking transmission path $L_{n,ij}$ are summed up [DIN EN ISO 12354-2 2017]:

$$L_n^{'} = 10 \lg \left(10^{0.1\,L_{n,d}} + \sum_{j=1}^{n_p} 10^{0.1\,L_{n,ij}} \right) \tag{3.49}$$

This opens up the need of input data of the acoustic properties of the building elements as well as of the junction applied.

The European standard DIN EN ISO 12354-1 [2017] describes the structure-borne energy which is transported across a junction by means of the vibration reduction index K_{ij} on the basis of the approach from Gerretsen [1979, 1994]. For instance, it is used to approximately predict the normalized impact level for the flanking transmission path $L_{n,ij}$ by means of Eq. (3.50). Thereby, this transmission path consists of the normalized impact level of the excited ceiling L_n as well as an optional reduction due to a floor covering ΔL, the mean sound insulation index R of source and receiver component as well as an optional reduction

due to a lining in front of the receiver component ΔR. Moreover, it comprises the direction-averaged velocity level difference $< D_{v,ij} >$ and it is normalized by means of the logarithmic ratio of the component areas A. The index "situ" represents the quantities which prevail in factual field situations and $< \quad >$ represents direction-averaged quantities. [DIN EN ISO 12354-2 2017]

$$L_{n,ij} = L_{n,\text{situ}} - \Delta L_{\text{situ}} + \frac{R_{i,\text{situ}} - R_{j,\text{situ}}}{2}$$
$$- \Delta R_{j,\text{situ}} - < D_{v,ij,\text{situ}} > -5 \lg \left(\frac{A_i}{A_j} \right) \tag{3.50}$$

Velocity Level Difference

While planing a construction project, the idea is that the direction-averaged velocity level difference can be predicted by means of the direction-averaged vibration reduction index, the junction length l_{ij} as well as the equivalent absorption lengths a_i and a_j of the respective adjacent components i and j:

$$< D_{v,ij,\text{situ}} > = < K_{ij} > -10 \lg \left(\frac{l_{ij}}{\sqrt{a_{i,\text{situ}} \, a_{j,\text{situ}}}} \right) \tag{3.51}$$

The absorption length a_i considers the total loss factor η_{ii}^0 of the adjacent component i (cf. subsection 3.2.2), and is referred to as equivalent because a fictive critical frequency of $f_{\text{ref}} = 1000\,\text{Hz}$ is chosen. Hereby, c_0 constitutes the velocity of sound propagating in air and f_m states the band center frequency.

$$a_i = \eta_{ii}^0 A_i \frac{\pi^2}{c_0} \sqrt{f_m f_{\text{ref}}} \tag{3.52}$$

The vibration reduction index is an invariant quantity as the direction average of the velocity level differences $D_{v,ij}$ and $D_{v,ji}$ is normalized to the ratio of the junction length and of the equivalent absorption length of the adjacent components [DIN EN ISO 12354-1 2017].

$$< K_{ij} > = \frac{D_{v,ij} + D_{v,ji}}{2} + 10 \lg \left(\frac{l_{ij}}{\sqrt{a_i \, a_j}} \right) \tag{3.53}$$

$D_{v,ij}$ describes the velocity level difference between component i and j due to excitation of component i:

$$D_{v,ij} = L_{v,i} - L_{v,j} \tag{3.54}$$

Equation (3.51) contains the so-called "in-situ"-correction to predict the factual direction-averaged velocity level difference $< D_{v,ij,\text{situ}} >$ by means of the invariant vibration reduction index: The relation to the fictive critical frequency cancels and it is taken into account that total loss factor in the factual field situation is higher compared to a free-standing L-, T- or X-junction in the laboratory.

As shown in the subsequent paragraphs, the idealization of the junction by means of the vibration reduction index is only valid, if the SEA assumptions are fulfilled. In the frequency range below, coupling quantities like the vibration reduction index depend on the geometry of the adjacent components and thus, they cannot be exclusively described by the junction.

Excursus: Measured Velocity Level   The international standard DIN EN ISO 10848-1 [2006] defines how to proceed in the case of the corresponding measurement under laboratory conditions. The velocity level of a single component L_v results from the spatial average of the velocity levels $L_{v,k}$ at n_{mp} measurement positions.

$$L_v = 10 \lg \left(\frac{1}{n_{\text{mp}}} \sum_{k=1}^{n_{\text{mp}}} 10^{0.1 \, L_{v,k}} \right) \qquad \text{with} \ \ L_{v,k} = 20 \lg \left(\frac{\frac{|v_{z,k}|}{\sqrt{2}}}{v_{\text{ref}}} \right) \tag{3.55}$$

$L_{v,k}$ relates the time-averaged surface velocity perpendicular to the plate $\frac{|v_{z,k}|}{\sqrt{2}}$ to the reference velocity $v_{\text{ref}} = 10^{-9}$. Inserting $L_{v,k}$, the energetic mean of the measured velocities results:

$$L_v = 10 \lg \left(\frac{1}{n_{\text{mp}} \, v_{\text{ref}}^2} \sum_{k=1}^{n_{\text{mp}}} \frac{\left| \underline{v}_{z,k} \right|^2}{2} \right) \tag{3.56}$$

Transmission Coefficient and SEA Coupling Loss Factor

According to annex E of DIN EN ISO 12354-1 [2017], the vibration reduction index bases upon the transmission coefficient τ_{ij} between bending wave fields. Equation (3.57) contains the normalization to the critical frequency of the receiver component $f_{c,j}$ and to the fictive one f_{ref}. This corresponds to a normalization of the transmission coefficient regarding the material and the geometry of the receiver component and leads to the invariant vibration reduction index. Thus, it is direction independent for pure bending wave transmission as derived in subsection 4.2.2.

$$K_{ij} = -10 \lg (\tau_{ij}) + 5 \lg \left(\frac{f_{c,j}}{f_{\text{ref}}} \right) = -10 \lg (\tau_{ji}) + 5 \lg \left(\frac{f_{c,i}}{f_{\text{ref}}} \right) \tag{3.57}$$
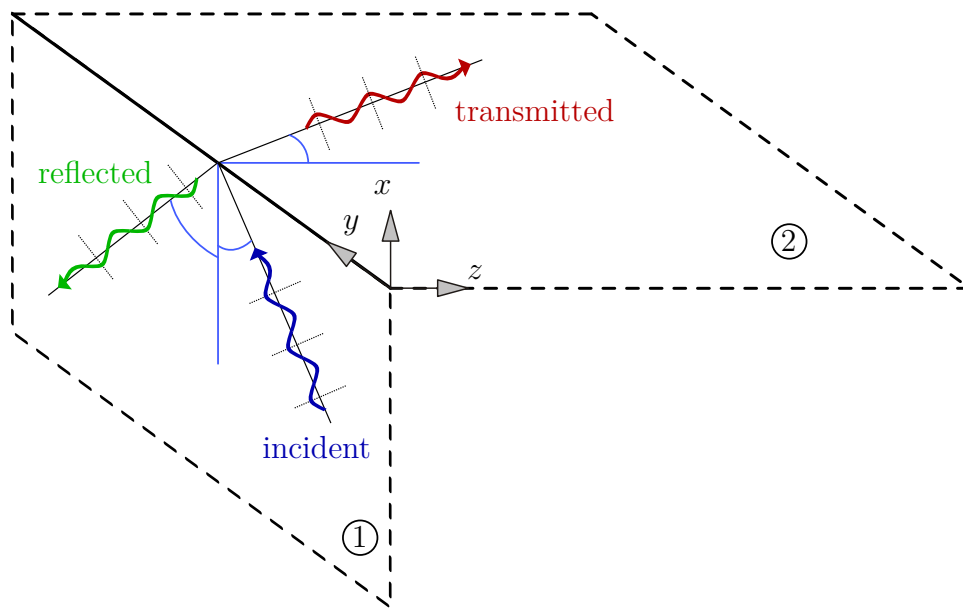
Figure 3.4: Incident, reflected and transmitted wave at an L-junction assuming only bending waves.

with the critical frequency

$$f_c = \sqrt{\frac{\rho\,h}{B}}\,\frac{c_0^2}{2\,\pi} \tag{3.58}$$

The transmission coefficient is defined as ratio of transmitted and incident power at a junction. Hence, the vibration reduction index is only applicable in the mid-frequency range where the prerequisites of the wave approach for plate-like structures apply (cf. introduction of chapter 3). As sketched in Fig. 3.4, this comprises the assumption, that a junction of two semi-infinite plates is investigated which is fulfilled if the reflections occur with a clearly smaller amplitude or incoherently to the excitation. Assuming a diffuse field, all angles of incidence are regarded to have the same probability. Hence, it can be integrated over the angle dependent transmission coefficient. In plates, the diffuse field assumption is first allowed at higher frequencies compared to the adjacent rooms. Reaching a sufficient modal density, it has to be taken into account that modes with very slightly differing eigenfrequencies may arise due to parallel edges and that these eigenfrequencies are not equally distributed over the frequency range. Here, the anatomy of wood and the different layers of CLT as well as possible window openings have a positive effect as they lead to additional, rather arbitrary reflections. Therefore, the modal density is not increased but the modes are spread more randomly over the frequency range. Applying the SEA, an equipartition of the modal energy over the frequency range is supposed as introduced in section 2.3. This equipartition

is accordingly expected over the angles of incidence. Therefore, by means of the angle-independent transmission coefficient the coupling loss factor η_{ij} between two subsystems can be calculated [Hopkins 2007]:

$$\eta_{ij} = \frac{\tau_{ij}\, c_{g,i}\, l_{ij}}{2\pi^2 f A_i} \tag{3.59}$$

The energy is transported with the group wave velocity $c_{g,i}$. Solving Eq. (3.59) regarding τ_{ij} and inserting it into Eq. (3.57), the vibration reduction index on the basis of η_{ij} results, which has been included into the actual draft of DIN EN ISO 12354-1 [2017]:

$$K_{ij} = -10\,\lg\left(\eta_{ij}\frac{\pi^2\, A_i}{c_0\, l_{ij}}\sqrt{\frac{f_{c,i}}{f_{c,j}}}\sqrt{f_{\mathrm{ref}}f}\right) \tag{3.60}$$

Here, thin plate theory is assumed which constitutes another limitation of the vibration reduction index beside the exclusive transmission between bending wave fields. According to subsection 2.2.3, the cross-over frequency from thin to thick plates depends on the group wave velocity for the vibration reduction index. Introducing the group wave velocity of effective bending waves (cf. Eq. (2.43)) and the corresponding coupling loss factor enables an extension to thick plates:

$$K_{ij} = -10\,\lg\left(\frac{\eta_{ij}\, 2\pi^2 f A_i}{c_{g,\mathrm{eff},i}\, l_{ij}}\right) + 5\,\lg\left(\frac{f_{c,j}}{f_{\mathrm{ref}}}\right) \tag{3.61}$$

Thus, the vibration reduction index describes the exchange between subsystems of effective bending waves. Since they consist of bending and out-of-plane shear waves, they represent the oscillation perpendicular to the plate also at higher frequencies. By contrast, in-plane wave transmission is not included.

Coupling Loss Factors from the EFA

The energy exchange between every wave field of two adjacent plates is described by the coupling loss factor computed with the EFA (cf. subsection 3.2.2). In contrast to the SEA, the EFA enables a prediction for a specific scenario at lower frequencies. Due to the deterministic procedure, the postulation of a statistical equipartition of modal energies does not apply in the case of the EFA. The different velocities, by which the energy is transported in the individual wave fields, is implicitly comprised in the coupling loss factor. Applying (3.61), the group wave velocity of only one wave type can be considered. Hence, even using coupling

loss factors from the EFA a limitation to effective bending waves or more precisely to the frequency range, where the bending wave transmission prevails, results.

To only account for the bending wave transmission already while determining the coupling loss factors, the bending wave energy is estimated by means of the out-of-plane velocity averaged over all surface nodes $n_{\mathrm{sn},i}$ of plate i for the excitation of plate j. In the style of a measurement, the time-averaged, total energy in Eq. (3.40) is replaced by twice the perpendicular translational part of the time-averaged, kinetic energy depending on the mass m_i.

$$E_{ij} = 2\,E_{ij,\mathrm{kin}}(v_z) = \frac{m_i}{n_{\mathrm{sn},i}} \sum_{k=1}^{n_{\mathrm{sn},i}} \frac{|\underline{v}_{z,k}|^2}{2} = \frac{m_i}{2\,n_{\mathrm{sn},i}} \sum_{k=1}^{n_{\mathrm{sn},i}} \Re\left(\underline{v}_{z,k}\right)^2 + \Im\left(\underline{v}_{z,k}\right)^2 \tag{3.62}$$

Simplified Approach Assuming only Two Subsystems Neglecting the energy flow into a third or more subsystems, η_{ij} can be approximated by Eq. (3.63) for subsystem i being excited. To avoid using the EFA in this procedure, the total loss factor η_j^0 of subsystem j must be estimated e.g. by empirical expressions from Hopkins [2007] or measuring the structural reverberation time.

$$\eta_{ij} = \frac{E_{ji}}{E_{ii}}\eta_j^0 \tag{3.63}$$

If the total energies in Eq. (3.63) are replaced by the expression (3.62) before the resulting η_{ij} is inserted into Eq. (3.60), the direction-averaged vibration reduction index based on the velocity level difference results as depicted in Eq. (3.53). Due to the averaging over both transmission directions, the mass of the components is eliminated.

3.3 Robust Estimation of the Energy Influence Coefficients

The EFA offers the possibility to compute either the energy influence coefficients for a specific load scenario or - in case the load is unknown - for a so-called Rain-on-the-Roof (RotR) excitation. The latter shall lead to robust energy influence coefficients which are as universal as possible for various types of loads to be able to generally assess the vibroacoustic behavior of a junction. Therefore, RotR shall ensure the participation of all modes in the system response. Furthermore, the excitation shall be statistically independent to avoid a coherent modal response and to fulfill the SEA assumption of equipartition of modal energy. [Hopkins 2007]

The concept of RotR is introduced in subsection 3.3.1. Starting with the theoretical concept, implementations and implications related to SEA assumptions are discussed. Finally the statistical properties of the presented implementation inside the EFA are derived. To be able to retrieve robust quantities, an additional averaging over realizations with varying load sets of RotR is used. In Eq. (3.64), the mathematical problem description from section 3.1 is augmented and explained in detail in subsection 3.3.2.

$$\overline{A}_{ij} = \frac{1}{n_r} \sum_r^{n_r} \tilde{A}_{ij} = \frac{1}{n_r} \sum_r^{n_r} \frac{\int_{f_l}^{f_u} \int_0^T \int_{\Theta_i} E_e\left(\mathbf{x},t,f\right) \, d\Theta dt df}{\int_{f_l}^{f_u} \int_0^T \int_{\Theta_j} P_e\left(\mathbf{x},t,f\right) \, d\Theta dt df} \tag{3.64}$$

In subsection 3.3.3, a concept is presented to estimate the deviation of the sample mean from the true mean. Moreover, for a desired accuracy the necessary number of realizations can be predicted.

3.3.1 Rain-on-the-Roof

Theoretical Concept

The pressure $p(x,y,t)$ on the plate due to an ideal RotR excitation is zero mean and uncorrelated as well as homogeneous and stationary in space and time, respectively. Within this thesis, the characteristics stationary and homogeneous imply second order stationary and second order homogeneous, respectively. Whereas second order stationary means that the mean and the variance of a random process are constant within the time domain as well as the autocorrelation function depends only on the temporal distance between two points, second order homogeneous denotes the spatial equivalent for a random field [Papaioannou 2016].

The characteristics of any stationary signal can be determined by the mean and the autocorrelation function. The latter one describes the correlation between two points in time and space. The autocorrelation of the ideal RotR excitation is characterized by dirac delta functions δ and a constant amplitude S_0:

$$R_{pp}(\xi_x,\xi_y,\tau) = \mathrm{E}\left[p(x,y,t)\, p(x + \xi_x, y + \xi_y, t + \tau)\right] = S_0\, \delta(\xi_x)\delta(\xi_y)\delta(\tau) \tag{3.65}$$

It depends only on the vector (ξ_x,ξ_y) between the two observation points and the time interval τ between the two observations. For $\xi_x = \xi_y = \tau = 0$ the autocorrelation function corresponds to the mean square of the signal going to infinity, otherwise it is equal zero.

Performing a threefold Fourier transformation, the three-dimensional spectral density yields:

$$S_{pp}(k_x,k_y,\omega) = \int_{-\infty}^{\infty} \int_{-\infty}^{\infty} \int_{-\infty}^{\infty} R_{pp}(\xi_x,\xi_y,\tau)e^{-i(k_x\xi_x+k_y\xi_y+\omega\tau)}d\xi_x d\xi_y d\tau = S_0 \tag{3.66}$$

It is constant and therefore independent of frequency as every frequency component is equally represented which is the definition of white noise. To reproduce it physically, the random character has to be limited to a certain frequency range. [Nilsson and Liu 2015, 2016]

Applying RotR within the scope of a modal approach, the modal force of mode i with the corresponding eigenvector Φ_i is

$$p_i = \int_0^b \int_0^l p(x,y,t)\,\Phi_i(x,y)\,dxdy \tag{3.67}$$

and has the cross-correlation of two modal forces

$$R_{p_i p_j}(\tau) = \mathrm{E}\left[p_i(t)p_j(t+\tau)\right] = S_0\,\delta(\tau)\,\delta_{ij} \tag{3.68}$$

where δ_{ij} states the Kronecker delta resulting from the orthonormality of the normalized eigenmodes. Thus, the modal forces are uncorrelated white noises with the same power spectral density S_0. [Lafont et al 2013]

Implementation and Implications Related to SEA Assumptions

For a strict RotR field, it would be necessary to excite an infinitely large frequency band by an infinite number of uncorrelated excitation points. Hence, to perform a realizable RotR excitation, different approaches have been presented in literature. Lafont et al [2013] compares a point force with a set of random point forces having a constant power spectral density in a frequency band. They observe the energy at different points on a plate to examine if the vibration field is diffuse. Another SEA assumption, namely the energy equipartition, is verified comparing the modal energies. Lafont et al [2013] show that energy equipartition is a direct consequence of RotR excitation and leads to diffuse field conditions. The converse is not true as the diffuse field state can either be reached by suitable values of damping (low) and frequency (high) or forced by a RotR excitation. The RotR excitation is approximated by increasing the number of forces and it results that a large number is convenient to fulfill the two mentioned SEA assumptions. At low frequencies where the structure shows modal behavior, neither equipartition of energy nor a diffuse field occur. The latter can be reached by RotR excitation. On a highly damped structure, a dominant direct field arises due to a

single load oscillating with a large excitation frequency. Using RotR instead, equipartition of energy can be reached and hence the plate is dominated by the diffuse field. In the scope of the EFA, the influence of the number of loads for RotR and of their locations is discussed in section 4.5 and subsection 4.3.3.

[Mace 2003] proposes a load vector whose amplitude is proportional to the local mass density of the corresponding subsystem. Within the scope of a component-mode synthesis, all subsystem modes are excited by equal modal forces (cf. Eq. (3.67)) such that the direct wavefield receives a uniform power input. To make the excitation incoherent, it is spatially delta-correlated [Mace and Shorter 2000].

Statistical Properties of the Implementation inside the EFA

For the EFA, the RotR excitation is realized by a spatially varying phase distribution which is modeled as a random field. At each location on the plate, the phase has the same distribution. Therefore, $\phi(x,y)$ defines a strictly homogeneous, random field, where the marginal distributions at each point are described by independent uniform distributions $\mathcal{U}(0,2\pi)$ with the mean equal π. The autocorrelation coefficient function of the phase can be described by dirac delta correlation functions depending only on the distance between two locations (ξ_x,ξ_y):

$$\rho_{\phi\phi} = \delta(\xi_x)\delta(\xi_y) \tag{3.69}$$

Based on a time-harmonic excitation, the random process $p(x,y,t)$ is generated by the spatially varying phase:

$$p(x,y,t) = p_0 \cos\left(\Omega t + \phi(x,y)\right) \tag{3.70}$$

Thereby, the random field indicates an individual phase shift for each spatial location.

Subsequently, the autocorrelation function and the three-dimensional spectral density are compared to the theoretical concept of the RotR excitation introduced in Eq. (3.65) and (3.66), respectively. Since all locations on the plate are independent and identically distributed as $\mathcal{U}(0,2\pi)$, the notation $\varphi = \phi(x,y)$ is introduced. Firstly, the mean value of the

excitation $p(x,y,t)$ is computed [Lutes and Sarkani 2004]:

$$\mu_p(x,y,t) = \text{E}[p(x,y,t)] = p_0\,\text{E}\left[\cos\left(\Omega t + \phi(x,y)\right)\right] \tag{3.71}$$

$$= p_0 \int_{-\infty}^{\infty} f_\varphi(\varphi)\cos\left(\Omega t + \varphi\right)d\varphi \tag{3.72}$$

$$= p_0 \int_{0}^{2\pi} \frac{1}{2\pi}\cos\left(\Omega t + \varphi\right)d\varphi = 0 \tag{3.73}$$

The autocovariance function K_{pp} corresponds to the autocorrelation function R_{pp} because the mean value is equal to zero and therefore, it does not affect K_{pp}:

$$K_{pp} = \text{E}\left[p(x_1,y_1,t_1)\,p(x_2,y_2,t_2)\right] - \mu_p(x_1,y_1,t_1)\mu_p(x_2,y_2,t_2) = R_{pp} \tag{3.74}$$

The autocorrelation function of $p(x,y,t)$ is derived by means of the subsequent expressions:

$$R_{pp} = \text{E}\left[p(x_1,y_1,t_1)\,p(x_2,y_2,t_2)\right] \tag{3.75}$$

$$= p_0^2\,\text{E}\left[\cos\left(\Omega t_1 + \phi(x_1,y_1)\right)\cos\left(\Omega t_2 + \phi(x_2,y_2)\right)\right] \tag{3.76}$$

To determine the expected value in expression (3.76), two cases have to be distinguished:

Case 1: $x_1 \neq x_2 \vee y_1 \neq y_2$
Here, the two random variables at location x_1, y_1 and x_2, y_2 are uncorrelated, independent and identically distributed:

$$R_{pp} = p_0^2\left\{\int_{-\infty}^{\infty}\int_{-\infty}^{\infty} f_{\varphi_1}(\varphi_1)f_{\varphi_2}(\varphi_2)\cos\left(\Omega t_1 + \varphi_1\right)\cos\left(\Omega t_2 + \varphi_2\right)d\varphi_2 d\varphi_1\right\}$$

$$= p_0^2\left\{\int_{0}^{2\pi}\int_{0}^{2\pi} \frac{1}{(2\pi)^2}\cos\left(\Omega t_1 + \varphi_1\right)\cos\left(\Omega t_2 + \varphi_2\right)d\varphi_2 d\varphi_1\right\} = 0 \tag{3.77}$$

Case 2: $x_1 = x_2, y_1 = y_2 \rightarrow \phi(x_1,y_1) = \phi(x_2,y_2) = \varphi$
Now, both locations coincide and thus, the phase shift can be described by the same variable φ. The identity $\cos(\alpha)\cos(\beta)2 = \cos(\alpha + \beta) + \cos(\alpha - \beta)$ is applied to the expression (3.76):

$$R_{pp} = \frac{p_0^2}{2}\left\{\int_{0}^{2\pi} \frac{1}{2\pi}\cos\left[\Omega(t_1 + t_2) + 2\varphi\right] + cos\left[\Omega(t_2 - t_1)\right]d\varphi\right\}$$

$$= \frac{p_0^2}{2}\cos\left[\Omega(t_2 - t_1)\right] \tag{3.78}$$

The resulting expression depends only on the difference between the two points in time $\tau = t_2 - t_1$. Hence, the excitation possesses stationarity of the mean value and the autocorrelation function. Therefore, the autocorrelation can be written as:

$$R_{pp}(\tau) = \frac{p_0^2}{2} \cos(\Omega\tau) \tag{3.79}$$

Merging both cases, the spatial correlation behavior is expressed by dirac delta correlation functions depending only on the distance between two locations (ξ_x, ξ_y):

$$R_{pp}(\xi_x, \xi_y, \tau) = \frac{p_0^2}{2} \cos(\Omega\tau)\, \delta(\xi_x)\delta(\xi_y) \tag{3.80}$$

As the signal is time-harmonic, its autocorrelation function yields a harmonic function with the same period $T = \frac{2\pi}{\Omega}$. With the assumption that the elements are infinitesimal small, which might be nearly fulfilled at low frequencies relating the element side length to the wave length, the expression holds for the scenario that all surface elements within a subsystem are loaded ($n_l =$ max.). The effect due to an approximation by a reduced number of loaded elements is investigated in section 4.5.

Considering the mesh of the FE model, the random field consisting of an infinite number of random variables is discretized by means of the midpoint rule to one random variable per surface element ϕ_e. Therefore, the number as well as the size of the surface elements coincides with the stochastic elements. Hence, the RotR concept is expressed by means of element-wise Heaviside step functions H:

$$p_{n_l}(x, y, t) = p_0 \sum_e^{n_l} \cos(\Omega t + \phi_e)\, H(x - x_{e-}, x_{e+} - x)\, H(y - y_{e-}, y_{e+} - y) \tag{3.81}$$

Thereby, the indices + and - represent the edges of the loaded element at a distance of $\frac{h_e}{2}$ from the element center x_e and y_e which is exemplarily demonstrated for the x-direction:

$$x_{e-} = x_e - \frac{h_e}{2} \qquad x_{e+} = x_e + \frac{h_e}{2} \tag{3.82}$$

The RotR excitation of the ceiling of an L-junction is illustrated in Fig. 3.5 by different shades of red for different phases.
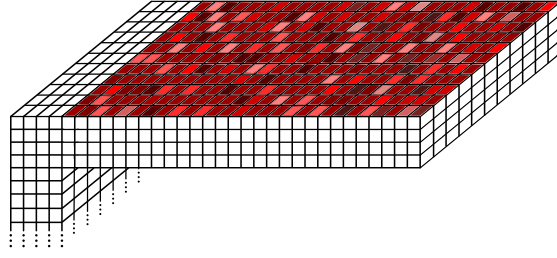
Figure 3.5: RotR: Loading all surface elements of the ceiling of an L-junction. The shades of red indicate the varying phase.

In the original space (x,y), the power spectral density of the random process $p(x,y,t)$ results from a Fourier transform of Eq. (3.80) [Nilsson and Liu 2015; Brigham 1988]:

$$S_{pp}\left(\xi_x,\xi_y,\omega\right) = \delta(\xi_x)\delta(\xi_y) \int_{-\infty}^{\infty} R_{pp}(\tau)e^{-i\omega\tau}d\tau \tag{3.83}$$

$$= \delta(\xi_x)\delta(\xi_y)\frac{p_0^2}{2} \int_{-\infty}^{\infty} \cos\left(\Omega\tau\right) e^{-i\omega\tau}d\tau \tag{3.84}$$

$$= \delta(\xi_x)\delta(\xi_y)\frac{\pi\, p_0^2}{2} \left[\delta(\omega - \Omega) + \delta(\omega + \Omega)\right] \tag{3.85}$$

Performing a threefold Fourier transformation, the three-dimensional spectral density yields in the wave number domain (k_x,k_y):

$$S_{pp}(k_x,k_y,\omega) = \int_{-\infty}^{\infty} \int_{-\infty}^{\infty} \int_{-\infty}^{\infty} R_{pp}(\xi_x,\xi_y,\tau)e^{-i(k_x\xi_x+k_y\xi_y+\omega\tau)}d\xi_x d\xi_y d\tau \tag{3.86}$$

$$= \frac{\pi\, p_0^2}{2} \left[\delta(\omega - \Omega) + \delta(\omega + \Omega)\right] \tag{3.87}$$

A stationary process leads to a symmetric correlation function related to τ (cf. Eq. (3.80)). Hence, it results an even spectral density. Therefore, the physically realizable one-sided spectral density G_{pp} can be defined:

$$G_{pp}\left(k_x,k_y,\omega\right) = 2S_{pp}\left(k_x,k_y,\omega\right) = \pi\, p_0^2\, \delta(\omega - \Omega) \qquad \text{for } \omega \geq 0 \tag{3.88}$$

$$G_{pp}\left(k_x,k_y,f\right) = \frac{p_0^2}{2}\, \delta\left(f - f_k\right) \qquad \text{for } f \geq 0 \tag{3.89}$$

In the presented approach, the amplitude of the spectral density is independent of the frequency using the the same pressure amplitude p_0 at each frequency of excitation f_k. Unlike white noise, which corresponds to a broad band signal with a constant spectral density over the whole frequency band, selected frequencies are excited subsequently with the same spectral density followed by a numerical interpolation as explained in subsection 3.1.4. Compared to the theoretical RotR concept described in Eq. (3.65) and (3.66), the limit

case of the presented RotR concept, which consists of a harmonic excitation of all elements having an infinitesimal small side length, is also homogeneous, stationary and uncorrelated in space, but correlated in time according to Eq. (3.80).

Once, the auto- and cross-spectral densities of the excitation are calculated, the spectral densities of displacement and velocity can be determined if the frequency response function is known. Hereby, the time average of the kinetic and potential energy as well as of the input power can be computed.

As shown for a single degree of freedom system in Nilsson and Liu [2015, 2016], the kinetic and potential energy are equal for white noise excitation. This holds for harmonic excitation only at resonance. For white noise, the time average of the total energy is proportional to the time average of the input power. In the case of harmonic excitation, this relationship depends on the type of damping. As shown in subsection 2.1.4 for the applied, stiffness proportional damping, the proportionality holds between the input power and the potential energy, whereas in case of viscous damping the input power would be proportional to the kinetic energy.

3.3.2 Averaging over Realizations

As mentioned in subsection 3.1.2, pressure is applied on selected elements to avoid singularities in the presented approach. Loading each element (n_l=max.) perpendicular to the surface with the same pressure and a random phase results in an approximation of a spatially delta-correlated excitation. Due to loading at the surface and unlike the SEA, a non-resonant excitation of predominantly thickness modes is induced (cf. subsection 2.2.5). To quantify the influence of the random phase on the energy influence coefficient, its statistical behavior is investigated by comparing different realizations of the above mentioned loading. Therefore, the coefficient of variation c_A is used, which is a relative measure as it normalizes the sample standard deviation s_A by the sample mean $\overline{A}$ (cf. Eq. (3.90) to (3.92)) [Papaioannou 2016]. The band averaged energy influence coefficient $\tilde{A}_{ij}^r$ of one single realization r results from Eq. (3.41). For readability, its notation is purified to A^r.

$$\mathrm{E}\left[A\right] = \overline{A} = \frac{1}{n_r} \sum_{r=1}^{n_r} A^r \tag{3.90}$$

$$\mathrm{Var}\left[A\right] = s_A^2 = \frac{1}{n_r - 1} \sum_{r=1}^{n_r} \left(A^r - \overline{A}\right)^2 \tag{3.91}$$

$$c_A = \frac{s_A}{\overline{A}} \tag{3.92}$$

Contrary to the weighted averaging per frequency band, the average over n_r different realizations is performed unweighted. The latter technique is chosen due to reasons of simplicity regarding further statistical evaluations. If the power is used as a weighting factor, this will lead to an additional correlated random variable like in Eq. (3.41). Equation (3.93) shows the relationship between the two averaging techniques by an second order Taylor series expansion, where ρ_{EP} denotes the Pearson correlation coefficient between energy and power. The expression in the inner brackets scaled by c_P, the coefficient of variation of the power, makes the difference. Since c_P becomes small with increasing frequency, the two averaging techniques slightly differ only at low frequencies comparing the standard deviation and the mean (cf. Fig. 4.50 in subsection 4.5.2).

$$\overline{A} = \mathrm{E}\left[A\right] = \mathrm{E}\left[\frac{E}{P}\right] \approx \frac{\overline{E}}{\overline{P}}\left(1 + c_P\left(c_P - \rho_{EP}\, s_E\right)\right) \tag{3.93}$$

3.3.3 Confidence Interval of the True Mean - Number of Realizations

The upcoming question is, if the true mean of the energy influence coefficient μ_A, which results from an unlimited number of repetitions, can be estimated with a certain precision by averaging over an affordable number of realizations $n_{r,min}$. One possible measure is the confidence interval which potentially includes the true mean. If the execution of $n_{r,min}$ realizations is repeated, the confidence level describes for how many cases the interval will include the true mean. A certain confidence level of $(1 - \alpha)$ is related to a confidence interval I by $\Pr(\mu_A \in I) = 1 - \alpha$. Hence, the $100\,(1 - \alpha)\,\%$ confidence interval for the true mean results in [Zeidler 2013]

$$\overline{A} - t_{(1-\frac{\alpha}{2})}\frac{s_A}{\sqrt{n_r}} < \mu_A < \overline{A} + t_{(1-\frac{\alpha}{2})}\frac{s_A}{\sqrt{n_r}} \tag{3.94}$$

whereby the variance of the sample mean $\overline{A}$ is estimated by:

$$\mathrm{Var}[\overline{A}] = \frac{\mathrm{Var}\left[A\right]}{n_r} = \frac{s_A^2}{n_r} \tag{3.95}$$

In Eq. (3.94), $t_{(1-\frac{\alpha}{2})}$ describes the $(1 - \frac{\alpha}{2})$ quantile of Student's t-distribution with $n_r - 1$ degrees of freedom [Zeidler 2013]. Equation (3.94) is based on the assumption that the

mean value follows a normal distribution with $\overline{A} \sim \mathcal{N}(\mu_A, \frac{\sigma_A}{\sqrt{n_r}})$ [Zeidler 2013]. This holds accordingly to the central limit theorem as the energy influence coefficient can be considered as an independent and identically distributed random variable. As the sample standard deviation is used to replace the true one, the quantile values are taken from the t-distribution instead of the normal distribution [Zeidler 2013]. Inserting Eq. (3.92) in Eq. (3.94) leads to the following limits of the confidence interval:

$$\overline{A}\left(1 \mp t_{(1-\frac{\alpha}{2})}\frac{c_A}{\sqrt{n_r}}\right) \tag{3.96}$$

There are different possibilities to characterize the uncertainty. As the energy influence coefficient shows a high variation in magnitude over the entire frequency range, a relative, logarithmic deviation is chosen as a measure. Hence, the level difference between the sample and the true mean should be smaller than the relative error D:

$$|L_{\overline{A}} - L_{\mu_A}| < D \qquad \text{with } L_A = 10\lg\left(\frac{A}{A_{\text{ref}}}\right) \text{ and } A_{\text{ref}} = 10^{-12} \tag{3.97}$$

Expression (3.97) can be rewritten as:

$$\left|10\lg\frac{\overline{A}}{\mu_A}\right| < D \qquad \Leftrightarrow \quad -D < 10\lg\frac{\overline{A}}{\mu_A} < D$$

After some transformations, the following interval arises:

$$\Leftrightarrow \quad 10^{\frac{-D}{10}}\,\overline{A} < \quad \mu_A \quad < 10^{\frac{D}{10}}\,\overline{A} \tag{3.98}$$

$$\Leftrightarrow \quad \underbrace{\left(1 - 10^{\frac{D}{10}}\right)\frac{\sqrt{n_r}}{c_A}}_{t_l} < \underbrace{\frac{\overline{A} - \mu_A}{\frac{s_A}{\sqrt{n_r}}}}_{:=T \sim t_{n_r-1}} < \underbrace{\left(1 - 10^{\frac{-D}{10}}\right)\frac{\sqrt{n_r}}{c_A}}_{t_u} \tag{3.99}$$

If expression (3.97) should be fulfilled with a probability of $(1-\alpha)$, it holds equivalently:

$$\Pr\left(|L_{\overline{A}} - L_{\mu_A}| < D\right) = 1 - \alpha$$
$$\Leftrightarrow \quad \Pr\left(t_l < T < t_u\right) = 1 - \alpha$$
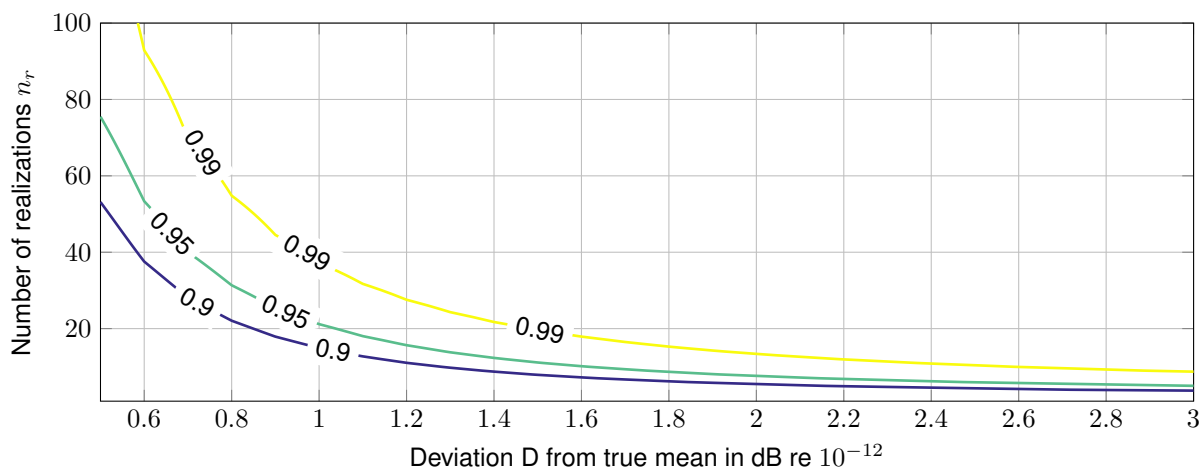
Figure 3.6: Number of realizations n_r for the deviation D from the true mean μ_A based on $c_A = 0.5$.

The probability that T lies in the interval of t_l and t_u can be expressed by evaluating the cumulative distribution function of the Student's t-distribution F_T at the interval limits [Zeidler 2013]. These are determined in Eq. (3.99).

$$\Leftrightarrow F_T(t_u) - F_T(t_l) = 1 - \alpha \tag{3.100}$$

Expression (3.100) either delivers n_{min} by solving it numerically or is evaluated for explicit values of n_r, D and c_A to be depicted in contour plots like in Fig. 3.6. These curves are calculated on the basis of the coefficient of variation $c_A = 0.5$. For the investigation in subsection 4.5.1, $c_A = 0.5$ is the worst case if e.g. the frequency range below the first thickness-stretch resonance (3860 Hz) and an excitation with greater or equal five loads is considered (cf. Fig. 4.49). Choosing e.g. a maximum deviation of $D = 1$ dB from the true mean, a simulation consisting of a minimum number of $n = 37$ realizations has to be performed that - repeating the simulation several times - in 99 % of the repetitions the true mean lies within the corresponding confidence interval. In the case, the required number of realizations becomes small the prerequisites of the presented procedure might be violated.

Having performed the required number of realizations, its logarithmic deviation from the true mean can be determined by means of Eq. (3.100). Therefore, the corresponding number of realizations, the resulting coefficient of variation as well as the desired confidence level is inserted. Equation (3.98) delivers the respective confidence interval of the true mean. The confidence interval for a confidence level of 99 % is shown exemplarily in Fig. 3.7 together with the sample mean of 37 realizations for a RotR excitation with five loads. According to the corresponding investigation in subsection 4.5.1, the coefficient of variation varies over the frequency (cf. Fig. 4.49). Thus, only at 200 Hz the deviation reaches 1 dB and above
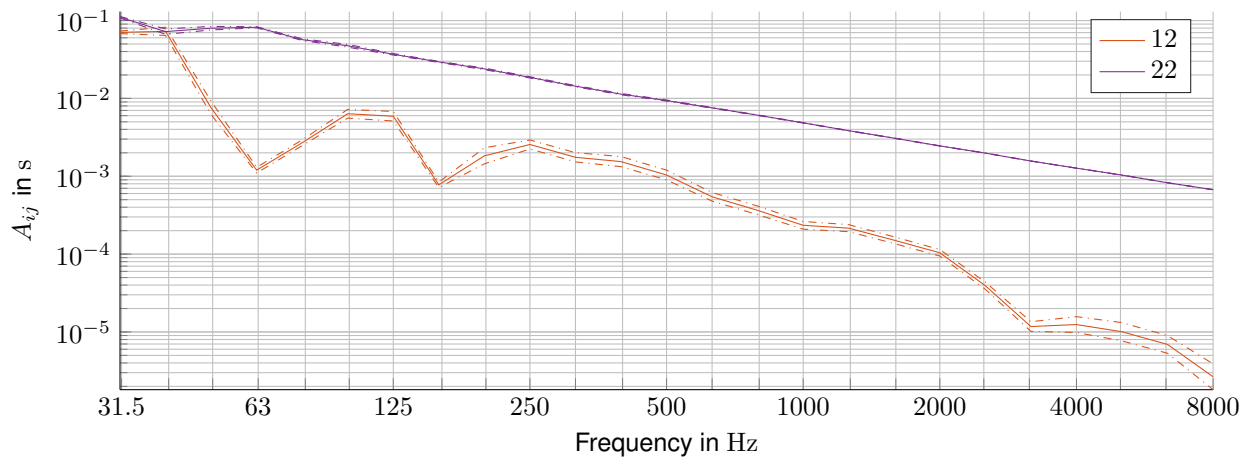
Figure 3.7: Sample mean (—) plus $99\,\%$ confidence interval $(-\cdot-)$ of energy influence coefficients A_{ij} based on 37 realizations for $n_l = 5$.

the first thickness-stretch resonance the deviation is greater $D = 1$ dB resulting in a larger confidence interval.

The presented procedure opens up the possibility to find a minimum number of realizations in order to compute energy influence coefficients within a certain confidence interval [Winter et al 2017c]. Furthermore, it can be applied to other random variables like coupling loss factors by considering their statistical behavior. In addition, other uncertainties can be covered like choosing the material data as random input variables.

4 Investigations by means of the Energy Flow Analysis

In this chapter, the EFA is applied to various scenarios: On the one hand to show the possibilities which the EFA offers and on the other hand to describe the frequency dependent transmission behavior of junctions which consist of CLT components. It starts with an overview of the used configurations together with modeling aspects and comparisons to measurements in section 4.1. Section 4.2 focuses on the wave types and the transmission behavior of different types of plates starting with a pinned L-junction of thin, isotropic plates and ending up with a non-pinned L-junction of thick, orthotropic plates. Thereby, the vibration reduction index is discussed and compared to analytical solutions of the SEA. Section 4.3 continues with thick, orthotropic plates which represent CLT components. Thereby, geometry and point of excitation are varied to examine the corresponding sensitivity of the energy flow in dependency on the frequency range. Moreover, modifications at the junctions are performed (cf. subsection 4.4): Firstly, an elastic interlayer is inserted between wall and ceiling to model different types of connections, secondly, a ceiling is connected via a bracket to a continuous wall and thirdly, from two over three up to four components are connected leading to a comparison of L-, T- and X-junction. Finally, the effect of the used number of loads for a RotR excitation is examined comparing 100 realizations and their statistical properties on each of six different numbers of loads.

4.1 Used Configurations and Modeling Aspects

This section gives a summary over the used configurations and includes necessary modeling aspects. It starts with an overview over the FE models of the different types of junctions and their possible modifications (cf. subsection 4.1.1). In subsection 4.1.2, the material and geometry parameters used within this thesis are introduced on the basis of comparisons with measurements and referred to the corresponding subsections. Moreover, the modeling and

possible configurations of an elastic interlayer are presented in subsection 4.1.3. Subsection 4.1.4 lists shortly the different types of loads to excite the subsystems. The necessary resolution in the space and the frequency domain have been determined by extensive studies. Their results are summarized in the corresponding subsections 4.1.5 and 4.1.6 as basis configuration for the subsequent investigations. In subsection 4.1.7, the analytical solutions, which are used for comparisons, are briefly introduced including their boundary conditions.

4.1.1 Models

In this paragraph, the used models are described starting with an short overview:

— Plate

⌐ L-junction with rigid connection of wall and ceiling

⌐ L-junction with elastic interlayer between wall and ceiling

⊢ T-junction with rigid connection of the subsystems

⊢ T-junction with elastic interlayer between the ceiling and each wall

⊢ T-junction with rigid connection of the walls whereby the ceiling is connected via bracket plus elastic interlayer on top

+ X-junction with rigid connection of the subsystems

+ X-junction with rigid connection of the ceilings and elastic interlayer between the ceilings and each wall

+ X-junction with separated ceilings and elastic interlayer between the ceilings and each wall

The models are designed as shell and as solid element models. The corresponding element types with quadratic shape functions, Shell281 and Solid186, are selected in ANSYS®. The boundaries opposite to the junction are simply supported. Therefore, the displacement degrees of freedom are held, whereby for the solid element model, this applies only to the degrees of freedom in the middle plane in order to allow rotations. The solid element models contain at least four elements across the thickness to enable shear deformations and through thickness effects. The shell elements are based on the Mindlin plate theory [Mindlin 1951].

(a) Plate

(b) L-junction

(c) T-junction

(d) T-junction: Shell element model

(e) T-junction with continuous wall

(f) X-junction
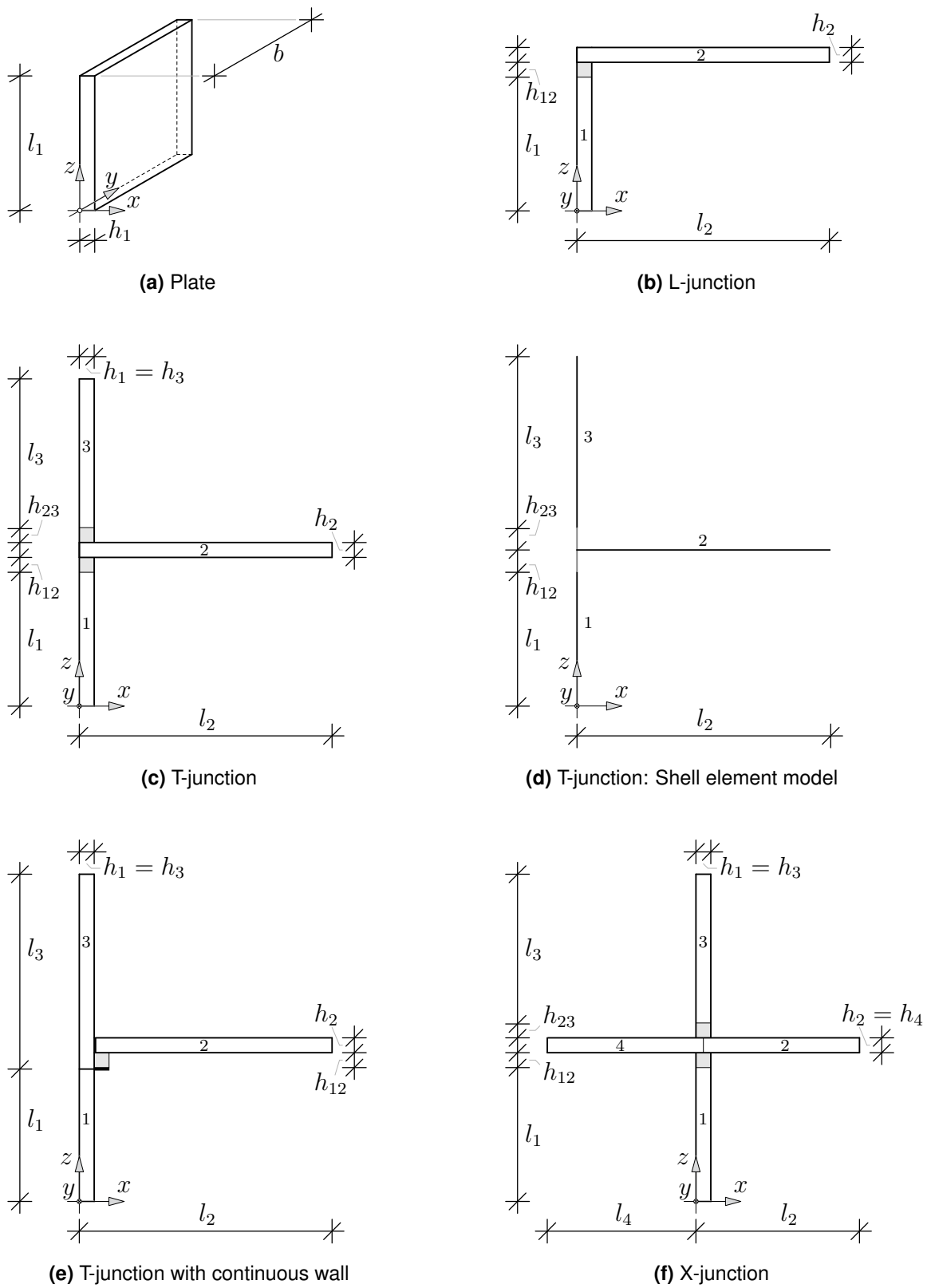
Figure 4.1: Geometry and subsystem numbering of the solid element models and of one exemplary shell element model in (d) including elastic interlayers or spring-damper elements, respectively.

Table 4.1: Material parameters of timber boards which form the layers of CLT [DIN EN 338 2016; Niemz and Caduff 2008].

	x	y	z
E	$1.1\,10^{10}$	$3.667\,10^{8}$	$3.667\,10^{8}$
	yx	zx	zy
G	$6.9\,10^{8}$	$6.9\,10^{8}$	$6.9\,10^{7}$
ν	$1.4\,10^{-2}$	$1.4\,10^{-2}$	$3.0\,10^{-1}$
ρ		450	
D		$1.2\,10^{-2}$	

Additionally to the axonometry of the plate, a selection of the different junction geometries is sketched as side elevation in Fig. 4.1. Thereby, the indices of the geometry parameters are chosen according to the counterclockwise numbering of the subsystems. For clarity, the geometry of the shell element model is only shown exemplarily for the T-junction in Fig 4.1d. In the case of shell element models, the elastic interlayer is represented by spring-damper elements (COMBIN14) [Winter et al 2016]. For each model, the rigid connection results by setting h_{ij}, which represents the thickness of the elastic layer or of the spring-damper element between subsystem i and j, equal to zero.

The T-junction with a continuous wall due to the rigid connection of both wall subsystems is only modeled as solid element model. As shown in Fig 4.1e, a bracket with an elastic interlayer on top is mounted to the wall. Thereby, the elastic interlayer and the ceiling on top of the elastic interlayer are not connected to the wall.

Pinned Junction   Optionally, a simple support can be added at the junction of wall and ceiling. Since rotations are allowed, the additional simple support shall only admit bending wave transmission and leads to the denomination pinned L-, T- or X-junction. In the case of the solid element model, the displacement degrees of freedom in the center of the junction, which is defined by the intersection of the middle planes of wall and ceiling, are fixed.

4.1.2 Physical Properties of the Subsystems

As explained in section 2.1, CLT consists of several layers of timber boards which are glued together crosswise. For the individual layers, Tab. 4.1 shows the material properties. Assuming the strength class C24 for each timber board, values from DIN EN 338 [2016], Niemz and Caduff [2008] are used within the joint research project showing a reasonable agreement

Table 4.2: Homogenized material parameters of wall and ceiling in their local coordinate system.

	Wall			Ceiling / Single plate		
	x	y	z	x	y	z
E	$1.061\,10^{10}$	$7.605\,10^{8}$	$3.667\,10^{8}$	$8.243\,10^{9}$	$3.123\,10^{9}$	$3.667\,10^{8}$
	yx	zx	zy	yx	zx	zy
G	$6.9\,10^{8}$	$1.725\,10^{8}$	$9.857\,10^{7}$	$6.9\,10^{8}$	$1.725\,10^{8}$	$9.857\,10^{7}$
ν	$8.5\,10^{-2}$	$6.1\,10^{-2}$	$18.4\,10^{-2}$	$12.9\,10^{-2}$	$6.3\,10^{-2}$	$12.2\,10^{-2}$
ρ			450			
D			$1.2\,10^{-2}$			

Table 4.3: Used geometries for junctions consisting of walls and ceilings or for a single plate.

(Sub)section	Wall			Ceiling			Single plate		
	l	b	h	l	b	h	l	b	h
2.1.4, 2.2, 2.3.2							2.662	3	0.162
4.1.2	2.5	3	0.081	3.45	3	0.162	2.662	3	0.162
4.1.6, 4.2.4, 4.4.1, 4.5	2.5	3	0.081	3.45	3	0.162			
4.3.1	2.5	3/1	0.162/0.081	2.662/3.45	3/1	0.162	2.662	3	0.162
4.3.2	2.5	2/3/4	0.081	2	2/3/4	0.162			
4.3.3	2.5	3	0.081	1/2/3/4	3	0.162			
4.3.4, 4.3.5, 4.4.2, 4.4.3	2.5	3	0.081	3.45	3	0.162			
	2.5	3	0.081	3.2	3	0.162			

between measured and computed natural frequencies at an L-junction [Mecking et al 2017a; Paolini et al 2017].

Whereas the wall consists of three layers with the layup 0°/90°/0°, the ceiling contains six layers with the layup 0°/90°/0°/0°/90°/0°. Thereby, each layer is 0.027 m thick [Deutsches Institut für Bautechnik 2009, 2014]. Since both layups are symmetric to the middle plane, the orthotropic material parameters of the layers can be homogenized according to the procedure explained in subsection 2.1.3. The homogenized material parameters of the CLT plates depend on their layup and thus, they differ for wall and ceiling (cf. Tab. 4.2). Except for section 4.5 and introductory examples with isotropic material in subsection 4.2.2 and 4.2.3, all investigations are based on the material parameters in Tab. 4.2, whereby studies at single plates are performed with the same properties as the ceiling. To complete the applied physical properties, Tab. 4.3 shows the varying dimensions of the subsystems related to the corresponding subsections.

(a) Number of modes per one-third octave band

(b) Energy due to RotR excitation
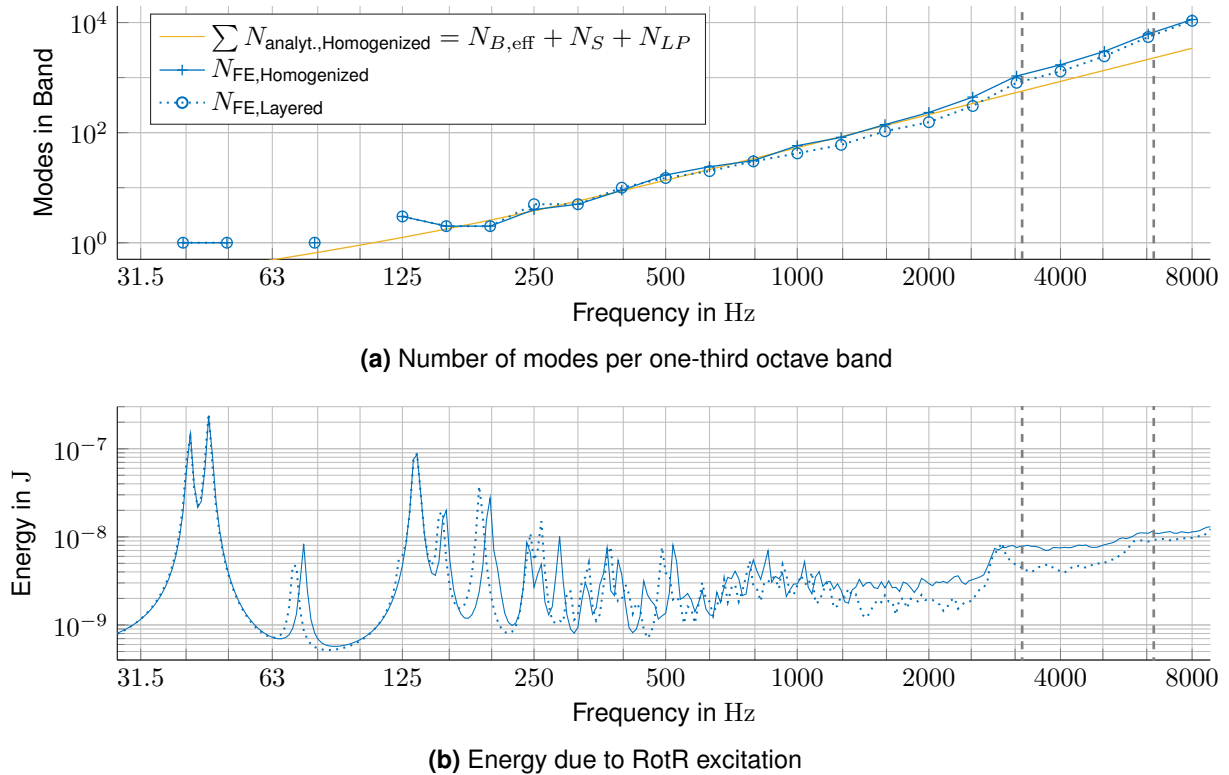
Figure 4.2: Single plate: Model considering each timber layer separately ($\cdots$) compared to homogenized material parameters ($-$); Thickness-stretch resonances of the homogenized material ($\vdots$).

Modeling of Cross Laminated Timber: Layered vs. Homogenized

To investigate the effect of using the material parameters which are homogenized through the thickness, comparisons at a single-axis spanned ceiling as well as at an L-junction have been performed. In both investigations, a model considering each timber layer separately is compared to a model with the homogenized material parameters using the same mesh. To cope with the shear deformation of the individual timber layers also at high frequencies, two solid elements are used across the thickness of each layer.

Firstly, the number of modes per one-third octave band of a single plate is opposed. Figure 4.2a shows a good agreement between the layered and the homogenized model up to 800 Hz. Above, less modes arise in the layered model, but both FE models identify the thickness modes at a similar frequency. This leads to an increase close to the first thickness-stretch resonance compared to the analytical estimation which uses the homogenized material parameters.

Secondly, the layered and the homogenized model of the plate are excited at the same 100 locations by RotR. The resulting energy in Fig. 4.2b shows an almost perfect match of the

(a) 71 Hz   **(b)** 134 Hz   **(c)** 153 Hz   **(d)** 189 Hz
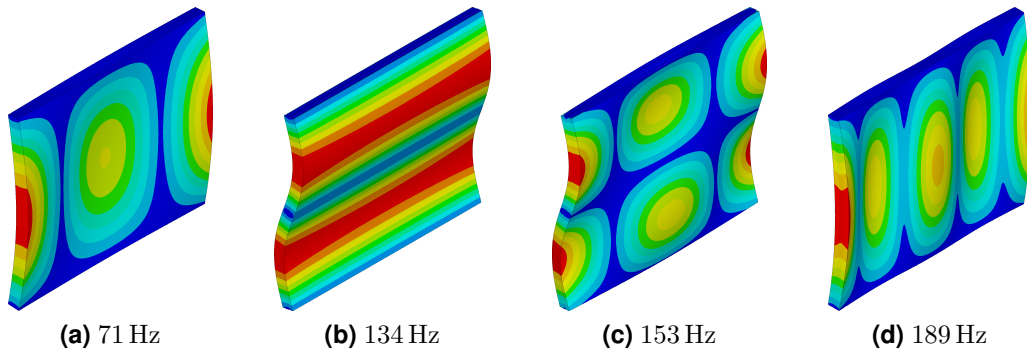
Figure 4.3: Mode shapes of a single-axis spanned plate whose model considers each timber layer separately; Colors indicate vector sum of displacements.
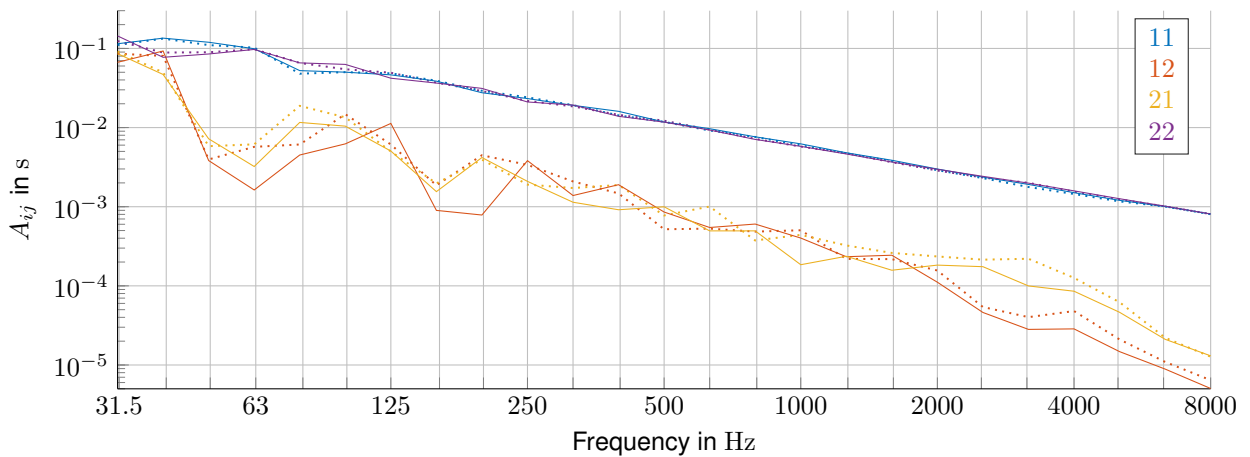
Figure 4.4: Frequency averaged energy influence coefficients of an L-junction: Model considering each timber layer separately ($\cdots$) compared to homogenized material parameters ($-$).

resonances at 41, 45 and 134 Hz, whereas the resonances at 71, 154 and 189 Hz are shifted to higher frequencies for the homogenized model. The corresponding mode shapes in Fig. 4.3 indicate that the homogenized elastic modulus perpendicular to the principal span axis of the plate, E_y, is overestimated by Eq. (2.23). Applying the homogenization, an equivalent, static bending stiffness is assumed for both principal axis of the CLT plate. For mid and high frequencies, the characteristic behavior of both models is similar. For the homogenized model, the higher number of modes per one-third octave band results in a higher energy level above 1000 Hz. Both energy curves escalate for the resonant excitation of the first and the second thickness modes. The layered model exhibits a comparatively sharp peak shortly before the first thickness-stretch resonance, $f_{TM,1}(c_{L,z})$, which is analytically estimated by means of the homogenized material assuming an infinite plate (cf. Eq. (2.44)).

Thirdly, the frequency averaged energy influence coefficients of an L-junction are compared in Fig 4.4 for a RotR excitation. The energy flow into the adjacent components, which is

described by the off-diagonal entries $\tilde{A}_{ij}$ of the energy influence coefficient matrix, shows a good agreement in the frequency range up to 50 Hz, where the first eigenfrequencies are relevant. Whereas the influence of the eigenfrequencies, which are moved due to the homogenization, becomes visible in the frequency range between 63 Hz and 250 Hz, the high modal density leads to similar curves above 250 Hz up to 2000 Hz. Above 2000 Hz, the homogenized model underestimates the energy flow compared to the layered model.

The further investigations within this thesis are performed by homogenized material parameters neglecting the peculiarities of the layered model. The homogenized material simplifies the modeling and meshing inside the FEM and it enables the use of shell elements. Moreover, it facilitates comparisons to analytical computations by means of the SEA.

Comparison to Measurements

Figures 4.5 and 4.6 show the energy influence coefficients of two different L-junctions on the basis of measurements and simulations, which are both evaluated by the EFA. A flexible (screwed) junction as well as a junction with a damped, elastic interlayer (Sylodyn ND) have been constructed and measured in the laboratory [Mecking et al 2017a]. Both types of junctions are introduced more detailed in subsection 4.1.3.

In the measurement, each component is excited successively at two different positions by an electro-dynamic shaker. The force and acceleration at the shaker position is determined by means of an impedance head. It has a limited accuracy of $+/-5°$ determining the phase shift between force and acceleration [PCB Piezotronics 2017] and thus leads to uncertainties determining the input power particularly for non-resonant contributions. The subsystem energies are approximated by the surface velocities perpendicular to the plate applying Eq. (3.62). They are measured by accelerometers at 54 and 81 positions arranged in an irregular grid on the wall and the ceiling, respectively [Mecking et al 2017a]. Above 300 Hz, the chosen grid becomes too rough to resolve the bending waves [Mecking 2014]. It does not fulfill the Shannon-Nyquist criterion in the space domain [Winter 2012]. For higher frequencies and thus a sufficiently large modal overlap, the spatial variation of the amplitudes might be small enough in order to neglect the Shannon-Nyquist criterion for the evaluation of space averaged energies [Mecking et al 2017b]. The evaluation of the energy influence coefficients resulting from two different shaker positions per component is performed by means of Eq. (3.64).

Within the scope of the simulation, it is theoretically possible to use the same excitation and observation positions as in the measurement. However, the results are prone to be
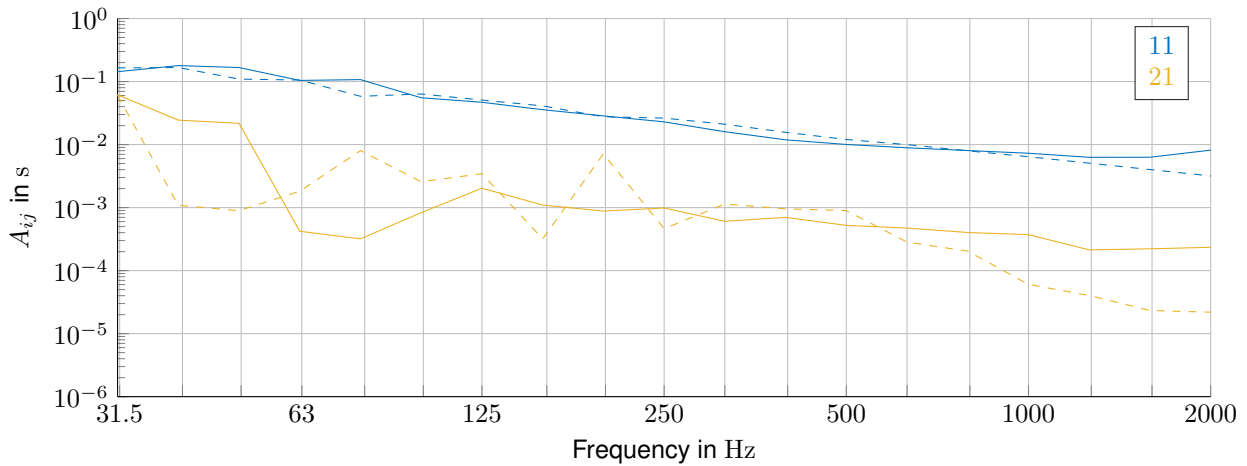
(a) Excitation of subsystem 1
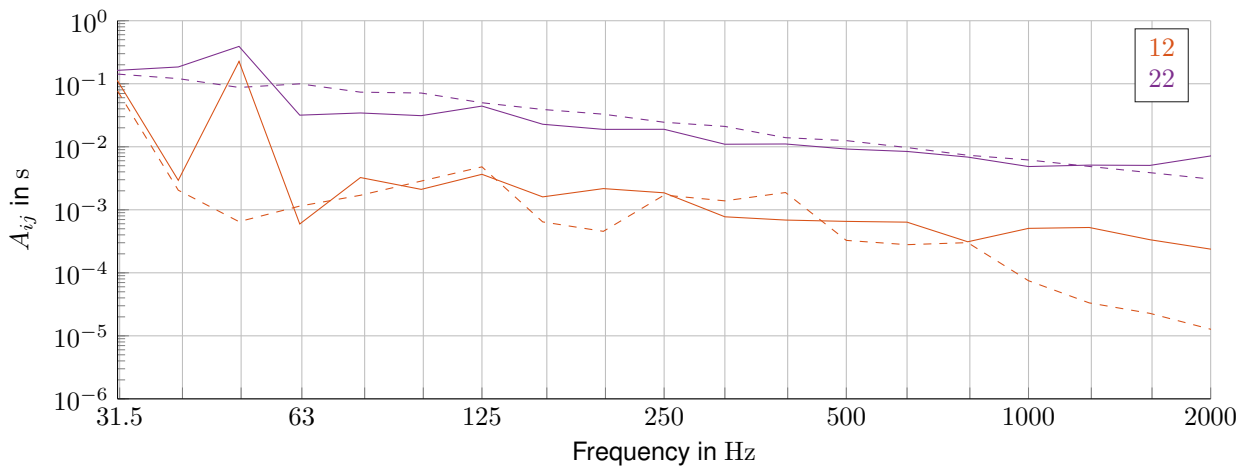
(b) Excitation of subsystem 2

Figure 4.5: Frequency averaged energy influence coefficients $\tilde{A}_{ij}$ of an L-junction with a damped, elastic interlayer (Sylodyn ND): Calculated by the EFA on the basis of $(-)$ measurements (excitation with an electro-dynamic shaker successively at two positions per component, evaluation of selected surface velocities perpendicular to the plate) or $(--)$ numerical simulations (excitation by RotR with 100 loads perpendicular to the plate, evaluation of potential and kinetic energy).

quite sensitive due to the very specific excitation scenario and the low resolution in space for the evaluation of surface velocities. This means, small errors in the model assumptions have an high impact on the results. Therefore, the aim of the simulations is to classify the junctions preferably universally. Thus, both L-junctions are excited by RotR consisting of 100 loads which are randomly distributed and act perpendicular to the plates. Moreover, the subsystem energy is determined exactly by summing up the potential and the kinetic energy.

Comparing measurement and simulation, Fig. 4.5 and 4.6 demonstrate that the main diag-
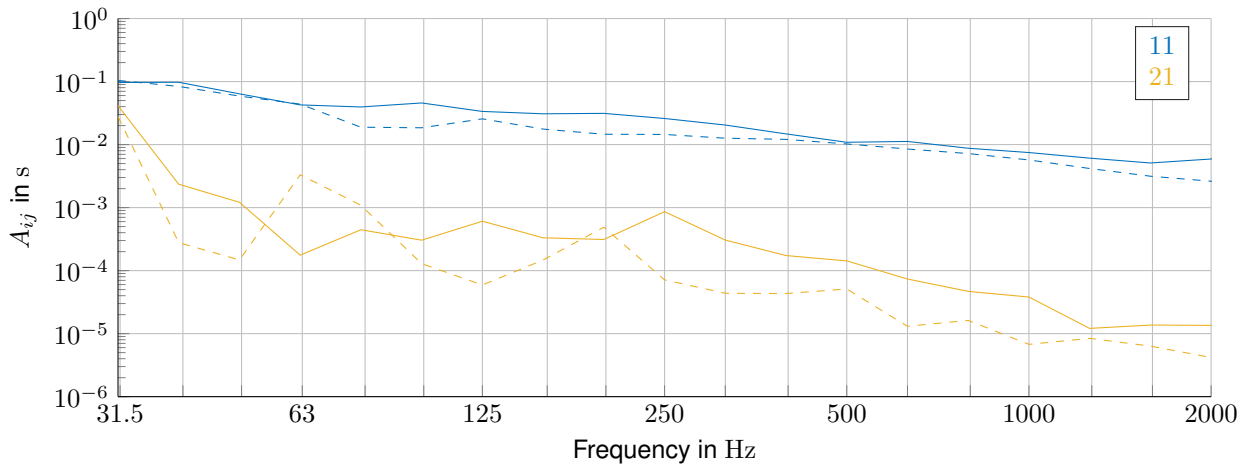
(a) Excitation of subsystem 1
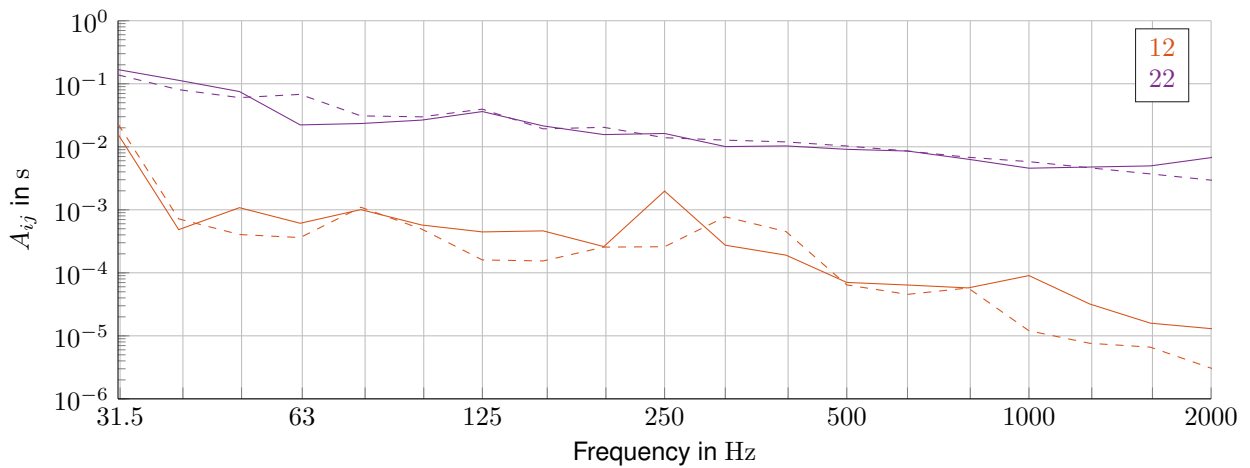
(b) Excitation of subsystem 2

Figure 4.6: Frequency averaged energy influence coefficients $\tilde{A}_{ij}$ of an L-junction with a damped, elastic interlayer (Sylodyn ND): Calculated by the EFA on the basis of $(-)$ measurements (excitation with an electro-dynamic shaker successively at two positions per component, evaluation of selected surface velocities perpendicular to the plate) or $(--)$ numerical simulations (excitation by RotR with 100 loads perpendicular to the plate, evaluation of potential and kinetic energy).

onal entries A_{ii} show a reasonable agreement up to $1600\,\mathrm{Hz}$. This indicates an acceptable choice of the physical properties for the components, which are listed in Tab. 4.2 and 4.3.

Different effects might be responsible for the deviations at high frequencies: Due to the thickness modes, the subsystem energies are overestimated by evaluating only the surface velocities as demonstrated in subsection 4.2.4. If the factual stiffness perpendicular to the grain is about $30\,\%$ lower than listed for the boards in Tab. 4.1, the stiffness in thickness direction of the CLT (cf. Tab. 4.2) is reduced correspondingly. Hence, the CLT plates already start to vibrate at resonance above $1600\,\mathrm{Hz}$ according to Eq. (2.44). Moreover, the stinger has its first resonance above $1100\,\mathrm{Hz}$ which clearly affects the measurement results

[Mecking 2014]. For instance, the phase shift between force and acceleration shows significant deviations which yields an incorrect input power.

In the majority of the one-third octave bands below 1000 Hz, the off-diagonal entry A_{12}, which describes the normalized energy in subsystem 1 due to the excitation of subsystem 2, shows a qualitatively comparable behavior for each of the two different junctions. The opposite direction is represented by A_{21} in Fig. 4.5a and 4.6a. Here, the energy transmission differs up to one order of magnitude between measurement and simulation especially for the junction with the damped, elastic interlayer. According to Fig. 4.6a, the decoupling effect of the Sylodyn ND is overestimated in the numerical model predicting the energy flow from the wall to the ceiling.

At low frequencies, the outliers indicate that the model could be optimized with respect to the boundary and coupling conditions. Therefore, a model updating regarding force-induced vibrations of the coupled structure has to be performed since a comparison of well-separated eigenfrequencies and eigenmodes, like in Paolini et al [2016], does not consider absolute values. Ideally, the model updating is continued up to high frequencies in order to predict the energy flow more precisely. However, the modal overlap increases with the investigated frequency. This requires alternative updating techniques which also cope with a possibly frequency dependent behavior of the coupling properties.

The high modal spacing at low frequencies might lead to punctually large deviations, since the assumption $E_{ij} = 2\,E_{ij,\mathrm{kin}}(v_z)$ is only fulfilled at resonance. In the frequency range above the first global bending mode shapes and below the thickness resonances, the normalized energy of the indirectly excited components A_{ij} is underestimated if only the surface velocities perpendicular to the plane are measured. As explained in subsection 4.2.4, the contribution of the in-plane waves and effects due to the rotatory inertia are neglected. Subsection 4.3.3 illustrates that the different types of loadings excite different modes and thus lead to an individual energy flow across the junction which might provoke deviations especially at low and at high frequencies.

Performing measurements over such a wide frequency range is challenging and thus, a comparison to simulations is linked to various uncertainties. As a result, the comparison shows that the numerical model opens up the possibility to demonstrate the qualitative overall behavior of two different, real L-junctions. The numerical models with the applied physical properties serve as basis for various studies and variations in the subsequent sections. Thus, reaching an optimal match of the coupling behavior in each one-third octave band is not central within the scope of this comparison.

4.1.3 Elastic Interlayer

The elastic interlayer consists of four layers of solid elements through thickness to enable shear deformations within the interlayer (cf. Fig. 4.7). In order to comply with a maximum element aspect ratio of 1:4, these solid elements have much smaller edge lengths compared to the adjacent elements of the components. To attach the elements of the interlayer to the components, constrained equations between the nodes at the interface are used in the same manner as in Kohrmann [2017]. They open up the possibility of a rigid contact by interpolating the nodal displacements and thus, of an economic meshing of the whole structure.

The material properties in the left column of Tab. 4.4 are used to represent the flexible behavior of a screwed connection. The density of the interlayer corresponds to the one of the CLT components. The elastic modulus and the Poisson's ratio result from a model updating at low frequencies in comparison with measured natural frequencies of an L-junction [Paolini et al 2017]. As screws were used in reality, the impedance difference occurs at the interface between the two CLT plates. In the FE model, the reduced force and moment transmission compared to a perfectly rigid junction is also taken into account by the interlayer. Thereby, the soft material enables a decoupling of the movement of the connected plates.

For all modifications, the interlayer modeled with solid elements is 12.5 mm thick according to the factual thickness of the specific elastomer Sylodyn ND [Getzner Werkstoffe GmbH 2012]. This product was used in the measurement setup. For modeling an elastomer with solid elements, its material properties are recalculated by Negreira et al [2014] and Paolini et al [2017] since in the manufacturer's data sheet they are determined based on a compression test not taking into account the obstruction of transverse deformations. For that calculation, the manufacturer Getzner Werkstoffe GmbH provided the static shear modulus and the density. At low frequencies, a comparison with measured natural frequencies of an L-junction showed that the screwed junction with elastomer can be represented by an elastic interlayer with the recalculated elastomer properties [Paolini et al 2017]. Investigating the energy flow over a wide frequency range, the frequency dependent behavior of the elastic modulus becomes additionally relevant. Due to a lack of data, the elastic modulus is extrapolated for frequencies above 1000 Hz on the basis of the manufacturer's data sheet [Getzner Werkstoffe GmbH 2012].

Moreover, the damping properties of the elastic interlayer are decisive for the energy flow into the adjacent component. In contrast to the SEA, the EFA is able to model non-conservative couplings. Therefore, the frequency dependent damping behavior of the elastomer is taken into account and thus also extrapolated for frequencies $f > 1000$ Hz. The used material
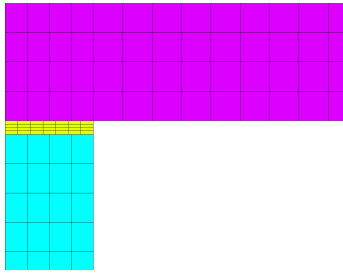
Figure 4.7: Detail of FE model: Elastic interlayer between wall and ceiling.

Table 4.4: Material and geometry properties of the elastic interlayer to model different types of junctions.

	Flexible (screwed)	Elastic interlayer (Sylodyn ND)
E	$1.18 \, 10^7$	cf. Tab. A.2
ν	0	0.386
ρ	450	700
D	0	0 or cf. Tab. A.2
h		0.0125

properties to model the elastomer Sylodyn ND are given in Tab. 4.4 whereby the frequency dependent parameters are listed in Tab. A.2.

4.1.4 Types of Loading

As introduced in subsection 3.1.2, loads are realized by means of pressure on selected elements. By contrast to nodal loads, singularities and thus a dependency on the mesh grid can be avoided as shown in Winter and Müller [2017]. The EFA opens up the possibility to apply any number of loads with individual directions, phase shifts and locations.

The loads act mostly perpendicular to the plates, apart from subsection 4.3.4 where out-of-plane and in-plane loading is compared at a T-junction. This is especially relevant for machinery induced vibration. Generally, two standard configurations are used: Either a single load positioned in the center of the plates or a RotR excitation with randomly selected locations is chosen (cf. subsection 3.3.1). RotR is principally performed using 100 loads whereby a comparison between different numbers of loads for RotR is demonstrated in section 4.5 also including the limit case where all surface elements of a subsystem are loaded (cf. Fig. 3.5). Since RotR excites nearly every mode, its application shall lead to an energy flow within the structure which is as representative as possible. This serves for a general prediction independently of the loading. By contrast, the single load describes a specific scenario. Since the single load acts in the node of a set of mode shapes, they do not contribute to this individual energy flow. Independently of the number of loads, the total force is always 1 N and thus the resulting energies are normalized to an input force of 1 N.

Shell element models ignore through thickness effects. Solid element models behave comparably if a load is applied which is equally distributed across the thickness (cf. subsection 4.3.1 and Fig. 4.17). By comparisons with loads at different locations across the thickness of a

plate, thickness resonances are identified. This study serves to select the appropriate element type depending on the loading and the frequency range.

4.1.5 Resolution in Space: Meshing

The meshing of the FE model is oriented at the maximum frequency since there, the minimum wave length occurs. This corresponds to the effective bending wave length which is calculated by means of the effective bending wave velocity given in Eq. (2.38) or approximated in Eq. (2.39):

$$\lambda_{B,\text{eff}} = \frac{c_{B,\text{eff}}}{f} \tag{4.1}$$

The effective bending wave length has to be discretized by at least four elements with quadratic shape functions marking the maximum element side length. This relation was heuristically determined on the basis of an extensive study at a plate with varying boundary conditions and loading directions as well as at an L-junction with varying densities. The investigations are presented in detail by Winter and Müller [2017] and show that in the case of frequency averaged quantities per one-third octave band, only three elements per wavelength can be used. This coincides with the results of Thompson and Pinsky [1994], which recommend three elements per wavelength in the case of quadratic shape functions. Beside a maximum element side length, the element side ratio should also be taken into account. In the present studies, it does not exceed a ratio of 1:2 except for the elastic interlayers whose elements are limited to 1:4.

4.1.6 Resolution in Frequency: Numerical Interpolation

Different techniques are compared for the numerical interpolation and integration of energy and power leading to frequency averaged energy influence coefficients per one-third octave bands according to Eq. (3.41): The composite rectangle rule (cf. Eq. (3.36)), the composite trapezoidal rule (cf. Eq. (3.38)), polynomial interpolation of order two and five as well as a cubic spline interpolation. Using higher order polynomials does not lead to a better approximation as they are not appropriate to describe the sharp peaks at the resonances and they tend to oscillations especially at the borders [Zeidler 2013]. This can be avoided by splines. Choosing cubic splines, they are defined piece-wisely by polynomials of order three and twice continuously differentiable. Thus, they have their maximum curvature at the discrete frequency points, whereas in between they are as smooth as possible. To evaluate as

Table 4.5: Number of necessary frequency steps per one-third octave band for a deviation below 5% from the reference solution evaluated for energy influence coefficients A_{ij}, subsystem energies E_{ij} and input power P_j [Meisinger 2017].

	Center frequency f_m:	$\leq 1000\text{Hz}$		$> 1000\text{Hz}$	
		Number of necessary frequency steps for a deviation $< 5\%$:			
	Interpolation method	average	maximum	average	maximum
A_{ij}	Rectangle	15	60	6	10
	Trapezoidal	8	12	5	8
	Polynomial $p = 2$	8	15	5	10
	Polynomial $p = 5$	10	15	5	10
	Cubic spline	8	12	4	8
E_{ij}	Rectangle	30	120	20	30
	Trapezoidal	10	15	5	8
	Polynomial $p = 2$	10	20	5	8
	Polynomial $p = 5$	12	20	5	10
	Cubic spline	10	15	5	8
P_j	Rectangle	20	60	15	24
	Trapezoidal	8	15	2	6
	Polynomial $p = 2$	12	15	2	6
	Polynomial $p = 5$	12	20	2	6
	Cubic spline	10	15	2	6

few discrete frequency points as possible, the composite trapezoidal rule, which is introduced in subsection 3.1.4, results to be the most efficient together with the spline interpolation (cf. Tab. 4.5).

The investigations are performed at an L-junction, whose material and geometry data is given in Tab. 4.2 and 4.3. A reference solution is computed with 120 discrete frequency points per one-third octave band. Generally, a logarithmically equidistant spacing over frequency is used, which is introduced in subsection 3.1.4. As a result of the comparison with the reference solution, the necessary number of frequency points per one-third octave band decreases for higher frequency bands. With increasing frequency, the modal density as well as the modal overlap factor increase, which has a smoothing effect on the curves of power, energy and energy influence coefficients. This influence is verified and confirmed by a parametric study whereby single material and geometry parameters are varied systematically. Reducing the material damping increases significantly the number of necessary frequency steps as the curves become sharper. The variation of the density has nearly no effect, which would also be valid for the variation of the stiffness, since it provokes just a shift of the eigenfrequencies in the frequency range.

Especially at low frequencies, where the modal behavior dominates, taking the quotient of subsystem energy and input power to receive the energy influence coefficients leads to a

slight reduction of the necessary number of steps per one-third octave band as common peaks due to resonances cancel each other or at least lead to a reduced peak. Generally, the energy or the energy influence coefficient of the non-excited subsystem is decisive since these quantities contain the modal contributions of the excited subsystem and of the non-excited subsystem.

Since the necessary number of frequency points per one-third octave band decreases with increasing frequency, the frequency range can be partitioned into different ranges. At low frequencies, a higher number of discrete frequencies is evaluated using a coarser mesh for the FE model. At high frequencies, the mesh must be refined according to subsection 4.1.5 and the number of frequency steps can be reduced. Table 4.5 offers a division above the one-third octave band of $1000\,\mathrm{Hz}$ ($f_u = 1223\,\mathrm{Hz}$) close by the first thickness mode of the system, which is the thickness shear resonance of the ceiling at $1445\,\mathrm{Hz}$. Alternatively, a division above the one-third octave band of $2000\,\mathrm{Hz}$ would lead to only six frequency steps for the upper frequency range using the trapezoidal rule.

For the subsequent investigations, the resolution in the frequency range is chosen to twelve steps per one-third octave band. Using the composite trapezoidal rule, this leads to a maximum error of 5% for the frequency averaged values of the energy influence coefficients according to Tab. 4.5 using the physical properties given in Tab. 4.2 and 4.3. Within this thesis, the frequency average is always performed over one-third octave bands. This holds also for analytical quantities like the number of modes which are summed up per one-third octave band.

4.1.7 Analytical Solutions

As a first check of the FE model, the first four eigenfrequencies of an four-sided simply supported, orthotropic Kirchhoff plate can be calculated which are given in the appendix A.2. For comparisons of the energy transmission, analytical, wave-based solutions are calculated. In the case of isotropic material, an in-house GUI (Graphical User Interface) of the Chair of Structural Mechanics is used [Panagiotopoulos et al 2015]. It is based on MATLAB® and can be accessed via `https://github.com/ChairOfStructuralMechanicsTUM/SEA-Matlab-GUI`. The GUI offers both approaches: Either the bending only approach with the pinned junction or the bending and in-plane waves approach where the junction is free to rotate and to undergo displacements [Hopkins 2007; Craik 2003]. The later boundary

conditions as well as the thick plate theory are implemented inside the commercial software VAOne® which is applied for comparisons with junctions between thick plates out of orthotropic material.

4.2 Plates Forming an L-Junction: Thin, Isotropic vs. Thick, Orthotropic

Firstly, two different approaches to define a thin plate limit are opposed for isotropic and orthotropic plates in subsection 4.2.1. In the the subsequent two subsection, an L-junction consisting of thin, isotropic plates is investigated. Thereby, the wave types occurring in thin plates are identified by estimating the translational parts of the energy. It is shown, that transmission behavior changes due to a simple support at the junction in subsection 4.2.2 compared to a junction without support in subsection 4.2.3. The results are compared to the wave approach, which constitutes a basis for the SEA. Moreover, subsection 4.2.2 explains exemplarily how the transmission behavior of strongly coupled structures can be described more robustly by a RotR excitation.

In subsection 4.2.4, the material is changed to orthotropic and the thickness is increased, which is appropriate for CLT. The changed properties lead to a thick plate already at low frequencies and the low elastic modulus perpendicular to the plane of the plate leads to thickness modes in the frequency range of building acoustics. The behavior and restrictions of thick plates compared to thin ones is described and depicted.

4.2.1 Thin Plate Limit of Isotropic and Orthotropic Plates

If the quotient of the elastic modulus and the density is large combined with a small thickness, the thin plate limit occurs at high frequencies according to expression (2.36) which is solved for the frequency in Eq. (4.2). To emphasize the proportionality between the limiting frequency and the physical properties of the plate, the Poisson's ratio is assumed to be negligible for the expression on the right hand side:

$$f_{h=\frac{\lambda}{6}} = \frac{1}{36\sqrt{3}} \frac{1}{h} \sqrt{\frac{E}{\rho\left(1-\nu^2\right)}} \qquad\qquad \sim \frac{1}{h}\sqrt{\frac{E}{\rho}} \qquad\qquad (4.2)$$

The cross-over frequency of Eq. (2.37) considers additionally the shear stiffness which results in a different proportionality relationship:

$$f_s = \frac{\kappa}{2\pi} \frac{G}{h} \sqrt{\frac{1 + \nu^2}{E\rho}} \qquad\qquad \sim \frac{G}{h} \sqrt{\frac{1}{E\rho}} \qquad\qquad (4.3)$$

In the case of isotropic material the identity $G = \frac{E}{2(1+\nu)}$ leads to the same proportionality as in Eq. (4.2):

$$f_s = \frac{\kappa}{4\pi} \frac{1}{h(1+\nu)} \sqrt{\frac{E(1+\nu^2)}{\rho}} \qquad\qquad \sim \frac{1}{h} \sqrt{\frac{E}{\rho}} \qquad\qquad (4.4)$$

The thin plate limit of an orthotropic plate is preferbly calculated by the cross-over frequency f_s in Eq. (2.37) or (4.3) since the individual shear stiffness is included. As mentioned in section 2.2, the following approximations can be used for orthotropic material: $E = \sqrt{E_x E_y}$, $G = \sqrt{G_{xz} G_{yz}}$ and $\nu^2 = \nu_{xy}\nu_{yx}$. As introduced in subsection 2.2.3, f_s refers to the phase velocity, whereas for the subsequent, energetic considerations, the energetic thin plate limit $\frac{f_s}{4}$ applies on the basis of the group velocity.

4.2.2 Thin, Isotropic Plates: Bending Waves Only

The two models of the L-junction examined in this subsection and in the subsequent subsection 4.2.3 differ in an additional simple support at the junction of wall and ceiling. The additional simply support shall only admit bending wave transmission and leads to the denomination pinned L-junction. Generally, the calculations base on a solid element model (cf. Fig. 4.1b). For comparisons, a shell element model is used which is then explicitly mentioned. A single, perpendicular load is applied in the center of both plates to excite the same type of mode shapes in each subsystem. Several mode shapes have a node in the center of the plate and therefore, they are not excited. In a second step, a RotR excitation is applied consisting of 100 loads which are distributed randomly over the surface of the plate in order to excite almost every mode - ideally in equal measure.

Table 4.6 shows the isotropic material properties and the dimensions of the investigated L-junction. The large area of the plates leads to a high modal density (cf. subsection 2.3.2) which moves the SEA limit related to a sufficient number of modes per band to the low frequency range. As depicted in Fig. 4.8b, more than five modes per band are available in both subsystems above $160\,\mathrm{Hz}$ to contribute to the energy transport. The modal overlap factor (cf. Eq. (2.66)) is greater than unity from $315\,\mathrm{Hz}$ on. As shown in Fig. 4.8a, the thin

(a) Wave velocities and energetic thin plate limit $\frac{f_s}{4}$ (cf. section 2.2).

(b) Number of modes per one-third octave band for wall ($-$) and ceiling ($--$).
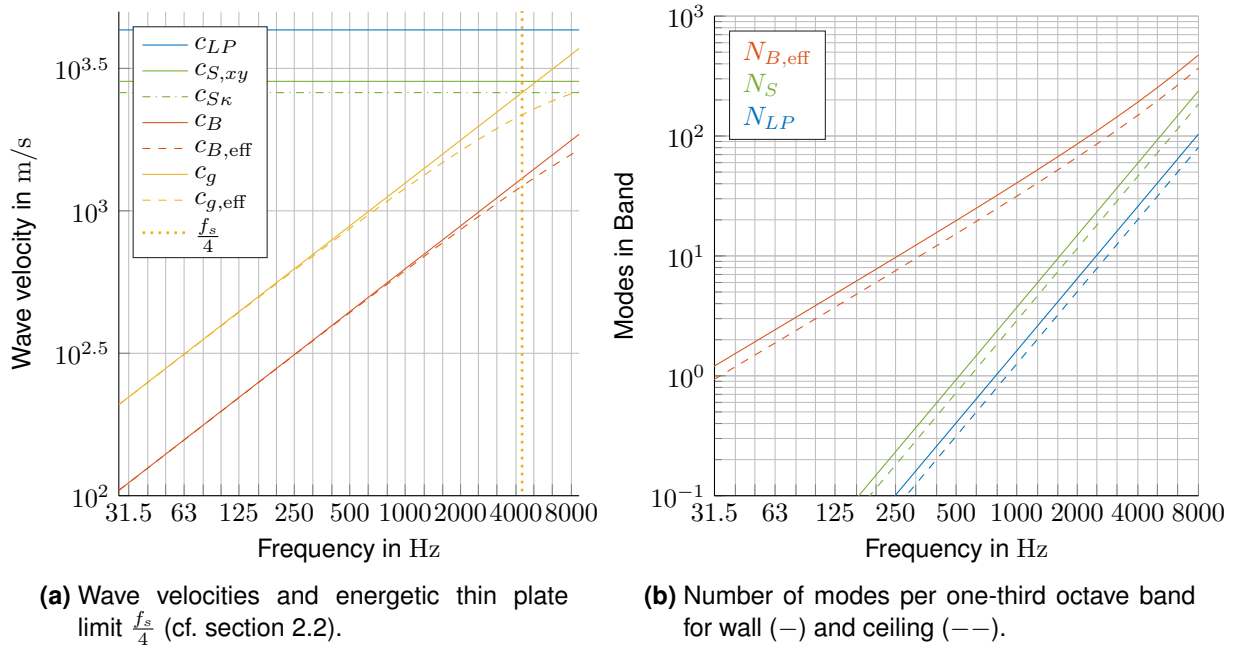
Figure 4.8: Dynamic properties of the thin, isotropic plates listed in Tab. 4.6.

Table 4.6: L-junction: Material and geometry properties of the thin, isotropic plates.

E	$8.243 \, 10^{10}$
ν	$12.9 \, 10^{-2}$
ρ	450
D	$1.2 \, 10^{-2}$
Wall $l_1 \times b \times h_1$	$5.8 \times 3.55 \times 0.05$
Ceiling $l_2 \times b \times h_2$	$4.5 \times 3.55 \times 0.05$

plate theory covers almost the entire, investigated frequency range up to the energetic thin plate limit $\frac{f_s}{4} = 4318\,\text{Hz}$, where the bending group wave velocity equals to the corrected out-of-plane shear wave velocity. Hence, a wide frequency range remains to apply the SEA in a simplified manner where the bending wave subsystem represents the entire dynamic behavior of a plate-like component. This coincides with the assumptions for the vibration reduction index derived in subsection 3.2.4.

Modal Behavior   The simple support at the junction of wall and ceiling shall omit a translation of the junction line which would lead to in-plane waves within the components. The support takes up the horizontal and vertical forces, whereas moments are transmitted due to the rigid connection of the components. A modal analysis confirms that even at high frequencies almost only bending modes occur.

(a) 45 Hz   **(b)** 46 Hz   **(c)** 58 Hz   **(d)** 469 Hz
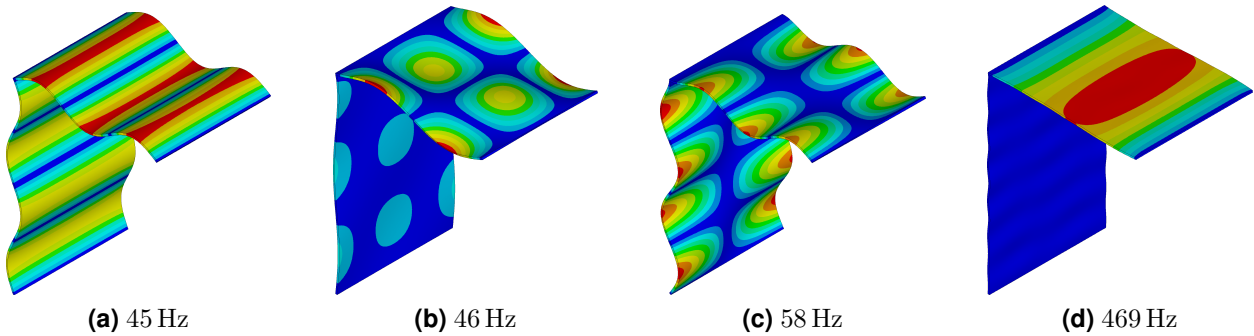
Figure 4.9: Mode shapes of the pinned L-junction consisting of isotropic, thin plates; Colors indicate vector sum of displacements.

Figure 4.9 illustrates mode shapes by means of the vector sum of the displacements. The modes in Fig. 4.9a, b and c result from bending waves which propagate in one (a) or in two plate directions (b,c). The mode shapes in Fig. 4.9a and c show a global behavior as the total structure vibrates whereby the colors of the mode shape in Fig. 4.9a indicate higher amplitudes in the ceiling. Figure 4.9b presents a mode shape which is localized in the ceiling.

Since in-plane modes, like the one at 469 Hz in Fig. 4.9d, have no relevant displacement perpendicular to the plate, they are hardly excitable by a load perpendicular to the plate. Consequently, only bending waves shall be excited and transmitted.

Excursus: Strong Coupling at Low Frequencies – Single Load vs. RotR

By means of the current example, the influence of the loading on strongly coupled structures is discussed. The definitions of strong and weak coupling are introduced in subsection 3.2.3 and 2.3.3, respectively. From the first to the fourth row, Fig. 4.10 shows subsystem energies, energy influence coefficients, loss factors and condition numbers. On the left, they are collocated for the excitation by the single load in the center of each subsystem and on the right for the RotR excitation using 100 randomly distributed loads. At certain frequencies, one off-diagonal entry A_{ij} of the energy influence coefficients matrix rises above one main diagonal entry A_{ii}. This happens up to 250 Hz for RotR and up to 350 Hz for the single load, which demonstrates Fig. 4.10 up to 100 Hz. Up to 80 Hz, A_{ij} results sometimes even higher than both main diagonal entries using the single load. This indicates strong coupling, which is confirmed by high values of the condition number as explained in subsection 3.2.3. Thus, the coupling loss factors have either values which are much higher than the damping loss factors [Cremer and Heckl 1996] or they are negative depending on the modal behavior.

In the first case, global mode shapes like the ones in Fig. 4.9a or 4.9c are excited. They are indicated by the frequency of intersection of main and off-diagonal entries of the energy influence coefficients matrix and include the fact that not all diagonal entries A_{ii} are bigger than any off-diagonal entry A_{ij}. In the second case, modes which are localized in one subsystem, like the one depicted in Fig. 4.9b, are excited more easily by a unit power injected into the other subsystem. As described in subsection 3.2.3, a negative back-flow of modal energy results to fulfill the energy balance. This happens at frequencies where one off-diagonal term A_{ij} is bigger than any main diagonal entry A_{ii}. Due to the logarithmic scale, the coupling loss factors are not depicted if they are negative.

In the following paragraphs, both cases are explained at distinct frequencies, which are marked by vertical dots in Fig. 4.10, on the basis of selected mode shapes, which are depicted in Fig. 4.9. The results due to the single load are compared to the ones due to RotR. Both loadings act perpendicular to the wall (subsystem 1) and the ceiling (subsystem 2), respectively. In the case of the energy E_{ij} or the energy influence coefficient A_{ij}, the first index i represents the observed subsystem and the second index j the excited subsystem as introduced in subsection 3.1.3 and 3.2.1. The coupling loss factor η_{ij} describes the portion of the energy in the subsystem i which is transmitted to the subsystem j (cf. subsection 3.2.2).

Global Modes: High Coupling Loss Factors   The single load is able to excite the global mode shape at $45\,\mathrm{Hz}$ in the center of the ceiling but not in the center of the wall since the load acts in the node of the mode shape. There, the mode shows no displacement which is indicated by the blue color in Fig. 4.9a. Therefore, the energies due to excitation of the wall, E_{i1}, are smaller than due to excitation of the ceiling, E_{i2}. As the mode shape oscillates globally, the different subsystem energies due to one load case j are almost of the same size ($E_{1j} \approx E_{2j}$). Using a RotR excitation instead of the single load, the mode shape can be excited in both subsystems leading to subsystem energies of similar size for both load cases and subsystems as depicted in the upper right graph of Fig. 4.10. For a single load, the energy flow into subsystem i appears to be independent of the excited subsystem as $A_{i1} = A_{i2}$. For RotR, the energy influence coefficients are not equal but of similar size and thus still indicating strong coupling. For both types of excitation, the coupling loss factors are bigger than the damping loss factors as shown in the third row of Fig. 4.10. For the single load, the damping loss factors deviate significantly from the hysteretic material damping at $45\,\mathrm{Hz}$.
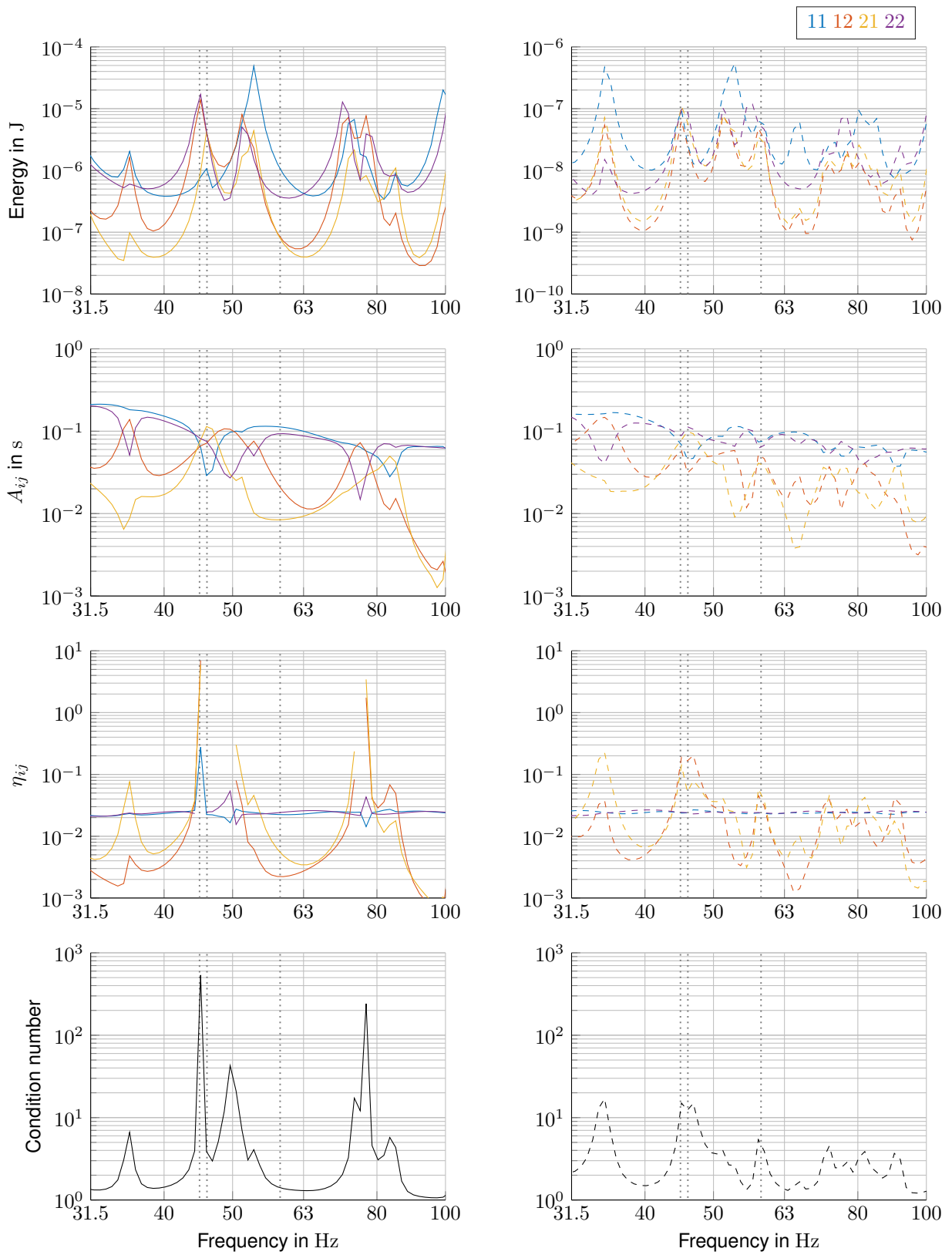
Figure 4.10: Pinned L-junction out of isotropic, thin plates: On the left, excited in the center of each subsystem by a single load ($-$) and on the right for RotR excitation ($--$); Investigated frequencies (:).

Indirect Excitation of Localized Mode: Negative Coupling Loss Factors   The single load is not able to excite the mode shape at 46 Hz in the center of the ceiling as it acts in the node according to Fig. 4.9b. Thus, the adjacent global mode at 45 Hz is excited ($E_{12} = E_{22}$) and its off-resonant contribution still dominates the energy distribution at 46 Hz ($E_{i2} > E_{i1}$, $P_2 > P_1$). Loading the wall, most of the energy flows into the ceiling due to the indirect excitation of the mode shape localized in the ceiling ($E_{21} > E_{11}$). In the upper left graph of Fig. 4.10, the curves of the subsystem energies are depicted for single load excitation. Normalizing the subsystem energies by the corresponding input power, the energy influence coefficients result in the order $A_{21} > A_{22} = A_{12} > A_{11}$ as $P_2 > P_1$. As one off-diagonal entry A_{ij} of the energy influence coefficients matrix $[A]$ is bigger than any diagonal entry A_{ii}, negative coupling loss factors result describing the non-resonant energy back flow.

Using RotR, the mode shape localized in the ceiling is directly excited and thus the energy in the ceiling is dominating for both load cases ($E_{2j} >> E_{1j}$). The energy influence coefficients have the order $A_{22} > A_{21} >> A_{11} > A_{12}$. As not all diagonal entries A_{ii} are bigger than any off-diagonal entry A_{ij}, strong coupling still occurs. Thus, coupling loss factors are bigger than the damping loss factors. The different quantities for RotR excitation are depicted in the graphs on the right of Fig. 4.10.

As the single load excites only few of the available modes directly, the combination of indirect excitation and slight vibration in the directly excited subsystem leads to non-resonant energy back flows and thus to negative coupling loss factors. For the investigated structure, this can be avoided by RotR since all modes are excited also directly. In addition, RotR provokes the more universal coupling behavior.

If the single load acts on both plates in the node of a global mode shape, the strong coupling behavior cannot be identified which is the case for the mode shape at 58 Hz in Fig. 4.9c. However, the coupling loss factors are bigger than the damping loss factors if RotR is applied, which excites the global mode shape in both plates.

Translational Parts of the Kinetic Energy

To estimate the contribution of excited and transmitted bending waves, the perpendicular translational part of the kinetic energy $\tilde{E}_{\mathrm{kin},i1}(v_z)$ (cf. Eq. (3.62)), which is based on the oscillations perpendicular to the plate, is evaluated. Moreover, $\tilde{E}_{\mathrm{kin},i1}(v_z)$ is opposed to the the total translational energy $\tilde{E}_{\mathrm{kin},i1}(v_x,v_y,v_z)$, which is based on the sum of the squared nodal velocities of all three spatial directions. Compared to the kinetic energy, the rotatory

(a) Pinned L-junction: Only bending waves

(b) L-junction: Bending and in-plane waves
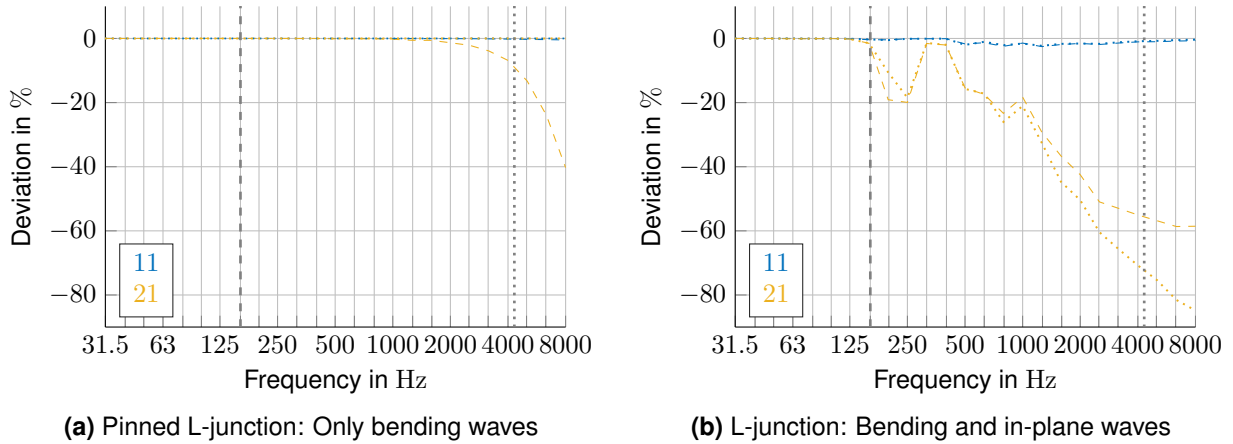
Figure 4.11: Comparison of solid $(--)$ and shell $(\cdots)$ element model: Deviation of the perpendicular part $\tilde{E}_{\mathrm{kin},i1}(v_z)$ from the total translational energy $\tilde{E}_{\mathrm{kin},i1}(v_x,v_y,v_z)$. The frequency averaged energies of both subsystems i are compared for a perpendicular excitation of subsystem 1; Five modes per band ($\vdots$); Energetic thin plate limit (:).

inertia is neglected, which becomes relevant at higher frequencies as the bending wave length decreases and thus the curvature of the plates increases.

Summing up the squared nodal velocities leads, within the scope of the numerical integration, to an error which increases with frequency. Integrating the nodal velocities by means of the element shape functions, the translational part of the kinetic energy can be computed exactly in the framework of the approximate solution of FE. As a post-processing, this involves a extensive numerical effort which was only used at particular frequencies to verify the results.

Figure 4.11a represents the pinned L-junction and Fig. 4.11b the non-pinned one, which is examined more in detail in subsection 4.2.3. Both graphs confront the solid element model with the shell element model using frequency averaged values per one-third octave band. Loading subsystem 1, energy 11 represents the energy in the excited subsystem and energy 21 the energy in the adjacent subsystem. The total translational energy and the perpendicular part of the translational energy are almost identical up to 1000 Hz for all four variants presented in Fig. 4.11.

As the L-junction is pinned, mainly bending waves are excited and transmitted also above the thin plate limit in the case of the shell element model (cf. Fig. 4.11a). The in-plane velocities v_x and v_y do not contribute to the subsystem energy - neither in the directly excited subsystem (11) nor in the indirectly excited subsystem (21). For the shell element model, the pinned junction results in an ideal, pure bending wave transmission since here $E_{\mathrm{kin}}(v_z) = E_{\mathrm{kin}}(v_x,v_y,v_z)$.

In the case of the solid element model, the nodal velocities are evaluated at the middle plane of the plates. At the surface, the in-plane velocities, which can be assumed linearly across the cross section in bending, are maximal and lead to an overestimation of the total translational energy. According to Fig. 4.11a, bending to in-plane wave transmission is admitted above 1000 Hz since in the case of the solid element model, the simple support at the junction is not able to impede any translation over the whole cross section of the adjacent plates.

In contrast, the transmission behavior of the non-pinned junction in Fig. 4.11b is completely different. As shown in Fig. 4.11b, the deviation of $E_{\text{kin}}(v_z)$ has an outlier for both solid and shell element model in the one-third octave bands of 200 Hz and 250 Hz. This behavior is confirmed by a modal analysis, which considers the factual boundary conditions, showing an in-plane mode of the ceiling at 223 Hz (cf. Fig. 4.13), whereas the analytical estimation in Fig. 4.8b firstly predicts one in-plane mode in the one-third octave band of 500 Hz. From 500 Hz on, the deviation of $E_{\text{kin}}(v_z)$ increases continously with frequency, whereby in the case of the shell element model, the portion of transmitted bending waves drops down faster above 1000 Hz.

Loss Factors   The energy influence coefficients A_{ij,v_z} and A_{ij} result from normalizing the corresponding energies $2\,E_{\text{kin},ij}(v_z)$ and E_{ij} by the input power. $2\,E_{\text{kin},ij}(v_z)$ states twice the perpendicular translational part of the kinetic energy. It is based on the sum of the squared nodal surface velocities perpendicular to the plate as the energy would be derived from the oscillations in the case of a measurement (cf. Eq. (3.62)). E_{ij} represents the total subsystem energy, which consists of the sum of kinetic and potential element energies (cf. Eq. (3.35)). For resonant oscillations, it holds $E_{\text{kin},ij} = E_{\text{pot},ij}$. Moreover, a thin plate dominated by bending waves allows the simplification $E_{\text{kin},ij} = E_{\text{kin},ij}(v_z)$. Hence, $2\,E_{\text{kin},ij}(v_z)$ accords with E_{ij} only for resonant oscillations.

To calculate the coupling loss factors, the energy influence coefficients matrix has to be inverted. This is exemplarily performed for the two subsystem case:

$$\left[\eta^0 \right] = \frac{1}{\Omega} \left[A \right]^{-1} \tag{4.5}$$

$$\begin{bmatrix} \eta_{11} + \eta_{12} & -\eta_{21} \\ -\eta_{12} & \eta_{22} + \eta_{21} \end{bmatrix} = \frac{1}{\Omega \det [A]} \begin{bmatrix} A_{22} & -A_{12} \\ -A_{21} & A_{11} \end{bmatrix} \tag{4.6}$$

$$= \frac{1}{\Omega \left(A_{11} A_{22} - A_{12} A_{21} \right)} \begin{bmatrix} A_{22} & -A_{12} \\ -A_{21} & A_{11} \end{bmatrix} \tag{4.7}$$

If weak coupling is assumed, the product of $A_{12}A_{21}$ becomes very small compared to $A_{11}A_{22}$ and is therefore neglected. Because the deviations between A_{ij,v_z} and A_{ij} are higher for the off-diagonal entries as for the main diagonal entries of the energy influence coefficients matrix, the coupling loss factors are affected less:

$$\begin{bmatrix} \eta_{11} + \eta_{12} & -\eta_{21} \\ -\eta_{12} & \eta_{22} + \eta_{21} \end{bmatrix} \approx \frac{1}{\Omega} \begin{bmatrix} \frac{1}{A_{11}} & \frac{-A_{12}}{A_{11}A_{22}} \\ \frac{-A_{21}}{A_{11}A_{22}} & \frac{1}{A_{22}} \end{bmatrix} \tag{4.8}$$

The small deviation between η_{ij,v_z} and η_{ij} can also be identified comparing the corresponding values of the vibration reduction index in Fig. 4.12a, which is discussed in the subsequent paragraph.

Vibration Reduction Index Figure 4.12 shows the direction and frequency averaged vibration reduction index based on different methods. As explained in subsection 3.2.4, the vibration reduction index can be calculated analytically by means of the transmission coefficient τ_{ij} which results from the wave approach. For the case of pure bending, the vibration reduction index based on τ_{ij} is identical for both transmission directions due to the correction by the critical frequency $f_{c,j}$ (cf. Eq. (3.57)):

$$K(\tau_{ij}) = K(\tau_{ji}) = <K(\tau_{ij})> = -10 \lg(\tau_{ij}) + 5 \lg\left(\frac{f_{c,j}}{f_{\text{ref}}}\right) \tag{4.9}$$

τ_{ij} and τ_{ji} are linked by the consistency relation (cf. Eq. (2.51)) between two SEA subsystems, which is introduced in subsection 2.3.1:

$$\eta_{ij} n_i = \eta_{ji} n_j \tag{4.10}$$

The modal density of a bending wave subsystem is expressed by physical properties inserting Eq. (2.60) and (2.64). Equation (3.59) contributes the relation between τ_{ij} and η_{ij}:

$$\frac{\tau_{ij} l_{ij}}{2\pi^2 c_{B,i}} \frac{f A_i c_{g,i}}{f A_i c_{g,i}} = \frac{\tau_{ji} l_{ij}}{2\pi^2 c_{B,j}} \frac{f A_j c_{g,j}}{f A_j c_{g,j}} \tag{4.11}$$

The dependency on the direction is linked to elastic modulus, thickness and density of both plates. Solving for τ_{ij}, this can be expressed by the ratio of the bending wave velocities or of the critical frequencies:

$$\tau_{ij} = \tau_{ji} \frac{c_{B,j}}{c_{B,i}} = \tau_{ji} \sqrt{\frac{f_{c,i}}{f_{c,j}}} \tag{4.12}$$

The calculation based on τ_{ij} is opposed to the direction averaged vibration reduction index computed by means of the EFA. In doing so, either the coupling loss factor η_{ij}, which is based on the total energy, or η_{ij,v_z}, which is estimated by the perpendicular translational part of the kinetic energy, is inserted into Eq. (3.61). According to Fig. 4.12, the two curves are almost identical above the frequency limit of five modes per one-third octave band and below the energetic thin plate limit of $\frac{f_s}{4} = 4318\,\mathrm{Hz}$. In this range, kinetic and potential energy nearly coincide and the plates can considered to be thin. Due to the perpendicular excitation of the thin plate, mainly bending waves are excited and due to the pinned junction mainly bending waves are transmitted. Since τ_{ij} considers only bending to bending transmission, this leads to a acceptable accordance between the EFA and the analytical calculation in the frequency range where the SEA requirements and the thin plate theory are fulfilled. Here, also the vibration reduction indices based on the EFA are almost identical for the two different directions using the single load. For RotR, deviations up to $4\,\mathrm{dB}$ occur between the different transmission directions since the loading is not symmetric. The direction dependent vibration reduction indices are not depicted.

The simplified option of the vibration reduction index $K(D_{v,ij})$ bases upon the velocity level difference $D_{v,ij}$ (cf. Eq. (3.53)). Analogously to the calculation by η_{ij,v_z}, only the surface velocity perpendicular to the plate is used. Both calculations are identical if the system consists of only two subsystems and the total loss factor in Eq. (3.52) is taken from the EFA. The neglect of in-plane energy contributions and of possibly further adjacent subsystems constitute key assumptions for the simplified computation of the vibration reduction index by means of $D_{v,ij}$ according to DIN EN ISO 12354-1 [2017] based on the approach of Gerretsen [1979].

The idea of the vibration reduction index reaches its limits: An evaluation for negative coupling loss factors, where the power flow is only marginally determined by the adjacent components (cf. subsection 3.2.3), contradicts the basic assumptions of the vibration reduction index. Moreover, the vibration reduction index cannot be evaluated at frequencies, where the coupling loss factors are negative, since it is a logarithmic measure. Including these frequencies in terms of one-third octave band averages leads to physically wrong results. For the single load, the vibration reduction index must not be interpreted in the one-third octave band of 40, 50 and 80 Hz according to Fig. 4.10. The single load in the center of the plate draws a worst case scenario since very few modes are excited.

According to Fig. 4.10 and 4.12a, the RotR excitation takes effect already at low frequencies as the vibration reduction index can be evaluated through the entire frequency range having only small oscillations. At higher frequencies, the vibration reduction index tends to be
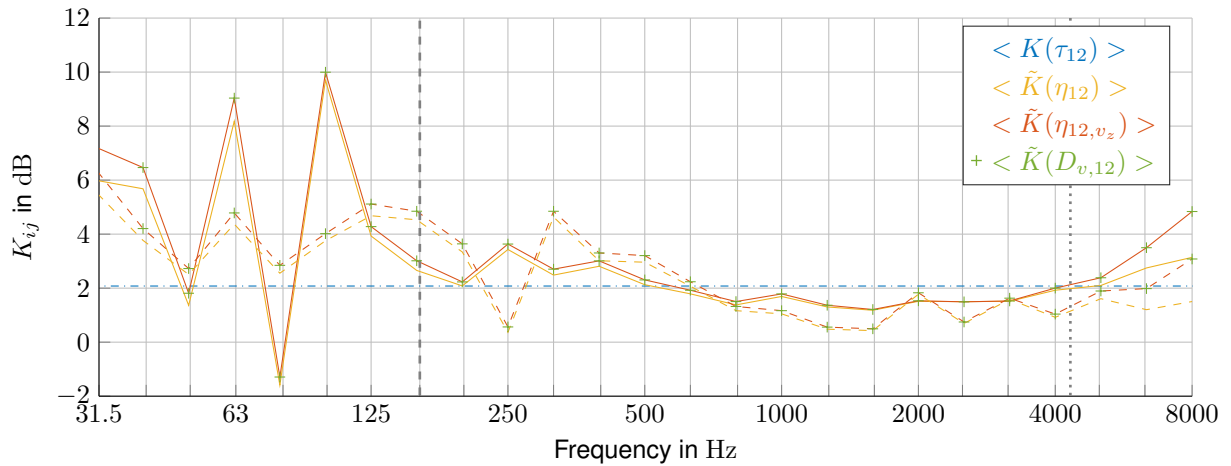
(a) Solid element model
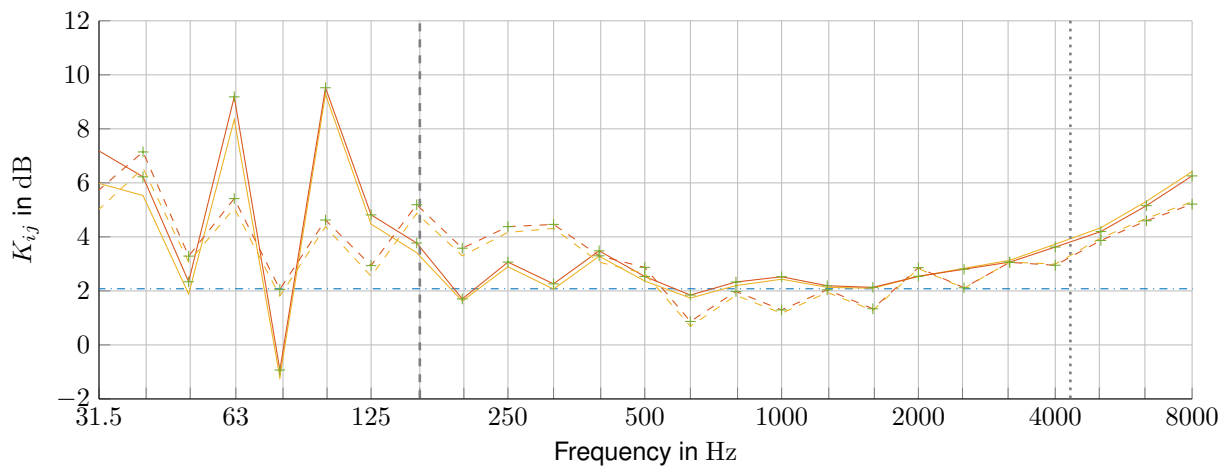
(b) Shell element model

Figure 4.12: Pinned L-junction: Direction and frequency averaged vibration reduction index $< \tilde{K}_{12} >$ for single load $(-)$ and RotR excitation $(--)$ compared to the wave approach $(-\cdot-)$; Five modes per band $(\dashv)$; Energetic thin plate limit $(:)$.

slightly smaller compared to the one for the single load as more modes are excited which contribute to an increased energy exchange between the two subsystems.

By contrast with the solid element model in Fig. 4.12a, the shell element model in Fig. 4.12b shows a slightly better agreement with the analytical solution. This is not astonishing since both are based on the Mindlin plate theory. As discussed above, in the shell element model any displacement of the junction is impeded which conincides with the boundary conditions of the chosen analytical solution to only transmit bending waves.

(a) Vector sum of displacements

(b) Lateral view
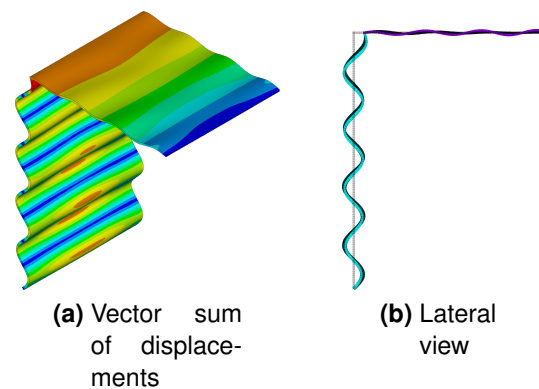
Figure 4.13: Mode shape at $223\,\mathrm{Hz}$ of the non-pinned L-junction consisting of isotropic, thin plates.

4.2.3 Thin, Isotropic Plates: Bending and In-plane Waves

The two models of the L-junction (cf. Tab. 4.6) examined in this subsection and in the previous subsection 4.2.2 differ in an optional simple support at the junction between wall and ceiling. Without the simple support, the junction is able to perform translational movements additionally to the rotational ones. This opens up the possibility to transmit in-plane waves as shown in the foregoing subsection 4.2.2 by means of the in-plane and out-of-plane components of the translational energy.

Modal Behavior Figure 4.13 visualizes exemplarily the behavior of the non-pinned L-junction. The mode shape consists of bending waves in the wall and longitudinal in-plane waves in the ceiling since the junction is able to displace. The colors in Fig. 4.13a illustrate the vector sum of the displacements and indicate that the in-plane displacement of the ceiling decreases from the junction towards the simply supported end. Figure 4.13b shows clearly the horizontal displacement of the junction compared to the undeformed structure in the background.

Vibration Reduction Index As the junction is free to rotate and to undergo displacements, the analytical wave approach also accounts for in-plane waves. For each plate-like component, it considers subsystems for shear and for quasi-longitudinal waves beside the bending wave subsystem. Thus, the number of transmissions paths and transmission coefficients increases. Whereas the wave approach for only bending waves yields transmission coefficients that are independent of frequency (cf. $K(\tau_{12})$ in Fig. 4.12), the wave approach for bending and in-plane waves gives transmission coefficients that vary with frequency (cf. Fig. 4.14). To

(a) Solid element model

(b) Shell element model
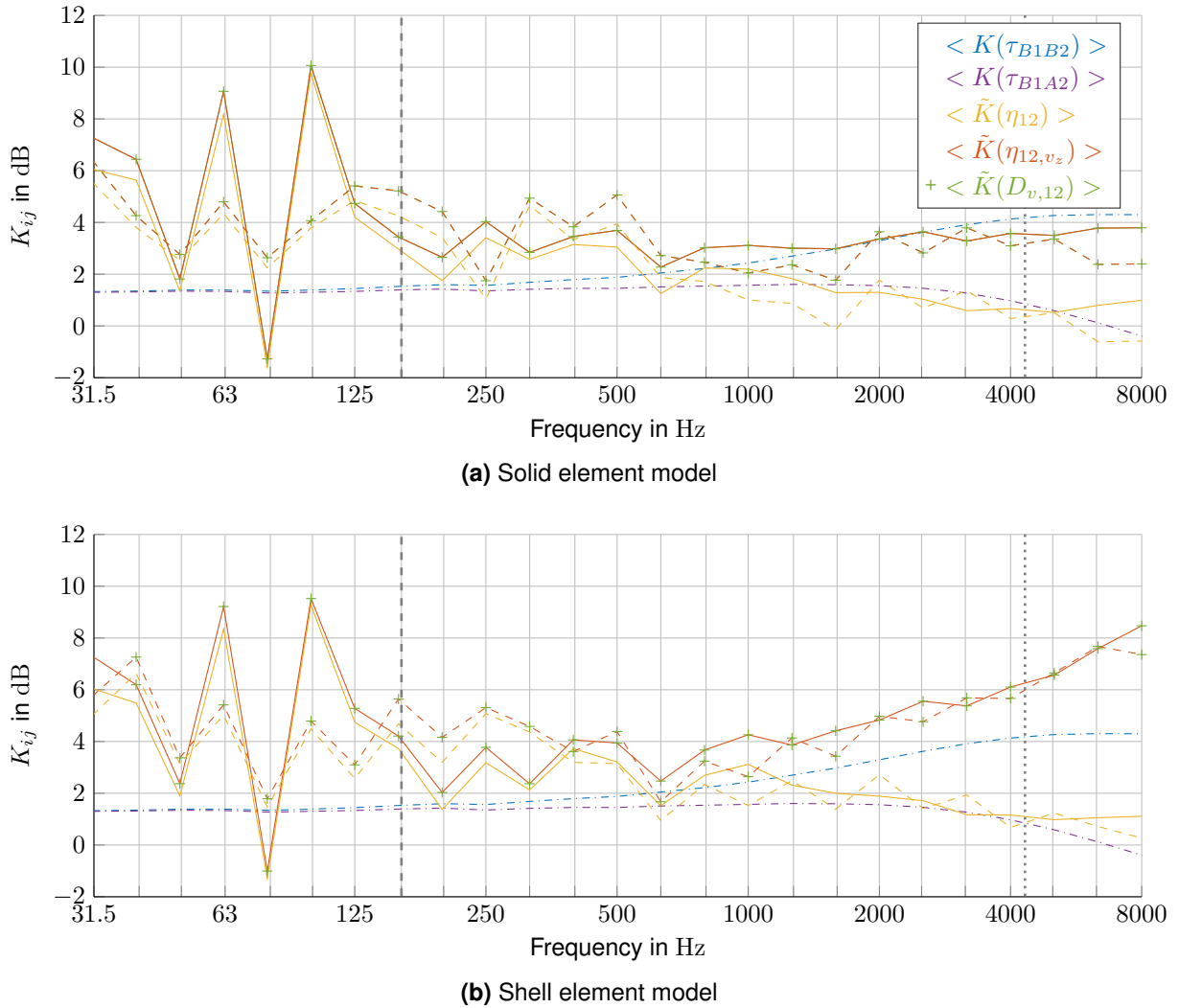
Figure 4.14: L-junction: Direction and frequency averaged vibration reduction index $< \tilde{K}_{12} >$ for single load $(-)$ and RotR excitation $(--)$ compared to the wave approach $(- \cdot -)$; Five modes per band $(\vdots)$; Energetic thin plate limit $(:)$.

distinguish the transmission between bending, shear, longitudinal and the sum of all three wave fields, the corresponding initials are used in the index of τ.

Firstly, the vibration reduction index is calculated on the basis of τ_{B1B2} which corresponds to the approach of DIN EN ISO 12354-1 [2017]. As $K(\tau_{B1B2})$ considers only the transmission between the two bending wave subsystems, the analytical solution is compared to $K(\eta_{12,v_z})$ from the EFA. $K(\eta_{12,v_z})$ uses only the surface velocities perpendicular to the plate to estimate the bending wave energy and is identical to $K(D_{v,12})$ for the two subsystem case as η_j^0 in Eq. (3.63) is taken from the EFA. Figure 4.14a shows a good agreement of the qualitative behavior for both single load and RotR with the analytical solution from 630 Hz on.

Secondly, the vibration reduction index $K(\eta_{ij})$ shall consider the entire transmission across

the junction. Thereby, also in-plane waves in the excited subsystem which lead to bending waves in the non-excited, radiating subsystem are considered. Therefore, the coupling loss factors from the EFA are used which take into account the total subsystem energy and thus all wave types. Dividing the coupling loss factor by the group velocity of the effective bending waves, $c_{g,\text{eff}}$, according to Eq. (3.61) leads to an inconsistent vibration reduction index as the longitudinal waves propagate faster (cf. Fig. 4.8a). Hence, the concept of the vibration reduction index reaches its limits. For the analytical calculation, the transmission coefficients are used which give a consistent solution for the vibration reduction index. Assuming an excitation of the bending wave subsystem in the source plate, the transmission into all three subsystems of the receiver plate is summed up:

$$\tau_{B1A2} = \tau_{B1B2} + \tau_{B1S2} + \tau_{B1L2} \tag{4.13}$$

Above 630 Hz, the corresponding vibration reduction index $K(\tau_{B1A2})$ coincides qualitatively with $K(\eta_{ij})$ for a perpendicular excitation. Thereby, the contribution of the in-plane waves leads to a clearly smaller vibration reduction index.

In the one-third octave band of 630 Hz, the first in-plane mode and a total of 20 modes arise. Moreover, the modal overlap factor is greater than two according to the analytical estimation.

Below 630 Hz, the analytical solution seems to give just a lower limit for the vibration reduction index. Wilhelm [2017] confirms the results of this comparison at an L-junction with two identical plates having the same properties as the current ceiling. Due to the symmetric structure, which has double eigenvalues, strong coupling is fortified and thus almost no results are obtained for the vibration reduction index below the SEA limit of five modes per band at 160 Hz. Above, the analytical solution is approximated from below showing accordance above 800 Hz.

Figure 4.14b shows the vibration reduction index based on a shell element model compared to the analytical solution. Especially above 630 Hz, the shell element model leads to increased vibration reduction indices. This means, less energy is transmitted across the junction. Looking at the bending wave transmission, the shell element model leads to a clearly higher vibration reduction index compared to the analytical solution. At the energetic thin plate limit, the difference is about 2 dB.

Comparing the FE models with the analytical solution in Fig. 4.14, the shell element model leads to a vibration reduction index, which is higher or equal compared to the analytical

solution, whereas the solid element model leads to values which are equal or smaller for high frequencies.

4.2.4 Thick, Orthotropic Plates

Choosing thicknesses which are within a realistic range for CLT plates, the thin plate theory is only valid to model the energy flow at low frequencies. The limiting frequency equals $\frac{f_s}{4} = 60$ and $155\,\text{Hz}$ for the subsystems 2 and 1, respectively. Their geometric dimensions and their orthotropic material properties are given in Tab. 4.3. The thick plate theory and thus, the shell element model are limited to the first thickness-shear resonance of the thickest component. At $1445\,\text{Hz}$, the first thickness-shear mode of the ceiling might be excited which can only identified by means of solid elements. Since the wall is half as thick as the ceiling, the first thickness-shear resonance of the wall is located at $2289\,\text{Hz}$ and is therefore not decisive for the element choice. The influence of the thickness modes is shown in detail in subsection 4.3.1.

Modal Behavior, Energy Influence Coefficients and Loss Factors   RotR with 100 randomly distributed single loads is chosen. The perpendicular load mainly excites bending waves. Therefore, the main diagonal entries A_{22} and A_{22,v_z} in Fig. 4.16a differ only slightly below the first thickness resonances. Above, the subsystem energies and thus the energy influence coefficients are clearly overestimated on the basis of v_z, which is the surface velocity perpendicular to the plate, because at the surface the thickness-stretch resonances have their maximum displacements as sketched in Fig. 2.11. Hence, also the resulting coupling and damping loss factors should not be interpreted above the first thickness-shear resonance: According to Fig. 4.16c, the damping loss factor of the ceiling η_{22,v_z} is significantly underestimated compared to η_{22} above of the first thickness-shear resonance ($1445\,\text{Hz}$). In this high range, the first thickness-stretch resonance ($3267\,\text{Hz}$) occurs. Figure 4.15d represents a coupled mode shape which is dominated by thickness-shear and thickness-stretch oscillations.

Already at low frequencies, the curves of A_{12} are separated from A_{12,v_z} according to Fig. 4.16a. This indicates in-plane wave transmission as the junction is not pinned (cf. Fig. 4.15b) and the increasing relevance of the rotatory inertia since the plate is subject to the thick plate theory. Thereby, the shear deformation allows an additional rotation of the cross section as depicted in Fig. 4.15c for the mode shape at $448\,\text{Hz}$. In contrast, Fig. 4.15a shows the first mode shape at $26\,\text{Hz}$ fulfilling the thin plate assumption since the cross section remains

(a) Pure bending at $26\,\mathrm{Hz}$

(b) Bending (wall) and longitudinal (ceiling) at $201\,\mathrm{Hz}$

(c) Bending and shear at $448\,\mathrm{Hz}$

(d) Thickness-shear and thickness-stretch at $2199\,\mathrm{Hz}$
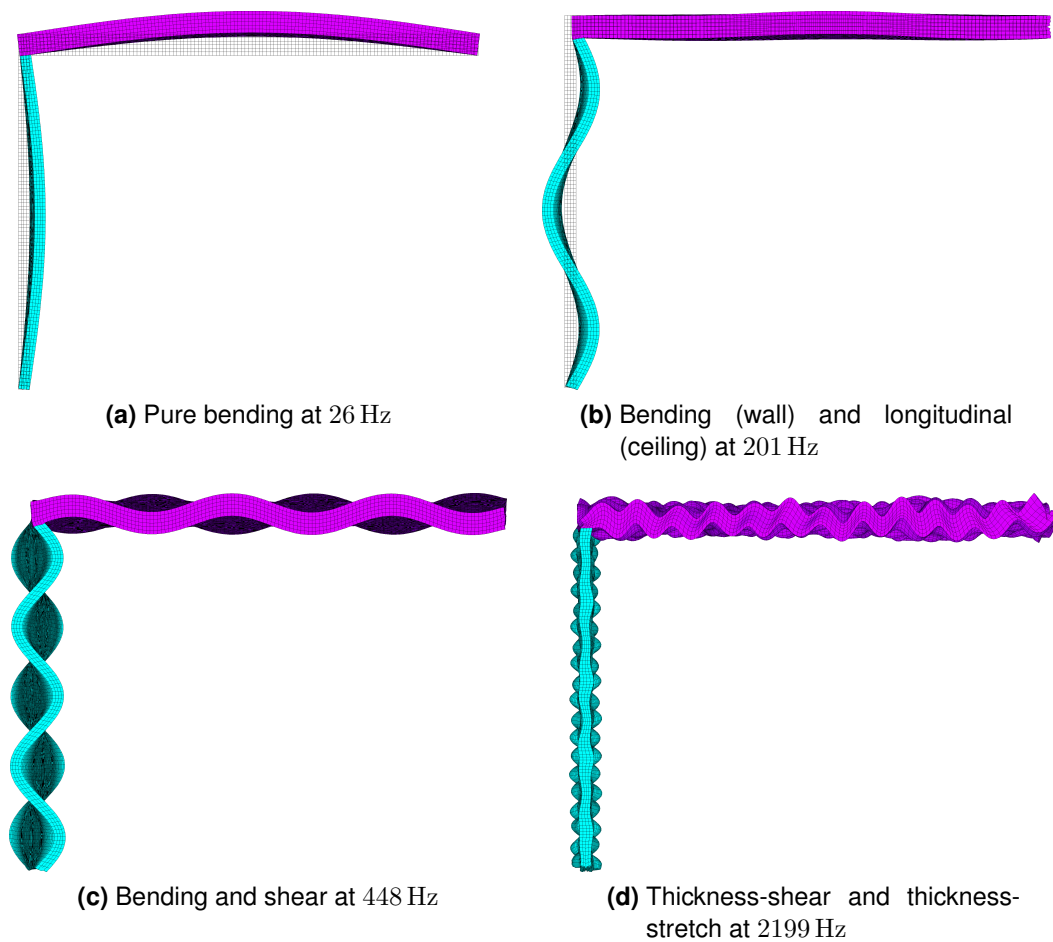
Figure 4.15: Lateral view: Mode shapes of the L-junction consisting of orthotropic plates.

perpendicular to the middle plane. Thus, it holds $A_{12} = A_{12,v_z}$ and only bending waves are transmitted.

Strong coupling   Below $125\,\mathrm{Hz}$, the off-diagonal entry A_{12} is crossing the main diagonal entry A_{22} at several frequencies which indicates strong coupling. Between 100 and $125\,\mathrm{Hz}$, global bending modes occur, which lead to almost identical values of A_{ij} and A_{ij,v_z}. High values of the condition number arise together with high coupling loss factors according to Fig. 4.16b and 4.16c. In the one-third octave band of $31.5\,\mathrm{Hz}$, negative coupling loss factors show up as modes which are localized in one subsystem are excited more easily by a load in the other one. Thus, one off-diagonal entry is larger than all other entries of the energy influence coefficients matrix. Strong coupling is introduced in subsection 3.2.3 and explained more in detail at an example in subsection 4.2.2. Due to negative values, the frequency averaged coupling loss factors contain physically wrong results in the one-third octave band of $31.5\,\mathrm{Hz}$. These negative values indicate that the coupling loss factors do not fulfill the

requirements of a proper-SEA matrix. Therefore, also derived quantities like the vibration reduction index reach its limits.

Vibration Reduction Index $K(\eta_{ij,v_z})$ and the approximation $K(D_{v,ij})$ are identical because the structure consists of two subsystems and for $K(D_{v,ij})$, η_j^0 is taken from the EFA (cf. Eq. (3.63)). $K(\eta_{ij})$ starts to differ from $K(\eta_{ij,v_z})$ at low frequencies as A_{ij} deviates from A_{ij,v_z} due to the contribution of in-plane waves and rotary inertia. As long as $K(\eta_{ij})$ and $K(\eta_{ij,v_z})$ are identical, the transmission behavior can be described by means of the vibration reduction index. Above this frequency range, the calculation based on η_{ij} considering all wave types and $c_{g,\text{eff}}$ representing only bending waves is inconsistent. As also analytically shown in subsection 4.2.3, the contribution of the in-plane waves leads to a clearly smaller vibration reduction index. This effect, which is neglected by the approach of Gerretsen [1979], is also demonstrated by Hopkins [2007, 2014] and Hopkins et al [2016] for heavy weight masonry constructions.

The formulas in DIN EN ISO 12354-1 [2017] are based on c_g, whereas $c_{g,\text{eff}}$, which is used within this thesis, opens up the possibility that $K(\eta_{ij,v_z})$ represents the bending wave transmission between two subsystems also at higher frequencies. Above the first thickness resonance, the surface velocity perpendicular to the plate overestimates the perpendicular translational energy and thereby the transmission behavior. Thus, $K(\eta_{ij,v_z})$ is decreasing above 1000 Hz. Using $K(\eta_{ij,v_z})$, e.g. in-plane waves in the excited subsystem leading to bending waves in the non-excited, radiating subsystem are not considered.

The limitations of the vibration reduction index depend on the way it is computed. As shown within this section, there are different options proposed by the DIN EN ISO 12354-1 [2017]. Their validity can be augmented in the frequency range using the effective group velocity of bending waves. Only in the case of pure bending wave transmission and fulfilling the SEA criteria, the vibration reduction index characterizes the energy transfer comprehensively. This is the case as long as $< \tilde{K}(\eta_{ij}) >$ and $< \tilde{K}(\eta_{ij,v_z}) >$ are identical.
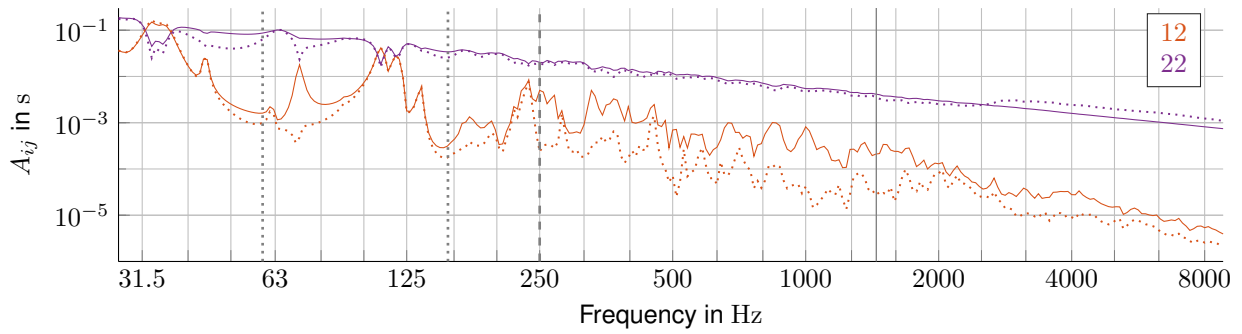
(a) Energy influence coefficients for the excitation of subsystem 2
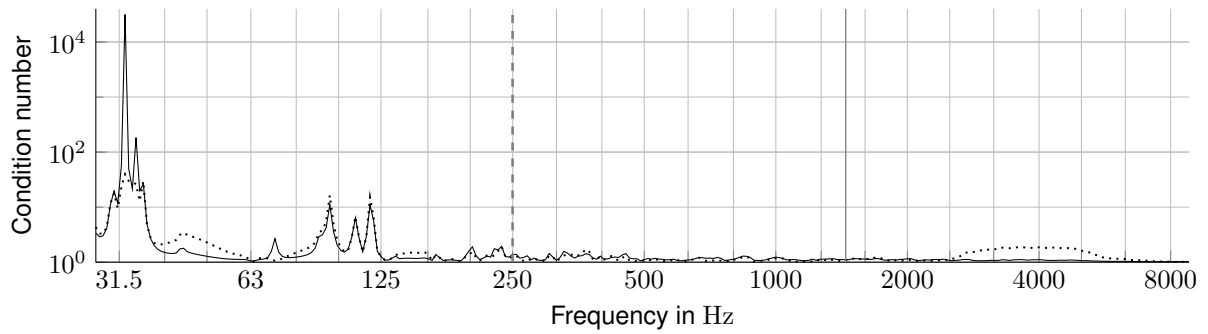
(b) Condition number of the energy influence coefficients matrix $[A]$
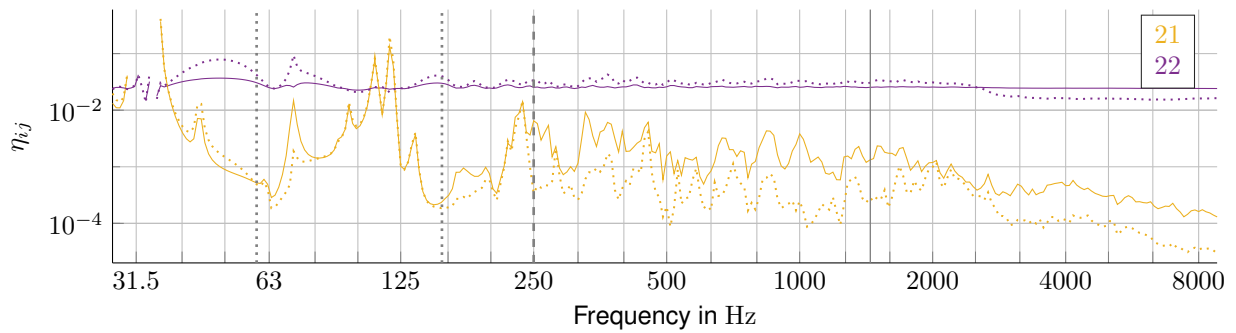
(c) Damping and coupling loss factors η_{2i} quantifying the losses of subsystem 2
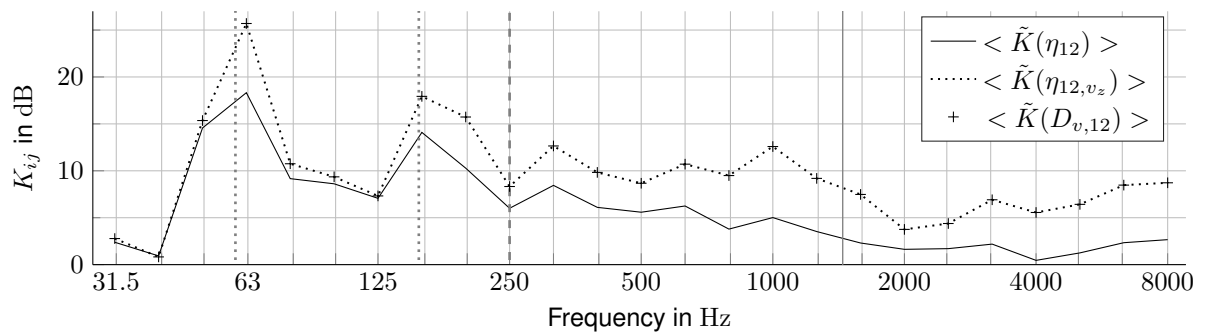
(d) Direction and frequency averaged vibration reduction index $< \tilde{K}_{12} >$ based on EFA

Figure 4.16: L-junction out of orthotropic, thick plates excited by RotR; EFA based on total energy E_{ij} $(-)$ or on perpendicular translatoric part $2\,E_{\mathrm{kin},ij}(v_z)$ $(\cdots)$; Energetic thin plate limit of subsystem 2 and 1 (:); Five modes per band ($\vdots$); First thickness-shear mode of subsystem 2 ($|$).

4.3 Variation of Geometry and Excitation

Geometry and point of excitation will be varied in the subsequent subsections to investigate the corresponding sensitivity of the energy flow.

Subsection 4.3.1 investigates the influence of the thickness modes by varying the excitation across the thickness. Comparing the energy flow with and without the excitation of thickness modes, their effect on the structure-borne sound transmission especially at high frequencies is shown. In the subsections 4.3.2 and 4.3.3, the frequency range is split by means of the number of modes, the modal overlap factor and the first thickness resonance. Each range is characterized differently by the impact of the width, the length and the point of excitation on the energy flow and on the input power.

Beside the location of the excitation across the thickness and across the plane of a plate, the direction plays an important role. In subsection 4.3.4, the results caused by a RotR excitation of 100 in-plane loads are compared to the results due to an out-of-plane excitation at the same 100 locations. The effect of the random phase of RotR is examined in subsection 4.3.5 performing a comparison with a phase-conform excitation at these 100 locations.

4.3.1 Thickness Modes in Orthotropic Plates

To identify and separate the effects of the thickness modes harmonic analyses with different load cases are investigated. All load cases are shown in Fig. 4.17. They have in common that the load acts in the center of the plate on the area of one element. First the plates are excited with a distributed pressure across the thickness to have a generalized load equal to zero for the simple thickness modes. Then, the pressure acts on the surface of the plate which corresponds to a more realistic scenario. If the pressure is applied in the middle plane of the plate the generalized load of the first thickness resonances is zero (cf. Fig. 2.11). As a start, a single, two-sided simply supported plate is examined followed by an L-junction consisting of a wall and a ceiling. For comparability, the wall has here the same material properties as given for the ceiling and single plate in Tab. 4.2. This leads to identical through-thickness resonances for the initial dimensions which are depicted in Tab. 4.3.
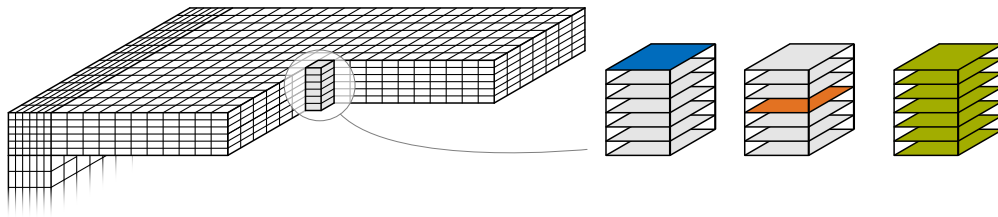
Figure 4.17: Variation of the load distribution through the thickness to excite or ignore thickness modes.

Numerical Investigation of a Single Plate

Fig. 4.18a shows a significant jump of the energy due the surface load at high frequencies. The curve reaches a plateau close by the first thickness-stretch mode at 3269 Hz. For the middle plane load the big jump moves towards the second thickness resonances as it acts in the node of the first eigenmodes. The distributed load across the thickness of a plate seems to be a rather non-realistic load case. However, as shown in Fig. 4.18b the response behavior is almost identical even for high frequencies performing a harmonic analysis of a plate modeled by shell elements.

Comparing the energies in Fig. 4.18a the surface load even leads at low frequencies to a small non-resonant contribution of potential energy E_{pot}, because the excitation occurs in the stiffness controlled region of the thickness modes. Figure 4.19 shows that the input power P perceives the same increase as E_{pot} in between resonance frequencies due to the stiffness proportional damping as explained in subsection 2.1.4. Hence, below the thickness resonances the mechanical behavior can be visualized by an additional complex, energy dissipating spring where the surface or middle plane load is acting on. In the mid-frequency range, the increased modal overlap of the thickness resonances leads to a negative plateau of the deviation of A_{11} due to the surface or middle plane load, either compared to the shell element model in Fig. 4.18b or compared to the distributed load in Fig. 4.19. Comparing surface and middle plane load, Fig. 4.18b shows that the closer the non-resonant excited thickness mode is to the observed frequency, the higher is its modal contribution and therefore the additional energy dissipation. If the plate is excited at resonance, it occurs a steady energy exchange between kinetic and potential energy. So averaged over one period, both energy types are of the same size yielding $A_{11} = \frac{2\,E_{\mathrm{pot},11}}{P_1}$. Due to the stiffness proportional damping (cf. Eq. (2.25)) almost no deviation with respect to the shell element model occurs for clearly separated eigenmodes in Fig. 4.18b. These very small differences of max. 2.5 % result from slightly mismatching eigenfrequencies comparing the solid and the shell element model. This
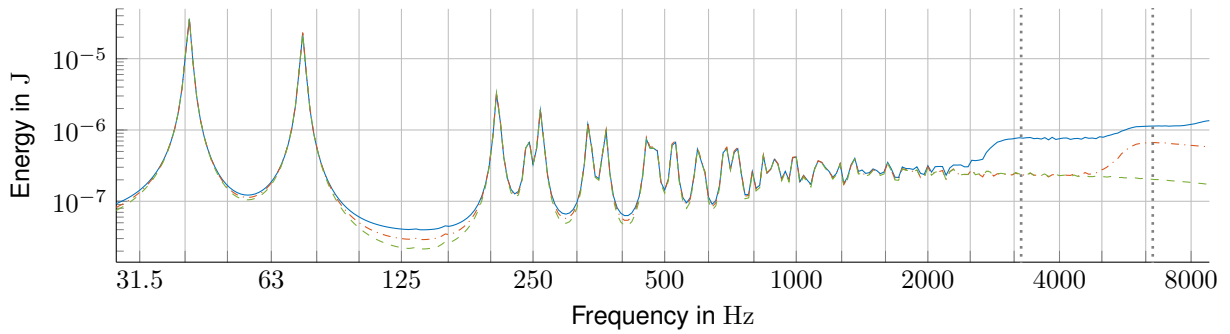
(a) Time averaged total energy of the plate
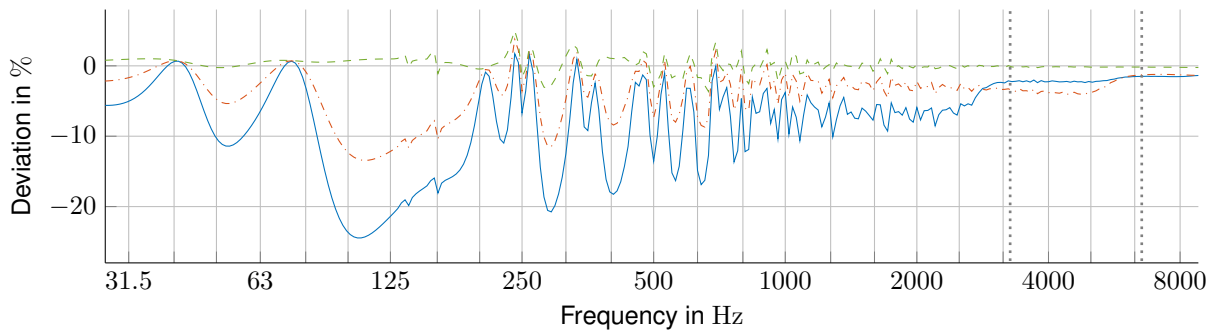
(b) Deviation of the energy influence coefficients A_{11} with respect to the shell element model

Figure 4.18: Plate out of solid elements excited at different locations: On the Surface $(-)$, in the middle plane $(- \cdot -)$ and distributed through the thickness $(--)$; Thickness-stretch resonances $(:)$
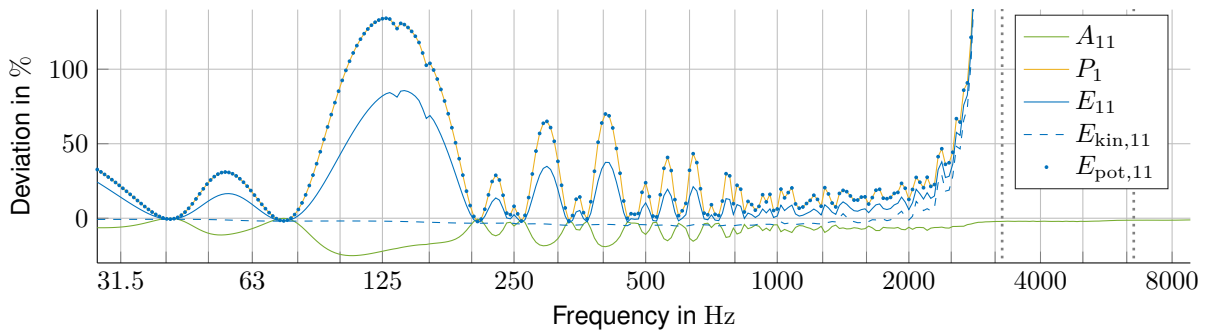
Figure 4.19: Deviation between surface and distributed load; Thickness-stretch resonances $(:)$

confirms Fig. 4.19 showing the deviation of surface and distributed load applied at the same solid element model.

Numerical Investigation of an L-junction

The L-junction, whose geometry is sketched in Fig. 4.1b, is simply supported at the bottom of the wall (subsystem 1) and at the edge of the ceiling (subsystem 2) opposite the connection. First an energy flow analysis is performed for both load cases mentioned above: the surface

(a) Variation of geometry: $+$ initial (symmetric L), $\Diamond$ $b/3$, $\bigcirc$ $(1.3\,l_2)$, $\square$ $h_1/2$

(b) Variation of junction: $-$ initial (rigid), $--$ plus damped, elastic interlayer
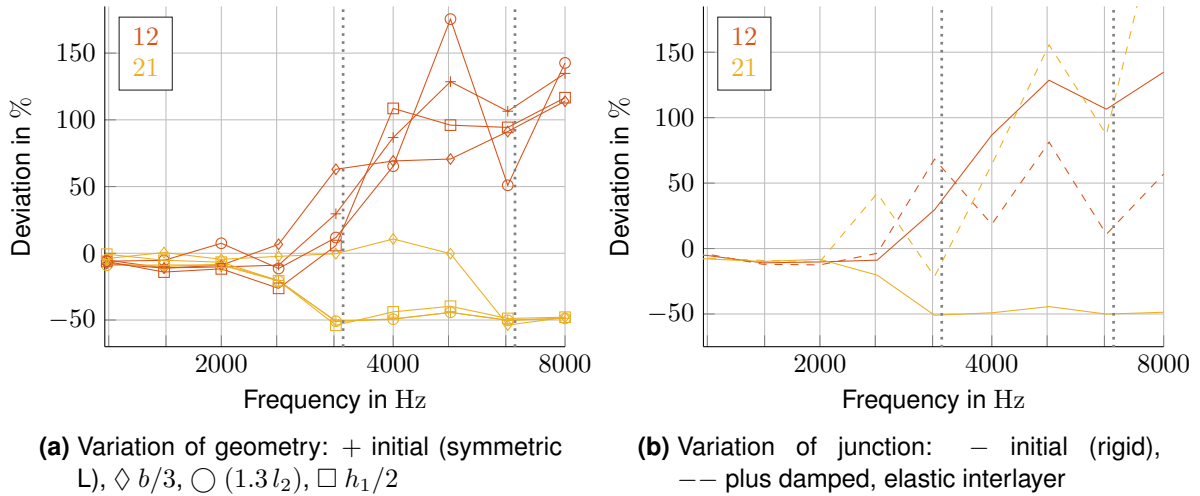
Figure 4.20: Deviation of $\tilde{A}_{ij}$ between surface and distributed load for different setups; Initial model: Rigidly connected, geometrically symmetric L-junction; Thickness-stretch resonances ($:$).

load and the distributed load. The first one leads to an – at high frequencies significant – increase of energy. This growth also holds for the energy in the adjacent plate. Hence, the subsystem energy generally depends on the location across the thickness where the total force of $1\,\mathrm{N}$ is applied to the plate.

Another question is how the additional energy is spread over the different subsystems. Therefore, the energies in the excited plate and in the adjacent one are normalized with respect to the input power which results in the energy influence coefficients A_{ij}. By varying geometry, material and the junction extensive studies have been performed. As a result, the deviation of A_{ij} between surface and distributed load is mainly reliant on the thickness of the excited subsystem j. This indicate Eq. (2.44) and Fig. 4.20a which are interpreted in the subsequent paragraphs: For instance, halving the thickness of the wall doubles the frequency of its first thickness resonances (e.g. $f_{TM,1}(c_{L,z}) = 6538\,\mathrm{Hz}$). Thus, the onset of the deviation of A_{21} between the two loadings moves also to the doubled frequency compared to the initial geometry, which consists of a geometrically symmetric L-junction. In contrast, changing the length of the ceiling leads to an identical deviation for A_{21} and a similar one for A_{12}. Also reducing the width of the whole L-junction from 3 to $1\,\mathrm{m}$ leads to similar deviations.

Whereas the surface load leads always to an increase of the energy E_{ij} also in the adjacent subsystem, the sign of the deviation of A_{ij} principally depends on the type of the junction of the two subsystems. It plays a role which degrees of freedom of each plate are coupled, its stiffness in direction of the load and if there is an elastic layer in between. As depicted in Fig. 4.1b, the edge of the wall is connected to the bottom face of the ceiling which leads to a dominant energy transfer path from wall to ceiling at high frequencies. For the distributed
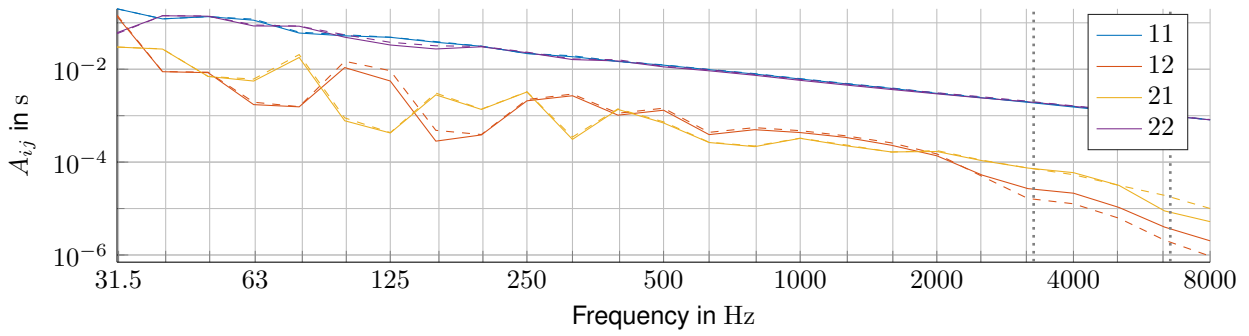
Figure 4.21: Rigidly connected L-junction with $h_1 = 0.5\,h_2$: $\tilde{A}_{ij}$ of surface $(-)$ and distributed load $(--)$; Thickness-stretch resonances $(:)$

load on the wall the coupled nodes at the bottom face of the ceiling are excited in phase, whereas by choosing the surface load just an additional (anti-)symmetric vibration pattern is superposed. This contains almost no effective displacement and leads only to a small increase of the energy E_{21} ending up in a negative deviation of A_{21} as depicted in Fig. 4.20a. The energy flow A_{21} (from wall to ceiling) related to a unit input power is halved using the surface load above the first thickness-stretch resonance of the wall. In contrast, the energy transfer from the ceiling to the wall A_{12} is comparatively low at high frequencies for the distributed load. The surface load is responsible for higher displacements of the faces of the ceiling and leads to a big increase of the transferred energy E_{12}. Hence, A_{12} is doubled above the first thickness-stretch resonance of the ceiling.

Figure 4.21 shows the absolute values of the energy influence coefficients for both, surface and distributed load. Thereby the increase of A_{12} and the decrease of A_{21} close to the first simple thickness-stretch resonance of the excited subsystem 2 respectively 1 can be identified. The main diagonal entries are not depicted because they are not affected.

A damped, elastic interlayer with the frequency dependent properties given in Tab. 4.4 and A.2 is modeled by inserting a thin layer of solid elements between wall and ceiling. This reduces the energy flow across the junction as shown in subsection 4.4.1. Moreover, it can be shown that the distribution of the additional energy due to the surface load strongly depends on the properties of the junction. In this case, Fig. 4.20b illustrates a change of sign for the deviation of A_{21}. To sum it up, by decoupling the two components significantly less energy flows across the junction. Here, using a surface load instead of a distributed load leads to an increase in both directions.

Thickness Modes - Conclusion

The resonance frequencies of thickness modes depend on the thickness of the plate, on the density and on the stiffness $E_{S,z}$ or the shear modulus G_{zi}, respectively. CLT has a comparatively low stiffness perpendicular to the plate and therefore the thickness resonances might occur inside the relevant frequency range for building acoustics - i.e. below 5 kHz. The thickness-stretch resonances lead to dips in the sound reduction of a plate. Moreover, the energy flow across junctions of orthotropic plates changes if thickness resonances are taken into account. Hence, they influence airborne as well as structure-borne sound transmission especially in the high frequency range. An adequate amount of layers of solid elements can build up physical behavior of a plate correctly which already results at low frequencies in slight changes of the energy due to the consideration of non-resonant contribution of the thickness modes. Whereas a model out of shell elements based on the Mindlin wave approximation does not consider effects related to the thickness direction of a plate. [Winter et al 2017b]

4.3.2 Variation of System Width

The width of an L-junction has been varied from 2 over 3 up to 4 m. A complete description of geometry and material parameters shows Tab 4.3. The two orthotropic plates are excited in the center by a single, perpendicular load. The influence of the width depends on the frequency which can be divided into three ranges. In the first range, the dynamic behavior is dominated by well-separated modes whereby the width has an effect on a big part of their resonance frequencies. With increasing number of modes and a higher modal overlap, the influence of the width becomes already less decisive for the modal behavior. For the compared structures, the second range starts at 630 Hz where the smallest subsystem also has ten modes per one-third octave band and its modal overlap factor is above one (cf. Fig. 4.22b). The third range starts at the first thickness-stretch resonance of the affected subsystem: This applies to the excited subsystem in the case of the input power (cf. Fig. 4.22a), whereas in the case of the energy influence coefficients, it is related to the observed subsystem (cf. Fig. 4.22c). In this high frequency range, the dynamic behavior is dominated by thickness modes which are independent of the width of the structure.

Table 4.7 sums up the influence of the width on the frequency averaged input power and on the frequency averaged energy influence coefficients for these three ranges. According to Fig. 4.22a, the impact of the width on the input power is decreasing with increasing
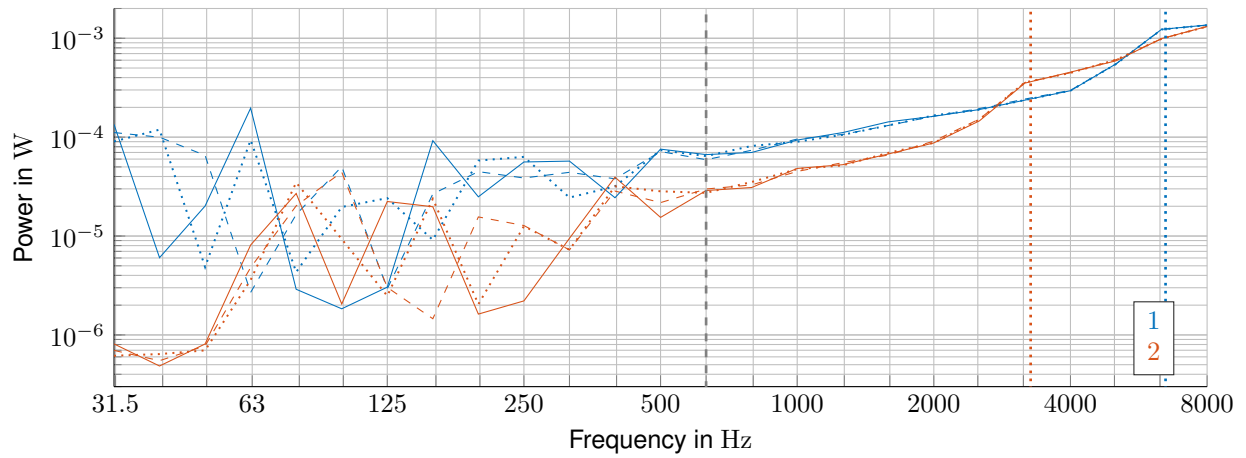
(a) Frequency averaged input power into subsystem 1 and 2
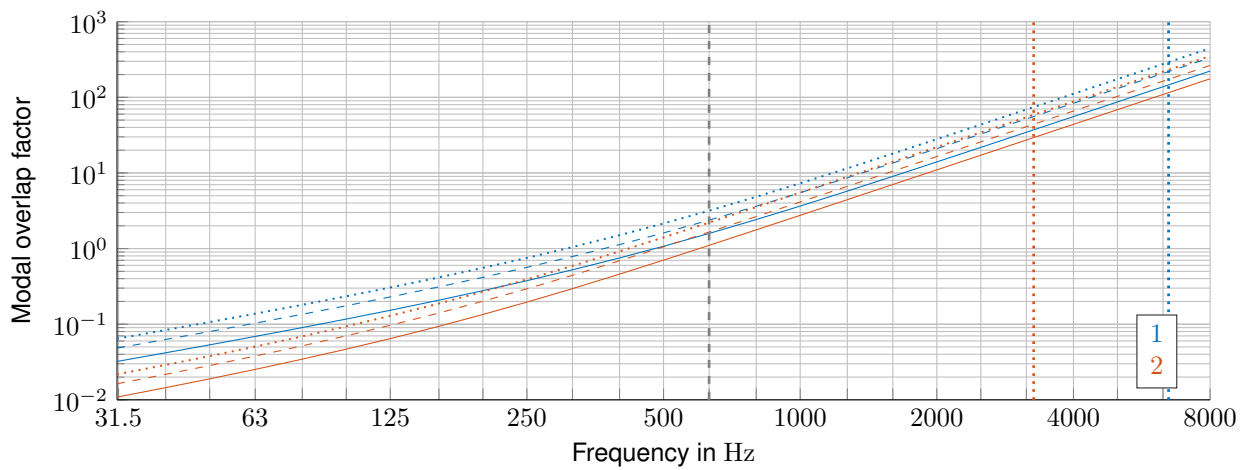
(b) Modal overlap factor of subsystem 1 and 2
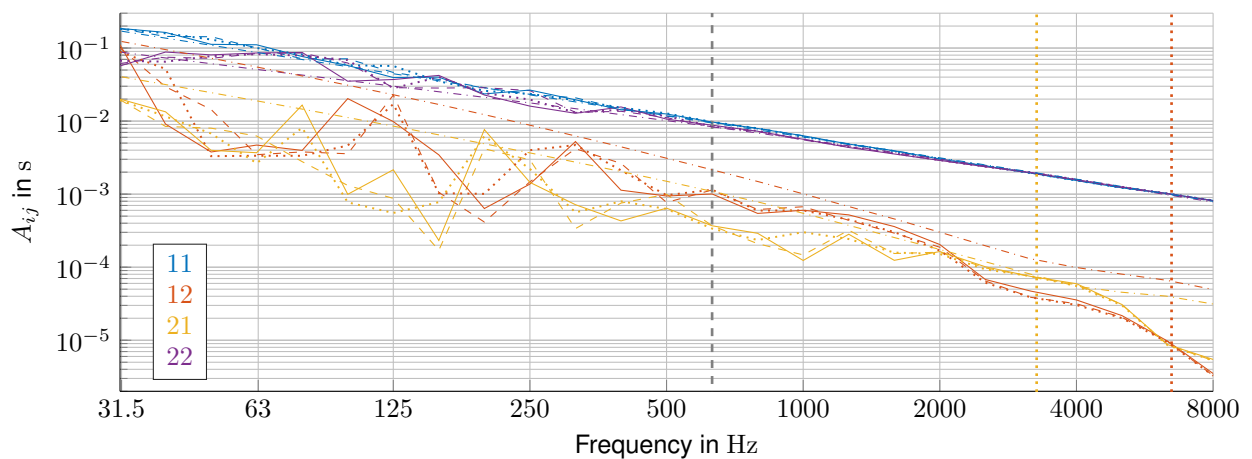
(c) Frequency averaged energy influence coefficients compared to the SEA $(-\cdot-)$

Figure 4.22: Comparison of L-junctions with different widths: $2\,\mathrm{m}\,(-)$, $3\,\mathrm{m}\,(--)$ and $4\,\mathrm{m}\,(\cdots)$; $N \geq 10$ and $M \geq 1$ for each subsystem $(\vdots)$; First thickness-stretch resonance of subsystem 2 and 1 (:).

Table 4.7: Influence of the variation of the width of an L-junction: The deviation of the frequency averaged quantities $\tilde{P}_i$ and $\tilde{A}_{ij}$ is classified by the number of modes per one-third octave band N and the modal overlap factor M of the smallest subsystem as well as by the first thickness-stretch resonance $f_{TM,1,i}(c_{L,z})$ of subsystem i: Large $> 20\,\%$, small $\leq 20\,\%$, very small $\leq 5\,\%$ [Müller 2017].

	$M < 1,\ N < 10$	$M > 1,\ N > 10$	$f > f_{TM,1,i}(c_{L,z})$
$\tilde{P}_i$	large	small	very small
$\tilde{A}_{ii}$	small	very small; The wider b, the bigger A_{ii}	no
$\tilde{A}_{ij}$	large	small; The wider b, the smaller A_{ij}	small

frequency. In the second range, the deviation is less than $10\,\%$. The off-diagonal entries of the energy influence coefficients matrix show a similar dependency on the width and the frequency, whereas the main diagonal entries behave even more robust as depicted in Fig. 4.22c. Since in the second frequency range the systems of different width show a similar modal behavior but still slightly depend on the width, the following relation is found. For a wider system, more energy remains in the excited subsystem and less energy is transmitted to the adjacent subsystems.

Predicting the energy flow by means of an SEA model with a line junction between wall and ceiling, neither the width nor the point of excitation matters. The SEA predicts the maximum possible, resonant energy transmission since it assumes that all resonant modes are excited, whereas in this case, the EFA tends to predict the minimum possible energy transmission since it uses a single load in the center of each plate. Thereby, many modes cannot be excited. At low and high frequencies, the deviations between the SEA and the EFA are at most, since the SEA model is restricted to plate-like structures with a sufficient modal density (cf. subsection 4.5.3).

4.3.3 Variation of Ceiling Length and Excitation Point

Constructing multistory timber buildings, the different stories have often a standardized height leading to a constant height of the walls. Due to different types of rooms and related space requirements, the length of the ceilings changes.

Comparing different L-junctions with varying length of the ceiling (cf. Tab. 4.3), the influence on the frequency averaged input power and the frequency averaged energy influence coefficients is examined. By contrast to subsection 4.3.2, where all subsystems are affected

Table 4.8: Influence of the variation of the length of subsystem 2: The deviation of the frequency averaged quantities $\tilde{P}_i$ and $\tilde{A}_{ij}$ is classified by the number of modes per one-third octave band N and the modal overlap factor M of the smallest subsystem as well as by the first thickness-stretch resonance $f_{TM,1}(c_{L,z})$ of subsystem 2: Large $> 20\,\%$, small $\leq 20\,\%$, very small $\leq 5\,\%$ [Müller 2017].

	$M < 1,\, N < 10$	$M > 1,\, N > 10$	$f > f_{TM,1}(c_{L,z})$
$\tilde{P}_1$	small	very small	no
$\tilde{P}_2$	large	small	very small
$\tilde{A}_{11}$	small	very small	no
$\tilde{A}_{12}$	large	large The longer l_2, the smaller A_{12}.	large For RotR: $A_{12} \sim \frac{1}{l_2}$
$\tilde{A}_{21}$	large	large	very small
$\tilde{A}_{22}$	large	small The longer l_2, the bigger A_{22}.	very small

equivalently by changing the width of the junction, it has to be distinguished between varied (2) and non-varied subsystem (1) interpreting the deviation of the frequency averaged quantities in Tab. 4.8.

Firstly, the length of the ceiling is varied from 1 to 4 m by 1 m and always excited in the center. Secondly, the load is located always at 0.5 m from the junction for the four different ceiling lengths. Thirdly, the distance of the load from the junction is step-wise increased, whereas the length of the ceiling is constant. Fourthly, the four different ceilings are excited by RotR. These four steps help to separate the influence of the ceiling length and of the location of the load on the energy flow. Whereas the ceiling length influences the reverberant field, the location of the load influences the direct field contribution at the junction.

Single Load in the Center of Ceilings of Different Length

For the first investigation, the length of the ceiling is increased from 1 m up to 4 m by 1 m steps. A single, perpendicular load is acting in the center of the ceiling and the wall, respectively. Whereas the power injected into the wall is almost unaffected by the variation of the length of the ceiling (cf. Fig. 4.23a), the input power due to the excitation of the ceiling strongly depends on its length as the eigenfrequencies of the ceiling do. As shown in Fig. 4.23b, the dependency is reduced for higher frequencies and it is negligible above the first thickness-stretch resonance of the ceiling. The frequency averaged energy influence coefficients which are related to either an excitation or an observation of subsystem 2 also show large deviations at low frequencies according to Fig. 4.23c and 4.23d. Due to an
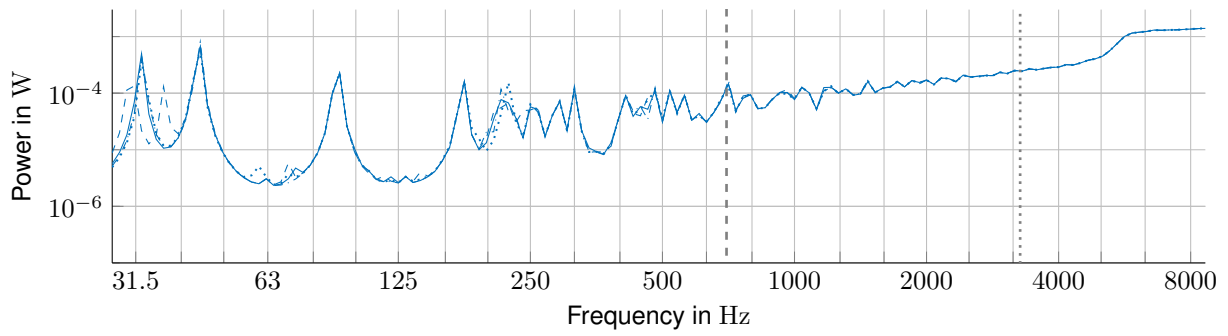
(a) Input power into subsystem 1
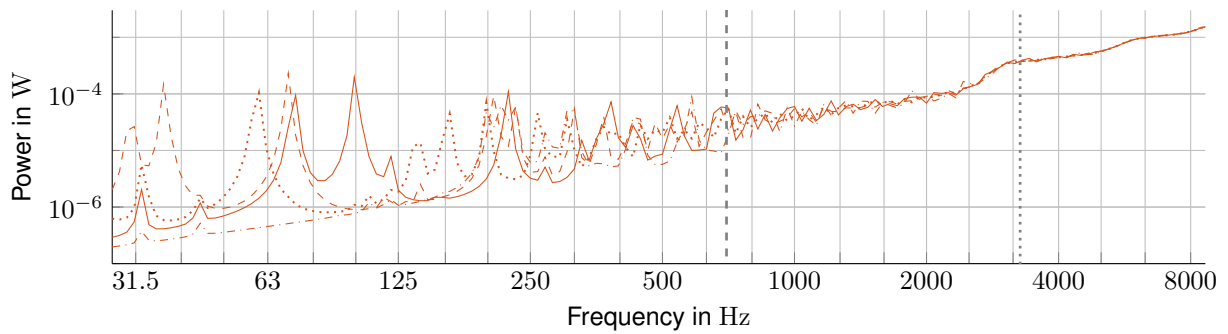
(b) Input power into subsystem 2
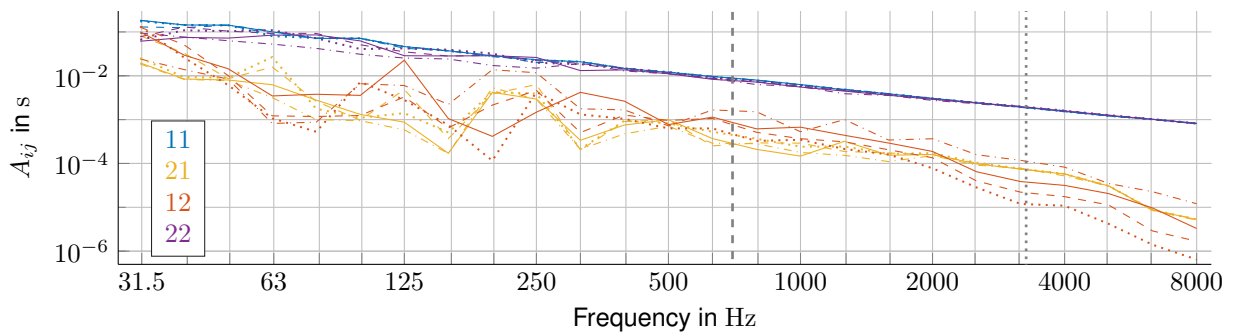
(c) Frequency averaged energy influence coefficients
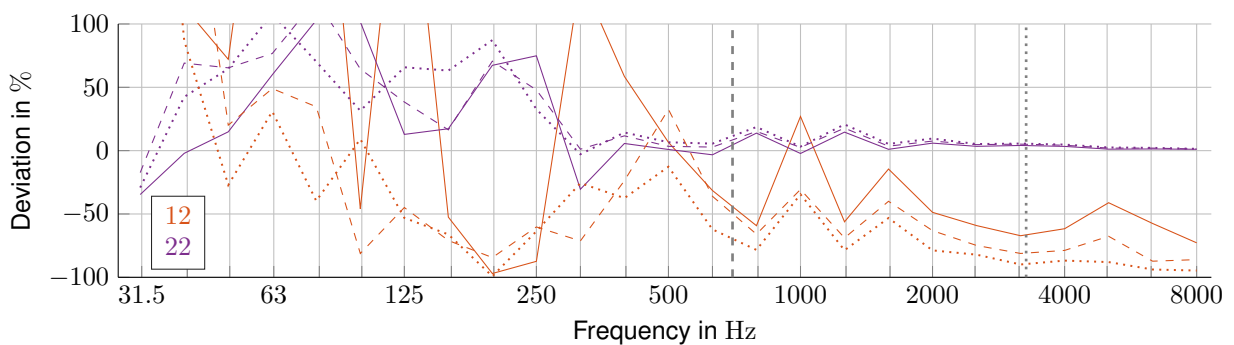
(d) Deviation of frequency averaged input energy influence coefficients with respect to $l_2 = 1\,\mathrm{m}$

Figure 4.23: L-junction excited in the center of each subsystem. Comparison between different lengths of the ceiling: $1\,\mathrm{m}$ ($- \cdot -$), $2\,\mathrm{m}$ ($-$), $3\,\mathrm{m}$ ($--$) and $4\,\mathrm{m}$ ($\cdots$); $N \geq 10$ and $M \geq 1$ for each subsystem ($\vdots$); First thickness-stretch resonance of the ceiling (:).

(a) $1\,\mathrm{m}$ **(b)** $l_2 = 2\,\mathrm{m}$ **(c)** $l_2 = 3\,\mathrm{m}$ **(d)** $l_2 = 4\,\mathrm{m}$
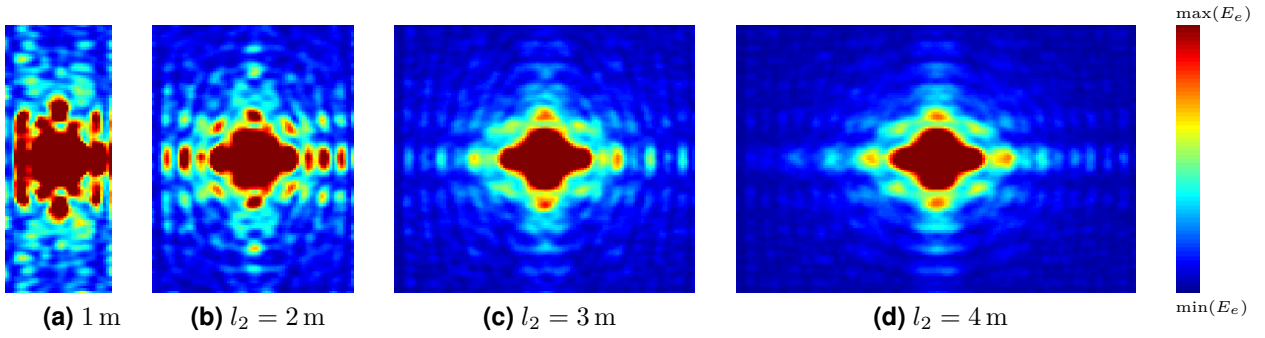
Figure 4.24: Energy distribution at $3299\,\mathrm{Hz}$ due to single load in the center of ceilings of different length l_2.

increased number of modes per one-third octave band, the different ceilings show a similar modal behavior and therefore a similar excitability above $700\,\mathrm{Hz}$. This demonstrates the low deviation of $\tilde{A}_{22}$ for different ceiling lengths l_2 related to $\tilde{A}_{22}$ for $l_2 = 1\,\mathrm{m}$ in Fig. 4.23d. A relationship between the length of the ceiling and the energy influence coefficients due to excitation of the ceiling, $\tilde{A}_{i2}$, can be recognized. The longer the ceiling, the bigger is $\tilde{A}_{22}$ and the smaller is $\tilde{A}_{12}$ and also $\tilde{\eta}_{21}$, which is not depicted. This relation fits to the analytical dependency from the SEA between l_i and η_{ij} according to Eq. (3.59). Thereby, the width of the subsystems b corresponds to the length of the junction l_{ij} and thus can be canceled. Since all remaining parameters are independent of the length of subsystem i, the following proportionality can be derived:

$$\eta_{ij} = \frac{\tau_{ij}\, c_{g,i}\, l_{ij}}{2\pi^2 f l_i\, b} \quad \rightarrow \quad \eta_{ij} \sim \frac{1}{l_i} \tag{4.14}$$

As the wall remains constant, $\tilde{A}_{11}$ is only slightly affected at low frequencies as illustrated in Fig. 4.23c. $\tilde{A}_{21}$ describes the energy in the ceiling normalized by the input power into the wall and demonstrates that the amount of transmitted energy strongly depends on the length of the receiving ceiling up to its first thickness-stretch resonance. Then, the energy flow is dominated by the thickness modes which behave independently of the subsystem length.

By means of the top view, Fig. 4.24 displays the time-averaged energy distribution in the ceilings of different length excited in their center. The single load oscillates at $f = 3299\,\mathrm{Hz}$ which is slightly above the first thickness-stretch resonance at $3269\,\mathrm{Hz}$. The colors illustrate that the energy quickly decays from the point of excitation towards the boundaries. The shorter the ceiling, the more energy is reflected and the more energy seems to arrive at the junction, which is at the left edge of the plates in Fig. 4.24. The first four element rows of the ceiling are on top of the wall. Their coloring visualizes that a large amount of the energy is reflected due to the geometrical discontinuity. This effect is demonstrated most clearly by
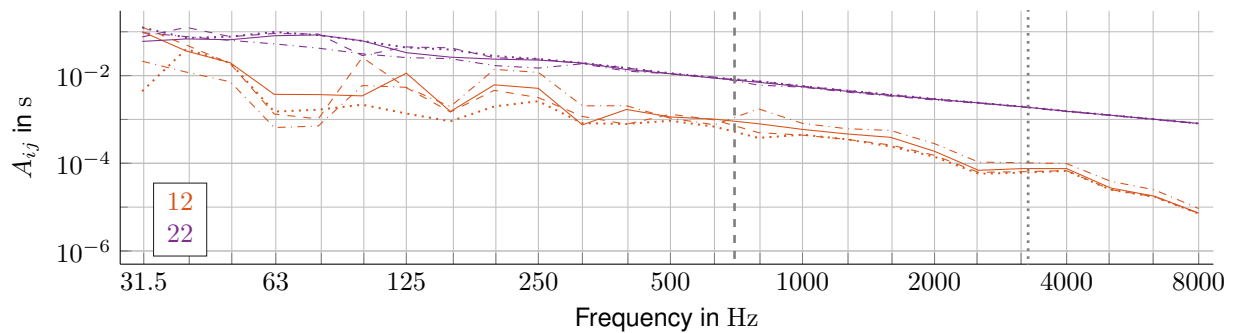
Figure 4.25: L-junction: Frequency averaged energy influence coefficients due to excitation of the ceiling at $0.5\,\mathrm{m}$ from the junction: Comparison between different lengths of the ceiling: $1\,\mathrm{m}$ $(-\cdot-)$, $2\,\mathrm{m}$ $(-)$, $3\,\mathrm{m}$ $(--)$ and $4\,\mathrm{m}$ $(\cdots)$; $N \geq 10$ and $M \geq 1$ for each subsystem ($\vdots$); First thickness-stretch resonance of the ceiling (:).

(a) $1\,\mathrm{m}$ **(b)** $l_2 = 2\,\mathrm{m}$ **(c)** $l_2 = 3\,\mathrm{m}$
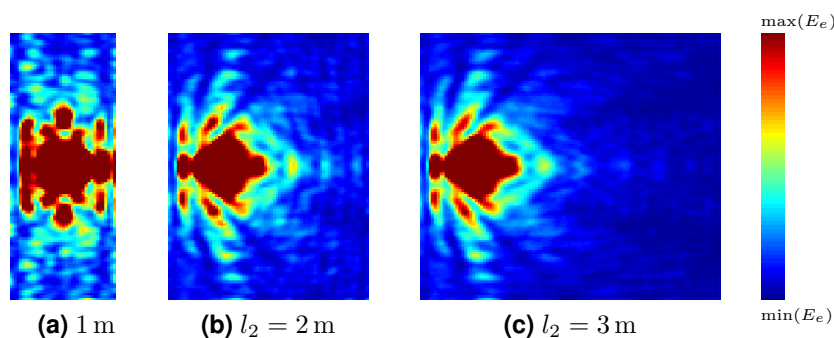
Figure 4.26: Energy distribution at $3299\,\mathrm{Hz}$ due to single load at $0.5\,\mathrm{m}$ from the junction for ceilings of different length l_2.

the ceiling of $1\,\mathrm{m}$ length in Fig. 4.24a. For the ceilings of $3\,\mathrm{m}$ and $4\,\mathrm{m}$ length, the direct field of the single load seems to be mostly faded away before reaching the junction.

Single Load at a Fixed Distance to the Junction on Ceilings of Different Length

According to Fig. 4.24, the location of the load or more precisely its distance to the junction influences the energy flow beside the length of the excited subsystem especially at higher frequencies. To separate the two effects, the load acts at a fixed distance of $0.5\,\mathrm{m}$ from the junction for different lengths of the ceiling. The position is close to the center of the ceiling of $1\,\mathrm{m}$ length and is not changed for longer ceilings. For the load in the center of the plate, $\tilde{A}_{12}$ deviates up to $100\,\%$ between the ceilings of $1\,\mathrm{m}$ and $4\,\mathrm{m}$ also at high frequencies in Fig. 4.23d. For the fixed position, $\tilde{A}_{12}$ converges with increasing frequency according to Fig. 4.25. The curves of $3\,\mathrm{m}$ and $4\,\mathrm{m}$ behave almost identical above $1000\,\mathrm{Hz}$ and the curve of $2\,\mathrm{m}$ joins above $4000\,\mathrm{Hz}$. Only the ceiling of $1\,\mathrm{m}$ length leads to an higher energy flow into the wall also at high frequencies due to the short distance between point of excitation, reflecting boundary and junction. For longer ceilings, the distance between load and junction is the same but the
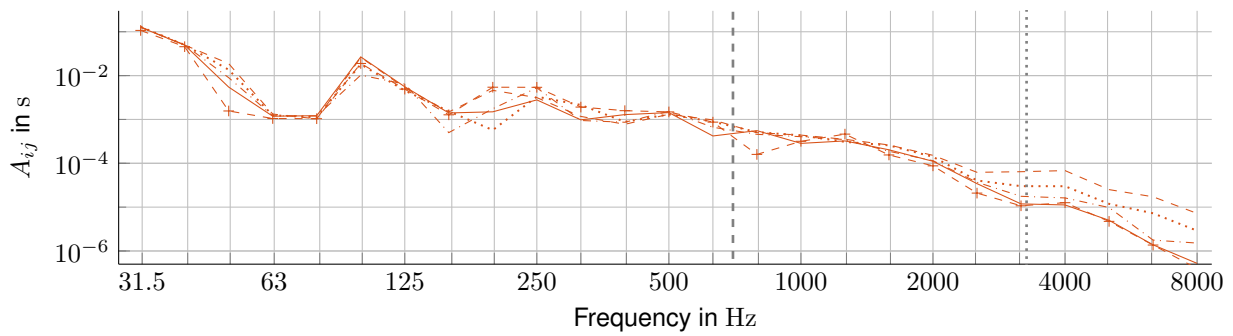
Figure 4.27: L-junction: Frequency averaged energy influence coefficients $\tilde{A}_{12}$ due to excitation of the ceiling which is $3\,\mathrm{m}$ long and excited at increasing distance from the junction: $0.5\,\mathrm{m}$ $(--)$, $1.0\,\mathrm{m}$ $(\cdots)$, $1.5\,\mathrm{m}$ $(-\cdot-)$, $2.1\,\mathrm{m}$ $(-)$ and $2.6\,\mathrm{m}$ $(-+-)$; $N \geq 10$ and $M \geq 1$ for each subsystem $(\vdots)$; First thickness-stretch resonance of the ceiling (:).

energy is able to decay towards the other boundaries of the plate almost without reflections according to Fig. 4.26. This leads to the conclusion that the higher the frequency the less decisive is the length of the ceiling. The energy flow starts to become exclusively dependent on the location of the excitation which will be examined in the following paragraph.

Fixed Length of the Ceiling: Variation of the Point of Excitation

Figure 4.27 shows the energy flow into the wall for different points of excitation on the ceiling. The ceiling is $3\,\mathrm{m}$ long and is excited firstly at a distance of $0.5\,\mathrm{m}$ from the junction. The distance is subsequently increased by approximately $0.5\,\mathrm{m}$. Thereby, the dashed curve of $\tilde{A}_{12}$ in Fig. 4.25 and 4.27 can be used as a reference curve for comparisons as it represents the same configuration (ceiling length $3\,\mathrm{m}$, distance of load to junction $0.5\,\mathrm{m}$). For the fixed location of the excitation, the curves for different lengths of ceiling converge with increasing frequency as already shown in Fig. 4.25. For the fixed ceiling length, the different points of excitation lead to a divergence above the first thickness-stretch resonance which is ordered by the distance to the junction (cf. Fig. 4.27). Hence, the further away the load is, the less energy is transmitted into the adjacent component. Comparing the two furthest load positions, they show an almost identical behavior in the high frequency range. This indicates that the direct field is decayed within the distance of approximately $2\,\mathrm{m}$ and thus mostly reverberant energy flows across the junction for farther excitation points.

The statistical investigations in section 4.5 confirm this diverging behavior of the energy flow at high frequencies and also indicate a dependency on the locations where the sending subsystem is excited: Above the first thickness-stretch resonance, the coefficient of variation of $\tilde{A}_{12}$ increases significantly using RotR with less or equal ten loads comparing 100 different
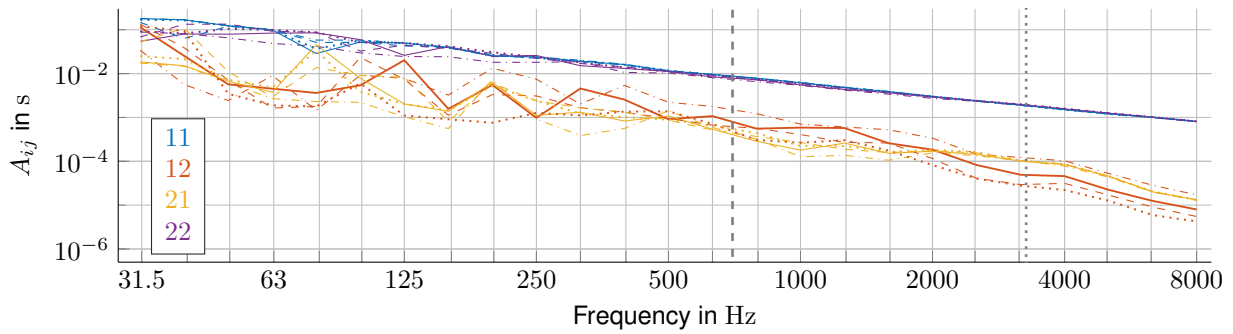
Figure 4.28: Frequency averaged energy influence coefficients of an L-junction excited by RotR with $n_l = 100$: Comparison between different lengths of the ceiling: 1 m ($- \cdot -$), 2 m ($-$), 3 m ($--$) and 4 m ($\cdots$); $N \geq 10$ and $M \geq 1$ for each subsystem ($\vdots$); First thickness-stretch resonance of the ceiling (:).
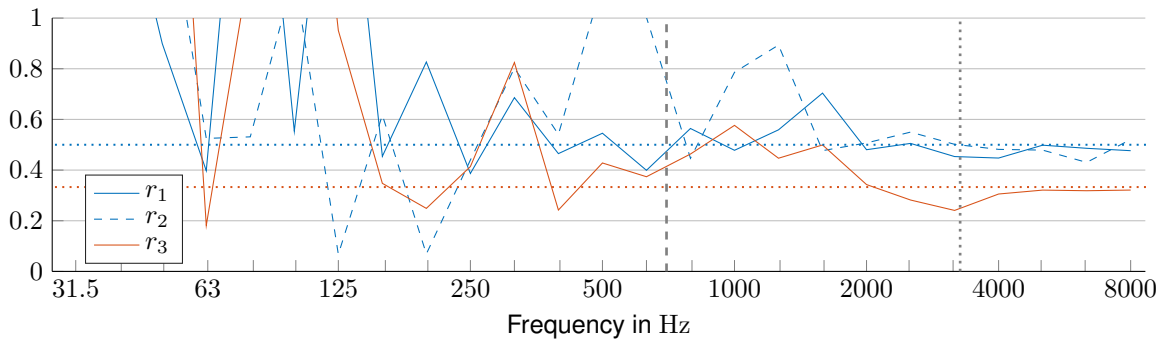
Figure 4.29: Ratio of $\tilde{A}_{12}$ between different lengths of ceiling for RotR: $r_1 = \frac{\tilde{A}_{12}(l_2=2)}{\tilde{A}_{12}(l_2=1)}$, $r_2 = \frac{\tilde{A}_{12}(l_2=4)}{\tilde{A}_{12}(l_2=2)}$ and $r_3 = \frac{\tilde{A}_{12}(l_2=3)}{\tilde{A}_{12}(l_2=1)}$; $N \geq 10$ and $M \geq 1$ for each subsystem ($\vdots$); First thickness-stretch resonance of the ceiling (:).

realizations as shown in Fig. 4.49. For 50 and 100 loads, only a small increase of the coefficient of variation happens, whereas it is not affected by the first thickness-stretch resonance if all elements on the surface are excited and thus only the random phase shift of each loaded element is varied between the different realizations.

RotR on Ceilings of Different Length

Now, RotR consisting of 100 loads is used to excite the L-junction. Thereby, the length of the ceiling is varied from 1 m up to 4 m by 1 m steps. For each length, the 100 loads are randomly distributed on the plate. At first glance, RotR in Fig. 4.28 and the single load excitation in Fig. 4.23c lead to similar frequency averaged energy influence coefficients and show a comparable influence of the length of ceiling as mentioned in Tab. 4.8. But beside the fact that RotR is able to excite more modes at low frequencies, the different curves of $\tilde{A}_{12}$ seem to be parallel above the first thickness-stretch resonance. As Fig. 4.28 is depicted

in logarithmic scale, the different ceilings are related by a constant factor which is illustrated in Fig. 4.29. It results an indirect proportionality between ceiling length and the energy transmission into the wall above the first thickness-stretch resonance:

$$A_{12} \sim \frac{1}{l_2} \tag{4.15}$$

It demonstrates that the random distribution of the loads on the ceiling results in an equal distribution for a sufficient number of loads. Thus, the average load density decreases for larger plates and also the energy which is contributed by the direct field is reduced at the junction. Counting the number of loaded elements in the first three rows next to the junction, they are halved for the doubled ceiling length in the presented calculations.

4.3.4 In-plane vs. Out-of-plane Loading at a T-Junction

Inside the EFA, the energy is normalized with respect to the input power leading to energy influence coefficients. The time-averaged power, which is injected into the structure at the point $\mathbf{z} = (x,y,z)$, is linked to the admittance of the structure $\underline{Y}$ or to its reciprocal, the impedance $\underline{Z}$ [Cremer 1988]:

$$P_p(\mathbf{z},f) = \frac{1}{2} \Re\left(\underline{F}^* \, \underline{v}\right) = \frac{1}{2} \Re\left(\underline{F}\underline{F}^* \, \frac{\underline{v}}{\underline{F}}\right) = \frac{1}{2} \, |\underline{F}|^2 \, \Re\left(\underline{Y}\right) = \frac{1}{2} \, |\underline{F}|^2 \, \Re\left(\frac{1}{\underline{Z}}\right) \tag{4.16}$$

Applying a load of $1\,\mathrm{N}$ in in-plane direction instead of perpendicular to the plate, e.g. to model a machinery induced vibration, a smaller input power results as the driving-point impedance $\underline{Z}$ is higher. Figure 4.30 shows the input power exciting the lower wall of a T-junction. Its geometry and the counterclockwise numbering of the rigidly connected subsystems are illustrated in Fig. 4.1c. The loads point either perpendicular to the plane or in randomly chosen directions in the plane of the plate. In both cases, the pressure is applied on the same 100 elements whereby each is oscillating with a random phase shift. Whereas the input power due to the out-of-plane load shows a jump right before the first thickness-stretch resonance of the wall, the in-plane load excites the thickness-shear modes. Close by the thickness-shear resonances which lead to a displacement in y-direction - parallel to the junction line, a big jump occurs. The thickness-shear modes oscillating in x-direction can be identified by small peaks.

Figure 4.32a shows, that the energy flow into the adjacent subsystems is high compared to the case of a loading perpendicular to the plate, whereas the energy flow into the directly
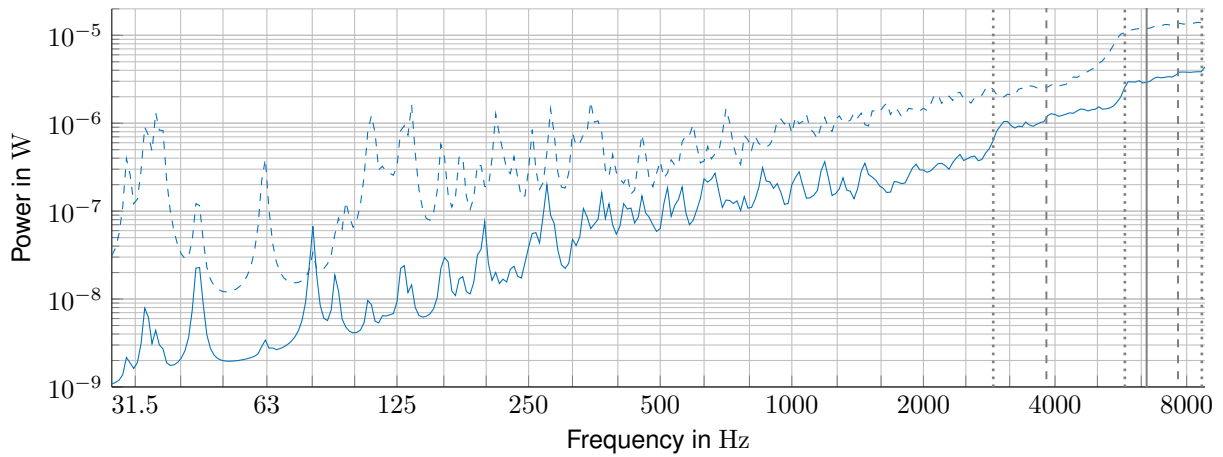
Figure 4.30: Input power exciting subsystem 1 with 100 loads (RotR) in in-plane $(-)$ or in out-of-plane direction $(--)$; Simple thickness resonances oscillating in in-plane or out-of-plane direction: $f_{TM}\ (c_{S,zy})$ (:), $f_{TM}\ (c_{S,zx})$ (¦), $f_{TM}\ (c_{S,z})$ (|).

excited subsystem is smaller. At high frequencies, the two types of excitation differ less as the plate-like behavior of the subsystems gives more and more way to modal couplings with through thickness resonances. The energy transmission into the ceiling dominates for both excitations as in the case of the investigated T-junction, the lower and the upper wall are separated by the ceiling.

Figure 4.31 demonstrates the energy flow into the different subsystems by means of $\tilde{A}_{ij}$ and $\tilde{A}_{ij,v_z}$, whose energy results exclusively from the surface velocity perpendicular to the plate, for the in-plane excitation of the lower wall (subsystem 1). The in-plane load leads to a considerable difference between $\tilde{A}_{11}$ and $\tilde{A}_{11,v_z}$ which confirms that mainly in-plane waves are excited in the lower wall. In the ceiling (subsystem 2), which is mounted perpendicular to the wall, it causes mainly bending waves. Therefore, $\tilde{A}_{21}$ and $\tilde{A}_{21,v_z}$ show similar values above 250 Hz. Comparing $\tilde{A}_{31}$ and $\tilde{A}_{31,v_z}$, they show a big difference in magnitude and thus, the transmission into the upper wall (subsystem 3) is dominated by in-plane waves.

The coupling between the subsystems is stronger if the excitation is in in-plane direction since the same amount of input power leads to higher flanking transmission [Wilhelm 2017]. The stronger coupling is also indicated by higher values of the condition number in Fig. 4.32b and confirmed by proportions of coupling and damping loss factors in Fig. 4.32c. Above 500 Hz, the damping loss factors become almost identical for the two different excitations indicating that the damping and coupling loss factors are independent and fulfill the corresponding SEA assumption.

Counting only the in-plane modes in Fig. 4.33, the walls reach five modes in the one-third octave band of 1000 Hz, whereas five bending modes are already available above 250 Hz. In
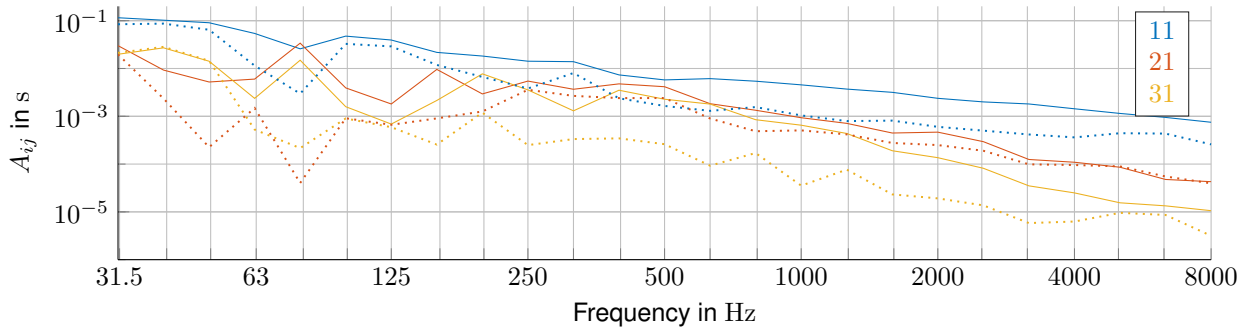
Figure 4.31: Energy influence coefficients $\tilde{A}_{i1}$ ($-$) and $\tilde{A}_{i1,v_z}$ ($\cdots$) due to in-plane excitation.
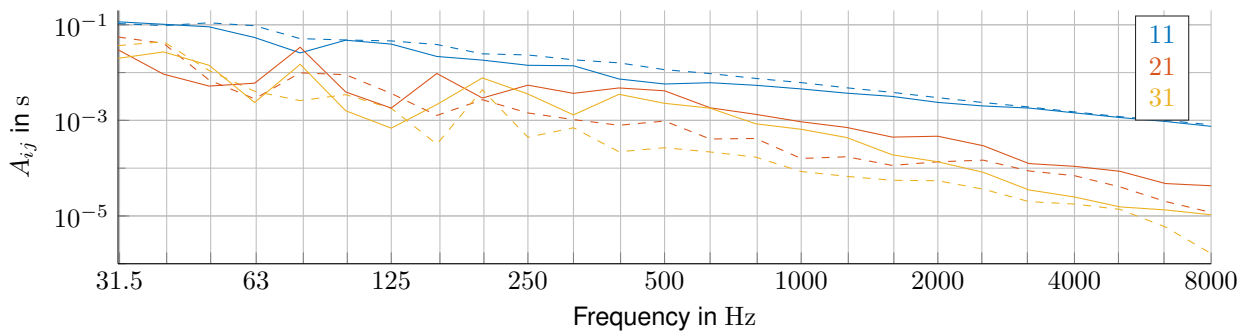
(a) Energy influence coefficients $\tilde{A}_{i1}$ due to excitation of subsystem 1
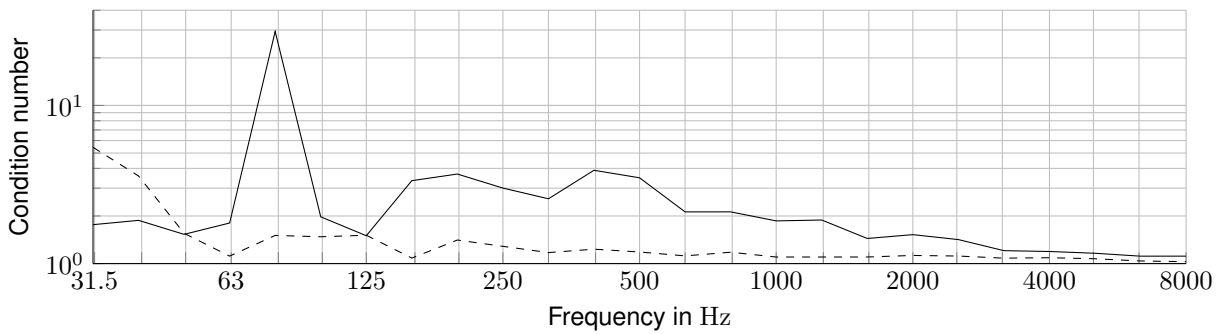
(b) Condition number of the energy influence coefficients matrix $\left[\tilde{A}\right]$
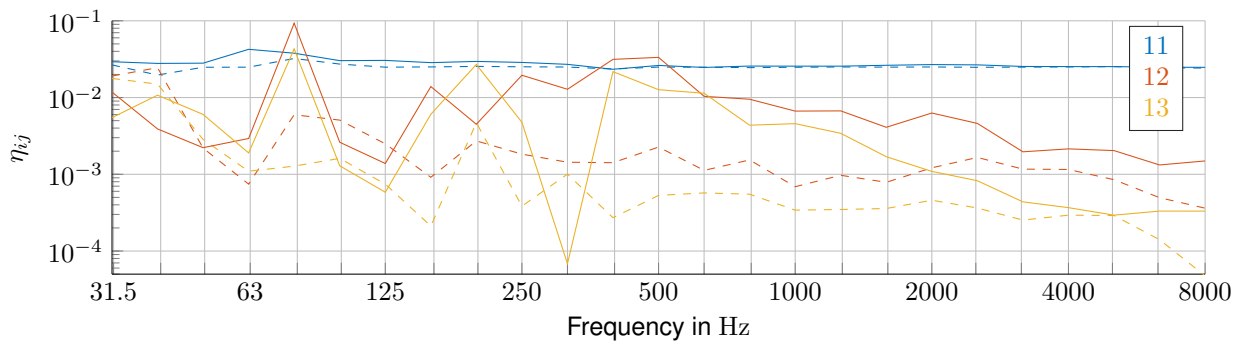
(c) Loss factors $\tilde{\eta}_{1j}$ quantifying the losses of subsystem 1

Figure 4.32: Exciting a T-junction by RotR with 100 loads pointing in-plane ($-$) or in out-of-plane ($--$) direction: Frequency averaged quantities.
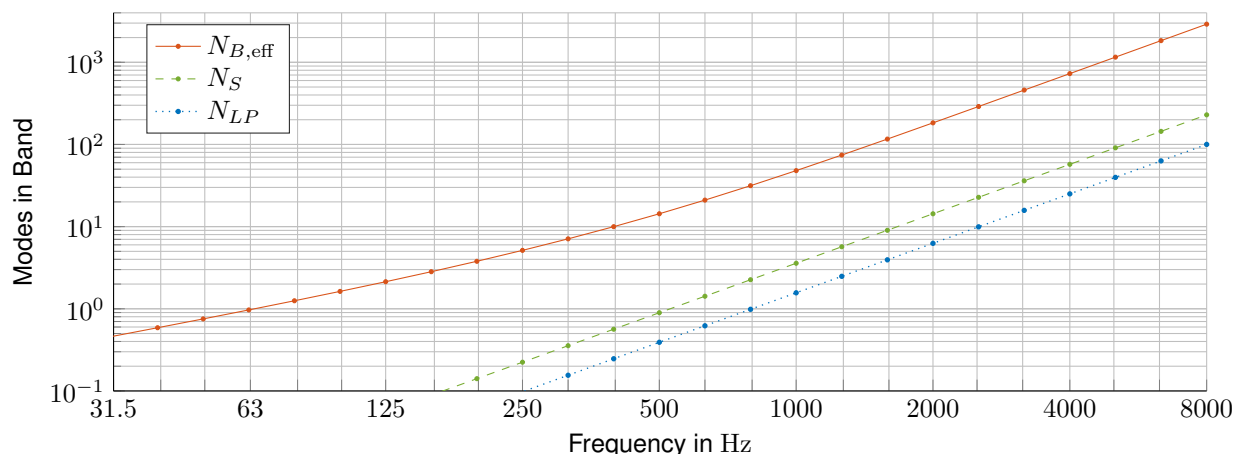
Figure 4.33: Modes per one-third octave band.

the case of an out-of-plane load, bending waves are excited in all subsystems. By contrast, due to an in-plane load only the geometry can lead to a significant contribution of bending modes e.g. in the case of a transmission from wall to ceiling as shown above in Fig. 4.31 comparing $\tilde{A}_{ij}$ and $\tilde{A}_{ij,v_z}$. Hence, for an in-plane excitation the range of applicability of the SEA is reduced to few one-third octave bands below the first thickness-shear resonance of the structure which occurs here at $1445\,\mathrm{Hz}$ in the ceiling.

4.3.5 Effect of the Random Phase of RotR

For the ideal RotR excitation, the entire plate is loaded with loads having different, random phases as described in subsection 3.3.1. As this is numerically expensive, the effect of a reduced number of loads is investigated in section 4.5. Below the first thickness resonances, the mean of 100 realizations of RotR with a reduced number loads converges to the same values of the energy influence coefficients compared to RotR with loading all surface elements.

Exciting all elements without phase shift would lead to a generalized load vector of zero and thus to zero input power for symmetric mode shapes. Using only 100 loaded elements without phase shift in between them appears to be a rough approximation of a fully correlated load over the whole surface. Therefore, the effect of the random phase for RotR with a reduced number of loads is investigated in dependency of the frequency range: 100 loads with random phases (RotR) are compared to 100 loads at the same locations but without phase shift in between.

Figures 4.34a b and c present the input power exciting the subsystems 1, 2 and 3 of a T-junction, which consists of two walls which are separated by the ceiling (cf. Fig. 4.1c). All
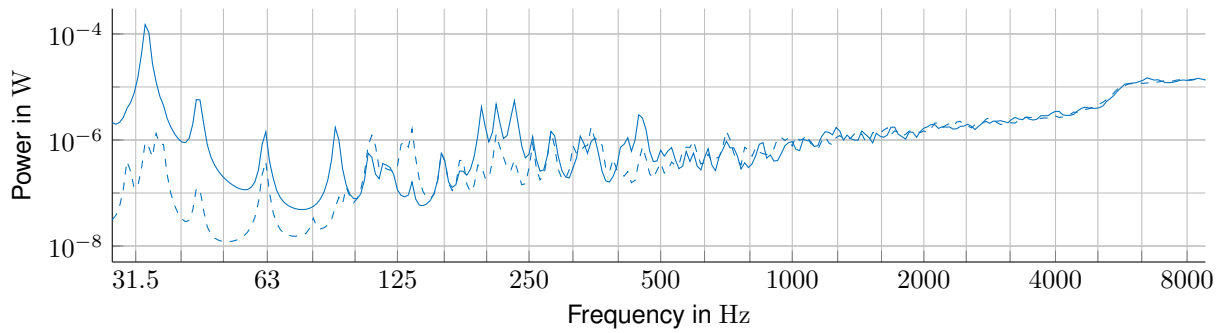
(a) Input power into subsystem 1
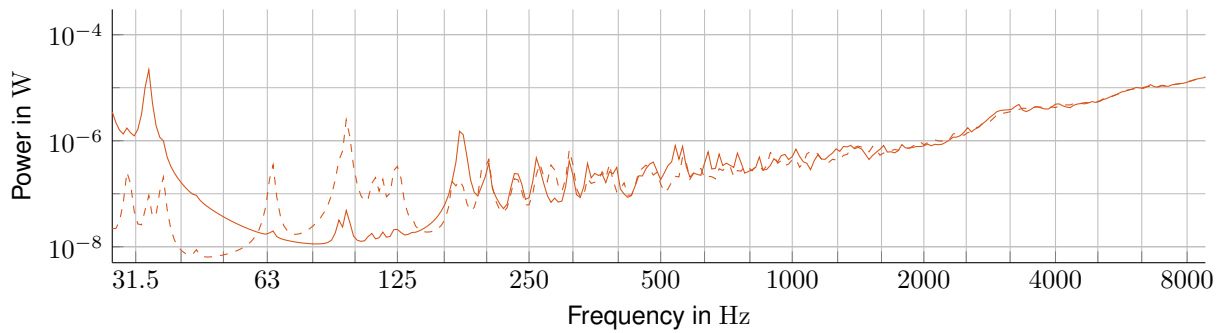
(b) Input power into subsystem 2
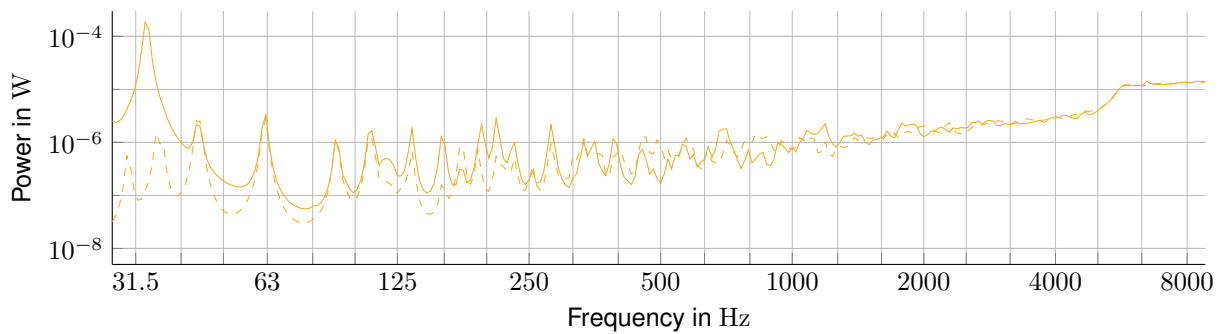
(c) Input power into subsystem 3
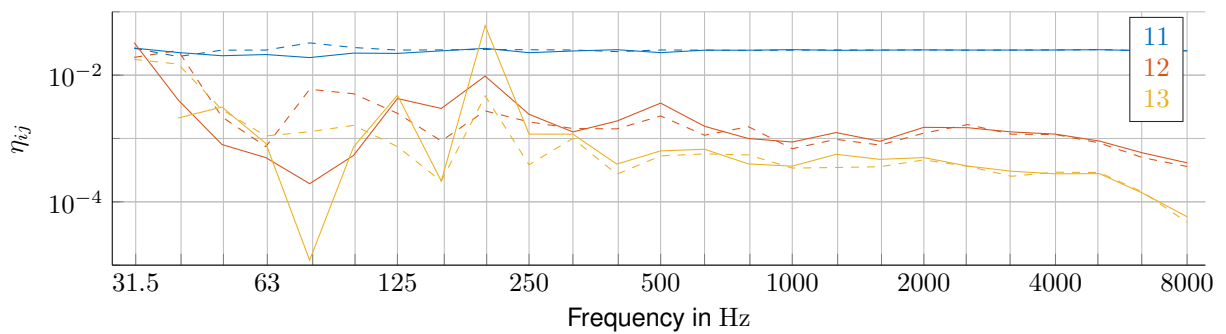
(d) Frequency averaged loss factors η_{1j} quantifying the losses of subsystem 1

Figure 4.34: T-junction excited by 100 loads, either correlated without phase shift $(-)$ or with random phase as RotR $(--)$.

(a) 26 Hz   **(b)** 34 Hz   **(c)** 65 Hz   **(d)** 96 Hz
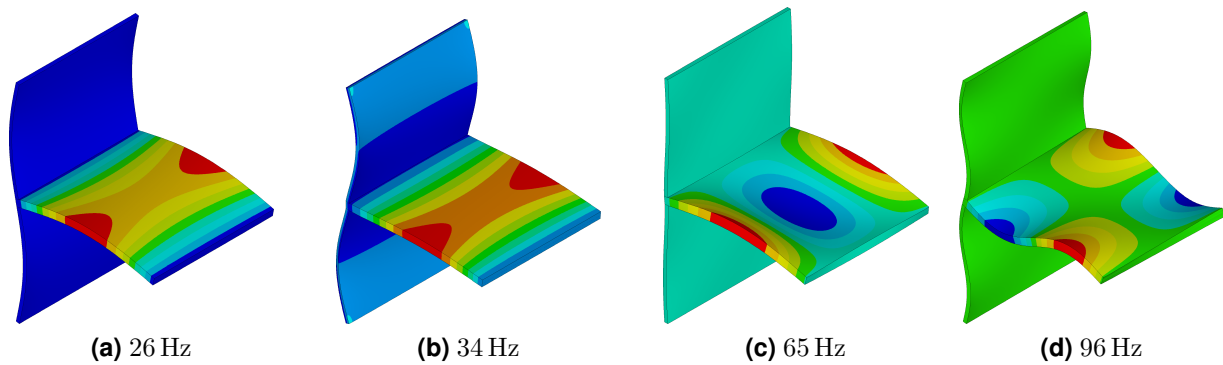
Figure 4.35: Mode shapes of a T-junction; Colors indicate displacements perpendicular to the ceiling.

components are rigidly connected. The two curves of correlated loads and of the uncorrelated ones converge towards higher frequencies since there, small wavelengths omit a correlated behavior. At low frequencies, where between one or two half-waves fit into a side length of the plate, the correlated loads can on the one hand lead to a dominant excitation of single resonances and on the other hand, to their cancellation depending on the location of the 100 loads and on the mode shape. The mode shapes in Fig. 4.35a and b correspond to the first case since all correlated loads act in phase in the same half-wave of the mode shapes. The high values of the input power around 31.5 Hz in Fig. 4.34b confirm the phase-conform excitation of the mode shapes. In Fig. 4.35c and d, the ceiling contains symmetric mode shapes with inversely phased regions which would lead to a generalized load vector of zero exciting the whole surface in-phase. Due to the random spatial distribution of the 100 loads used in this investigation, the generalized load vector of the mode shape at 65 Hz is almost zero since its contribution to the input power is negligible according to Fig. 4.34b. By contrast, the resonance at 96 Hz is clearly visible but significantly smaller compared to the uncorrelated RotR excitation at the same locations.

The frequency averaged loss factors in Fig. 4.34d demonstrate that the effect of the phase shift of the loads decreases with increasing frequency and that an uncorrelated RotR excitation is important especially at low frequencies. Due to the correlated excitation, the coupling loss factor $\tilde{\eta}_{13}$ exceeds the damping loss factor $\tilde{\eta}_{11}$ around 200 Hz and provocates strong coupling.

4.4 Modifications at the Junction

In subsection 4.4.1 an L-junction is investigated whereby the junction itself is modified. In the foregoing investigations, the individual components are connected rigidly. To model the

flexibility of a screwed junction, an elastic interlayer is inserted in the FE model. To systematically reduce the structure-borne sound transmission over the junction, an impedance difference is introduced by means of an elastic interlayer with the material properties of an elastomer. This elastomer is optionally damped. The effect of elastic interlayers depends on its material properties which is also demonstrated on the basis of measurements by Winter et al [2015] and Mecking et al [2017a].

In subsection 4.4.2, the wall of a T-junction is not separated in two components and the ceiling is connected by a steel bracket with an elastic interlayer on top. This leads to strong coupling of the walls over a wide frequency range. This violation of the SEA assumptions also leads to negative coupling loss factors.

To characterize the properties of the junction itself, isolated junction geometries, like an L-, a T- or an X-junction, are cut out of a building assuming that the influence of the remaining structure is negligible. In subsection 4.4.3, the energy flow within these junction geometries is compared showing the influence of a third or fourth additional subsystem. In the case of the X-junction, the two ceilings are optionally completely separated.

Table 4.2 and 4.3 (cf. p. 73) show the material and geometry of the setups used in the subsequent subsections. Preliminary investigations were performed within the scope of Wilhelm [2017] with similar configurations but lower resolution in frequency and space.

4.4.1 Elastic Interlayer: Variation of the Connection Strength

In the FE model, a thin isotropic interlayer is inserted between adjacent components (cf. Fig. 4.7) to model different types of junctions as described in subsection 4.1.3. Dependent on the material properties of the layer (cf. Tab. 4.4), either a flexible connection or an elastic interlayer is modeled, which can additionally be damped. In the following passages, four different types of junctions are compared: rigid, flexible (screwed), elastic interlayer (undamped) and damped, elastic interlayer (Sylodyn ND). Therefore, additionally $A_{L_i j}$ is evaluated leading to a non-symmetric energy influence coefficients matrix. $A_{L_i j}$ is the energy of the layer L_i normalized to a unit power input due to loading of subsystem j. All modifications have in common that they reduce the energy transmission between two components compared to the rigid junction. The material change at the interface leads to an impedance difference [Cremer 1967]. The higher the difference is, the lower is the sound transmission. The reduction of the sound transmission depends thereby on the wave type.

In Fig. 4.37, the energy influence coefficients represent the normalized energy in the two subsystems of an L-junction as well as in the elastic interlayer for the excitation of subsystem 1.

Flexible Junction

Figure 4.37a compares the rigid and the flexible (screwed) junction, which is modeled by an undamped, elastic interlayer of solid elements. In the case of the rigid junction, the energy influence coefficients of both subsystems are of the same size at 64 Hz if subsystem 1 is excited ($A_{11} = A_{21}$). This indicates strong coupling (cf. subsection 3.2.3, 4.2.2). A mode shape localized in subsystem 2 leads mainly to this equal energy distribution. In the case of the flexible junction, the normalized energy in subsystem 2, A_{21}, is smaller. The elastic interlayer reduces the coupling as more energy remains in the excited subsystem. Between 160 Hz and 500 Hz the effect of the elastic interlayer seems to be negligible as the energy flow into the non-excited subsystem 2, A_{21}, is of similar size for both types of junctions according to Fig. 4.37a.

From 500 Hz on, in-plane waves begin additionally to contribute to the energy flow into the adjacent subsystem, whereas at low frequencies only bending waves are transmitted. In both plates, at least one in-plane mode per one-third octave band occurs on average at 500 Hz. Above 500 Hz, the energy influence coefficients A_{21} of the two different junctions start to deviate. Compared to the rigid junction, the energy flow over the flexible junction is clearly reduced until the first thickness-shear resonances of the elastic interlayer at 4181 Hz. In the frequency range between 500 and 4181 Hz, the flow into the elastic interlayer and the flow across it into subsystem 2 is of similar size.

The thickness-shear resonances are excited due to the perpendicular load on the wall leading to horizontal displacements at the interface of the wall and the elastic interlayer. At these thickness resonances, A_{21} has similar values compared to the rigid case. There, the transmission reaches a maximum. This effect is analytically shown for two semi-infinite plates connected by an elastic interlayer by Mees and Vermeir [1993]. According to Eq. (4.17), the first thickness-shear resonance is at 4181 Hz, which corresponds to the first peak above 4000 Hz of the normalized energy inside the interlayer, A_{L_11}. The shear plane has a short side, which is the thickness of the wall, and a long side, which is the length of the junction (cf. Fig. 4.36). To consider the parabolic shear stress distribution due to displacements along the short side of the elastic interlayer, the shear correction factor κ is applied as
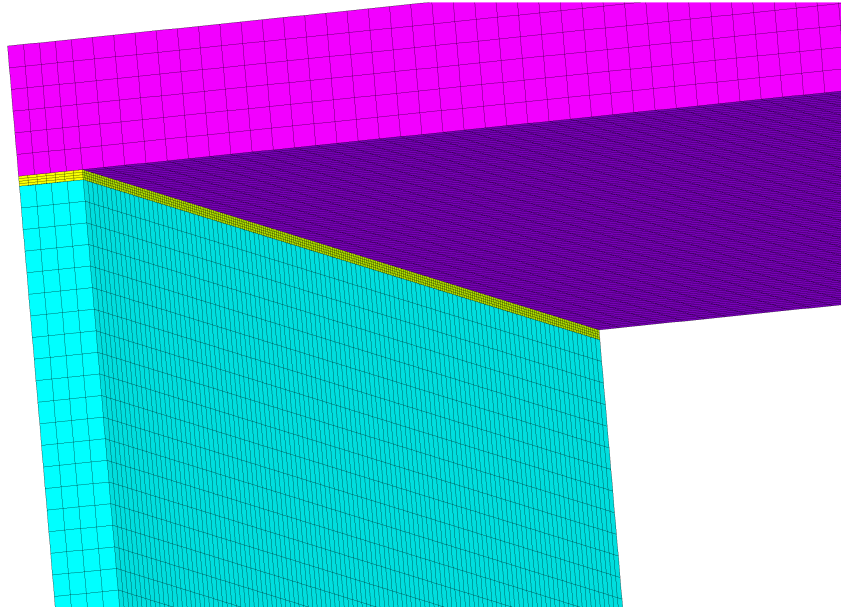
Figure 4.36: Axonometry of the FE model: Elastic interlayer between wall and ceiling.

explained in subsection 2.2.2:

$$f_{TM,1}(\kappa G) = \sqrt{\frac{\kappa G}{\rho}} \, \frac{1}{2h_{L_1}} = 4181 \, \text{Hz} \tag{4.17}$$

To predict thickness-shear resonances with displacements along the length of junction, the elastic interlayer is assumed to be infinite and thus Eq. (2.44) is applied. The calculated thickness-shear resonance is close to the second peak in Fig. 4.37a:

$$f_{TM,1}(G) = \sqrt{\frac{G}{\rho}} \, \frac{1}{2h_{L_1}} = 4580 \, \text{Hz} \tag{4.18}$$

In the presented investigation, the FE model contains an elastic interlayer to represent the flexible behavior of a screwed junction. The analogous model was determined at low frequencies (cf. subsection 4.1.3). Thus, the thickness modes within the elastic interlayer are artefacts of the FE model. As soon as the first thickness-shear mode of the elastic interlayer vibrates at resonance, the FE model is no longer valid, because this behavior does not correspond to a screwed connection. The limiting frequency can be estimated by Eq. (4.17). To increase the validity of the FE model either the mass of the interlayer could be set to zero or a thinner layer could be used for the model updating which then should be performed up to high frequencies.

At a T- or X-junction where both walls are flexible connected to the ceiling, the transmission
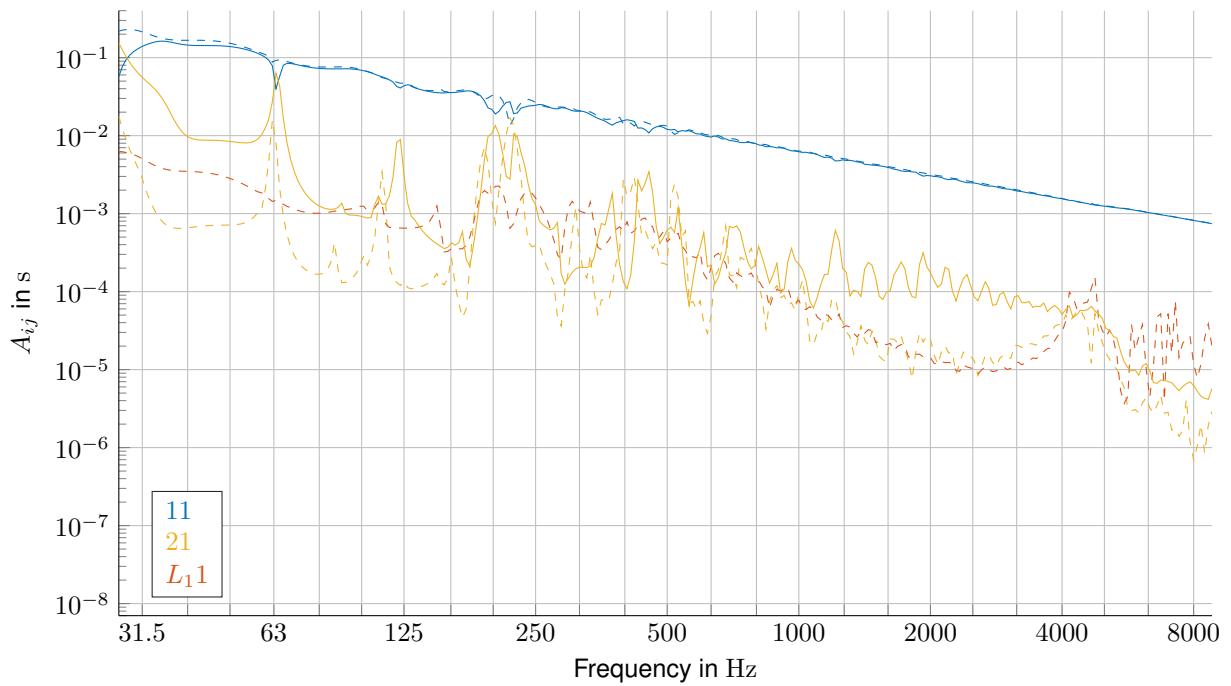
(a) Rigid $(-)$ vs. flexible $(--)$
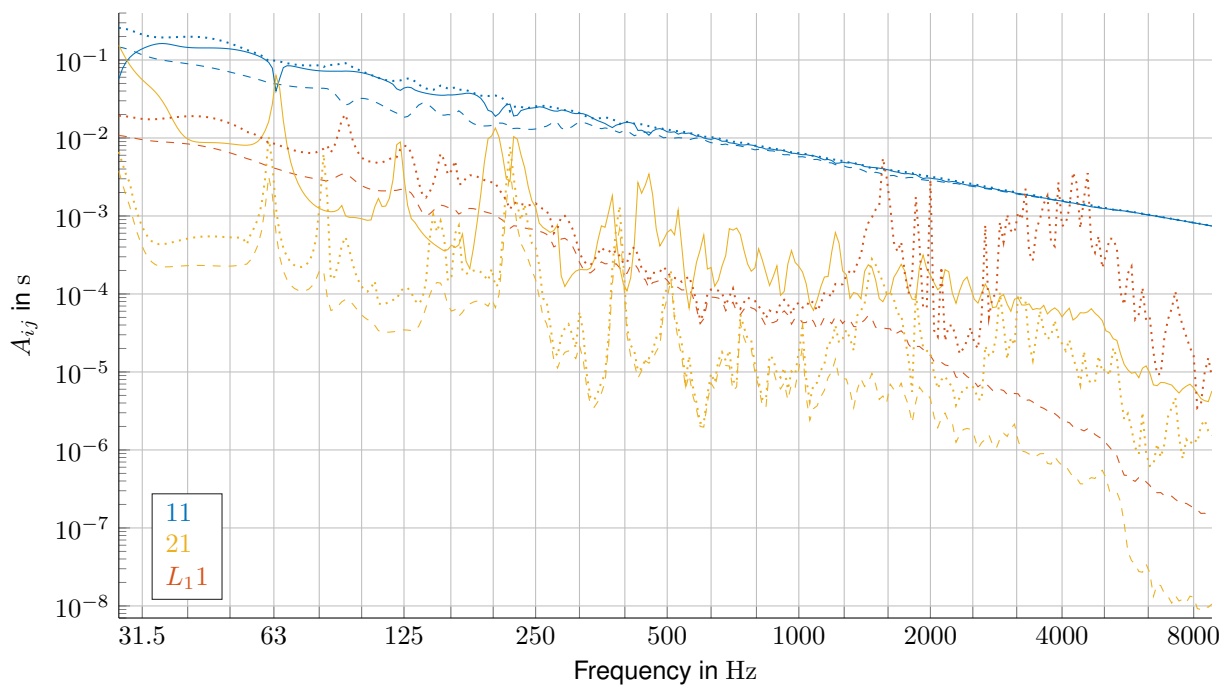
(b) Rigid $(-)$ vs. undamped, elastic interlayer $(\cdots)$ vs. damped, elastic interlayer $(--)$

Figure 4.37: Energy influence coefficients of different junctions for the excitation of subsystem 1.

from lower to upper wall is more reduced compared to the transmission into the ceiling as the energy has to cross twice an elastic interlayer (cf. subsection 4.4.3). This leads to a change from excited bending waves in the lower wall to in-plane waves and then back to bending waves in the upper wall [Wilhelm 2017].

Undamped vs. Damped, Elastic Interlayer: (Non)-Conservative Coupling

In the case, the elastic interlayer is mounted in the real junction, the thickness-shear resonances form part of the dynamic behavior of the junction. If the interlayer is undamped, then they contribute significantly to the energy distribution inside the structure. In Fig. 4.37b, $A_{L_1 1}$ of the undamped interlayer shows its first thickness-shear resonance at $1557\,\text{Hz}$ which coincides with Eq. (4.18) if the material properties of Tab. 4.4 and A.2 are inserted. For higher frequencies, the multiples of this thickness-shear resonance as well as thickness-stretch resonances can be identified by peak picking. The peaks of $A_{L_1 1}$ are partly above the normalized energy in the directly excited subsystem A_{11}. In the frequency range of the thickness resonances of the elastic interlayer, the material damping plays an important role. Neglecting it leads to this - at first glance - non-realistic energy distribution. Then, the thickness modes of the interlayer occur in a completely undamped material, whereas the subsystems are slightly damped.

According to Fig. 4.37b, the damping eliminates the effect of the thickness resonances. It shows, that damped, elastic interlayers, like the modeled Sylodyn ND, are able to reduce the transmission also in the frequency range of its thickness resonances. Here, the peaks of $A_{L_1 1}$ are cut since damping is most effective close to the resonance frequencies. This aspect is explained by simplifying Eq. (3.14) in order to describe the displacement of a single degree of freedom system:

$$u(\Omega) = \frac{F}{K - i\eta K - \Omega^2 M} \tag{4.19}$$

Equation (4.19) shows that, at resonance for $\Omega = \omega = \sqrt{\frac{K}{M}}$, the loss factor is decisive as the stiffness and the mass term cancel each other out:

$$K - \omega^2 M = 0 \tag{4.20}$$
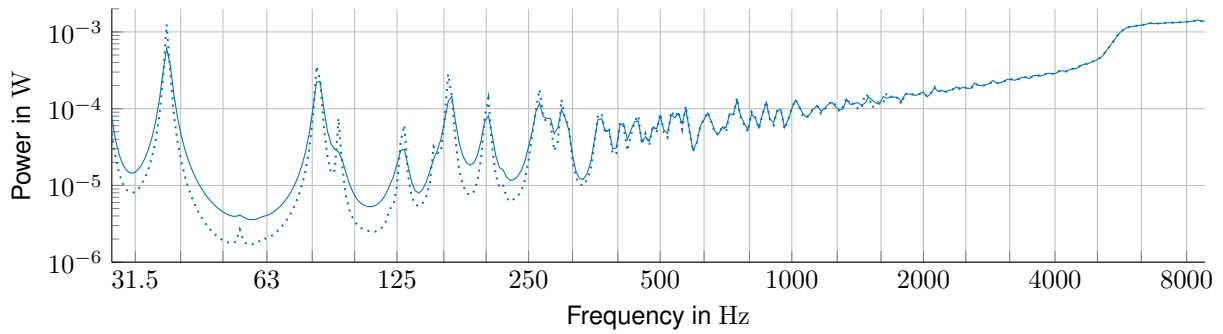
(a) Comparison of the input power into the wall
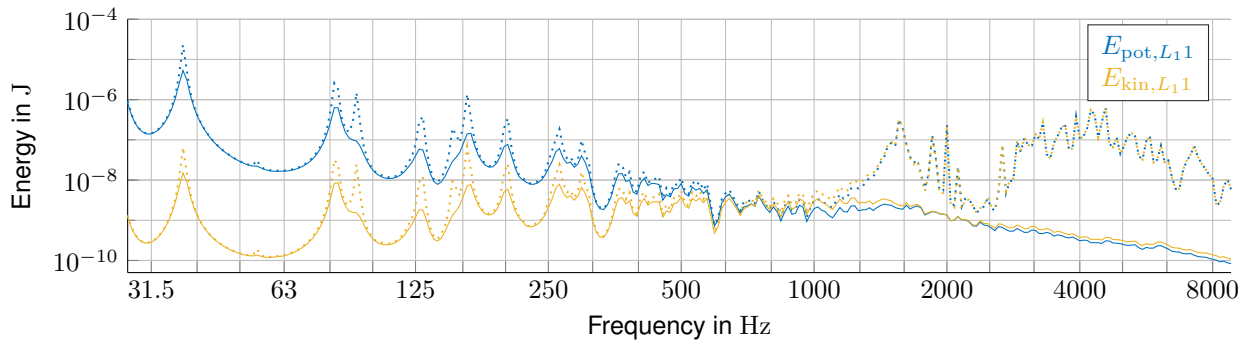
(b) Comparison of the energy inside the elastic interlayer due to excitation of the wall

Figure 4.38: L-junction with undamped ($\cdots$) or damped ($-$), elastic interlayer between wall and ceiling.

Thus, the displacement is indirectly proportional to the damping:

$$u(\Omega = \omega) = \frac{F}{-i\eta K} \tag{4.21}$$

This effect emerges more clearly for the energy as $E \sim u^2$ (cf. subsection 3.1.3) and flattens the energy curve in the range of the resonances (cf. Fig. 4.38b).

Figure 4.38a shows the input power into subsystem 1 for an L-junction with an elastic interlayer. The influence of the damping of the interlayer is especially noticeable at low frequencies, where the resonances of the system are well-separated: For the input power, the peaks become smaller, whereas the values in between the resonances become higher. This indicates that the input power integrated over the entire frequency domain is independent of damping. For the energy curve, the damping leads only to a flattening in the range of the resonances as shown above. In the high frequency range, where the thickness modes of the interlayer vibrate at resonance, this holds also for the energy influence coefficients (cf. Fig. 4.37b) since the input power is not influenced by the damping due to the high modal density.

At low frequencies, the bending wave transmission is diminished due to the smaller rotatory
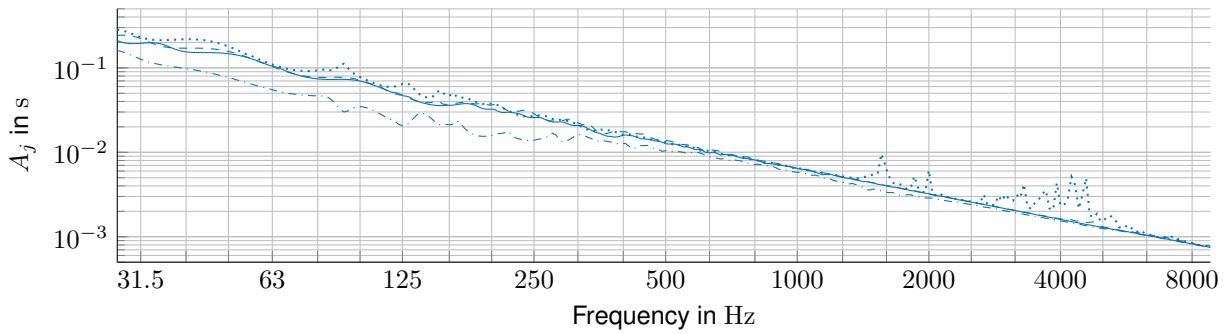
Figure 4.39: A_1, sum of the energy influence coefficients exciting subsystem 1, for different junctions: — rigid, —— flexible, $\cdots$ elastic interlayer, $- \cdot -$ damped, elastic interlayer.

stiffness of the L-junction with elastic interlayer compared to the rigid L-junction. Looking at the low frequency range of Fig. 4.38b, the potential energy of the elastic interlayer is much higher than the kinetic energy due to the large deformations resulting in a non-resonant excitation of the thickness modes in the stiffness dominated region of their amplification functions. For hysteretic damping, the input power is proportional to the potential energy of the total system according to Eq. (2.26). Already for the model with the undamped, elastic interlayer, reduced energy influence coefficients result in comparison to the rigid junction due to the high potential energy in the elastic interlayer. As the proportionality of the input power and the potential energy of the total system depends on the loss factor, the damping of the elastic interlayer leads to an additional increase of the input power. Thus, the energy influence coefficients have smaller values indicating a reduced energy flow into the adjacent subsystem, since the energy is normalized by the input power to compute energy influence coefficients.

Between 315 and $1000\,\text{Hz}$, the damping, which is increasing with frequency, has almost no effect. The kinetic energy of the interlayer approximates the potential energy (cf. Fig. 4.38b). Comparing the curves of the damped and the undamped case in Fig. 4.37b, A_{21} and A_{L_11} are similar, respectively. By contrast with the flexible junction, the energy flow into the adjacent subsystem is still small.

At high frequencies, the peaks in Fig. 4.38b result from the internal, thickness resonances of the undamped, elastic interlayer, whereas the peaks below $1000\,\text{Hz}$ result from resonances of the excited subsystem 1 which confirms the comparison with the corresponding input power in Fig. 4.38a. To sum it up, the stiffness proportional damping of the interlayer reduces the energy flow into the adjacent subsystem especially at high frequencies as it eliminates the thickness resonance peaks of the interlayer and at low frequencies since large deformations occur in the interlayer which result in a non-resonant excitation of the thickness modes.
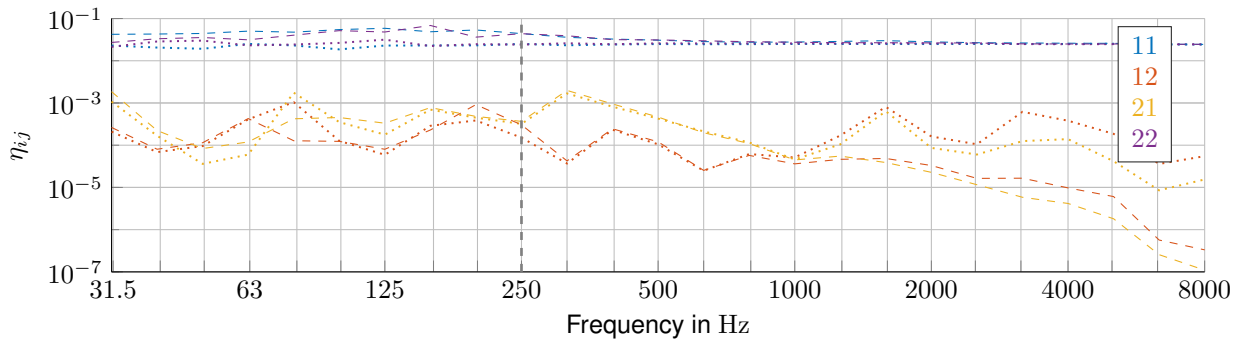
Figure 4.40: L-junction with undamped ($\cdots$) or damped ($--$), elastic interlayer between wall and ceiling: Comparison of the frequency averaged loss factors; Five modes per band and subsystem ($\vert$).

Summing up the energy influence coefficients over all m subsystems for one load case j, the total normalized energy A_j results:

$$A_j = \sum_i^m A_{ij} \tag{4.22}$$

Equation (4.22) corresponds to the addition of all entries belonging to column j of the energy influence coefficients matrix (cf. Eq. (3.40)). Compared to the damped interlayer, the undamped interlayer leads to a higher total normalized energy in Fig. 4.39 which corresponds to a lower damping averaged over the total structure. Whereas below 500 Hz, the damping affects the well-separated Eigenfrequencies of the components, above 1500 Hz, this is especially visibile due to the thickness resonances of the interlayer.

Neglecting the energy dissipated by the damped, elastic interlayer, the quadratic energy influence coefficients matrix, which represents the normalized energy flow into the subsystems, remains and can be inverted. Therefore, the resulting damping and coupling loss factors are affected by the non-conservative coupling. Fahy and de Yuan [1987] demonstrate analytically for two non-conservatively coupled oscillators that the power flow is not only proportional to the energy difference of the two oscillators but also to the absolute energy of the single oscillators. Moreover, the magnitude of the power flow depends on the direction. Sun et al [1987] show for continuous structures with a sufficient number of randomly distributed eigenfrequencies per band that the non-conservative coupling does almost not influence the exchange between the subsystems whereas it increases the damping loss factors. The damping loss factors do not only represent the internal losses of the corresponding subsystem but also losses of the elastic interlayer. Below the thickness resonances of the interlayer, these analytically gained results can be confirmed by the application of the EFA for more than five modes per one-third octave band. Exciting the interlayer at resonance, Fig. 4.40 demonstrates that the damping of the interlayer clearly affects the coupling loss factors, whereas

the damping loss factors are only slightly influenced because they are significantly higher than the coupling loss factors.

4.4.2 T-Junction with Continuous Wall and Bracket

As an alternative for the T-junction, the wall is not separated into two components and the ceiling is connected by a steel bracket with an elastic layer on top (cf. Fig. 4.1e). As the wall is continuous, strong coupling of subsystem 1 and 3 occurs over a wide frequency range due to a global modal behavior. The ceiling can be considered as weakly coupled to the wall. Thus, the energy is easily transmitted within the continuous wall between subsystem 1 and subsystem 3. The normalized energy in the lower wall is of similar size for an excitation of the upper or the lower wall as demonstrated in Fig. 4.41. For higher frequencies, $\tilde{A}_{13}$ starts to diverge slowly from $\tilde{A}_{11}$. Since the bending wave length decreases, more energy is dissipated in the excited subsystem and less is transmitted [Hambric et al 2016].

According to Fig. 4.43, strong coupling occurs up to $500\,\mathrm{Hz}$ since the coupling loss factors are partly higher than the damping loss factors (η_{13}, $\eta_{31} \geq \eta_{ii}$). The corresponding intersections of the energy influence coefficients are smoothed using frequency averaged quantities in Fig. 4.41. Moreover, Fig. 4.42 confirms strong coupling by high values of the condition number.

Up to $500\,\mathrm{Hz}$, the excitation of one of the wall subsystems mostly leads to a lower energy flow into the ceiling than the other way around ($\tilde{A}_{2i} < \tilde{A}_{i2}$ for $i = 1,3$). Since the load acts perpendicular to the components, a shear deformation of the elastic interlayer results due to the excitation of the wall, whereas for the excitation of the ceiling, a combination of longitudinal and rotational displacements arises. Since the shear stiffness of the interlayer is low compared to the longitudinal stiffness, the impedance difference for the excitation of the wall subsystems is higher which yields a more effective decoupling of the two components. This phenomenon is confirmed by the energy inside the elastic interlayer, which is between one and two orders of magnitude higher for an excitation of the ceiling (not depicted).

Between $500\,\mathrm{Hz}$ and the first thickness-shear resonance of the wall at $2889\,\mathrm{Hz}$, the exchange between wall and ceiling is of similar size for both directions ($\tilde{A}_{2i} \approx \tilde{A}_{i2}$ for $i = 1,3$). For higher frequencies, the length and width of the plates as well as the corresponding mode shapes seem to become insignificant for the energy flow due to the domination of the thickness modes. The coupling strength of the two subsystems forming the continuous wall is reduced which leads to a weakly coupled structure. Moreover, the exchange with the adjacent ceiling
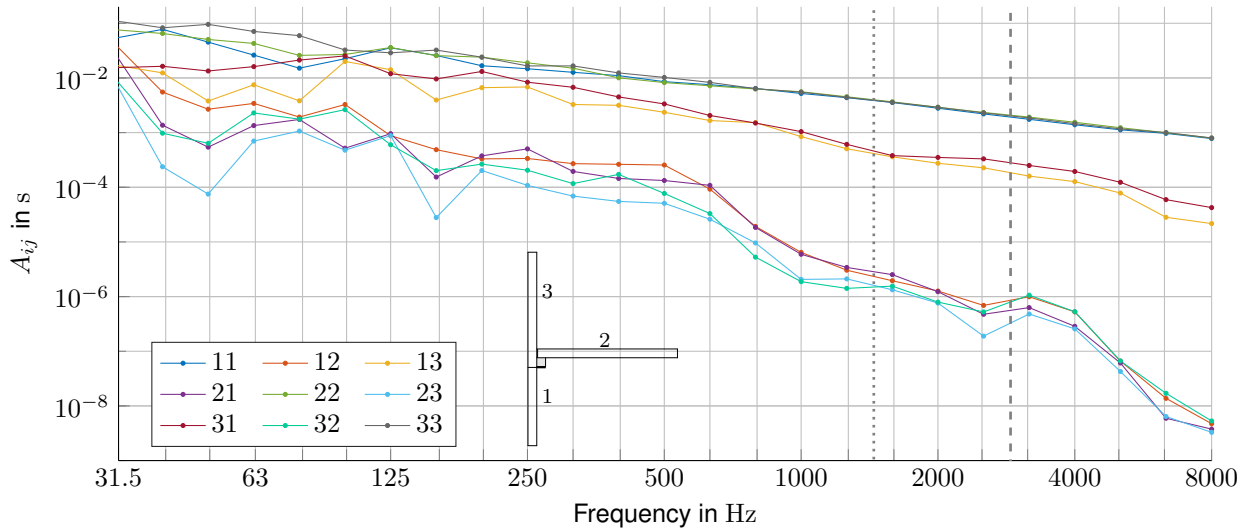
Figure 4.41: Frequency averaged energy influence coefficients of a T-junction with continuous wall; First thickness-shear resonance of ceiling (:) and wall (¦).

is almost only dominated by the thickness of the plates and thus, the energy flow is grouped into excitation of wall and of ceiling ($\tilde{A}_{21} = \tilde{A}_{23} < \tilde{A}_{12} = \tilde{A}_{32}$). This holds also true for the coupling loss factors ($\eta_{12} \approx \eta_{32}$, $\eta_{21} \approx \eta_{23}$) in Fig. 4.43.

Negative Coupling Loss Factors in the case of three subsystems

Below the first thickness-shear resonance of the ceiling at 1445 Hz, the energy exchange between ceiling and upper wall is always slightly smaller compared to the exchange with the lower wall (A_{23}, $A_{32} < A_{21}$, A_{12}). Combined with the relatively high energy transmission between the subsystems of the continuous wall (A_{13}, A_{31}), this leads to negative coupling loss factors η_{32} and η_{23}. To be able to clearly identify them and to avoid physically wrong results, the loss factors are not averaged over the frequency band as depicted in Fig. 4.43.

Since the structure contains couplings of significantly different strength, the energy influence coefficients can be divided into four groups according to their order of magnitude. This can lead to negative coupling loss factors. By contrast, the T-junction investigated in subsection 4.3.4, where the two walls are separated by the ceiling and the components are rigidly connected, has energy influence coefficients A_{ij} of similar size (cf. Fig. 4.32a) leading to positive coupling loss factors as the subsystems are weakly coupled for the out-of-plane excitation (cf. Fig. 4.32c). The inversion of the energy influence matrix $[A]$ (cf. Eq. (3.46)) to compute the coupling loss factor η_{ij} can be mathematically expressed by the subdeterminant $\det[A_{i,j}]$ whereby $[A_{i,j}]$ is a submatrix which results by canceling the row i and the column
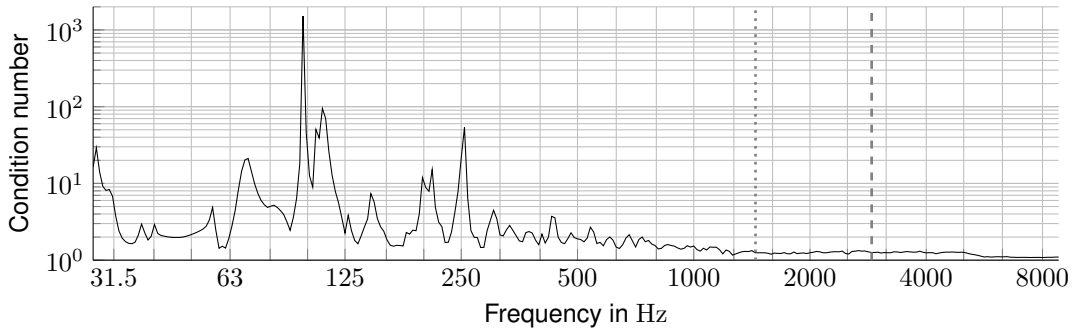
Figure 4.42: T-junction with continuous wall: Condition number of $[A]$; First thickness-shear resonance of ceiling (:) and wall (¦).
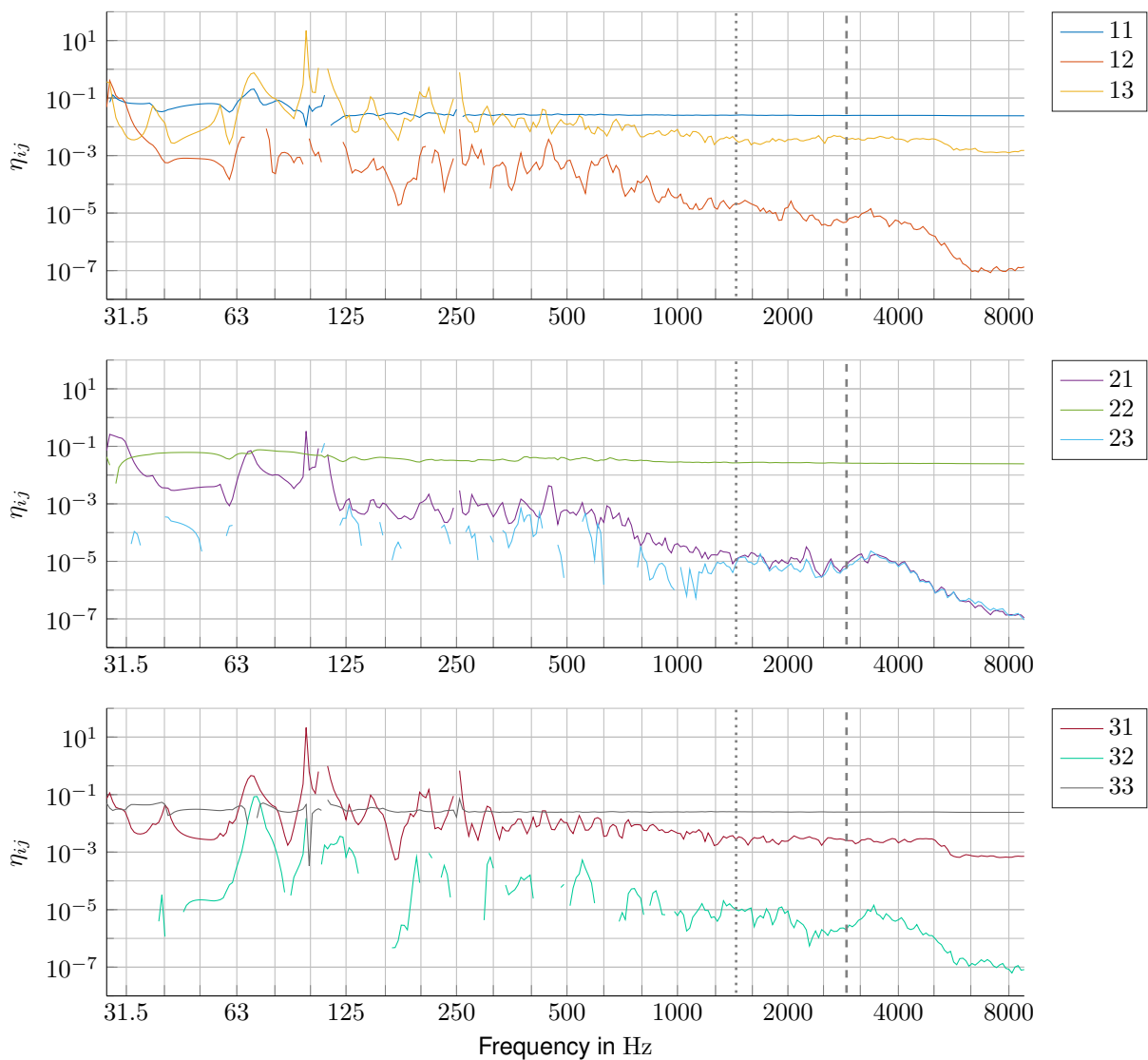
Figure 4.43: T-junction with continuous wall: Loss factors quantifying the losses of subsystem 1, 2 and 3 (negative values not depicted due to logarithmic scale); First thickness-shear resonance of ceiling (:) and wall (¦).

j of $[A]$ [Bronštejn et al 2016]:

$$\eta_{ij} = \frac{-1}{\Omega \det [A]} \left((-1)^{i+j} \det [A_{i,j}] \right) \tag{4.23}$$

According to Fig. 4.41, the energy influence coefficients matrix is diagonally dominant above $250\,\mathrm{Hz}$ and thus $\det [A]$ is positive. Hence, the subdeterminant $\det [A_{i,j}]$ has to be positive to receive a positive coupling loss factor η_{ij}. Since A_{13} is only a little less than A_{11} due to the continuous wall and A_{23} is slightly less than A_{21}, a negative coupling loss factor η_{32} might occur:

$$\det [A_{3,2}] = A_{11}A_{23} - A_{13}A_{21} > 0 \quad \rightarrow \quad \eta_{32} < 0 \tag{4.24}$$

Below the first thickness-shear resonance of the ceiling, this is the case at several discrete frequencies as depicted in Fig. 4.43. Above $500\,\mathrm{Hz}$, no strong coupling can be identified according to the definition in subsection 3.2.3 and 4.2.2 by energy influence coefficients and loss factors. Also the condition number has comparatively small values. Hence, it serves mainly to check if all subsystems are weakly coupled. Close by the first thickness-shear resonance of the ceiling, where no more negative coupling loss factors occur, an additional decrease of the condition number towards unity can be recognized.

Division into only two subsystems

The wall is divided into two subsystems at the discontinuity due to the connection of the bracket for the ceiling. The division into three subsystems gives detailed results about the energy flow into and from different parts of the continuous wall using energy influence coefficients. This can be useful for the prediction of the sound transmission in multistory buildings to distinguish between the sound transmission into two different floors.

An alternative abstraction of this T-junction would be a division into two subsystems considering the continuous wall as one waveguide since the modal behavior of the wall is widely not affected by the bracket. On the one hand, the higher abstraction leads to less resolution in space. On the other hand, the matrix is easier to invert which leads to numerically more robust coupling loss factors with higher precision since by the subsystem division is accounted for the strong coupling behavior. Thus, no negative coupling loss factors occur as demonstrated in Fig. 4.44. Exciting either the lower or the upper wall, the location of the respective 100 loaded elements influences the coupling loss factor $\tilde{\eta}_{12}$ below the first thickness-shear resonance of the wall. At higher frequencies, the energy flow depends on the
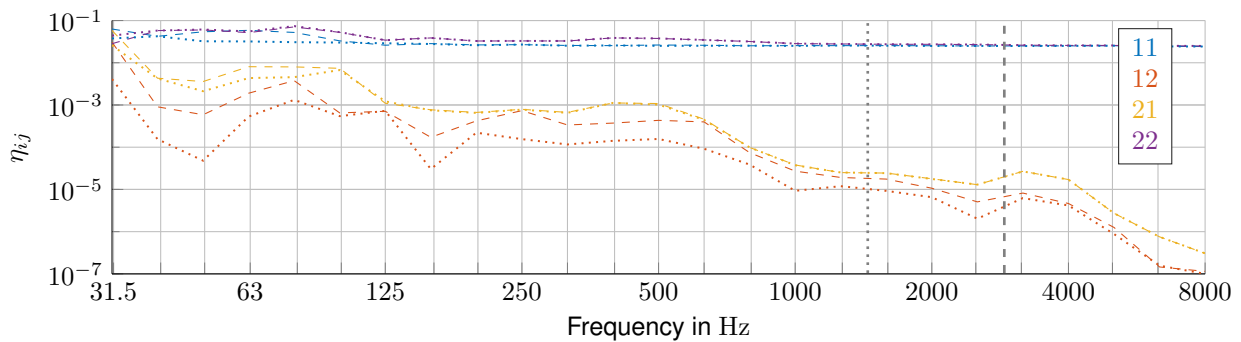
Figure 4.44: Frequency averaged loss factors of a T-junction with continuous wall divided into only two subsystems: Wall (1) and ceiling (2). Excitation of lower ($--$) or upper ($\cdots$) wall; First thickness-shear resonance of ceiling (:) and wall (¦).

distance of the loads from the junction as shown in subsection 4.3.3. Since both excitations lead to a similar load density, a similar $\tilde{\eta}_{12}$ results.

4.4.3 Comparison of L-, T- and X-Junction

In multistory buildings, three different types of junctions are distinguished. Depending on the location in the monolithic construction of Fig. 4.45a, either an L-, a T- or an X-junction (cf. Fig. 4.45b,c,d) is extracted. The transmission behavior of the specific junction is determined by means of the energy exchange between the adjacent components assuming that the influence of the remaining structure is negligible. This conforms to the SEA assumption of weak coupling. This is fulfilled, if the inverted energy influence coefficients matrix of the entire building is a proper-SEA matrix (cf. subsection 3.2.3). Then, the coupling loss factors depend only on the junction and its adjacent subsystems, since there is no indirect coupling.

In this subsection, the influence of additional components which adjoin at one junction is investigated by comparing an L-, a T- and an X-junction, whose components are connected flexible. Therefore, an elastic interlayer between wall and ceiling is used, whose properties are given in Tab. 4.4. In the case of the X-junction, the two subsystems representing the ceiling are either rigidly connected, which corresponds to a continuous ceiling, or separated. For comparability, the common subsystems of the four different junctions have the same physical properties and they are excited at the same locations by a RotR loading with identical phase shifts.

Figure 4.46a shows the energy flow into the lower wall (subsystem 1) and Fig. 4.46b into the right ceiling (subsystem 2) for the excitation of each subsystem of the four different
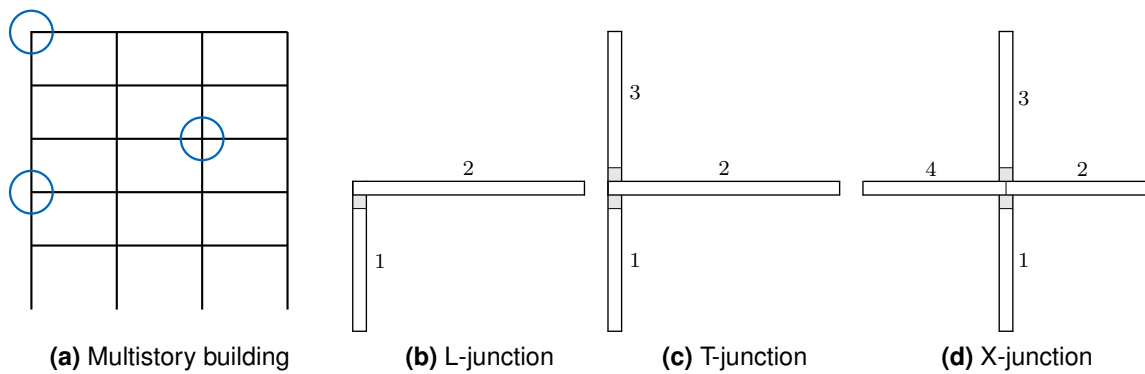
Figure 4.45: Different junction geometries in multistory buildings.

junctions: L, T, X with continuous ceiling and X with separated ceilings. Generally holds that the higher the number of subsystems is, the less normalized energy is transmitted into one subsystem. Due to the elastic interlayers between wall and ceiling, strong coupling does not occur in the investigated frequency range. Above 2500 Hz, the off-diagonal entries of the energy influence coefficients matrix start to increase with frequency and seem to approach similar, high values above 4000 Hz. There, the thickness resonances of the undamped, elastic interlayer dominate the transmission behavior (cf. subsection 4.4.1).

In Fig. 4.46a, the energy flow from the ceiling into the lower wall (A_{12}) is similar for the L- and the T-junction above 800 Hz. In the case of the X-junctions, both variants show similar energy flows into the wall independently of the excited ceiling ($A_{12} \approx A_{14}$). Comparing the normalized energy inside the lower wall in Fig. 4.46a, the excitation of the upper wall leads to a smaller energy flow than the excitation of the ceiling ($A_{13} < A_{12}, A_{14}$), except in some one-third octave bands around 250 Hz, as the energy has to pass two elastic interlayers.

From 250 Hz on, the transmission between the walls (A_{13}) of both X-junctions is quite similar and clearly smaller compared to the T-junction. At low frequencies, the X-junction with the connected ceilings leads to the highest energy transfer between the two walls. A_{11} results to be almost identical for the different junctions since neither the damping loss factor nor any other physical property of the subsystem is changed.

Comparing the energy flows into subsystem 2 in Fig. 4.46b, the distinct behavior of A_{24} attracts attention. The separation of the two ceilings takes effect and leads to a clearly smaller energy transfer, except in the one-third octave band of 125 Hz. Here, the mode shapes of both X-junctions have in common that the ceiling does either not participate (cf. Fig. 4.47a and d) or only one of the two ceiling subsystems is involved (cf. Fig. 4.47b and e) as they have a different length. This means, that independently of a separation of
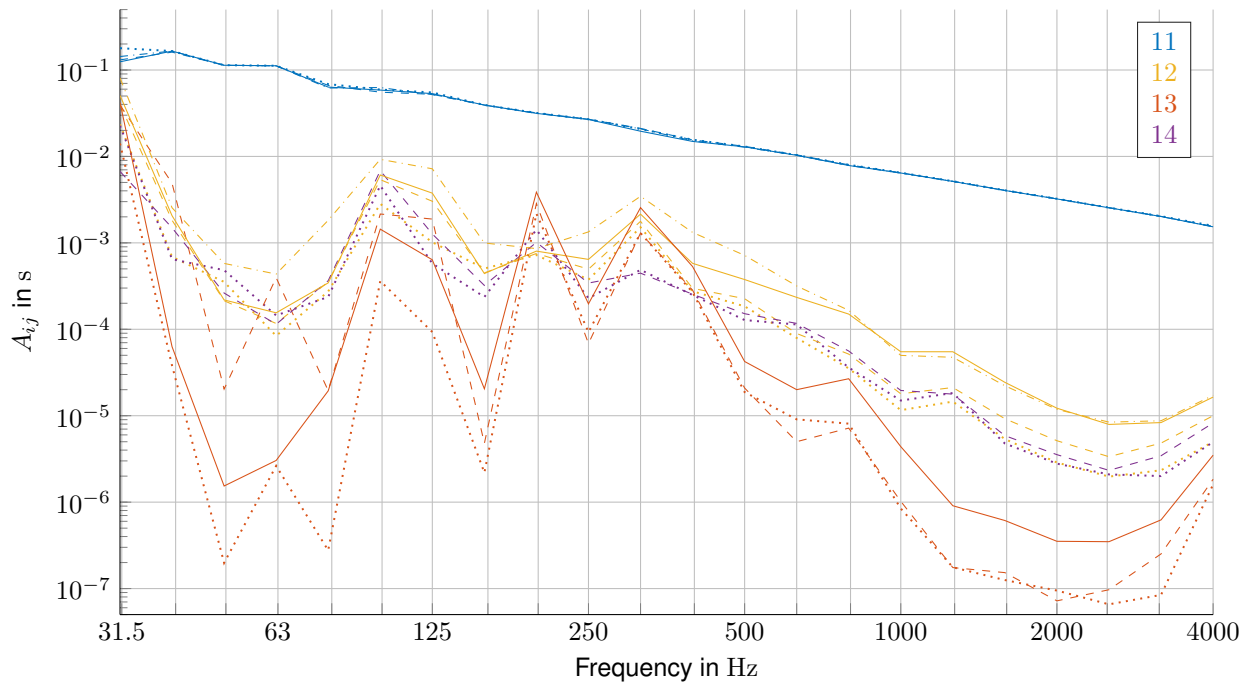
(a) Energy influence coefficients $\tilde{A}_{1j}$
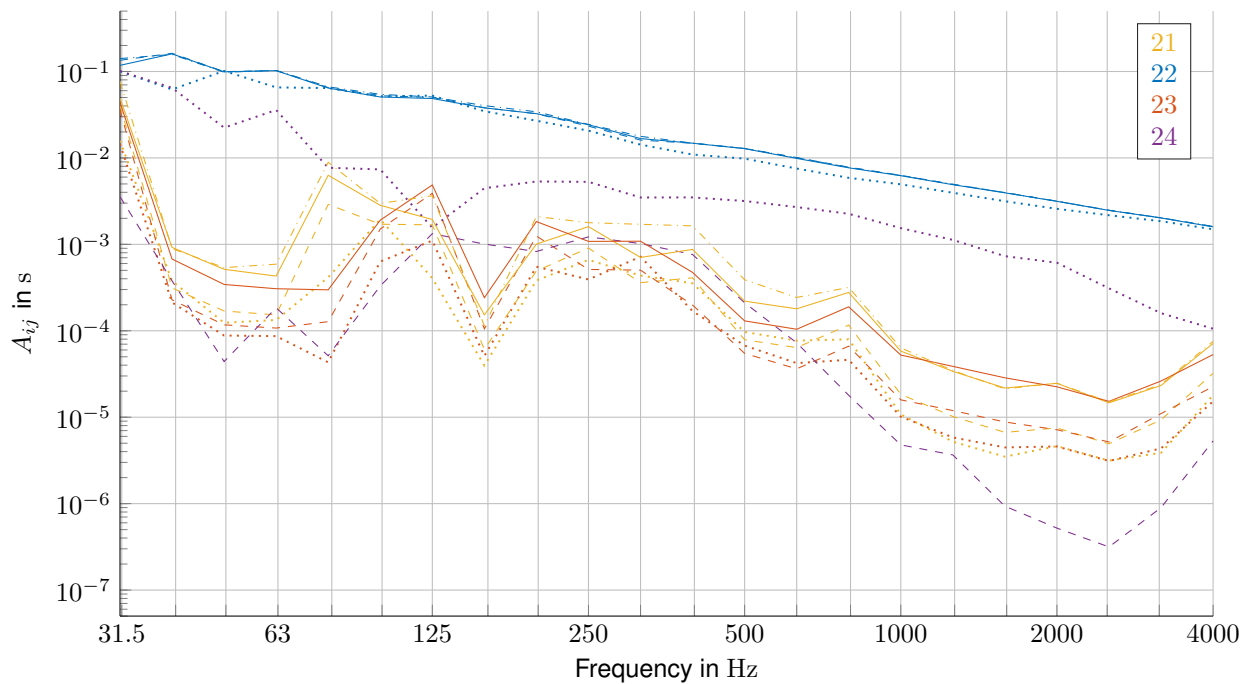
(b) Energy influence coefficients $\tilde{A}_{2j}$

Figure 4.46: Frequency averaged energy flow into subsystem 1 and 2, respectively, exciting the subsystems of the following junctions: L $(- \cdot -)$, T $(-)$, X $(\cdots)$ and X with separated ceilings $(--)$.

(a) 112 Hz   **(b)** 119 Hz   **(c)** 148 Hz

(d) 112 Hz   **(e)** 116 Hz
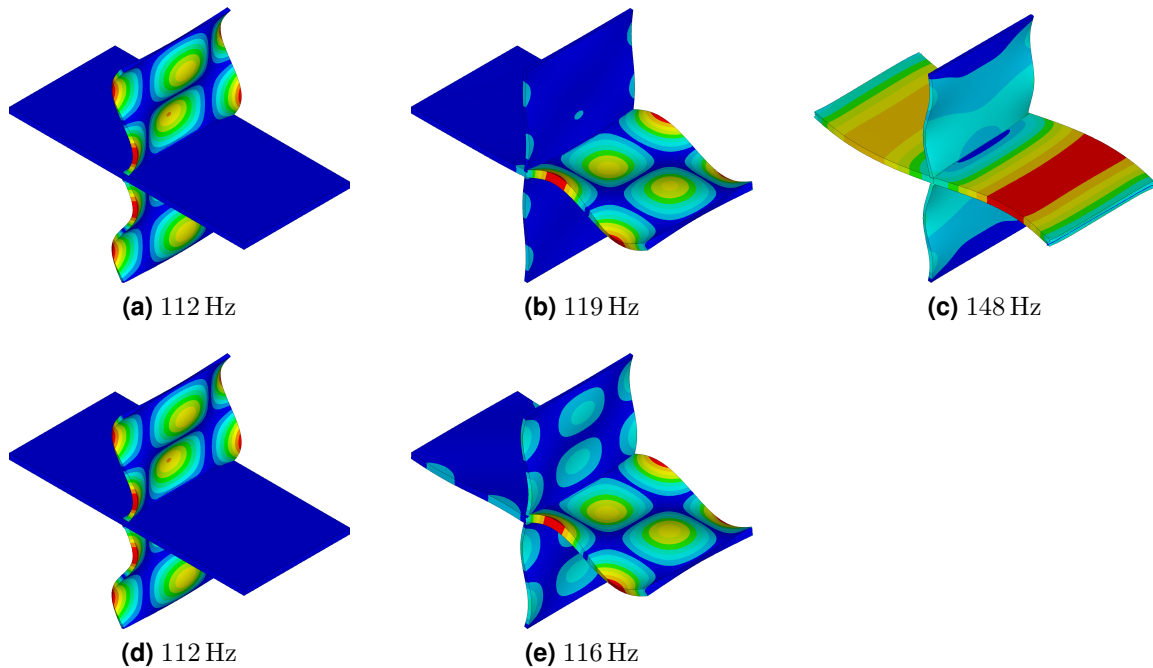
Figure 4.47: Mode shapes of the X-junction with continuous ceiling (top row) and with separated ceilings (bottom row); Colors indicate vector sum of displacements.

the ceiling there are almost no mode shapes to transport the energy horizontally from one ceiling subsystem to the other (A_{24}). Compared to A_{24}, the transmission from wall to ceiling (A_{21}, A_{23}) is of similar size for the continuous ceiling or it even dominates in the case of the separated ceiling. In Fig. 4.47c, the whole ceiling oscillates due to a combination of in-plane and bending waves. This modal behavior only arises for the X-junction with continuous ceiling.

The rigid connection of the two ceilings results in an energy influence coefficient A_{24} which is less than one order of magnitude smaller than A_{22} over a wide frequency range. Due to the high energy transfer into the adjacent ceiling, A_{22} is slightly reduced compared to the other junction geometries. The division into two subsystems still makes sense as the connection of the walls to the ceilings states a discontinuity where the energy is transmitted into the different components. Furthermore, the two ceiling subsystems are not strongly coupled with respect to the definition in subsection 3.2.3 and 4.2.2 since their energy influence coefficients do not coincide above 40 Hz. Moreover, the condition number in Fig. 4.48 indicates that the coupling is stronger compared to the other junctions. Since the lower wall and the upper wall have identical physical properties, their excitation by 100 loads at different locations leads to almost identical results above 800 Hz ($A_{21} = A_{23}$). At lower frequencies, the non-symmetrical spatial distribution of the loading excites different modes with different intensity.
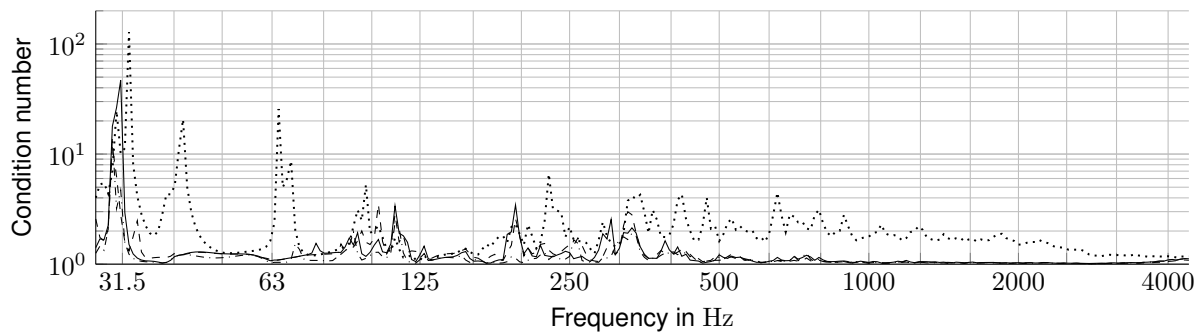
Figure 4.48: Condition number of $[A]$ for different junction geometries: L $(- \cdot -)$, T $(-)$, X $(\cdots)$ and X with separated ceilings $(--)$.

4.5 Statistical Examinations - Number of Loads

To predict the energy flow as representative as possible for a structure, in case of an unknown loading the average over several realizations of a varying RotR loading is taken. Loading each element at each frequency step leads to a high computational effort which is attempted to be minimized. Therefore, the number of loads shall be reduced. To be able to quantify its influence, 100 realizations are performed on each of six different numbers of loads. The criteria for the RotR excitation are still fulfilled as the forces are statistically independent to produce an incoherent modal response and subsequently equipartition of modal energy.

In subsection 4.5.1, the influence of the number of loads used for the RotR excitation is examined by means of the coefficient of variation. Moreover, the relation between input power and substem energy is compared for individual realizations in subsection 4.5.2. In subsection 4.5.3 the sample mean values are compared to the ensemble average calculated by the SEA and the confidence interval is illustrated to predict the true mean with a certain confidence level. The section is completed by concluding remarks in subsection 4.5.4. The used material slightly differs from the foregoing sections and is given in Tab. A.1. It is based on the same measurements at the L-junction within the joint research project [Mecking et al 2017a] whereby the error between selected measured and computed natural frequencies is minimized by means of an Bayesian updating [Paolini et al 2016]. The geometry is listed in Tab. 4.3.

4.5.1 Coefficient of Variation

Figure 4.49 shows the coefficient of variation for different numbers of loads. An increasing number of loads leads to a lower coefficient of variation for the energy influence coefficients
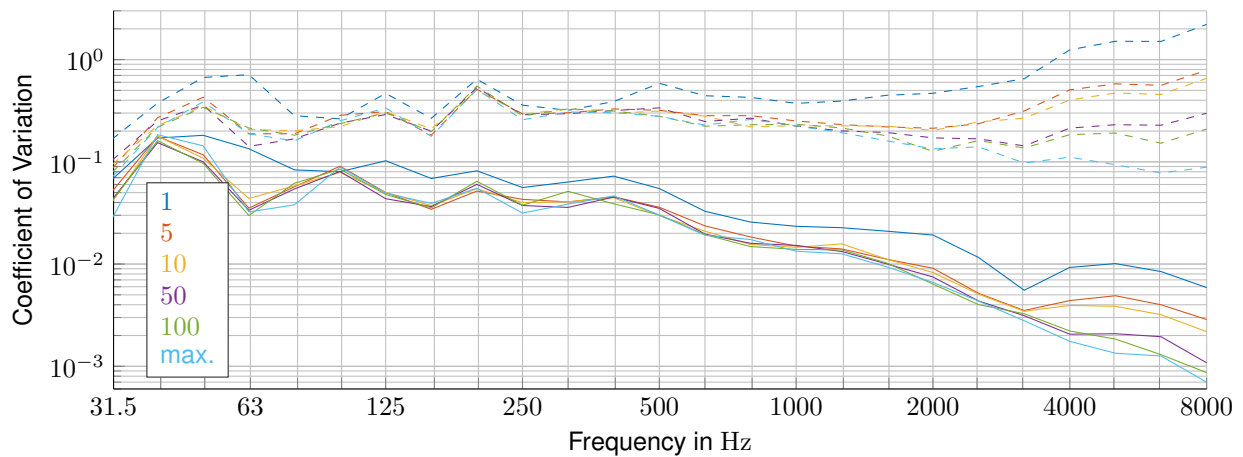
Figure 4.49: Coefficients of variation of A_{12} ($--$) and A_{22} ($-$) based on 100 realizations for different numbers of loads n_l; n_l=max. corresponds to loading each element per subsystem surface.

A_{12} and A_{22}. The single load leads to a significantly higher deviation between the individual realizations over the entire frequency range. For several loads per realization, the first thickness-shear resonances of the excited plate 2 at 1370 and 1823 Hz state the lower limit of different levels according to the number of loads. At the first thickness-stretch resonance (3860 Hz), the curves are already well separated. At low frequencies, one-third octave bands with few or none resonant modes might also lead to deviations. The coefficient of variation of the power P_2 decreases with increasing frequency as the locations of the loads become less decisive for shorter wavelengths. As P_2 is fully correlated over the entire frequency range with the energy in the excited subsystem E_{22}, its coefficient of variation and the one of A_{22} behave analogously. Due to a decreasing correlation coefficient ρ_{12} of P_2 and E_{12} the variation of A_{12} behaves differently. It remains in the same magnitude below the thickness resonances.

4.5.2 Individual Realizations: Input Power vs. Subsystem Energy

Figure 4.50 presents the relationship between the input power and the energy in the excited and the adjacent subsystem, respectively, for 100 realizations with a varying excitation pattern. Thereby, all elements on the surface of the plate are loaded (n_l=max.) as depicted in Fig. 3.5. Three selected one-third octave bands are depicted. The global modes in the 100 Hz one-third octave band lead to a high correlation of the input power with the energy in the excited and the indirectly excited subsystem, too. This definite relationship holds for the higher one-third octave bands only in the excited subsystem. It seems that in the non-excited one the energy behaves nearly independent of the injected power as the individual
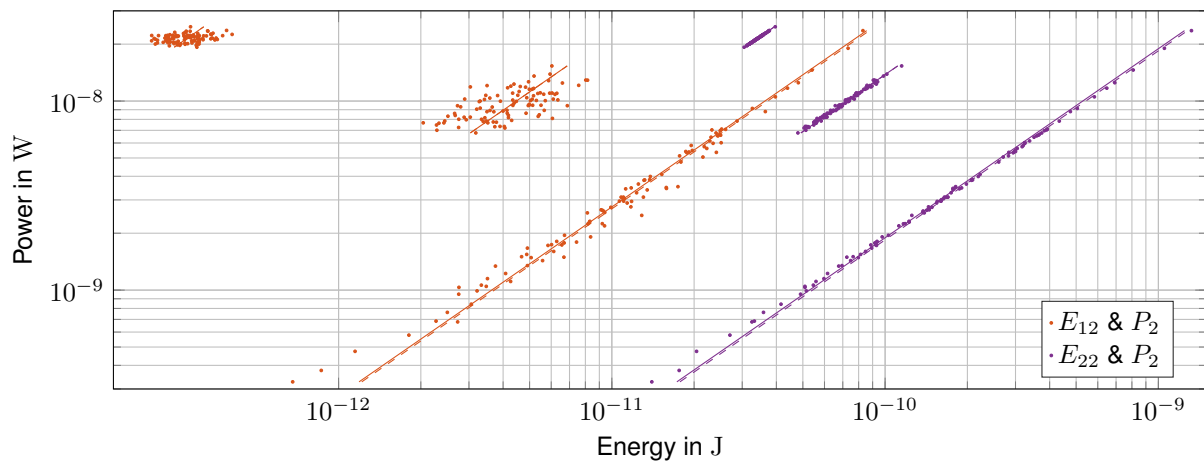
Figure 4.50: Input power vs. subsystem energy (n=100, n_l=max.): $\overline{A}$ $(-)$, $\overline{A}$ weighted by power $(--)$; from right to left: 100 Hz ($\rho_{12} = 0.99, \rho_{22} = 1.0$), 630 Hz ($\rho_{12} = 0.61, \rho_{22} = 1.0$) and 3150 Hz ($\rho_{12} = 0.25, \rho_{22} = 1.0$).

realizations form a cloud instead of a line. This indicates that the subsystems are weakly coupled. Compared to the excited subsystem the energetic level is orders of magnitudes smaller. According to the investigations in subsection 4.3.3, the latter is influenced by the varying excitation pattern.

As mentioned in subsection 3.3.2, only at low frequencies it makes a difference if the energy influence coefficients are averaged unweighted (cf. Eq. (3.90)) or if the input power is used as a weigthing factor (cf. Eq. (3.41)). Hence, only for the one-third octave band of 100 Hz the two line types corresponding to the two arithmetic averages over the individual realizations can be distinguished.

4.5.3 Sample Mean, Confidence Interval - Comparison to the SEA

According to Fig. 4.51, the arithmetic sample mean values of the energy influence coefficients, $\overline{A}_{22}$ and $\overline{A}_{12}$, show some small deviations for different numbers of loads at low frequencies. Varying the number of loads leads to different levels of $\overline{A}_{12}$ in the high frequency range where the thickness modes vibrate at resonance. Here, the coefficients of variation of A_{12} reach high values especially for a low number of loads as depicted in Fig. 4.49.

Since a high coefficient of variation results in a large confidence interval, Fig. 4.52 demonstrates that the true mean could be independent of the number of loads also at high frequencies: For the limit cases $n_l = 1$, $n_l = 100$ and $n_l =$max., the sample mean as well as the 99 % confidence interval is illustrated. Since the confidence interval of the true mean for $n_l = 100$ is part of the confidence interval for $n_l = 1$, it is possible that both cases have a
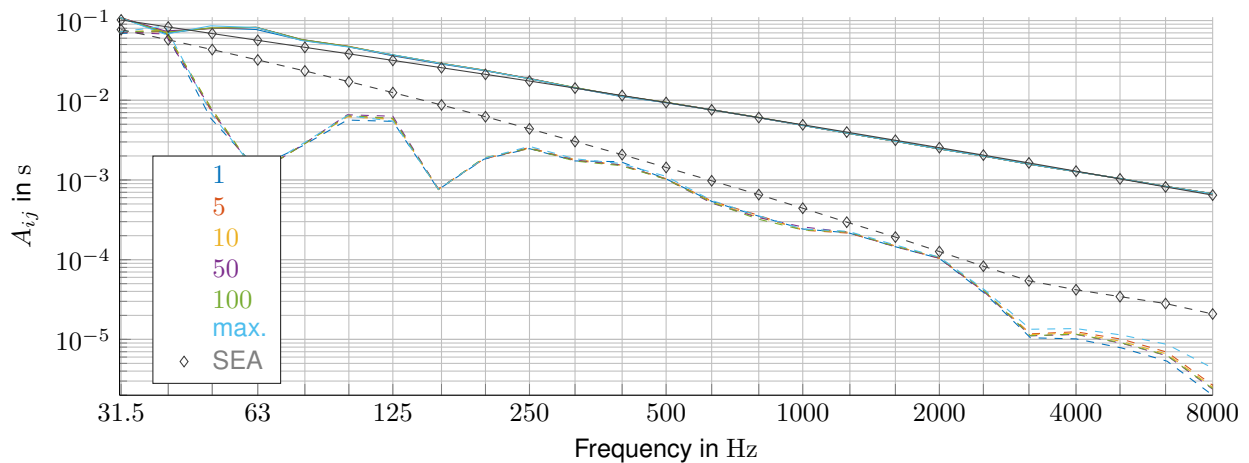
Figure 4.51: Sample mean value of A_{12} ($--$) and A_{22} ($-$) based on 100 realizations of different numbers of loads n_l compared to ensemble average from the SEA.

common true mean. This also holds for the not depicted confidence intervals of $n_l = 5$, 10 and 50 since each of them is part of all confidence intervals which belong to a lower number of loads.

By contrast, the true mean of $n_l =$ max. is not part of the intersection of $n_l = 1$ and $n_l = 100$ above the first thickness-stretch resonance (cf. Fig. 4.52). As demonstrated in subsection 4.3.3, the energy flow depends at high frequencies on the location of the load and its distance to the junction. Applying different numbers of loads for the RotR excitation results in differently large load densities, which are equally distributed on the plate and therefore also at the junction. In summary, the load density and thus the number of loads of the RotR excitation are responsible for the amount of energy which is transmitted into the adjacent component at high frequencies as indicated by Fig. 4.51.

Comparison to the SEA

As shown in Fig. 4.51, the energy flow in the L-junction is also investigated by means of the SEA. In the SEA model, the rigid connection of wall and ceiling is modeled by a line coupling. Here, only the bending waves are excited by a unit input power for the comparison with the energy flow in the EFA model, where the plates are excited by a perpendicular RotR excitation. To compare the normalized energies of each plate, the contributions of bending, shear and longitudinal waves are summed up in the SEA model .

The excitation of the bending waves in subsystem 2 results in an almost identical ensemble average for the normalized energy in the excited subsystem (A_{22}) comparing the SEA and the
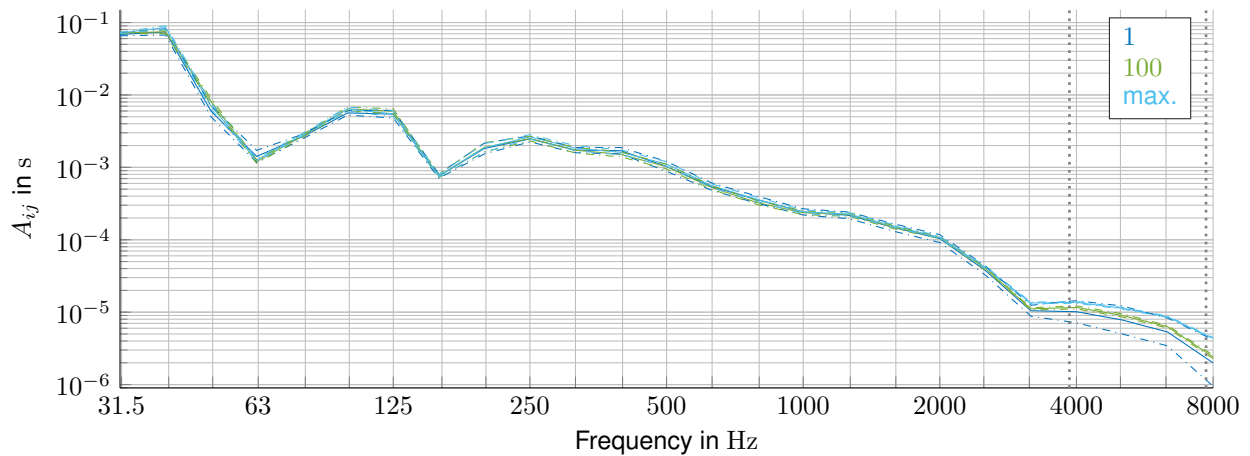
Figure 4.52: Sample mean $(-)$ plus 99% confidence interval $(-\cdot-)$ of energy influence coefficient A_{12} based on 100 realizations for $n_l = 1$, 100 and max.; Thickness-stretch resonances (:).

EFA model. The normalized energy in the adjacent subsystem A_{12} is overestimated at low and high frequencies as the assumptions of the SEA and of the Mindlin wave approximation are not fulfilled, respectively. In the one-third octave band of $250\,\mathrm{Hz}$ the decisive subsystem has five modes per band reaching a modal overlap factor of unity at $315\,\mathrm{Hz}$.

4.5.4 Conclusion

In case the load is unknown, a robust estimation of the energy flow is needed for a general prediction of sound transmission. The SEA delivers an ensemble average within a limited frequency range. The EFA can also be applied at low frequencies with a small amount of modes as well as at high frequencies taking thickness modes into account. One realization of the EFA delivers a prediction for one specific load case. By averaging over randomly varying load cases, a robust energy flow with respect to the load can be predicted. The resulting energy influence coefficients are as universal as possible to be able to generally assess the vibroacoustic behavior of a junction. In subsection 3.3.3, a procedure is shown to find a minimum number of realizations to compute energy influence coefficients within a certain confidence interval (cf. Fig. 3.6). As a higher number of loads leads to a lower coefficient of variation, the number of realizations can be reduced to reach a certain confidence level. [Winter et al 2017c]

5 Summary: Energy Flow Prediction Depending on the Frequency Range

The investigations of various junctions consisting mostly of CLT plates, which are illustrated in chapter 4, demonstrate that the frequency range can be partitioned into different ranges. Thereby, the vibrational behavior of the components, which depends on their physical properties, defines the basis for the partitioning. A proposal for a division into a low, a mid and a high frequency range is given. The ranges cover the extended frequency range of building acoustics. They are distinguished in the subsequent paragraphs.

5.1 Low Frequency Range

The low frequency range is characterized by well separated modes leading to a low modal density. Here, a deterministic prediction is important since geometric dimensions (cf. subsection 4.3.2, 4.3.3) as well as the type of excitation (cf. subsection 4.2.2, 4.3.5) are decisive for the vibration behavior and for the energy flow into adjacent components. Thereby, RotR can help to reduce the influence of strong coupling and thus, to avoid negative coupling loss factors (cf. subsection 4.2.2). In the case of a single load, the influence of the load location on the frequency-averaged quantities is limited as long as it acts sufficiently outside of the nodal lines of the mode shapes (cf. subsection 4.3.3).

The prerequisites for analytical solutions like the wave approach, which constitutes a basis for the SEA, are not fulfilled and their predictions mostly overestimate the energy transmission (cf. subsection 4.5.3). Using the EFA, a coarse mesh combined with a high resolution in the frequency range is appropriate for structure-borne sound predictions in the low frequency range (cf. subsection 4.1.5, 4.1.6).

An evaluation of the energy flow by means of the energy influence coefficients is recommended, whereby an inversion to loss factors is also possible. Their precision can be affected

by a bad conditioning of the energy influence coefficients matrix. The generation of coupling loss factors by the EFA for the use in SEA models can lead to difficulties since negative coupling loss factors tend to occur due to non-resonant transmission or strong coupling.

The engineering measure recommended by DIN EN ISO 12354-1 [2017] is the vibration reduction index, which characterizes the energy transmission over a junction only in dependency of the properties of the junction itself. Complying with this definition, the vibration reduction index cannot be determined in the low frequency range since the SEA assumptions are not fulfilled. By means of the EFA, coupling loss factors and resultant vibration reduction indices can be calculated with the restriction that they depend on the geometry of the adjacent components and on the load case. Since mainly bending waves occur, a consistent computation of the vibration reduction index by means of the coupling loss factor from the EFA and the group velocity of the effective bending waves is possible (cf. section 4.2).

Compared to the rigid junction, the bending wave transmission of a junction with elastic interlayer is diminished due to the smaller rotatory stiffness. Especially at low frequencies, large deformations of the interlayer occur resulting in a non-resonant excitation of its thickness modes. Thereby, the stiffness proportional damping of the interlayer additionally reduces the energy flow into the adjacent subsystem (cf. subsection 4.4.1).

A single plate can be modeled easily by shell elements, which neglect the small amount of non-resonant contribution of potential energy due to the disregard of through-thickness effects (cf. subsection 4.3.1). In contrast, the response of a structure consisting of plate-like components is sensitive to the element choice. The reduction to the middle plane and distinct implementations of a junction influence significantly the eigenfrequencies, computed either by shell or by solid element models. Indeed, the boundary conditions as well as the ratio between dimension and wave length are decisive for the eigenfrequencies [Winter et al 2017a].

5.2 Mid Frequency Range

Within this thesis, the mid frequency range is defined to start where the SEA gives suitable predictions. The lower limit can be determined by a sufficient number of modes per one-third octave band. On the basis of the performed comparisons in section 4.2 and especially in subsection 4.5.3, five modes per band and a modal overlap factor greater or equal unity resulted to be convenient since then comparable results are obtained by the EFA and the SEA. This coincides with established opinions e.g. formulated by Müller [1999], Culla and

Sestieri [2006] as well as Fahy and Mohammed [1992]. For in-plane excitation, the same rules apply, which lead to a shift of the frequency limit. In this case, the mid frequency range begins above five in-plane modes per one-third octave band (cf. subsection 4.3.4).

As the frequency rises, the wave lengths decrease and the number of modes per frequency band increases. The influence of the boundary conditions on the mode shapes fades. Hence, the difference between predictions based on shell or solid elements becomes smaller [Winter et al 2017a]. Whereas the subsystem length and width are decisive for the system response at low frequencies, the influence of the width cancels inside the mid frequency range (cf. subsection 4.3.2, 4.3.3). The frequency averaged quantities behave similarly for different widths if even the structure with the smallest width contains subsystems with more than ten modes per one-third octave band and a modal overlap factor greater than unity. Moreover, it becomes less decisive in the mid frequency range if a certain number of randomly distributed loads acts correlated or with a random phase (RotR) on the structure (cf. subsection 4.3.5).

As the prerequisites of the SEA are fulfilled, an evaluation of the structure-borne sound transmission is possible by means of energy influence coefficients and loss factors. The choice of the computational approach for the vibration reduction index depends on the objective of the quantity. Predicting only bending wave transmission, either the transmission coefficient between two bending wave subsystems or the coupling loss factor η_{v_z}, which is based on the perpendicular translational part of the kinetic energy, can be used. Thereby, no in-plane energy is taken into account; neither in the sending subsystem nor in the receiving one. In the case of CLT plates, the transition from thin to thick plate theory is mostly below the limit of five modes per band and thus, the in-plane energy contributes significantly to the transmission behavior in the mid frequency range. To comply with the thick plate theory for out-of-plane oscillations, the vibration reduction index is computed on the basis of the effective bending wave velocity.

By contrast, the different computational approaches of DIN EN ISO 12354-1 [2017] are based on the thin plate theory and only bending transmission as shown in subsection 3.2.4 by converting them. If the contribution of in-plane waves is taken into account, an alternative computation of the vibration reduction index is proposed. Either, the transmission coefficients – e.g. from the excited bending wave subsystem towards all subsystems which form part of the receiving plate – are summed up on the basis of the wave approach or the coupling loss factors from the EFA are used which represent the entire energy transmission between two plates (cf. subsection 4.2.3). In this case, the division of the coupling loss factor by the group velocity of the effective bending waves, which equals the group velocity of out-

of-plane shear waves for thick plates, is inconsistent since the energy of longitudinal waves is transported faster (cf. section 4.2).

The EFA is able to consider specific scenarios of loading across the plate, whereas the SEA is restricted to inject a certain power into a subsystem of a specific wave type. Moreover, non-conservative couplings like damped, elastic interlayers can be modeled by the EFA, whereas the classical SEA is restricted to conservative couplings. For the investigated structures, the stiffness proportional damping of the elastic interlayer shows the lowest impact on the energy flow in the mid frequency range. There, kinetic and potential energy converge to similar values but the thickness modes within the interlayer still do not vibrate at resonance (cf. subsection 4.4.1).

5.3 High Frequency Range

The first thickness-shear resonance of a plate is chosen as the lower limit of the high frequency range. This corresponds to the upper limit of the Mindlin plate theory since it is not able to describe through thickness effects. Whereas thickness-shear resonances are clearly visible by an in-plane excitation (cf. subsection 4.3.4), thickness-stretch resonances are excited by a common, out-of-plane surface loading. The thickness resonances clearly dominate the energy distribution in the high frequency range. They slightly change the dynamic behavior of a plate in the low frequency range. Their excitation can only be avoided by an equally distributed loading through the thickness (cf. subsection 4.3.1). Since the thickness modes lead to a maximum displacement at the top and the bottom plane of the plates, the kinetic energy is clearly overestimated if it is approximated by means of the surface velocities (cf. subsection 4.2.4).

Neither the shell elements nor the classical SEA of plate-like structures are able to represent through-thickness effects. To identify them, solid elements have to be used (cf. subsection 4.3.1). Thus, simplifications, like the energy estimation by means of surface velocities, and engineering quantities, like the vibration reduction index, which both were developed for thin plate-like structures are not suitable at high frequencies (cf. subsection 4.2.4).

The thickness resonances significantly increase the number of modes per one-third octave band and the modal overlap factor (cf. subsection 2.3.2). Therefore, a reduced resolution in the frequency range is sufficient, whereas the short effective bending wave length requires a system discretization with an increased number of degrees of freedom (cf. subsection 4.1.5,

4.1.6). This can be solved either by refining the mesh or by using higher order polynomials [Winter and Müller 2017].

Since the thickness resonances are independent of width and length of a subsystem, the width of a junction has no influence on the energy transmission (cf. subsection 4.3.2). Moreover, a change of length affects only the energy flow from the modified subsystem to neighboring subsystems at high frequencies (cf. subsection 4.3.3). For plates of appropriate size, the energy flow starts to become exclusively dependent on the location of the excitation or more precisely on the distance of the loading from the junction: If the plate is sufficiently large, almost no reflections of the direct field occur from other boundaries. Comparing 100 realizations of RotR with less or equal 10 loads, the coefficient of variation increases significantly for high frequencies since the location matters (cf. subsection 4.5). For a higher number of loads, they result in an equal distribution on the plate, which indicates the reduced coefficient of variation. Doubling the length of the ceiling, the load density is halved for a constant number of loads and thereby, a proportionality can be identified because the energy flow into the wall is halved as well (cf. subsection 4.3.3).

If the elastic interlayer is used to model a screwed connection, the FE model is no longer valid as soon as the first thickness mode of the interlayer vibrates at resonance. Being an artefact of the FE model, this behavior does not correspond to a screwed connection (cf. subsection 4.4.1, 4.4.3). In the case of a factual elastic interlayer, the importance of the damping can be clearly identified as it eliminates the thickness resonance peaks of the interlayer. Neglecting the damping leads to a maximum energy transmission into the adjacent component (cf. subsection 4.4.1).

As length and width of the plates become subordinated for the energy flow at high frequencies, the corresponding mode shapes also seem to become insignificant. Therefore, the coupling of the two subsystems forming the continuous wall of a T-junction is reduced and the exchange with the adjacent ceiling is almost only dominated by the thickness of the connected components. This leads to a weakly coupled structure (cf. subsection 4.4.2).

5.4 Classification of a Structure

As a result, an appropriate method, the correct model and convenient evaluation quantities have to be selected depending on the frequency range of interest.

Table 5.1: Validity of EFA and SEA with respect to the frequency range.

		Frequency range		
Low	$M \approx 1$ $N \approx 5$	Mid	$f =$ $f_{TM,1}(c_{S,zy})$	High
		SEA for plate-like structures		
	EFA using shell element models			
	EFA using solid element models			

Methods and Models   Within this thesis, the EFA using a solid or a shell element model is compared to the SEA based on the wave types of plate-like structures or assuming exclusively bending waves. Based on the investigations in chapter 4, Tab. 5.1 assigns the two methods and their models to the three different frequency ranges which are introduced in the sections 5.1 to 5.3. Whereas the EFA is applicable to any frequency range using solid elements, the shell element model is restricted to plate-like structures. This applies also to the SEA, which additionally requires about five modes per band indicating the compliance of the SEA assumptions. If the energetic thin plate limit is above the frequency limit of five modes per band, therein, the entire energy transmission might be predicted by the simplified SEA, considering each plate-like component only as a bending wave subsystem. Moreover, the validity of this assumption depends on the boundary conditions and of the loading. For typical CLT structures, the thin plate limit occurs below the frequency limit of five modes per band. This contradicts with the application of the prediction model according to DIN EN ISO 12354-1 [2017], which is based on the simplified SEA assumption [Gerretsen 1979].

Evaluation Quantities   Various evaluation quantities are introduced and compared within this thesis. Table 5.2 summarizes their applicability related to the low, mid and high frequency range. The quantities based on the surface velocity oscillating perpendicular to the plate consider only the bending wave transmission. Due to the thickness resonances, they overestimate the bending wave energy at high frequencies. The coupling loss factors based on the sum of kinetic and potential energy can be evaluated across the entire frequency range, such as the energy influence coefficients, which constitute the primary output quantity of the EFA. For the use of the coupling loss factors as input data in a classical SEA model, they ideally fulfill the requirements of a proper-SEA matrix. Only in the case of pure bending wave transmission and fulfilling the SEA criteria, the vibration reduction index represents the complete energy transfer. This is the case when $< \tilde{K}(\eta_{ij}) >$ and $< \tilde{K}(\eta_{ij,v_z}) >$ are identical. $< \tilde{K}(\eta_{ij}) >$ considers also the in-plane energy transmission. But the faster energy

Table 5.2: Validity of evaluation quantities with respect to the frequency range.

Frequency range					Comment
Low	$M \approx 1$ $N \approx 5$	Mid	$f =$ $f_{TM,1}(c_{S,zy})$	High	
		A_{ij}, η_{ij}			including negative η_{ij}
A_{ij,v_z}, η_{ij,v_z}			$\mid$		only bending wave transmission
	$\mid$	$\tilde{\eta}_{ij}$	$\mid$		as input data for an SEA model
	$\mid$	$K(\tau_{BiAj})$	$\mid$		from SEA of plate-like structures
	$\mid$	$K(\tau_{BiBj})$	$\mid$		from SEA: only bending wave transmission
		$\tilde{K}(\eta_{ij})$			inconsistent above $K(\eta_{ij}) = K(\eta_{ij,v_z})$
	$\tilde{K}(\eta_{ij,v_z})$		$\mid$		only bending wave transmission
	$\tilde{K}(D_{v,ij})$		$\mid$ $\mid$		$=K(\eta_{ij,v_z})$ for 2 subsystems using η_0 from EFA

transport by the longitudinal waves is ignored due to the division by the group velocity of the effective bending waves. This leads to an inconsistent quantity for higher frequencies.

The transmission coefficients enable a consistent computation of the vibration reduction index for the mid frequency range. To extend its validity to higher frequencies, additional wave types representing the through-thickness behavior should be considered in the wave approach.

Identification of Frequency Range Limits   The interactive, web-based application "Vibroacoustics of plates", which is explained in the appendix A.1, has been made available to identify the frequency range limits for a specific structure as a function of its physical properties. In the case of cross-wise layered plates like CLT, the material properties are firstly homogenized according to the procedure presented in subsection 2.1.3. Afterwards, important vibroacoustic properties of the considered plate, such as the velocities of the inherent wave types, are calculated by means of analytical solutions. Based on the wave velocities, the thin plate limit, the first thickness resonances, the number of modes per band and the modal overlap factor are computed among others. With the aid of Tab. 5.1 and 5.2, these vibroacoustic properties indicate which configuration should be selected to investigate the specific structure in the frequency range of interest. Additionally, an estimation for an appropriate side length of finite elements with quadratic shape functions is given according to subsection 4.1.5.

6 Conclusion and Outlook

6.1 Conclusion

The present thesis presents a numerical, hybrid approach, namely the EFA, for the prediction of the structure-borne sound transmission in the whole audio-frequency range. A structure modeled by FE is divided into subsystems according to the division into components. After exciting each subsystem separately by a time-harmonic surface load applied to single elements, the displacement solution of an FE model is computed. In the post-processing, input power and subsystem energy are calculated and averaged with respect to time and space to cope with the increasing effects of uncertainty and variability for higher frequencies. Optionally, the quantities are additionally averaged per frequency band to gain the governing equations for an averaged ensemble of coupled systems in the steady state. By taking the quotient of the subsystem energy and the corresponding input power, the energy influence coefficients are obtained to describe the normalized energy that flows through a structure. By inversion, coupling and damping loss factors can be computed. In the case, the SEA criteria are fulfilled, the loss factors can be used as input data either for an SEA model or for the computation of vibration reduction indices to perform a prediction according to DIN EN ISO 12354-1 [2017].

The EFA offers the possibility to compute either the energy influence coefficients for a specific load scenario or - in case the load is unknown - for a so-called RotR excitation, which is a spatially uncorrelated loading at randomly chosen locations with the aim to equally excite all modes. By averaging over different realizations of RotR, a robust energy flow with respect to the loading can be predicted. A procedure is presented to find a minimum number of realizations in order to predict energy influence coefficients within a certain confidence interval. This corresponds to an estimation of the true mean with a certain precision. It serves for a robust and general prediction of the energy transmission behavior of the investigated junction independently of the loading.

Moreover, RotR helps to reduce the influence of strong coupling at low frequencies and thus, to increase the reliability of the related coupling loss factors, which is indicated by a lower condition number. The importance of a non-random phase shift of the single loads decreases with increasing frequency since the spatial modal behavior becomes more and more uncorrelated.

The EFA is based on an FE model, which is directly solved over a wide frequency range, and therefore, various modeling aspects have to be taken into account. Recommendations for the configurations are given either related to the investigated structures or exclusively depending on physical properties. For the resolution in space, a rule of thumb could be found for the maximum element size in dependency of the effective bending wave length. Moreover, a logarithmically equidistant spacing in the frequency range and the numerical interpolation by the composite trapezoidal rule resulted to be efficient. For a high modal overlap, the number of frequency steps per band can be clearly reduced, whereas the meshing has to be refined and the use of solid elements are obligatory as soon as the first thickness-mode is excited at resonance. For CLT, this occurs at comparatively low frequencies since the elastic modulus of wood perpendicular to the fiber direction is about one thirtieth of the one in fiber direction.

The comparisons to analytical, wave-based solutions of the SEA confirm that the classical SEA is limited to plate-like structures with a sufficient number of about five modes per frequency band and a modal overlap factor greater unity. For an in-plane excitation, the range of applicability is even smaller, since only in-plane modes contribute to the energy transport and thus, the lower frequency limit is shifted to five in-plane modes per band. In practice, the structure-borne sound transmission is described by means of the vibration reduction index according to DIN EN ISO 12354-1 [2017]; DIN EN ISO 12354-2 [2017]. This procedure is based on a simplified version of the SEA assuming thin, semi-infinite plates which contain only bending waves [Gerretsen 1979]. The assumption of pure bending wave transmission reduces the upper limit of the applicability, whereas the semi-infinite behavior is only fulfilled above a certain frequency limit. In the case of CLT, the thick plate theory applies already at low frequencies. Hence, the range of applicability shrinks or vanishes completely since the upper limit might occur below the lower one. Therefore, alternative computation techniques are suggested.

The variation of geometry and loading shows a frequency dependent influence of these characteristics on the energy flow. The influence of the length and especially of the width, which coincides with the junction length, decreases with increasing frequency. The thickness is

relevant at low and especially at high frequencies because it is decisive for the cut-on frequencies of the thickness modes. In this high frequency range, the location of the loading and especially its distance to the junction becomes important. For RotR, a proportionality can be derived as it leads to an equally distributed load density: The energy flow into the adjacent component decreases for a decreasing load density on the sending component.

The effect of the connection strength is investigated in different manners. Firstly, an elastic interlayer is inserted between two components leading to a clearly reduced energy flow in most one-third octave bands. If the interlayer shall represent the flexible behavior of a screwed junction, the FE model is no longer valid as soon as the first thickness mode of the elastic interlayer vibrates at resonance, because this behavior does not correspond to a screwed connection. These artefacts of the FE model can be avoided setting the mass of the interlayer to zero. Secondly, the elastic interlayer receives additionally stiffness proportional damping properties. Thus, the energy flow into the adjacent subsystem is reduced. This is the case especially at high frequencies as the damping eliminates the thickness resonance peaks of the interlayer. At low frequencies, large deformations occur inside the interlayer resulting in a non-resonant excitation of its thickness modes. Then, the damping loss factors do not only represent the internal damping but also the coupling damping. The coupling loss factors are not affected above the frequency limit of five modes per band and below the thickness resonances of the elastic interlayer. Thirdly, strong coupling arises over a wide frequency range between the subsystems forming the continuous wall of a T-junction. Therefore, an alternative division leading to only one wall subsystem is presented whereby the reduced resolution in space leads to more precise and non-negative coupling loss factors. Fourthly, the separation of the ceiling of an X-junction results in a clear decoupling over the whole frequency range except of one one-third octave band, even though the ceilings are indirectly connected via the lower and upper wall. Fifthly it is obvious that the more components are connected at one junction, the less energy flows into each subsystem.

A detailed summary of the investigations assigned to the different frequency ranges and related to the corresponding subsections is given in chapter 5. It is suggested to divide the frequency domain into three different ranges, which offer distinct modeling techniques and evaluation quantities. The web-based application "Vibroacoustics of Plates" has been made available for the identification of the frequency range limits as a function of the physical properties of the structure of interest. The interactive application is primarily designed for plates which have a symmetric, cross-wise layup like CLT, and applies also to homogeneous, orthotropic or isotropic plates.

6.2 Outlook

In chapter 4, the EFA was applied to calculate the energy flow across junctions consisting of raw CLT plates. One of the aims was to classify the raw junction by means of the vibration reduction index for the prediction of the sound transmission according to DIN EN ISO 12354-1 [2017]. Afterwards, measures to improve the sound reduction like a floating floor or a lining in front of the wall can be considered additively, e.g. in the computation of the normalized impact level for the flanking transmission path $L_{n,ij}$ according to Eq. (3.50). For massive constructions, this generally leads to good results. Kohrmann [2017] showed that it could be necessary to look at coupled timber structures like the construction of a ceiling in its entirety including e.g. the effect of the air inside a suspended ceiling. Thus, the corresponding construction of walls and ceilings could be added to the FE model which states the basis for the EFA. The augmented model opens several opportunities. Firstly, the energy that flows through the construction could be described by introducing the floating floor or the lining as additional subsystems leading to a non-symmetric energy influence coefficients matrix as it is shown within this thesis for elastic interlayers. Secondly, an "integral" vibration reduction index could be calculated including the measures of improvement. On the one hand, their effect on the flanking transmission can be examined and on the other hand, the resulting normalized impact level for the flanking transmission path $L_{n,ij}$ can be compared to the additive, standard procedure according to Eq. (3.50). Thirdly, the effect of specific loadings like a walking person or a tapping machine as well as the impact of building service equipment could be investigated. Fourthly, a combination with an acoustical evaluation model based on Integral Transform Methods [Kohrmann 2017] would directly lead to the radiated sound power in the neighboring room on the basis of the surface velocities. Using e.g. an X-junction, various scenarios of sound transmission paths could be realized.

To obtain the energy in one component of a multistory building, the prediction model of DIN EN ISO 12354-1 [2017] usually considers only the energy exchange across the adjacent junctions. The "in-situ"-correction by the factual total loss factor neglects the energy flowing back from farther components. To quantify the energy flowing into one component from all other components necessitates to model the entire building including also longer flanking paths. These describe the energy which crosses more than one junction from the source subsystem to the receiving subsystem. The longer flanking paths might be rather relevant at low frequencies, where the coupling loss factors are comparatively high. In this frequency range, a shell element model can be used, which implicates a generally justifiable numerical effort. Hence, the importance of the individual transmission paths can be evaluated by the EFA with respect to the frequency range.

For the present investigations, homogenized material parameters of CLT as well as coupling parameters resulting from a model updating at low frequencies are used. Comparisons to energy influence coefficients based on measurements show that the input parameters should be updated over a wider frequency range. This is rather complicated because conventional updating techniques only cover the low frequency range of well-separated modes. Usually, a comparison of a modal analysis with measured eigenfrequencies and eigenmodes is performed leading only to the mass and to the stiffness parameters of a thin plate. For higher frequencies, the out-of-plane shear moduli become more decisive for the vibrational behavior, which confirms the thick plate theory as well as recent investigations related to CLT plates [Meisinger 2017; Schneider 2017]. To fit additionally coupling and damping parameters, a comparison of force-induced vibrations of the coupled structure has to be performed. In this regard, it should be taken into account that damping of timber clearly varies between bending and shear modes according to Labonnote [2012].

With increasing frequency, the modal overlap increases. This requires alternative model updating techniques which also cope with a possibly frequency dependent behavior. In this context, it is important to mention that the EFA is able to work with frequency dependent material parameters as shown for the damped, elastic interlayer. Moreover, comparisons showed that the homogenized model of the CLT parameters has a restricted validity. The homogenization enables the use of shell elements. It generally facilitates the meshing and it is a helpful tool for analytical estimations of plate-like structures. By contrast, a layered FE model of solid elements is able to improve the prediction especially at high frequencies. In conclusion it is to say that, firstly, updated parameters and secondly, a layered FE model could be used to increase the reliability of the results.

Since the numerical effort at high frequencies is rather large, the limitation of the classical SEA to plate-like structures could be omitted by introducing subsystems for the additional wave types at high frequencies. Alternatively, the EFA could be combined with the FE/WFE method. According to the presented investigations, the influence of the subsystem width and length decreases with increasing frequency. Thus, the FE/WFE method, which assumes semi-infinite plates, could be used for higher frequencies. The FE model of the junction, possibly together with a small segment of the adjacent plates, could be reused. A small stripe of the FE model of the plates serves to calculate the wave properties of the plates. Finally, the reflection and transmission coefficients can be calculated as basis for coupling loss factors or vibration reduction indices.

The criteria for a division of the frequency range have been gained by means of studies of the energy flow across junctions of orthotropic and isotropic plates. For the component of

interest, these criteria can be determined by means of its physical properties. Thus, the criteria open up the possibility to choose an appropriate method, the correct model and convenient evaluation quantities for other applications, too.

Generally, the EFA can be applied to predict the sound transmission between building components of any other material beside CLT plates. Moreover, the EFA is an appropriate method for automotive or aerospace structures and can be augmented by additional subsystems of the cavities introducing a Fluid Structure Interaction.

A Appendix

A.1 Web Application: Vibroacoustics of Plates

The web-based, interactive application "Vibroacoustics of Plates" is made available on the website of the Chair of Structural Mechanics (`https://www.bm.bgu.tum.de`). It can be also accessed directly via `http://go.tum.de/632541`. It offers two basic features:

Firstly, the material parameters of plates with orthotropic layers can be homogenized through the thickness according to subsection 2.1.3. Prerequisite is a symmetric, crosswise layup with respect to the middle plane as it is the case for CLT plates.

Secondly, dynamic properties of isotropic and orthotropic plates and of their wave types can be calculated on the basis of section 2.2, subsection 2.3.2 and 4.1.5 as well as appendix A.2:

- Wave velocities of bending, effective bending, in-plane shear, shear with out-of-plane propagation, shear (corrected) with out-of-plane displacement, quasi-longitudinal (in-plane) and out-of-plane longitudinal waves as well as group velocities of bending and effective bending waves.

- Limiting frequencies: Thin plate limit and energetic thin plate limit as well as first thickness-shear and thickness-stretch resonances.

- First four eigenfrequencies of a four-sided simply supported Kirchhoff plate

- Modes per one-third octave band of effective bending, in-plane shear and quasi-longitudinal modes.

- Modal density of effective bending, in-plane shear and quasi-longitudinal modes.

- Modal overlap factor of effective bending, in-plane shear and quasi-longitudinal modes.

- Approximation of the maximum element size for quadratic shape functions on the basis of the effective bending wave length.

Figure A.1: Web-based application "Vibroacoustics of Plates": Homogenization of material parameters and calculation of properties of plates and of their wave types.

The handling of the application depicted in Fig. A.1 can be classified in two steps:

1. Inserting of physical properties of a homogenous plate or of a single layer on the left (default values are given) and pressing "Apply".

In the case of a layered plate, the material properties are homogenized through the thickness. Thus, the input data of the single layer is overwritten by homogenized material parameters of the plate after pressing "Apply". The input data of the single layer can be checked by pressing the button "Show Input".

2. On the right, the various results listed above can be studied using e.g. the zoom function and saved as .png.

Remark

The web-based application "Vibroacoustics of Plates" is designed for experienced engineers. The application shall simply serve as a computation tool. The theoretical background is summarized within this thesis including references. It is the duty of the engineer to range the results and to consider further aspects which are not taken into account by the application.

A.2 Eigenfrequencies of Orthotropic Kirchhoff Plates

For orthotropic plates, the eigenfrequencies of a four-sided simply supported Kirchhoff plate can be calculated according to Leissa [1969]:

$$f_{mn} = \frac{\pi}{2l^2\sqrt{\mu}} \sqrt{B_x m^4 + 2B_{xy} m^2 n^2 \left(\frac{l}{b}\right)^2 + B_y n^4 \left(\frac{l}{b}\right)^4} \tag{A.1}$$

with

$$B_i = \frac{E_i h^3}{12\left(1 - \nu_{xy}\nu_{yx}\right)}, \quad i \in \{x,y\} \qquad \text{Bending stiffness}$$

$$B_{xy} = B_x \nu_{yx} + 2\frac{G_{xy} h^3}{12} \qquad \text{Torsional stiffness}$$

$$\mu = \rho\,h \qquad \text{Areal mass}$$

$$l, b, h \qquad \text{Length, width, thickness}$$

$$m, n \qquad \text{Number of half-waves in } x\text{-, } y\text{-direction}$$

A.3 Material Data

Table A.1: Homogenized material parameters of wall and ceiling used in section 4.5.

	Wall			Ceiling / Single plate		
	x	y	z	x	y	z
E	$1.071\,10^{10}$	$7.649\,10^8$	$6.507\,10^8$	$8.325\,10^9$	$3.152\,10^9$	$6.507\,10^8$
	yx	zx	zy	yx	zx	zy
G	$6.753\,10^8$	$1.570\,10^8$	$8.864\,10^7$	$6.753\,10^8$	$1.570\,10^8$	$8.864\,10^7$
ν	0.063	0.043	0.161	0.095	0.045	0.088
ρ			450			
D			0.012			

Table A.2: Frequency dependent parameters of the elastic interlayer to model Sylodyn ND [Getzner Werkstoffe GmbH 2012], extrapolated above $1000\,\mathrm{Hz}$ [Müller 2017].

Frequency in Hz	Dynamic elastic modulus in $10^6\,\frac{\mathrm{N}}{\mathrm{m}^2}$	Loss factor η
31.5	2.30	0.120
40	2.33	0.130
50	2.36	0.141
63	2.38	0.153
80	2.41	0.167
100	2.44	0.181
125	2.47	0.197
160	2.50	0.214
200	2.52	0.233
250	2.55	0.253
315	2.58	0.275
400	2.61	0.299
500	2.64	0.325
630	2.68	0.354
800	2.71	0.385
1000	2.74	0.418
1200	2.77	0.455
1600	2.80	0.494
2000	2.83	0.537
2500	2.87	0.584
3150	2.90	0.635
4000	2.94	0.690
5000	2.97	0.751
6300	3.00	0.816
8000	3.04	0.887

List of Figures

List of Tables

Bibliography

[Altenbach et al 1996]   ALTENBACH, H. ; ALTENBACH, J. ; RIKARDS, R. B.: *Einführung in die Mechanik der Laminat- und Sandwichtragwerke: Modellierung und Berechnung von Balken und Platten aus Verbundwerkstoffen ; 47 Tabellen.* Stuttgart : Dt. Verl. für Grundstoffindustrie, 1996. – ISBN 3-342-00681-1

[Ben Souf et al 2013]   BEN SOUF, M. A. ; BAREILLE, O. ; ICHCHOU, M. N. ; TROCLET, B. ; HADDAR, M.: Variability of coupling loss factors through a wave finite element technique. In: *Journal of Sound and Vibration* 332 (2013), Nr. 9, p. 2179–2190. – ISSN 0022460X

[Blaß and Görlacher 2002]   BLASS, H. ; GÖRLACHER, R.: Brettsperrholz - Berechnungsgrundlagen. In: *Holzbau- Kalender* (2002), Nr. 2, p. 580–598

[Bodig and Jayne 1993]   BODIG, J. ; JAYNE, B. A.: *Mechanics of wood and wood composites.* Reprint ed. with corr. Malabar Fla. : Krieger Publ, 1993. – ISBN 0-89464-777-6

[Brandner et al 2016]   BRANDNER, R. ; FLATSCHER, G. ; RINGHOFER, A. ; SCHICKHOFER, G. ; THIEL, A.: Cross laminated timber (CLT): Overview and development. In: *European Journal of Wood and Wood Products* 74 (2016), Nr. 3, p. 331–351. – ISSN 0018-3768

[Brigham 1988]   BRIGHAM, E. O.: *The fast Fourier Transform and its applications.* Englewood Cliffs NJ : Prentice-Hall, 1988 (Prentice-Hall signal processing series). – ISBN 0-13-307505-2

[Bronštejn et al 2016]   BRONŠTEJN, I. N. ; SEMENDJAEV, K. A. ; MUSIOL, G. ; MÜHLIG, H.: *Taschenbuch der Mathematik.* 10., überarbeitete Auflage. Haan-Gruiten : Verlag Europa-Lehrmittel - Nourney Vollmer GmbH & Co. KG, 2016. – ISBN 9783808557891

[Chappell et al 2014]   CHAPPELL, D. J. ; LÖCHEL, D. ; SØNDERGAARD, N. ; TANNER, G.: Dynamical energy analysis on mesh grids: A new tool for describing the vibro-acoustic response of complex mechanical structures. In: *Wave Motion* 51 (2014), Nr. 4, p. 589–597. – ISSN 01652125

[Châteauvieux-Hellwig et al 2017]   CHÂTEAUVIEUX-HELLWIG, C. ; SCHRAMM, M. ; RABOLD, A.: Schlussbericht: Vibroakustik im Planungsprozess für Holzbauten: Teilprojekt 4: Bauteilprüfung, FEM-Modellierung und Validierung / ift gemeinnützige Forschungs- und Entwicklungsgesellschaft mbH. Rosenheim, 2017. – Research Report. IGF-Vorhaben 18725N

[Chazot et al 2013]   Chazot, J.-D. ; Nennig, B. ; Perrey-Debain, E.: Performances of the Partition of Unity Finite Element Method for the analysis of two-dimensional interior sound fields with absorbing materials. In: *Journal of Sound and Vibration* 332 (2013), Nr. 8, p. 1918–1929. – ISSN 0022460X

[Cicirello and Langley 2013]   Cicirello, A. ; Langley, R. S.: The vibro-acoustic analysis of built-up systems using a hybrid method with parametric and non-parametric uncertainties. In: *Journal of Sound and Vibration* 332 (2013), Nr. 9, p. 2165–2178. – ISSN 0022460X

[Cook 1989]   Cook, R. D.: *Concepts and applications of finite element analysis.* New York, NY : Wiley, 1989. – ISBN 0471356050

[Craik 2003]   Craik, R. J. M.: *Sound transmission through buildings: Using statistical energy analysis.* Reprint. Aldershot : Ashgate, 2003. – ISBN 0-566-07572-5

[Cremer 1967]   Cremer, L.: *Körperschall: Physikalische Grundlagen und technische Anwendungen.* Berlin, Heidelberg : Springer Berlin Heidelberg, 1967. – ISBN 978-3-662-08185-3

[Cremer 1988]   Cremer, L.: *Structure-Borne Sound: Structural Vibrations and Sound Radiation at Audio Frequencies.* Berlin, Heidelberg : Springer Berlin Heidelberg, 1988. – ISBN 978-3-662-10123-0

[Cremer and Heckl 1996]   Cremer, L. ; Heckl, M.: *Körperschall: Physikalische Grundlagen und technische Anwendungen.* 2., völlig neu bearb. Aufl. Berlin u.a. : Springer, 1996. – ISBN 3-540-54631-6

[Culla and Sestieri 2006]   Culla, A. ; Sestieri, A.: Is it possible to treat confidentially SEA the wolf in sheep's clothing? In: *Mechanical Systems and Signal Processing* 20 (2006), Nr. 6, p. 1372–1399. – ISSN 08883270

[Deckers et al 2014]   Deckers, E. ; Atak, O. ; Coox, L. ; D'Amico, R. ; Devriendt, H. ; Jonckheere, S. ; Koo, K. ; Pluymers, B. ; Vandepitte, D. ; Desmet, W.: The wave based method: An overview of 15 years of research. In: *Wave Motion* 51 (2014), Nr. 4, p. 550–565. – ISSN 01652125

[Deutsches Institut für Bautechnik 2009]   Deutsches Institut für Bautechnik: *Allgemeine bauaufsichtliche Zulassung Z-9.1-501: MERK-Dickholz: Antragsteller: Finnforest Merk GmbH.* 2009

[Deutsches Institut für Bautechnik 2014]   Deutsches Institut für Bautechnik: *Allgemeine bauaufsichtliche Zulassung Z-9.1-501: Leno Brettsperrholz: Antragsteller: Merk Timber GmbH.* 2014

[DIN EN 338 2016]   DIN EN 338: *Structural timber - Strength classes, German version EN 338.* 2016

[DIN EN ISO 10848-1 2006]   DIN EN ISO 10848-1: *Akustik -Messung der Flankenübertragung von Luftschall und Trittschall - Teil 1 Rahmendokument.* 2006

[DIN EN ISO 12354-1 2017]   DIN EN ISO 12354-1: *Bauakustik - Berechnung der akustischen Eigenschaften von Gebäuden aus den Bauteileigenschaften - Teil 1: Luftschalldämmung zwischen Räumen.* 2017

[DIN EN ISO 12354-2 2017]   DIN EN ISO 12354-2: *Bauakustik - Berechnung der akustischen Eigenschaften von Gebäuden aus den Bauteileigenschaften - Teil 2: Trittschalldämmung zwischen Räumen.* 2017

[Fahy 1987]   FAHY, F. J.: *Sound and Structural Vibration: Radiation, Transmission and Response.* Oxford : Elsevier Science, 1987. – URL http://gbv.eblib.com/patron/FullRecord.aspx?p=1133684. – ISBN 9780122476716

[Fahy and Mohammed 1992]   FAHY, F. J. ; MOHAMMED, A. D.: A study of uncertainty in applications of sea to coupled beam and plate systems, part I: Computational experiments. In: *Journal of Sound and Vibration* 158 (1992), Nr. 1, p. 45–67. – ISSN 0022460X

[Fahy and de Yuan 1987]   FAHY, F. J. ; YUAN, Y. de: Power flow between non-conservatively coupled oscillators. In: *Journal of Sound and Vibration* 114 (1987), Nr. 1, p. 1–11. – ISSN 0022460X

[Fasold et al 1984]   FASOLD, W. (Editor.) ; KRAAK, W. (Editor.) ; SCHIRMER, W. (Editor.): *Taschenbuch Akustik.* VEB Verlag Technik, 1984

[Felippa 2004]   FELIPPA, C. A.: *Introduction to Finite Element Methods*, University of Colorado Boulder, Textbook, 2004. – URL http://www.colorado.edu/engineering/CAS/courses.d/IFEM.d

[Finnveden 2004]   FINNVEDEN, S.: Evaluation of modal density and groupvelocity by a finite element method. In: *Journal of Sound and Vibration* (2004), Nr. 273, p. 51–75. – ISSN 0022460X

[Finnveden 2011]   FINNVEDEN, S.: A quantitative criterion validating coupling power proportionality in statistical energy analysis. In: *Journal of Sound and Vibration* 330 (2011), Nr. 1, p. 87–109. – ISSN 0022460X

[Flodén et al 2014]   FLODÉN, O. ; PERSSON, K. ; SANDBERG, G.: Reduction methods for the dynamic analysis of substructure models of lightweight building structures. In: *Computers & Structures* 138 (2014), p. 49–61. – ISSN 00457949

[Fredö 1997]   FREDÖ, C. R.: A sea-like approach for the derivation of energy flow coefficients with a finite element model. In: *Journal of Sound and Vibration* 199 (1997), Nr. 4, p. 645–666. – ISSN 0022460X

[Gerretsen 1979]   GERRETSEN, E.: Calculation of the sound transmission between dwellings by partitions and flanking structures. In: *Applied Acoustics* 12 (1979), Nr. 6, p. 413–433. – ISSN 0003682X

[Gerretsen 1994]   GERRETSEN, E.: European developments in prediction models for building acoustics. In: *Acta Acustica* 2 (1994), p. 205–214

[Getzner Werkstoffe GmbH 2012]   Getzner Werkstoffe GmbH: *Data sheet of Sylodyn ND.* 2012

[Grimsel 1999]   Grimsel, M.: *Mechanisches Verhalten Holz: Struktur- und Parameteridentifikation eines anisotropen Werkstoffes.* Dresden, Technischen Universität, Dissertation, 1999

[Gülzow 2008]   Gülzow, A.: *Zerstörungsfreie Bestimmung der Biegesteifigkeiten von Brettsperrholzplatten,* Eidgenössische Technische Hochschule Zürich, Dissertation, 2008

[Hambric et al 2016]   Hambric, S. A. (Editor.) ; Sung, S. H. (Editor.) ; Nefske, D. J. (Editor.): *Engineering vibroacoustic analysis: Methods and applications.* 2016. – ISBN 9781119953449

[Haut et al 2017]   Haut, S. ; Mecking, S. ; Schanda, U.: Experimentelle Bestimmung des Abstrahlgrades und des inneren Verlustfaktors orthotroper Platten. In: *43. Jahrestagung für Akustik,* 2017, p. 489–492

[Heckl 1960]   Heckl, M.: Untersuchungen an orthotropen Platten. In: *Acta Acustica united with Acustica* 10 (1960), Nr. 2, p. 109–115(7). – ISSN 16101928

[Hopkins 2007]   Hopkins, C.: *Sound insulation: Theory into Practice.* 1st ed. Oxford : Butterworth-Heinemann, 2007. – ISBN 978-0-7506-6526-1

[Hopkins 2014]   Hopkins, C.: Determination of Vibration Reduction Indices Using Wave Theory for Junctions in Heavyweight Buildings. In: *Acta Acustica united with Acustica* 100 (2014), Nr. 6, p. 1056–1066. – ISSN 16101928

[Hopkins et al 2016]   Hopkins, C. ; Crispin, C. ; Poblet-Puig, J. ; Guigou-Carter, C.: Regression curves for vibration transmission across junctions of heavyweight walls and floors based on finite element methods and wave theory. In: *Applied Acoustics* 113 (2016), p. 7–21. – ISSN 0003682X

[Kihlmann 1967]   Kihlmann, T.: Transmission of Strucuture-Borne Sound in Buildings: A theoretical and experimental investigation / National Swedish Institute for Buidling Research. Stockholm, 1967. – Research Report. Tekniska Höcskolan i Lund

[Kohrmann 2017]   Kohrmann, M.: *Numerical Methods for the Vibro-Acoustic Assessment of Timber Floor Constructions.* München, Technische Universität München, Dissertation, 2017

[Kreutz and Müller 2014]   Kreutz, J. ; Müller, G.: Erweiterte Stabelemente unter Verwendung von Einheitsverformungszuständen am Querschnitt. In: *Bauingenieur* (2014), Nr. 05-2014, p. 216–224

[Labonnote 2012]   Labonnote, N.: *Damping in Timber Structures,* Norwegian University of Science and Technology, PhD thesis, 2012

[Lafont et al 2013] Lafont, T. ; Totaro, N. ; Le Bot, A.: Review of statistical energy analysis hypotheses in vibroacoustics. In: *Proceedings of the Royal Society A: Mathematical, Physical and Engineering Sciences* 470 (2013), Nr. 2162, p. 20130515. – ISSN 1364-5021

[de Langhe and Sas 1996] Langhe, K. de ; Sas, P.: Statistical analysis of the power injection method. In: *The Journal of the Acoustical Society of America* 100 (1996), Nr. 1, p. 294–303. – ISSN 1520-8524

[Langley 2008] Langley, R. S.: Recent advances and remaining challenges in the Statistical Energy Analysis of dynamic systems. In: *VII International Conference on Structural Dynamics*, 2008

[Langley and Heron 1990] Langley, R. S. ; Heron, K. H.: Elastic wave transmission through plate/beam junctions. In: *Journal of Sound and Vibration* 143 (1990), Nr. 2, p. 241–253. – ISSN 0022460X

[Leissa 1969] Leissa, A. W. ; United States (Editor.): Vibration of plates / NASA. 1969. – Research Report. Tabulated numerical results of theories of plate vibration

[Ljunggren 1991] Ljunggren, S.: Airborne sound insulation of thick walls. In: *The Journal of the Acoustical Society of America* 89 (1991), Nr. 5, p. 2338–2345. – ISSN 1520-8524

[Lutes and Sarkani 2004] Lutes, L. D. ; Sarkani, S.: *Random vibrations: Analysis of structural and mechanical systems.* Amsterdam : Elsevier Butterworth-Heinemann, 2004. – ISBN 9781280964374

[Lyon and DeJong 1995] Lyon, R. H. ; DeJong, R. G.: *Theory and application of statistical energy analysis.* 2. ed. Boston et al : Butterworth-Heinemann, 1995. – ISBN 0-7506-9111-5

[Mace 2003] Mace, B.: Statistical energy analysis, energy distribution models and system modes. In: *Journal of Sound and Vibration* 264 (2003), Nr. 2, p. 391–409. – ISSN 0022460X

[Mace et al 2013] Mace, B. ; Desmet, W. ; Pluymers, B.: Mid-Frequency Methods in Sound and Vibration—Part A. In: *Journal of Sound and Vibration* 332 (2013), Nr. 8, p. 1895–1896. – ISSN 0022460X

[Mace 1994] Mace, B. R.: On the statistical energy analysis hypothesis of coupling power proportionality and some implications of its failure. In: *Journal of Sound and Vibration* 178 (1994), Nr. 1, p. 95–112. – ISSN 0022460X

[Mace and Shorter 2000] Mace, B. R. ; Shorter, P. J.: Energy Flow Models from Finite Element Analysis. In: *Journal of Sound and Vibration* 233 (2000), Nr. 3, p. 369–389. – ISSN 0022460X

[Mecking 2014] Mecking, S.: *Bauteilstöße im Holzmassivbau - Messtechnische Bestimmung von Eingangsgrößen für eine Schallschutzprognose*, Hochschule Rosenheim, Masterarbeit, 2014

[Mecking et al 2017a]   Mecking, S. ; Kruse, T. ; Winter, C. ; Schanda, U.: Schluss-bericht: Vibroakustik im Planungsprozess für Holzbauten: Teilprojekt 3: Parameteren-twicklung und SEA-Modellierung / Hochschule Rosenheim. 2017. – Research Report. IGF-Vorhaben 18724N

[Mecking et al 2017b]   Mecking, S. ; Scheibengraber, M. ; Kruse, T. ; Schanda, U. ; Wellisch, U.: Experimentally based statistical analysis of the vibrational energy of CLT building elements. In: Gibbs, B. (Editor.): *Proceedings of the 24th International Congress on Sound and Vibration*, 2017

[Mees and Vermeir 1993]   Mees, P. ; Vermeir, O.: Structure-Borne Sound Transmission at Elastically Connected Plates. In: *Journal of Sound and Vibration* 166 (1993), Nr. 1, p. 55–76. – ISSN 0022460X

[Meier 2000]   Meier, A.: *Die Bedeutung des Verlustfaktors bei der Bestimmung der Schalldämmung im Prüfstand.* Aachen, RWTH Aachen, Dissertation, 2000

[Meisinger 2017]   Meisinger, M.: *Untersuchung der Sensitivität der Energieflussanalyse von Massivholzkonstruktionen hinsichtlich Frequenzauflösung, Materialeigenschaften und Laststellung*, Technische Universität München, Masterthesis, 2017

[Merkel and Öchsner 2014]   Merkel, M. ; Öchsner, A.: *Eindimensionale Finite Ele-mente: Ein Einstieg in die Methode.* 2., neu bearb. u. erg. Aufl. 2014. Berlin Heidelberg : Springer Berlin Heidelberg, 2014. – ISBN 978-3-642-54482-8

[Mindlin 1951]   Mindlin, R. D.: Influence of rotatory inertia and shear on flexural motions of isotropic, elastic plates. In: *Journal of Applied Mechanics* (1951), Nr. 18, p. 31–38

[Mindlin and Yang 2006]   Mindlin, R. D. (Editor.) ; Yang, J. (Editor.): *An introduc-tion to the mathematical theory of vibrations of elastic plates.* Hackensack, N.J : World Scientific, 2006. – ISBN 9789812703811

[Mitrou et al 2017]   Mitrou, G. ; Ferguson, N. ; Renno, J.: Wave transmission through two-dimensional structures by the hybrid FE/WFE approach. In: *Journal of Sound and Vibration* 389 (2017), p. 484–501. – ISSN 0022460X

[Möser and Kropp 2010]   Möser, M. ; Kropp, W.: *Körperschall: Physikalische Grundla-gen und technische Anwendungen.* Berlin, Heidelberg : Springer-Verlag Berlin Heidelberg, 2010 (SpringerLink : Bücher). – ISBN 3540490485

[Müller 1999]   Müller, G.: Die Statistische Energieanalyse - eine Methode der nu-merischen Akustik. In: Verein Deutscher Ingenieure (Editor.): *Maschinenakustik '99.* Düsseldorf : VDI-Verl., 1999 (VDI-Berichte), p. 23–45. – ISBN 3180914912

[Müller 2015]   Müller, G.: *Continuum Mechanics and Tensor Analysis*, Technische Uni-versität München, Lecture Notes, 2015

[Müller 2016]   Müller, G.: *Baudynamik*, Technische Universität München, Lecture Notes, 2016

[Müller and Groth 2007]   MÜLLER, G. ; GROTH, C.: *FEM für Praktiker: Grundlagen: Basiswissen und Arbeitsbeispiele zu FEM Anwendungen.* expert-Verlag, 2007. – ISBN 9783816926856

[Müller 2017]   MÜLLER, P.: *Energieflussanalyse von Brettsperrholzstößen - Frequenzabhängige Untersuchung geometrischer Abhängigkeiten unter Berücksichtigung von elastischen Zwischenlagen*, Technische Universität München, Masterthesis, 2017

[Negreira et al 2014]   NEGREIRA, J. ; AUSTRELL, P.-E. ; FLODÉN, O. ; BARD, D.: Characterisation of an Elastomer for Noise and Vibration Insulation in Lightweight Timber Buildings. In: *Building Acoustics* 21 (2014), Nr. 4, p. 251–276. – ISSN 1351-010X

[Niemz and Caduff 2008]   NIEMZ, P. ; CADUFF, D.: Untersuchungen zur Bestimmung der Poissonschen Konstanten an Fichtenholz. In: *Holz als Roh- und Werkstoff* 66 (2008), Nr. 1, p. 1–4. – ISSN 0018-3768

[Nilsson and Liu 2015]   NILSSON, A. ; LIU, B.: *Vibro-Acoustics: Volume 1.* Second edition. Berlin and Beijing : Springer and Science Press, 2015. – ISBN 9783662478073

[Nilsson and Liu 2016]   NILSSON, A. ; LIU, B.: *Vibro-Acoustics: Volume 2.* Second edition. Beijing and Heidelberg and New York and Dordrecht and London : Science Press and Springer, 2016. – ISBN 9783662479346

[Nishino and Honda 2006]   NISHINO, H. ; HONDA, I.: Prediction of vibration energy transmission in a structure consiting of thick elements. In: *The Thirteenth International Congress on Sound and Vibration*, 2006

[Panagiotopoulos et al 2015]   PANAGIOTOPOULOS, D. ; ROBL, C. ; MALIK, M. K. ; WINTER, C.: Statistical Energy Analysis in MATLAB / Technische Universität München. URL https://github.com/ChairOfStructuralMechanicsTUM/SEA-Matlab-GUI, 2015. – Research Report. Development of a Graphical User Interface

[Paolini et al 2016]   PAOLINI, A. ; FRISCHMANN, F. ; KOLLMANNSBERGER, S. ; RANK, E. ; MECKING, S. ; WINTER, C. ; BUCHSCHMID, M. ; MÜLLER, G.: Parameteridentifikation von Brettsperrholz-Elementen mittels Bayesscher Optimierung. In: *42. Jahrestagung für Akustik*, 2016, p. 523–526

[Paolini et al 2017]   PAOLINI, A. ; KOLLMANNSBERGER, S. ; WINTER, C. ; BUCHSCHMID, M. ; MÜLLER, G. ; RABOLD, A. ; MECKING, S. ; SCHANDA, U. ; RANK, E.: A high-order finite element model for vibration analysis of cross-laminated timber assemblies. In: *Building Acoustics* 24 (2017), Nr. 3, p. 135–158. – ISSN 1351-010X

[Papaioannou 2016]   PAPAIOANNOU, I.: *Stochastic Finite Element Methods*, Technische Universität München, Lecture Notes, 2016

[Pavic 2005]   PAVIC, G.: The role of damping on energy and power in vibrating systems. In: *Journal of Sound and Vibration* 281 (2005), Nr. 1-2, p. 45–71. – ISSN 0022460X

[PCB Piezotronics 2017]   PCB PIEZOTRONICS: *Data sheet of the mechanical impedance sensor 288D01.* 2017

[Pedersen 1995]   PEDERSEN, D. B.: Estimation of vibration attenuation through junctions of building structures. In: *Applied Acoustics* 46 (1995), Nr. 3, p. 285–305. – ISSN 0003682X

[Peiffer et al 2011]   PEIFFER, A. ; MÖSER, C. ; MEZNI, M. ; REDMANN, D.: FE-, SEA- und hybride Simulation des Innenlärms von Propellerflugzeugen. In: *37. Jahrestagung für Akustik*, 2011, p. 807–808

[Peiffer et al 2013]   PEIFFER, A. ; MÖSER, C. ; RÖDER, A.: Transmission loss modelling of double wall structures using hybrid simulation. In: *Proceedings of the International Conference on Acoustics*, 2013, p. 1161–1164. – ISBN 978-3-939296-05-8

[Petersen 2000]   PETERSEN, C.: *Dynamik der Baukonstruktionen.* Wiesbaden : Vieweg+Teubner Verlag, 2000. – ISBN 978-3-322-80315-3

[Råde and Westergren 2000]   RÅDE, L. ; WESTERGREN, B.: *Springers mathematische Formeln: Taschenbuch für Ingenieure Naturwissenschaftler Informatiker Wirtschaftswissenschaftler.* Berlin [u.a.] : Springer, 2000. – ISBN 3-540-67505-1

[Ranz 2007]   RANZ, T.: Ein feuchte- und temperaturabhängiger anisotroper Werkstoff: Holz. In: *Beiträge zur Materialtheorie* (2007), Nr. 02

[Renno and Mace 2013]   RENNO, J. M. ; MACE, B. R.: Calculation of reflection and transmission coefficients of joints using a hybrid finite element/wave and finite element approach. In: *Journal of Sound and Vibration* 332 (2013), Nr. 9, p. 2149–2164. – ISSN 0022460X

[Rindel 1994]   RINDEL, J.: Dispersion and Absorption of Structure-Borne Sound in Acoustically Thick Plates. In: *Applied Acoustics* 41 (1994), p. 97–111. – ISSN 0003682X

[Schickhofer et al 2010]   SCHICKHOFER, G. (Editor.) ; BOGENSPERGER, T. (Editor.) ; AUGUSTIN, M. (Editor.): *BSPhandbuch: Holz- Massivbauweise in Brettsperrholz ; Nachweise auf Basis des neuen europäischen Normenkonzepts.* 2. überarb. Aufl. Graz : Verl. der Techn. Univ, 2010. – ISBN 9783851251098

[Schneider 2017]   SCHNEIDER, F.: *Bayesian identification of cross laminated timber plates using surrogate models*, Technische Universität München, Masterthesis, 2017

[Schneider et al 2006]   SCHNEIDER, K.-J. (Editor.) ; GORIS, A. (Editor.) ; BERNER, K. (Editor.): *Bautabellen für Ingenieure: Mit Berechnungshinweisen und Beispielen ; [auf CD-ROM: Stabwerksprogramm IQ 100 B, Tools für den konstr. Ingenieurbau, Fachinformationen, Normentexte].* 17. Aufl. Neuwied : Werner, 2006. – ISBN 9783804152281

[Shorter and Langley 2005]   SHORTER, P. J. ; LANGLEY, R. S.: Vibro-acoustic analysis of complex systems. In: *Journal of Sound and Vibration* 288 (2005), Nr. 3, p. 669–699. – ISSN 0022460X

[Souza Lenzi et al 2013]   SOUZA LENZI, M. ; LEFTERIU, S. ; BERIOT, H. ; DESMET, W.: A fast frequency sweep approach using Padé approximations for solving Helmholtz finite element models. In: *Journal of Sound and Vibration* 332 (2013), Nr. 8, p. 1897–1917. – ISSN 0022460X

[Stritzelberger and von Estorff 2014] STRITZELBERGER, B. ; VON ESTORFF, O.: Die Energie-Finite-Elemente-Methode zur Anwendung im Schiffbau. In: *40. Jahrestagung für Akustik*, 2014, p. 391–392

[Sun et al 1987] SUN, J. C. ; CHOW, L. C. ; LALOR, N. ; RICHARDS, E. J.: Power flow and energy balance of non-conservatively coupled structures, II: Experimental verification of theory. In: *Journal of Sound and Vibration* 112 (1987), Nr. 2, p. 331–343. – ISSN 0022460X

[Tanner 2009] TANNER, G.: Dynamical energy analysis—Determining wave energy distributions in vibro-acoustical structures in the high-frequency regime. In: *Journal of Sound and Vibration* 320 (2009), Nr. 4–5, p. 1023–1038. – ISSN 0022460X

[Thite and Mace 2007] THITE, A. N. ; MACE, B. R.: Robust estimation of coupling loss factors from finite element analysis. In: *Journal of Sound and Vibration* 303 (2007), Nr. 3-5, p. 814–831. – ISSN 0022460X

[Thompson and Pinsky 1994] THOMPSON, L. L. ; PINSKY, P. M.: Complex wavenumber Fourier analysis of the p-version finite element method. In: *Computational Mechanics* 13 (1994), Nr. 4, p. 255–275. – ISSN 0178-7675

[Timoshenko 1922] TIMOSHENKO, S. P.: X. On the transverse vibrations of bars of uniform cross-section. In: *Philosophical Magazine Series 6* 43 (1922), Nr. 253, p. 125–131. – ISSN 1941-5982

[Timpte 2016] TIMPTE, A.: *Stoßstellen im Massivholzbau: Konstruktionen, akustische Kenngrößen, Schallschutzprognose.* Berlin, Technische Universität Berlin and Hochschule Rosenheim, Masterarbeit, 2016

[Vergote et al 2013] VERGOTE, K. ; VANMAELE, C. ; VANDEPITTE, D. ; DESMET, W.: An efficient wave based approach for the time-harmonic vibration analysis of 3D plate assemblies. In: *Journal of Sound and Vibration* 332 (2013), Nr. 8, p. 1930–1946. – ISSN 0022460X

[Wang and Lai 2005] WANG, C. ; LAI, J.: Discussions on "On the number of modes required for statistical energy analysis-based calculations". In: *Journal of Sound and Vibration* 281 (2005), Nr. 1-2, p. 475–480. – ISSN 0022460X

[Weineisen 2014] WEINEISEN, C.: *Modellierung einer Flugzeugstruktur mit der Statistischen Energieanalyse*, Technische Universität München, Masterthesis, 2014

[Werkle 2008] WERKLE, H.: *Finite Elemente in der Baustatik: Statik und Dynamik der Stab- und Flächentragwerke ; mit 43 Tabellen.* Wiesbaden : Vieweg, 2008. – ISBN 978-3-8348-9447-2

[Wilhelm 2017] WILHELM, T.: *Untersuchung der Körperschalltransmission von Massivholzkonstruktionen - Gegenüberstellung verschiedener Auswertegrößen innerhalb einer hybriden FEM-SEA-Methode*, Technische Universität München, Masterthesis, 2017

[Winter 2012]   Winter, C.: *Messtechnische Untersuchung leichter Deckentragwerke im Wellenzahlbereich und Prognose der abgestrahlten Schallleistung*, Technische Universität München, Masterthesis, 2012

[Winter et al 2014]   Winter, C. ; Buchschmid, M. ; Mecking, S. ; Weineisen, C. ; Müller, G. ; Schanda, U.:   Modelling the Sound Transmission across Junctions of Building Components by Energy Influence Coefficients. In: *IX International Conference on Structural Dynamics*, 2014, p. 3265–3271

[Winter et al 2015]   Winter, C. ; Buchschmid, M. ; Müller, G.:   Ein hybrider FEM/SEA Ansatz zur Prognose der Schallübertragung an Bauteilstößen. In: *41. Jahrestagung für Akustik*, 2015, p. 567–570

[Winter et al 2016]   Winter, C. ; Buchschmid, M. ; Müller, G.: Untersuchung leichter Massivholzkonstruktionen im mittleren und höheren Frequenzbereich. In: *42. Jahrestagung für Akustik*, 2016, p. 498–501

[Winter et al 2017a]   Winter, C. ; Buchschmid, M. ; Müller, G.: Beschreibung des Energieflusses über Stoßstellen leichter Massivholzkonstruktionen im mittleren und höheren Frequenzbereich. In: *43. Jahrestagung für Akustik*, 2017, p. 501–504

[Winter et al 2017b]   Winter, C. ; Buchschmid, M. ; Müller, G.:   Modeling of orthotropic plates out of cross laminated timber in the mid and high frequency range. In: *Procedia Engineering* 199 (2017), p. 1392–1397. – ISSN 18777058

[Winter et al 2017c]   Winter, C. ; Buchschmid, M. ; Müller, G.: Robust Estimation of the Energy Flow in Timber Structures. In: Gibbs, B. (Editor.): *Proceedings of the 24th International Congress on Sound and Vibration*, 2017, p. 1–8

[Winter and Müller 2017]   Winter, C. ; Müller, G.: Schlussbericht: Vibroakustik im Planungsprozess für Holzbauten: Teilprojekt 5: Frequenzbereichsabhängige Modellbildung zur Prognose der Körperschallausbreitung in Holzbauten / Technische Universität München. 2017. – Research Report. IGF-Vorhaben 18726N

[Woyczynski 2011]   Woyczynski, W. A.: *A first course in statistics for signal analysis.* Boston u.a. : Birkhäuser, 2011. – ISBN 0-8176-4398-2

[Yu 1996]   Yu, Y.-Y.: *Vibrations of Elastic Plates: Linear and Nonlinear Dynamical Modeling of Sandwiches, Laminated Composites, and Piezoelectric Layers.* New York : Springer, 1996. – ISBN 1461223385

[Zaveri 1984]   Zaveri, K.: *Modal analysis of large structures - multiple exciter systems.* 1st ed. Nærum : Brüel & Kjær, 1984. – ISBN 9788787355032

[Zeidler 2013]   Zeidler, E. (Editor.): *Springer-Taschenbuch der Mathematik.* Wiesbaden : Vieweg + Teubner, 2013. – ISBN 978-3-8348-2359-5